Intermediate Scale Laboratory Testing to Understand Mechanisms of Capillary and Dissolution Trapping during Injection and Post-Injection of CO_2 in Heterogeneous Geological Formations

FINAL SCIENTIFIC/TECHNICAL REPORT

Reporting Period: October 01, 2010 to December 31, 2014

Principal Authors:

Tissa Illangasekare (PI)

Luca Trevisan

Elif Agartan

Hiroko Mori

Javier Vargas-Johnson

Ana González-Nicolás

Abdullah Cihan (co-PI)

Jens Birkholzer (co-PI)

Quanlin Zhou (co-PI)

Date Report Issued:

March 31, 2015

DOE Award Number:

DE-FE0004630

Submitting Organization:

Colorado School of Mines

1500 Illinois street

Golden, CO 80401

USA

Disclaimer

Abstract

Carbon Capture and Storage (CCS) represents a technology aimed to reduce atmospheric loading of CO_2 from power plants and heavy industries by injecting it into deep geological formations, such as saline aquifers. A number of trapping mechanisms contribute to effective and secure storage of the injected CO_2 in supercritical fluid phase ($scCO_2$) in the formation over the long term. The primary trapping mechanisms are structural, residual, dissolution and mineralization. Knowledge gaps exist on how the heterogeneity of the formation manifested at all scales from the pore to the site scales affects trapping and parameterization of contributing mechanisms in models. An experimental and modeling study was conducted to fill these knowledge gaps. Experimental investigation of fundamental processes and mechanisms in field settings is not possible as it is not feasible to fully characterize the geologic heterogeneity at all relevant scales and gathering data on migration, trapping and dissolution of $scCO_2$. Laboratory experiments using $scCO_2$ under ambient conditions are also not feasible as it is technically challenging and cost prohibitive to develop large, two- or three-dimensional test systems with controlled high pressures to keep the $scCO_2$ as a liquid. Hence, an innovative approach that used surrogate fluids in place of $scCO_2$ and formation brine in multi-scale, synthetic aquifers test systems ranging in scales from centimeter to meter scale developed used. New modeling algorithms were developed to capture the processes controlled by the formation heterogeneity, and they were tested using the data from the laboratory test systems. The results and findings are expected to contribute toward better conceptual models, future improvements to DOE numerical codes, more accurate assessment of storage capacities, and optimized placement strategies. This report presents the experimental and modeling methods and research results.

Table of contents

LIST OF FIGURES

1 EXECUTIVE SUMMARY

Background and Objectives: Carbon Capture and Storage (CCS) represents a technology aimed to reduce atmospheric loading of CO_2 from power plants and heavy industries by injecting it into deep geological formations, such as saline aquifers. The storage process relies on the effectiveness of safely retaining the injected CO_2 in supercritical fluid phase ($scCO_2$) in the formation over the long term through a number of trapping mechanisms that include structural, residual, dissolution, and mineral trapping. Numerically based simulation models of trapping in deep geologic formations are increasingly going to play an important role in site selection and assessment of carbon storage potential, design of injection strategies and assessment of permanence. It is known that the natural heterogeneity of typical sedimentary formations has a significant effect on the propagation of the $scCO_2$ plume and eventually accumulating mobile phase underneath the caprock. However, knowledge gaps exist on how the heterogeneity of the formation manifested at all scales from the pore to the site scales affects trapping and how the mechanisms to be parameterized for modeling. *The primary objective of this research was to fill the knowledge gaps in the understanding of how $ScCO_2$ gets trapped trough processes associated with capillarity and dissolution in naturally heterogeneous, deep saline geologic formations.* Filling of these knowledge gaps is expected to contribute toward better conceptual models, improved numerical models, more accurate assessment of storage capacities, and optimized placement strategies. The data generated in highly controlled laboratory settings helped to evaluate the ability of existing models to capture the fundamental processes that contribute to capillary and dissolution trapping.

Approach: Since fully characterizing the geologic heterogeneity at all relevant scales and making observations on the spatial and temporal distribution of the migration and trapping of supercritical CO_2 are not practical, studying these trapping processes at a fundamental level is not feasible in field settings. Laboratory experiments using scCO2 under ambient conditions are also not feasible as it is technically challenging and cost prohibitive to develop large, two- or three-dimensional test systems with controlled high pressures to keep the scCO2 as a liquid. Hence, an innovative approach that used surrogate fluids in place of $scCO_2$ and formation brine in multi-scale, multiple length scales in synthetic sand reservoirs was developed and implemented. These experiments were designed to provide insight into the impact of natural geologic heterogeneity on the flow and trapping of $scCO_2$ under drainage and imbibition conditions. Basic to this approach was the use of surrogate for scCO2 and formation brines to simulate the interplay of governing forces that are expected under conditions in deep reservoirs. A series of immiscible displacement experiments was performed to observe and record the migration preferential entrapment of $scCO_2$ in well-defined heterogeneous sand packing configurations. A second set of multi-scale experiments were conducted with another suite of surrogate fluids to study dissolution of the trapped $scCO_2$ and the subsequent dissolution trapping through mechanisms of convective mixing and diffusion. Each of the capillary trapping experiment consisted of a drainage event simulating the injection of a non-wetting phase ($scCO_2$) into a brine-wetted reservoir, followed by a gravity relaxation period characterized by spontaneous imbibition at the trailing edge of the plume. Spatial and temporal variations of non-wetting phase saturation represent important features to evaluate capillary trapping; for this reason x-ray attenuation analysis was used as a non-destructive technique that allows the precise measurement of phase saturations throughout the entire flow domain. The data on the dissolution trapping were obtained by extracting aqueous samples from ports on the test tanks walls and conducting laboratory analysis to determine dissolved concentrations. Modeling algorithms were developed to obtain addition insights through numerical simulations.

Results and findings: Analysis of the experimental results complemented by numerical simulations suggests that intermediate-scale experiments with analog fluids can provide quantitative information about large-scale phenomena and therefore can be used to predict storage performance of natural reservoirs under a range of boundary conditions. In the above context, the discoveries and success stories:

- Successfully developed experimental methods to use surrogate fluids for supercritical and brine to conduct experiments under ambient laboratory conditions. Using these methods, we were able to generate highly accurate data to evaluate the ability of multiphase codes used in carbon storage modeling to capture important fundamental processes.
- Obtained new insights into how geologic heterogeneity affects capillary and dissolution trapping. These insights have helped us to develop improved conceptual models that will lead to methods to optimize injection schemes and make improvements to currently used DOE codes.
- Demonstrated how heterogeneity could be used to enhance stable trapping, controlled by capillarity and dissolution coupled with diffusion into low permeability zones of the formation. Fine-scale heterogeneities can contribute significantly to trapping of CO_2.
- Identified deficiencies and limitations of current multiphase models for their ability to capture some of the basic processes observed in the highly controlled experiments.
- Identified limitations in currently used constitutive models of fluid retention and relative permeability.
- Demonstrated that including hysteresis in constitutive models of the numerical models could significantly improve predictions of the plume migration and distribution during post-injection and that the hysteresis can have significant impact on capillary trapping.
- New insights into mechanisms CO2 exsolution when brine leaking from deep formations containing the dissolved gas reaches the shallow subsurface, specifically under heterogeneous conditions.

Recommendations:. Based on the research findings following recommendations are made for future research and technology development for CCS in deep geologic formations.

- The fundamental formulations of multiphase flows have to be revisited to evaluate their ability to capture heterogeneity-controlled trapping processes at all relevant scales.
- Further research is needed to develop and test physically-based constitutive models of capillary pressure-saturation and relative permeability applicable to natural rocks.
- Further research would be needed to find better models and more efficient algorithms for solving nonlinear hysteretic partial differential equations, as the existing methodology for solving two-phase flow equations with hysteresis is computationally much less efficient than the standard methods for models without hysteresis.
- Further research is needed to develop upscaling methodologies and/or efficient multi-scale modeling approaches for improving predictive ability of the models at field-scale. This is needed for taking into account heterogeneities at multiple scales and appropriately employing multiphase model parameters that are measured typically at laboratory-scale.
- In site characterization, attention should be given to identify low permeability zones where dissolved CO2 can be immobilized for long-term trapping.
- The contribution of leakage occurring between higher permeability formations through semi-confining layers should be factored into conceptual and numerical models of mixing used in dissolution trapping analysis.
- In site characterization, attention should be given to identify low permeability zones where dissolved CO2 can be immobilized for long-term trapping.
- The contribution of leakage occurring between higher permeability formations through semi-confining layers should be factored into conceptual and numerical models of mixing used in dissolution trapping analysis.

2 INTRODUCTION

During carbon storage operations, anthropogenic CO_2 emissions are captured from large stationary sources such as coal-fired power plants and subsequently injected into a geological repository at conditions above critical pressure and temperature. From a volumetric point of view, the supercritical state of CO_2 ($scCO_2$) ensures an improved degree of storage efficiency due to the higher density of the supercritical fluid with respect to the gaseous phase. However, due to the considerable density contrast between supercritical CO_2 and ambient brine, usually within the order of 30 – 40 % (Ennis-King and Paterson, 2003), gravity segregation is expected to reduce the sweep efficiency of the displacement process. Also, as pointed out by Tsang et al. (2002), because of the buoyancy drive, injected CO_2 will preferentially migrate to the top of the storage formation; leading to a larger areal extent than it would be for a buoyancy-neutral fluid.

Gravity segregation is a well-known phenomenon in secondary oil recovery operations where buoyancy effects can cause the displacing phase to bypass large portions of the reservoir, resulting in significantly lower oil recovery (Craig et al., 1957; Tchelepi and Orr, 1994). Placing injection points at deeper depths where density of scCO2 is greater than at lower depths can minimize this behavior. The "inject low and let rise" strategy (Bryant et al., 2008) has also been proposed to increase the migration distance of the buoyant $scCO_2$ plume through the reservoir, enhancing the interaction between CO_2 and resident brine and eventually promoting dissolution (Ennis-King and Paterson, 2003). Additionally, due to the high viscosity contrast between the two phases, displacement of resident brine by $scCO_2$ is characterized by an unfavorable mobility ratio $M = (k_r/\mu)_{displacing}/(k_r/\mu)_{displaced}$, tending to produce hydrodynamic instabilities and viscous fingering (Berg and Ott, 2012; Cinar et al., 2006; Lake, 1989). Overall, these phenomena cause an ineffective fluid displacement and lower CO_2 entrapment, representing a basic limitation to storage efficiency.

The movement of CO_2 through a brine-bearing reservoir consists of a displacement process called drainage, where the wetting phase is drained out of the pores by the non-wetting phase (NWP). The sweep efficiency of such displacement depends on the viscosity and density ratios of the two phases, the interfacial tension between them, and the displacing velocity of the non-wetting phase (Kuo et al., 2011). Several mechanisms contribute to the immobilization of CO_2 within the reservoir pore space during the injection and post-injection stages, and have been described extensively in the literature (Bachu and Adams, 2003; Benson and Cole, 2008; Ennis-

King and Paterson, 2003; Firoozabadi and Cheng, 2010; Nordbotten and Celia, 2011; Orr, 2009; Pruess and Garcia, 2002; Suekane et al., 2008). These mechanisms are: 1) *structural trapping* underneath confining flow barriers, 2) *capillary trapping* due to immobilization of the supercritical CO_2 within rock pores, 3) *dissolution trapping* in the formation water, and 4) *mineral trapping*, mainly via precipitation of carbonates. The interconnected free-phase CO_2 that is not immobilized by the mentioned processes represents the mobile fraction of the plume, which will keep moving driven by regional groundwater flow and buoyancy. The relative importance of each trapping mechanism over time is controlled by the corresponding dominant process, i.e. the advection-dominated multiphase flow will occur during the injection period, whereas slower phase-transfer processes will affect the time scale of dissolution and mineral trapping (Kopp et al., 2009). The concurrent forces acting on the migration and entrapment of the CO_2 plume will be viscous, gravity, and capillary forces, with their relative influences being expressed by dimensionless groups. The Capillary number describes the ratio of viscous to capillary forces, the Bond number describes the ratio between buoyancy and capillary forces, and the Gravity number describes the ratio between buoyancy and viscous forces (Løvoll et al., 2005). Each of the mentioned trapping processes is characterized by a degree of storage security (i.e. the unlikeliness of CO_2 leakage to the surface) and an associated time scale (Figure 1) that spans from decades for the injection period to millennia for the geochemical reaction time scale.

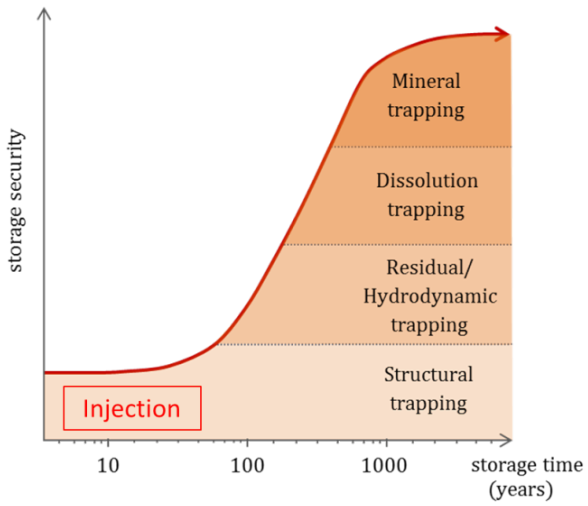

Figure 1 Time scales of main trapping mechanisms of CO_2 and their level of storage security (IPCC, 2005).

With the progression of time, the contribution of residual, solubility, and mineral trapping to safe storage increases, providing a long-term solution to the fixation of CO_2 (IPCC, 2005). Eventually, the carbon dioxide stored in the reservoir will be present in three different phases: 1) a CO_2-rich supercritical phase, 2) dissolved in the aqueous phase, or (3) precipitated in solid minerals (Pruess et al., 2003).

This report is organized as follows. In the rest of section 3, the background needed to follow the issues related to capillary and dissolution trapping investigated using experiments is presented. In Section 4 the details of the experimental methods used in selecting the test fluids and sands, multi-scale experiments in small and intermediate test tanks and methods used in developing the constitutive models for model inputs are presented. Section 5 presents all analysis conducted using the experimental data. Section 6 presents the analysis conducted using DOE codes and a code developed as a part of this research. Section 7 presents a summary of the findings that is followed by conclusions and recommendations in Section 8.

2.1 Structural and capillary trapping

On a short time scale, structural or stratigraphic trapping is the principal trapping mechanism, representing a primary factor for screening candidate storage reservoirs (Bachu, 2000; Hitchon, 1996). It involves a physical trap like a low-permeability caprock, which inhibits the upward movement of mobile $scCO_2$ toward drinking water aquifers and eventually back into the atmosphere. Suitable sealing formation characteristics would be considerable thickness and lateral continuity, geochemical and geomechanical stability, and absence of continuous and conductive faults. Even though structural trapping may keep the mobile fraction of the injected $scCO_2$ underground, the free phase will still represent a leakage risk due to preferential flow pathways such as poorly sealed abandoned wells or fractures. Another process that contributes to CO_2 trapping has been proposed is hydrodynamic trapping (Bachu et al., 1994; Hitchon, 1996; Larkin, 2010), which involves the displacement of mobile $scCO_2$ by the regional groundwater flow. The best scenario representing this category of trapping would be in a low-dipping aquifer with a considerable flow gradient that will ensure a down dip CO_2 movement toward regions of low potential, avoiding the need of stratigraphic barriers.

During the injection period of a typical storage scenario, the pressure of the CO_2 pumped into the reservoir is increased until the resident brine is displaced from the pore space, invading

first the larger voids and gradually increasing the saturation of the plume. Once the injection ceases and the CO_2 pressure at the well suddenly drops, a redistribution of the fluids throughout the reservoir follows, producing a flow reversal in the saturation history and leading to an imbibition process. After the surrounding brine has displaced the mobile fraction of the plume from the pore space, isolated CO_2 droplets will be disconnected from the continuous phase, leading to its effective immobilization. The trapped fraction of CO_2 subsequent to the imbibition process is defined as residual saturation and is a function of the maximum CO_2 saturation, or initial saturation S_{nw}^{i}, reached at the time of flow reversal (Akbarabadi and Piri, 2013; Land, 1968; Pentland et al., 2010). This residual trapping mechanism, also referred to as capillary trapping or relative permeability hysteresis trapping (Flett et al., 2004; Juanes et al., 2006; Suekane et al., 2008), is known to affect the flow of multiple fluid phases through porous media and it has been broadly studied in several areas of research, from soil physics, where the unsaturated zone above the water table represents a vital environment for plant roots, to the discipline of aquifer remediation and enhanced oil recovery (EOR), where capillary forces need to be overcome in order to clean up chemical spills or to increase production of hydrocarbons from reservoirs (Lake, 1989). In contrast, the ultimate goal of CCS is to maximize the storage capacity of deep geological formations by increasing CO_2 immobilization through several trapping mechanisms, including capillary trapping. Therefore, estimation of the residually trapped volume and saturation of CO_2 is fundamental for the assessment of trapping capacity of a potential reservoir (Bachu et al., 2007). Nevertheless, in situ measurements of this essential quantity are very challenging to obtain in the field, motivating this investigation in a dimensionally similar system under controlled laboratory settings.

The driving forces that control the migration of the $scCO_2$ plume while injection is occurring are gravity, capillarity, and the imposed pressure differential, while the spreading of the plume during post-injection involves the static balance between capillary and buoyancy forces. In the presence of an inclined sealing formation, the dipping angle of the stratigraphic limit will play a key role (Gasda et al., 2006), as well as the direction and magnitude of the regional groundwater flow (Larkin, 2010). An optimal injection scheme for an efficient storage scenario is the “inject low and let rise” method (Bryant et al., 2008). This method is intended to maximize the sweeping area of the plume and minimize the accumulation of mobile CO_2 phase under the caprock by releasing the supercritical fluid as deep as possible in the reservoir. Another

injection strategy known from EOR operations is the "chase brine" scheme (Ide et al., 2007; Qi et al., 2009), which has the goal of maximizing the contact area between the injected CO_2 and the resident brine, and eventually promoting dissolution. As sketched in Figure 2, once the injection of $scCO_2$ has ceased and the continuous phase plume (in dark gray) has reached the top of the storage formation, a fluid redistribution occurs, leaving behind a portion of the reservoir (in light gray) characterized by immobile $scCO_2$ at residual saturation S_{nw}^{r}. This volume is known as the plume footprint and covers a variety of residual saturations, ranging from very small fractions to maximum residual saturation $S_{nw}^{r,max}$. In particular, higher residual saturations are expected to be found close the injection well, whereas the front is going to be characterized by lower amounts of trapped CO_2. Furthermore, when a wetting phase flow comparable to a water drive in EOR operations is established upstream, any mobile fraction of the plume pooling underneath stratigraphic barriers will be eventually displaced updip. This process will affect some areas of the reservoir with a secondary drainage cycle, which will eventually lead to larger amounts of residually trapped CO_2.

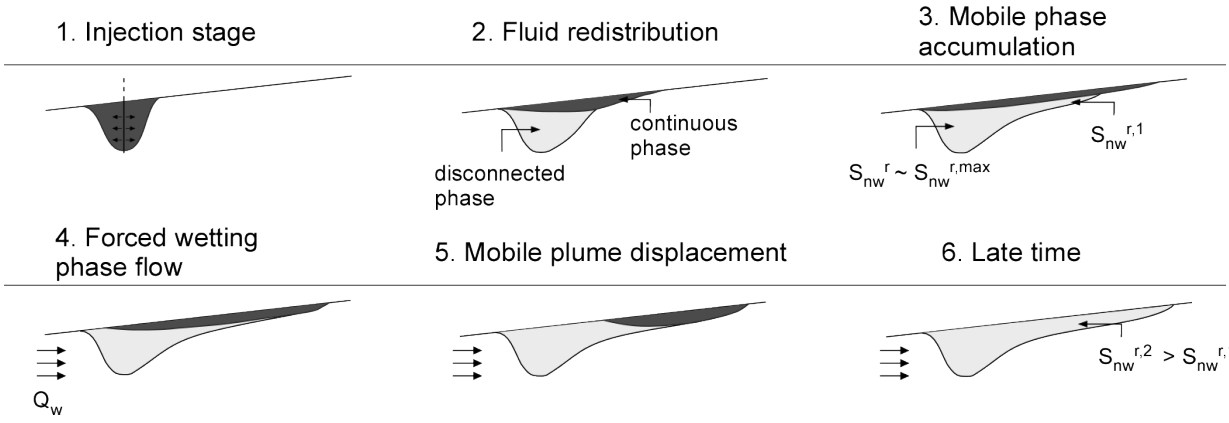

Figure 2 Conceptualization of the $scCO_2$ migration and entrapment problem through the hysteresis trapping mechanism; dark gray and light gray denote mobile phase and residual phase, respectively, arrows indicate direction of wetting phase flow Q_w.

With the assumption of dimensional similarity between the laboratory model and the field prototype, we aim to conduct immiscible displacement experiments to replicate injection and migration of $scCO_2$ in deep saline aquifers. The residual saturation of non-wetting phase (NWP) resulting from different Bond number scenarios will be analyzed in detail and correlated with the maximum saturation achieved at flow reversal to evaluate existing trapping models.

Based on experimental results on drainage-imbibition cycles through consolidated porous media, Land (1968) described the empirical relation of residual non-wetting phase saturation following the imbibition stage to initial non-wetting phase saturation occurring at the reversal point between drainage and imbibition. The formulation of this trapping model relies on the endpoint maximum residual non-wetting phase saturation, which corresponds to the effective initial non-wetting phase saturation equal to unity.

Through a series of laboratory experiments aimed to simulate reservoir conditions, Suekane et al. (2008) and Pentland et al. (2011) estimated trapped CO_2 saturations from the relationship between volume and pressure in an isothermal expansion.

Al Mansoori et al. (2009) and Pentland et al. (2010) used unconsolidated sand and analogue fluids at ambient conditions to measure the non-wetting phase residual trapping for a range of initial non-wetting phase saturations. The different initial non-wetting phase saturations were achieved by modifying the injection flow-rates, while the gravity effect was considered or neglected by running the experiment in vertical or horizontal columns, respectively.

A series of experiments were conducted in multi-scale test systems with the goal of improving the fundamental understanding of the mechanisms that contribute to structural and capillary trapping. The specific goal was to develop and implement an experimental method in test tanks under ambient laboratory conditions to make observations and generate data to improve the understanding of capillary trapping affected by fluid and formation properties. Since it is challenging to visualize multiphase flow processes occurring at high-pressure conditions at the meter scale, a testing method was developed based on the use of surrogate test fluids to replace the $scCO_2$ and saline formation water. To set a foundation for extrapolating experimental results to the field, we chose a set of dimensionless groups that define the relative contributions of buoyancy, viscous, and capillary forces to the displacement behavior of immiscible fluids. The experiments were designed with the goal of understanding and accurately quantifying the immobilization of the $scCO_2$-analog in a homogeneous formation confined by a slightly dipping structural barrier.

2.2 Dissolution trapping

As the microscopic blobs of $scCO_2$ at residual saturation will eventually dissolve into the surrounding brine, giving rise to a solute of carbon dioxide in brine that can store variable

amounts of CO_2 depending on its solubility at the existing temperature pressure, and salinity conditions. Besides retaining the injected gas in a more secure form, dissolution of carbon dioxide in the aqueous phase also leads to a more efficient storage, since the inverse partial molar volume (virtual density) of dissolved CO_2 is around 1.3 g/cm^3, while is less than 0.6 g/cm^3 at the supercritical state (Farajzadeh et al., 2011). In fact, while most dissolved gases reduce density of the solvent,, an unusual property of CO_2 is its capacity to increase the density of aqueous solutions up to 1% with respect to pure water density (Garcia, 2001). This behavior leads to the neutralization of buoyancy forces and the creation of unstable conditions once a layer of denser CO_2-rich phase forms above the ambient brine (Backhaus et al., 2011), triggering a density-dependent convective flow that ultimately enhances the dissolution process (Ennis-King et al., 2005).

The rate of increase in solution density depends on the salinity of the formation brine, mass fraction of CO_2, and temperature and pressure of the medium (Bachu and Adams, 2003; Garcia, 2001; Ohsumi et al., 1992). Since mobile gaseous CO_2 as a buoyant fluid has a general tendency of accumulating at the top of injection formations, dissolution preferably occurs there. The denser solution at the top then leads to the generation of gravitational instabilities in the system, which produces density-driven fingering that tends to move into deeper parts of the formation. This enhanced convective mixing of dissolved CO_2 increases the overall rate of dissolution in relatively homogeneous formations and ultimately results in a larger fraction of dissolved CO_2 versus mobile CO_2, which is considered an important trapping mechanism (Ennis-King et al., 2005).

Convective mixing has been extensively analyzed in several other application areas, such as in thermal systems and subsurface contaminant transport. These studies have been mainly based on theoretical approaches (Combarnous and Bories, 1975; Glass, 1993; Nield and Bejan, 2006; Schincariol et al., 1994, 1997; Simmons et al., 2001), but some experimental investigations have also been reported (Combarnous and Bories, 1975; Cooper et al., 1997; Elder, 1967; Schincariol and Schwartz, 1990). According to Holzbecher (1998), Benard was the first to experimentally study steady state heat convection using a box heated from the bottom in 1900. Rayleigh (1916) improved Benard's studies for heat convection in clear fluids. Horton and Rogers (1945) and Lapwood (1948) pioneered the study of convection in homogeneous porous

media by examining thermally driven convection, and determined the critical condition for the onset of convection using the Rayleigh number, Ra, given by:

$$Ra = \frac{k\Delta\rho gH}{D\mu\phi} \quad (1)$$

The Rayleigh number (*Ra*) is a dimensionless group of variables and parameters associated with buoyancy driven or convective flow (Horton and Rogers, 1945; Lapwood, 1948). In porous media, when *Ra* is greater than the critical value ($Ra_c=4\pi=\sim40$), the mixing is dominated by convection. If not, then diffusive mixing is observed. Eqn. (1) is used to calculate *Ra*, where *k* is the permeability (m^2), $\Delta\rho$ is the density difference between the fluids (kg/m^3), *g* is the gravitational acceleration (m/s^2), *H* is the thickness of the layer (m), *D* is the diffusion coefficient (m^2/s), μ is the viscosity of the background fluid (Pa.s) and ϕ is the porosity of the medium (-).

The density-driven convection of dissolved CO_2 in homogeneous porous media was examined in detail using theoretical and analytical approaches (Ennis-King and Paterson, 2005, 2007; Farajzadeh et al., 2007; Hassanzadeh et al., 2005; Hidalgo and Carrera, 2009; Nordbotten et al., 2005; Nordbotten and Celia, 2011; Pau et al., 2010; Pruess and Zhang, 2008; Riaz et al., 2006). In contrast, experimental studies are rather limited (Backhaus et al., 2011; Ennis-King and Paterson, 2003; Neufeld et al., 2010). Except for Neufeld et al. (2010) who performed experiments in two-dimensional (2-D) porous media using glass beads, the experiments were carried out either in Hele-Shaw cells or in one-dimensional (1-D) columns using either gaseous CO_2 and water (Aggelopoulos and Tsakiroglou, 2012; Farajzadeh et al., 2008; Kneafsey and Pruess, 2010) or surrogate fluids for $scCO_2$ and formation brine under ambient pressure and temperature conditions (Backhaus et al., 2011; Ennis-King and Paterson, 2003; Neufeld et al., 2010). These experimental studies mainly focused on the effects of fluid and formation parameters on the mass transfer rate, and the onset of instabilities leading to convective mixing. The results of these investigations and the extrapolation of understanding of analogous processes in heat convection show that convection is the dominant mechanism of mixing in homogeneous porous media. The onset of convection strongly depends on the porosity, permeability, thickness and aspect ratio of the medium, and the fluid properties, such as density difference between two fluids, salt concentration of brine and mass fraction of dissolved CO_2 in formation brine. Studies on heat convection in homogeneous porous media indicate that boundary conditions, aquifer

slope, groundwater flow and degree of heterogeneity are other factors affecting the onset of convection (Beck, 1972; Combarnous and Bories, 1975; Epherre, 1977; Nield and Bejan, 2006; Oostrom et al., 1992; Rees and Bassom, 2000; Ide et al., 2007, Tsai et al., 2013).

Effects of heterogeneity on mixing were studied theoretically by Nield and Simmons (2007), Nield and Kuznetsov (2007) and Simmons et al. (2010) in heat convection, and Prasad and Simmons (2003), Schincariol et al. (1994, 1997) and Simmons et al. (2001) in subsurface contaminant transport. Schincariol and Schwartz (1990) carried out experimental studies in layered and lenticular formations to determine the effects of salt concentrations and groundwater flow rates on density-driven flow characteristics to address the problems in flow systems. For layered systems, they found that even small permeability contrasts between layers led to a dense plume that accumulates along the bedding interphases. Numerical studies, carried out by McKibbin and O'Sullivan (1980) and McKibbin and Tyvand (1982) on periodic porous media, emphasized that the convection can be confined to one or a few layers for a small number of layers. However, the systems behave like a homogeneous single layer in the presence of many layers. In addition, the small permeability of the top layer is adequate to generate convective mixing in the bottom layer.

In contrast to other fields, there are only a limited number of experimental studies on the effect of heterogeneity on convective mixing and stable trapping of dissolved CO_2. Farajzadeh et al. (2008) experimentally investigated the importance of convection on mass transfer of gaseous CO_2 for dual-layer systems. Kneafsey and Pruess (2010) determined the dependence of size and location of fingers on permeability variations. Using numerical simulations, Green and Ennis-King (2010) explored how the presence of discontinuous shale lenses accelerates the convection process, and showed that the average breakthrough time of CO_2 at the formation bottom decreases with increasing length of shale lenses. Farajzadeh et al. (2011) and Ranganathan et al. (2012) carried out a detailed numerical study on the influence of the degree of spatial heterogeneity in permeability on the dissolution rate of $scCO_2$ in brine and onset of convection, and introduced three different spreading regimes: fingering, dispersion and channeling which are important regimes for stable trapping of dissolved CO_2.

As discussed above, most aspects of convective mixing have been investigated either in CO_2 sequestration or other density-driven flow literature. However, the effects of heterogeneity on the mixing and the stable trapping of dissolved CO_2 have not been adequately addressed.

Stable trapping of dissolved CO_2 is the secure and long term storage of dissolved CO_2 in deep saline formations. It is important to reduce the risk of leakage. The permanence of dissolved CO_2 in the formation depends on the geology and hydraulic properties of the units. The goal of this study is to investigate the role of mixing on the trapping of dissolved CO_2 using homogeneous and heterogeneous porous media laboratory experiments. The research is based on an investigation using surrogate test fluids in a 2-D test tank with various packing configurations under ambient pressure and temperature conditions. The impacts of formation permeability and structure, in layered systems and distinct block-wise heterogeneity, were also examined in the context of mixing and stable trapping.

A series of experiments were conducted in multi-scale test systems with the goal of improving the fundamental understanding of the mechanisms of dissolution trapping. The goal was to investigate the role of mixing on the trapping of dissolved CO_2 using homogeneous and heterogeneous porous media laboratory experiments. The research is based on an investigation using surrogate test fluids in a 2-D test tank with various packing configurations under ambient pressure and temperature conditions. The impacts of formation permeability and structure, in layered systems and distinct block-wise heterogeneity, were also examined in the context of mixing and stable trapping.

2.3 Constitutive models

The two basic constitutive relationships used in the study of the multi-phase flow are relationships between capillary pressure (P_c) and saturation (S_w) and between the relative permeability (k_r) and saturation (S_w). Various studies have suggested that these two constitutive relationships may be the most important parameters characterizing the behavior of multiphase flow systems (Doughty and Pruess, 2004; Flett et al., 2004; Juanes et al., 2006). In the case of geologic storage of CO_2, the two-phase flow of $scCO_2$ and brine in the formation is modeled. However, for two-phase flow system of $scCO_2$ and brine, it is difficult to develop these relationships in ambient laboratory settings because of the high pressures required to maintain CO_2 in a supercritical state. Moreover, some studies (Klute and Dirksen, 1986; Dane et al., 1992; Demond and Roberts, 1993) indicated that experimental methods to derive constitutive relationships of the $k_r - S_w$ are not well replicated. Also, the measurement ranges are restricted by constraints of laboratory experimental settings such as pressure, temperature, and scale.

Due to the difficulty of measuring the $k_r - S_w$ relationships directly, many modeling applications use empirically derived constitutive models from experimentally determined capillary pressure vs. saturation (Burdine, 1953; Brooks and Corey, 1964; Mualem, 1976; van Genuchten, 1980). To obtain these empirical $k_r - S_w$ relationships, the van Genuchten or Brooks and Corey model parameters are fitted to $P_c - S_w$ experimental results. The advantage of using models of $P_c - S_w$ is the derived $k_r - S_w$ relationships by avoiding direct experimental measurements (Chen et al., 1999). However, the applicability of these derived models is still uncertain because of the simplifying assumptions that are used in models like Mualem (1976) and Burdine (1953). Some studies (Fischer and Celia, 1999; Tuller and Or, 2002; Cihan et al., 2009) suggested that these constitutive models oversimplify the pore geometries, and it would result in discrepancies between derived models of $k_r - S_w$ relationships and those obtained experimentally. Thus, evaluating the adequacy of these constitutive models using experimental data is critical for better understanding the multiphase flow system and trapping mechanisms of $scCO_2$ in saline aquifers (Chen et al., 1999).

This research was aimed to obtain constitutive relationships using surrogate fluids for $scCO_2$ and brine. The derived and constitutive relationships were compared to verify their applicability.

3 EXPERIMENTAL METHODS

The scope of laboratory experiments is to best reproduce the conditions in deep geologic formations located at least 800 meters depth under ambient temperature and pressure conditions. The following sections describe the experimental methods used to address the research objectives of each of the project tasks mentioned above.

3.1 Capillary trapping (immiscible displacement) experiments

Immiscible flow dynamics in the context of geological carbon sequestration has been investigated experimentally by several research groups during the last decade (see, among others, (Cinar et al., 2009; Krevor et al., 2011; Lyle et al., 2005; Pentland et al., 2010; Perrin and Benson, 2010; Pini et al., 2012; Plug and Bruining, 2007; Suekane et al., 2005; Zhao et al., 2013). Laboratory experiments focusing on capillary trapping mechanism are often performed at the core scale, involving the injection of fluids at reservoir conditions. Also, core-flood experiments using reservoir rock samples provide critical information about the properties of the porous medium, such as constitutive relationships between capillary pressure, saturation, and relative permeability. However, conducting experiments at such a small scale can hinder the visualization of flow processes that are expected to occur at a larger scale. On the other hand, carrying out experiments under high-pressure conditions can be challenging at the meter scale. To overcome this practical limit of intermediate scale systems, analog fluids represent a convenient alternative to mimic the contrasts in density and viscosity that characterize real fluids (i.e. $scCO_2$ and brine) at reservoir pressure and temperature. In the present work, experimental analog systems at ambient conditions (1 atm, 20 °C) are used to recreate comparable density and viscosity contrasts between injected and displaced phases that actually exist at the injection formation ($P > 7.28$ MPa, $T > 31.1$ °C).

3.1.1 Selection of surrogate fluids

In order to avoid experimental complexity associated to high-pressure flow-cells at the meter-scale, and to achieve displacement velocities compatible with the measurement time of the x-ray attenuation device, the experiments were conducted with a pair of analog fluids at ambient conditions. The application of analog fluids at ambient conditions to mimic the behavior of

$scCO_2$-brine system has been widely documented in the literature for the replication of miscible displacement (DiCarlo et al., 2007; MacMinn and Juanes, 2013), dissolution enhanced by convective mixing (Backhaus et al., 2011; Neufeld et al., 2010), and immiscible displacement (Amaechi et al., 2014; Cinar et al., 2009; MacMinn and Juanes, 2013; Pentland et al., 2010). However, experimental studies of displacement and trapping of $scCO_2$ under deep reservoir conditions (T>31.1°C, P> 8MPa) have not yet been reported for two-dimensional test systems. This study analyzes the effectiveness of a set of immiscible surrogate fluids at ambient conditions (T=20°C, P=0.1MPa) to determine the flow regime and trapping capacity associated with interactions of capillary, viscous, and buoyancy forces in a synthetic aquifer. For the experiments that are presented, a set of surrogate fluids mimicking the density and viscosity contrasts of $scCO_2$ and brine at reservoir P,T conditions was identified. For this purpose, an aqueous solution of glycerol (80% w/w) was chosen to represent the wetting phase. The viscosity of the mixture was measured at 20°C with an AR-G2 rheometer (TA instruments) and was found to be in good agreement with the empirical parameterization presented by Cheng (2008). As shown in Figure 3, the properties of the wetting phase can be easily controlled by changing mass proportions of the two components (water and glycerol), resulting in a well-defined viscosity and density ratio between the $scCO_2$/brine analogs, aimed to fall in the range of values reported in the literature (Table 1).

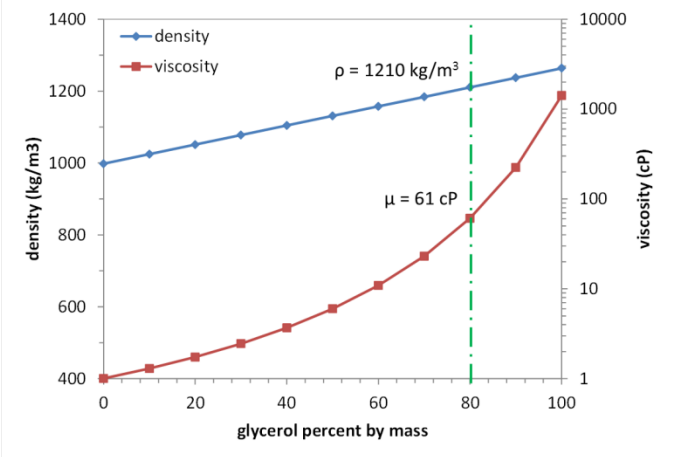

Figure 3 Variation of glycerol-water mixture density and viscosity for different mass proportions of glycerol.

The non-wetting phase (NWP) consisted of Soltrol 220 (Phillips 66), a low-toxicity, isoparaffinic solvent, widely used for experimental purposes (Fagerlund et al., 2007; Schroth et

al., 1998; Wildenschild et al., 2011). In order to allow for direct visualization of the flow and to increase x-ray attenuation contrast with the wetting phase, Soltrol 220 was dyed red with Sudan IV (Fisher Scientific) and doped with 10% w/w Iodoheptane (Alfa Aesar).The interfacial tension (IFT) between the two phases was measured with a CAM200 optical tensiometer (KSV instruments) at 20°C. The mass proportion of the glycerol-water mixture was 80:20 in order to obtain density and viscosity ratios between the two fluids that are in agreement with the parameter range observed in field settings (Table 1).

For the case presented here, the density and viscosity ratios of the laboratory fluids can be compared to a storage scenario in a 'cold' basin (geothermal gradient equal to 25°C/km and average surface temperature around 10°C) and injection into a rather 'shallow' reservoir (Nordbotten et al., 2005). At the Sleipner field in the North Sea, where $scCO_2$ is injected at 1012 meters below m.s.l., temperature and pressure conditions are estimated to be approximately 41°C and between 8 and 11 MPa, respectively (Arts et al., 2008). Under these conditions, using values from Singh et al. (2010), viscosity and density ratios between injected and resident phases are 0.075 and 0.745, respectively.

Table 1 Properties of surrogate fluids at ambient conditions and for actual fluids at reservoir conditions.

Phase	ρ (kg m^{-3})	μ (mPa·s)	μ_{nw}/μ_w	ρ_{nw}/ρ_w	IFT (mN m^{-1})
Soltrol 220	860	4.9	0.08	0.71	15
Glycerol-water	1210	61			
$scCO_2$	266-733[a] (760[c])	0.023-0.0611[a] (0.06[c])	0.026-0.20[a] (0.075[c])	0.22-0.75[a] (0.745[c])	19.8[b]
Brine	945-1230[a] (1020[c])	0.195-1.58[a] (0.8[c])			

[a] estimates from Nordbotten et al. (2005), T = 35-155°C, P = 10.5-31.5 MPa.
[b] measurement from Bennion and Bachu (2006), T = 43°C, P = 20 MPa, brine salinity = 2.7% wt.
[c] estimates from Singh et al. (2010) for Sleipner field.

3.1.2 Sands

Two main types of hydrophilic silica sands were used to pack the synthetic reservoirs in the tanks. Accusand type was employed in the experiments carried out in the "medium" tank

setup, whereas Granusil type was used in the "large" tank experiments, due to the large amount of sand needed and the higher cost of the Accusand grade. As shown in Figure 4, the main differences between the two porous media consists in the shape and the sorting of the grain sizes; Accusand sands have well-rounded grains and are very poorly-sorted (i.e. very uniform), whereas Granusil sands have very angular grains (more visible at the mm- than at the sub-mm-scale) and are slightly better-sorted. Although the effect of grain shape was not investigated in this study, it is worth noting that the different roughness of the grains' surfaces can lead to different degrees of contact angle hysteresis.

3.1.3 X-ray attenuation method

This section is aimed to provide general information about the implementation of x-ray measurements in the context of the immiscible displacement experiments. Central to the experimental approach is the use of x-ray attenuation to nondestructively determine the spatial and temporal distribution of the phase saturations in the test tanks. In fact, the main advantage of a non-destructive method such as x-ray attenuation lays in the ability to measure in-situ phase contents with high spatial accuracy (~2 mm) without disrupting the flow of multiple phases with probes or other sampling devices.

The attenuation of an x-ray beam traversing a porous medium is influenced by the saturation of fluid phases present in the pore space and the intensity of the beam (Oak and Ehrlich, 1988). The x-ray attenuation method is based on Beer-Lambert's law, which describes the change in energy intensity for a beam of mono-energetic photons traveling through a material with linear attenuation coefficient α and thickness x:

$$I/I_0 = e^{-\alpha x} \tag{2}$$

where I is the intensity of photons (photons/time) transmitted across the material and I_0 is the photon flux in the absence of a material or incident beam intensity. To measure the void fraction of the porous medium (i.e., porosity) as well as the amount of fluid phases in a non-invasive manner, a custom-designed x-ray attenuation device was employed. By moving the x-ray source (an AEG/Thomson x-ray tube with Tungsten filament) and photon detector (a PGT/HPGe connected to a multichannel analyzer) simultaneously along a predefined scanning grid, we were able to measure volumetric fractions of any of the phases inside the tank (glycerol-water, Soltrol 220, sand) and interpolate them in two dimensions to obtain contours of equal

saturations. These measurements represent a depth-average along the second horizontal axis (y) and an areal average over a sampling volume determined by the radius of the collimated x-ray beam (1 mm).

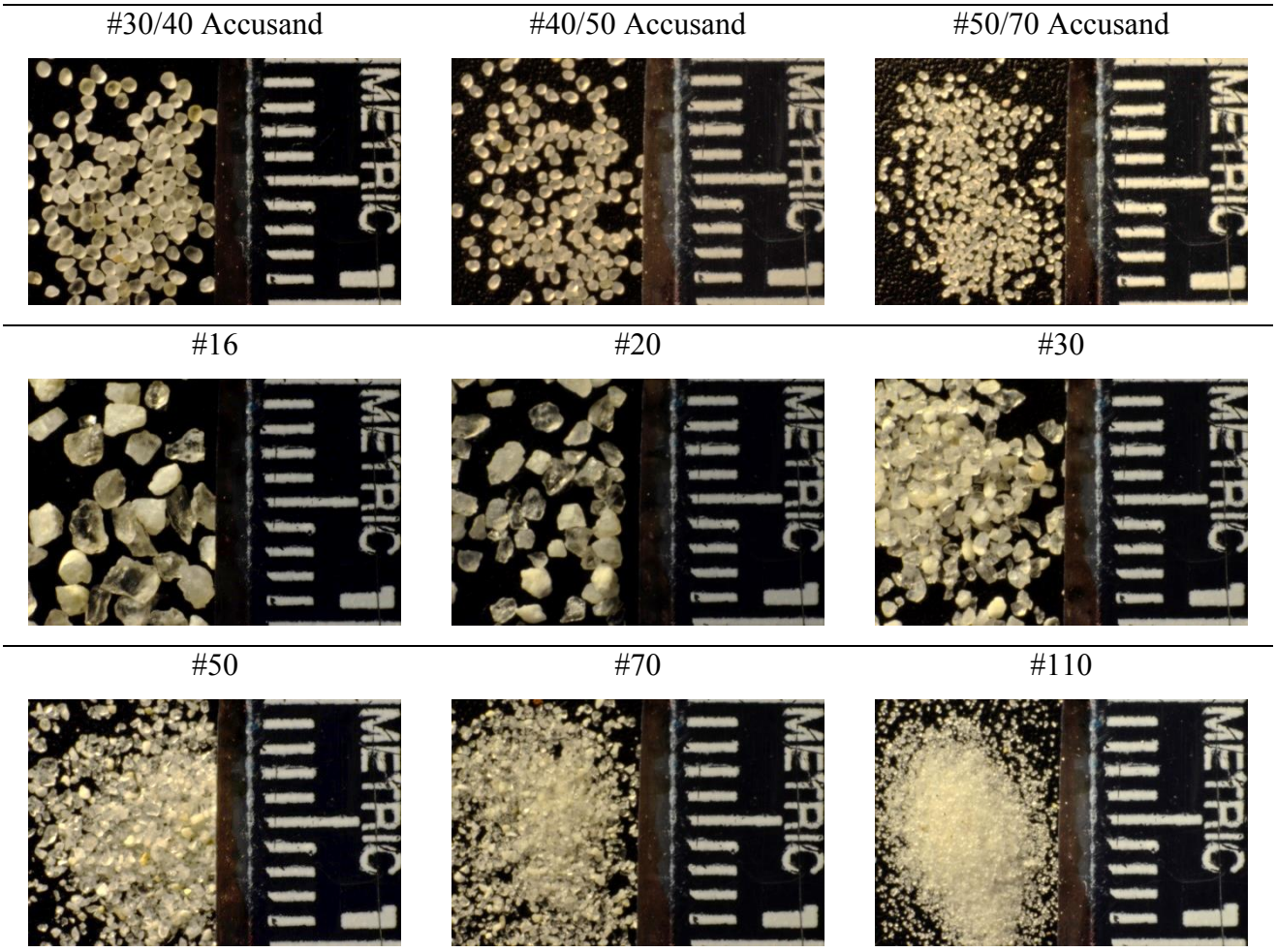

Figure 4 Grain sizes and shapes of the laboratory sands used in the immiscible displacement experiments. Differences in surface roughness and uniformity of size distribution are visible at the mm-scale.

The x-ray generator was operated with tube settings of 70 kV and 10 mA, while 2 heavy rare earth element filters (Erbium carbonate and Samarium carbonate) were used as absorption filters to condition the spectra. 10-s and 15-s detector live times were used for photon counting at each point in 3 ft. × 2 ft. and 8 ft. × 4 ft. tank configurations, respectively, resulting in average total measurement times of 28 s and 42 s, including the positioning routine.

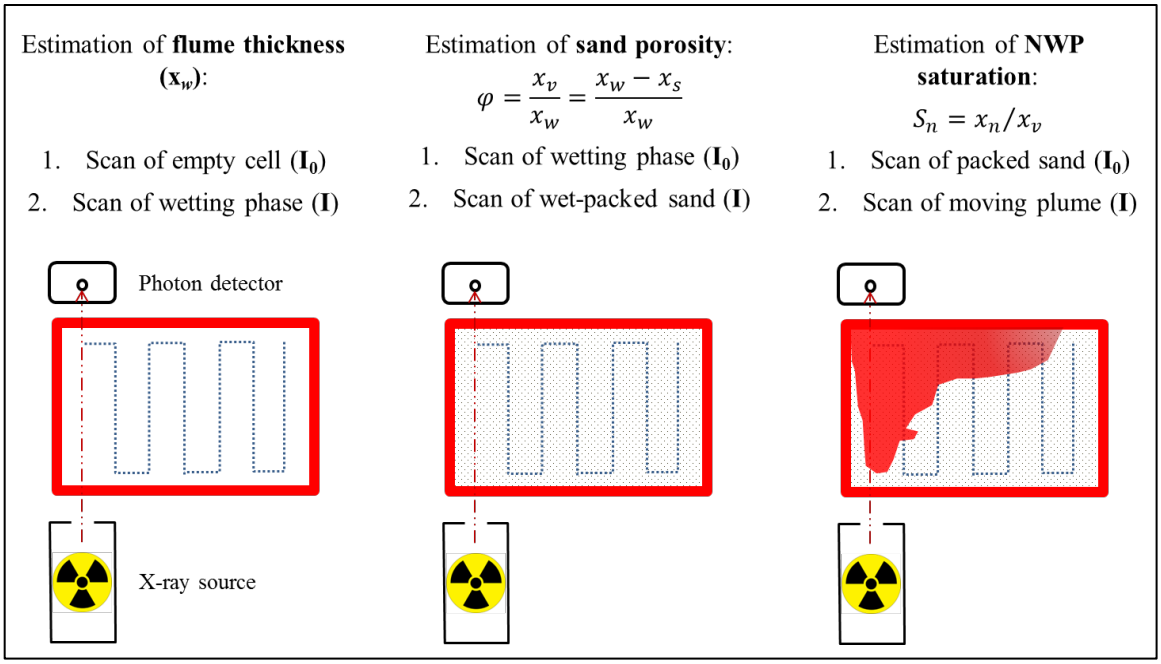

Figure 5 Experimental procedure for the estimation of multiple phase path lengths via x-ray attenuation method. Glycerol-water (xw), sand (xs), and Soltrol 220 (xn) path lengths are measured to estimate flume thickness, porosity, and NWP saturation, respectively.

As outlined in Figure 5, where each step describes the acquisition process of a phase path length, the following procedure was used to extrapolate sand porosity and NWP saturation from material path lengths:

a) The empty tank was entirely scanned with x-rays with the maximum attenuation configuration (5-6 aluminum plates in front of the detector window);

b) The tank was filled with the wetting phase and scanned with the same attenuation configuration as the previous step to quantify the spatial variation of tank width, which provides an estimate of the bulging of the acrylic walls;

c) The tank filled with the wetting phase was scanned again, with a lower attenuation configuration (3-4 aluminum plates);

d) The tank was wet-packed with the sands and scanned with the same attenuation configuration as the previous step to quantify the sand pathlength, which is required to calculate the sand porosity;

e) The tank filled with sand was scanned again, with the lowest attenuation configuration (0-1 aluminum plates);

f) During the spreading of the NWP plume, the tank was continuously scanned with the same attenuation configuration as the previous step to quantify the NWP pathlength, which is required to calculate the NWP saturation.

Prior to any path length estimation, linear attenuation coefficients for each phase had to be characterized and the accuracy of the x-ray attenuation device was tested by measuring material path lengths across known thicknesses. The method consisted of placing two 1.0-cm thick disposable spectrophotometry cuvettes within the path line of the x-ray beam. First the two cuvettes were filled with the wetting phase (i.e. glycerol-water mixture) for the baseline measurement I_0, then one cuvette was replaced with another containing the NWP, for the I measurement. The application of the Beer-Lambert law allowed for the estimation of the path length of the NWP, which was within 98% agreement (0.02 cm underestimated path length of 1 cm) of the exact width of the cuvette.

a. Scanning grids

Each data point is related to a measurement time, which is affected by the intensity of the emergent beam (higher intensity, longer measurement time) and the time required for the positioning routine. Consequently, less refined scanning grids require less time to cover a specific area than more refined ones; however, the lack in refinement can hinder the detection of saturation variations across shorter distances than the spacing between each data point.

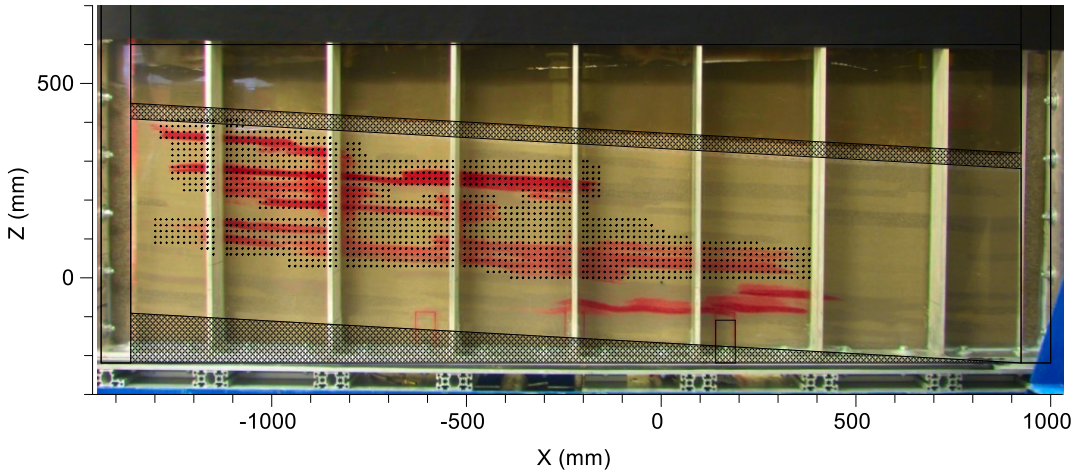

Figure 6 Example of x-ray scanning grid consisting of 1675 points with an average spacing of 1.5 cm × 1.5 cm.

Figure 6 shows an example of a plume with high saturation contrasts driven by layer-type heterogeneity with short vertical correlation. In order for the x-ray measurements to capture these small-scale variations, the scanning grid has to be designed appropriately.

b. Data interpolation and spatial moment analysis

As mentioned earlier, in order to optimize the overall time needed for a scanning grid to cover the plume extents, x-ray measurements were gathered only at points that lied within the plume. Doing so, some scanning grids were characterized by spatial irregularity in grid point coverage, leading to rough approximations of NWP saturations after data interpolation, as illustrated in Figure 7 (top). Data interpolation was carried out with Surfer (Golden Software, Inc.) using the *Triangulation with Linear Interpolation* method, which uses the optimal Delaunay triangulation. The algorithm creates triangles by drawing lines between data points. The original points are connected in such a way that no triangle edges are intersected by other triangles. The result is a patchwork of triangular faces over the extent of the grid.

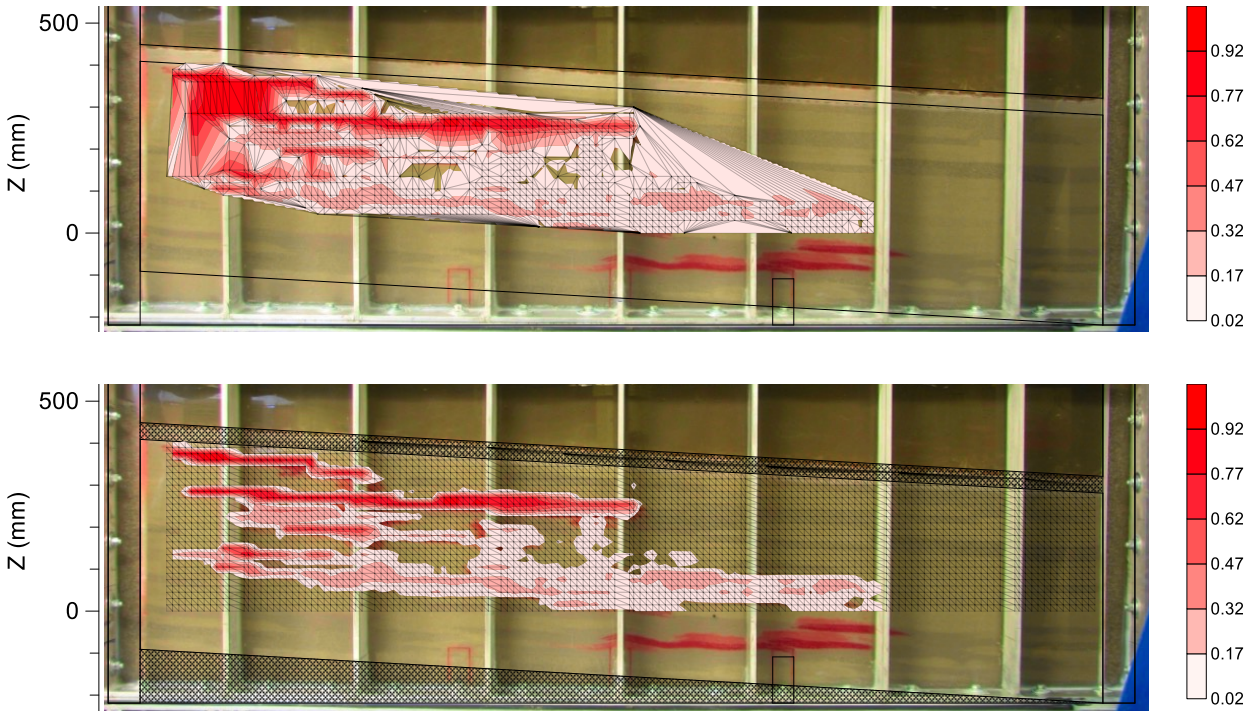

Figure 7 Example of Delaunay triangulation adapted to grid of data points before (top) and after (bottom) filling the grid voids with zero saturation values. Locations below Z=0 are not covered by x-ray measurements due to spatial limitations of the traversing system.

In order to avoid erroneous interpolation of the data, the voids of the scanning grid were filled with points of zero NWP saturation, resulting in a much sharper (and more truthful) estimation of plume volume, as shown in Figure 7 (bottom).

In addition to the visual inspection of aquifer by means of x-rays, the spreading of the plume throughout the various stages of the experiments is quantitatively assessed by following a common approach that is based on the analysis of spatial moment (Eichel et al., 2005; Fagerlund et al., 2007; Han et al., 2010; Kueper and Frind, 1991). For an immiscible plume, the latter are defined in a similar manner as for a solute concentration (Freyberg, 1986):

$$M_{ij}(t) = \iint \varphi(x,z) S_{NW}(x,z,t) x^i z^j dx dz \qquad (3)$$

where φ is the porosity (space-dependent), S_{NW} is the NWP saturation (space- and time-dependent), and x, z are the horizontal and vertical spatial coordinates, respectively. Since the saturation measurements are averaged across the width of the flow-cell, the y-direction is neglected in the calculation of the spatial moments. The first moments in the x- and z-direction

normalized by the total NWP volume present in the domain (M_{00}) describe the coordinates of the center of mass of the plume:

$$x_c = M_{10}/M_{00} \tag{4}$$

$$z_c = M_{01}/M_{00} \tag{5}$$

The second moments in the x- and z-directions about the center of mass provide a measure of the lateral spread of the plume:

$$\sigma_{xx} = M_{20}/M_{00} - x_c^2 \tag{6}$$

$$\sigma_{zz} = M_{02}/M_{00} - z_c^2 \tag{7}$$

3.1.4 Medium tank experiments

One of the key points of this investigation is that CO_2 trapping mechanisms affect each other in ways that are not readily apparent, since they occur over a wide range of time and length scales and are inevitably influenced by the inherent heterogeneity of natural subsurface formations. This complexity ultimately affects our ability to predict with confidence the fate of injected CO_2 and the success of the storage operation as a whole.

The local capillary trapping phenomenon (Saadatpoor et al., 2010) provides a good example of such complex behavior and it refers to the occurrence of locally high $scCO_2$ saturations (significantly above residual saturation) due to buildup of bulk phase behind so-called capillary barriers. The latter are associated with intra-reservoir heterogeneities of various sizes in the form of low-permeability features, such as lenses, lamina and/or beds (Ringrose et al., 1993). On the one hand, these barriers are considered beneficial to enhance the storage of CO_2 for various reasons: their presence doesn't depend on absolute seal integrity over an extended region, they can arrest the plume propagation both horizontally and vertically, and they allow for CO_2 trapping at saturations larger than those expected from residual trapping alone (Green and Ennis-King, 2010; Hesse and Woods, 2010; Saadatpoor et al., 2010). On the other hand, the presence of trapped CO_2 significantly reduces the relative permeability to the resident brine, thus slowing down the mixing and subsequent dissolution process of the two phases.

As suggested by Koltermann and Gorelick (1996), the primary control on flow paths of multiple fluids is exerted by hydraulic permeability. With reference to the example described above, heterogeneities will therefore become relevant as soon as their presence significantly

increases the overall variability in the permeability distribution of the given porous medium. Interestingly enough, permeability variations within length scales < 20 cm are reported for various depositional environments (Corbett et al., 1992). Additionally, parameters of the capillary pressure-saturation curve, such as the capillary entry pressure or the residual saturation values, can play a major role in controlling fluid displacement in a porous medium system governed by the interplay between viscous, gravity and capillary forces, as it would be the case for $scCO_2$-brine flow in a geological formation. As a matter of fact, such a displacement is characterized by a variety of patterns, including lateral spreading, preferential flow and pooling (Held and Illangasekare, 1995; Illangasekare et al., 1995), as well as front pinning (Zhao et al., 2013) and blunting (Golding et al., 2013; Zhao et al., 2014), which in turns affect the overall sweep efficiency of the injection process. The ability to link spatial heterogeneity of key properties of multiphase porous media systems to the spreading and distribution of each fluid phase is needed for their full characterization.

So far, the phenomenon of capillary heterogeneity in CO_2 trapping has been studied experimentally, mostly by means of core-flooding experiments at the mm-cm scale (Krevor et al., 2011; Pini and Benson, 2013a) and numerically, through reservoir- and core-scale simulations accounting for capillarity (Flett et al., 2007; Kuo et al., 2011; Saadatpoor et al., 2010). While numerical models need to be tested and validated against experimental observations, laboratory investigations that use reservoir cores do not allow for spatial control of the distribution of the heterogeneity in two or three dimensions at the cm-m scale. In the latter case, despite recent advances in the application of imaging techniques, such as x-ray computed tomography, to the characterization of 3-D core-flooding experiments, the range of geometries that can be investigated is still limited by the nature and size of the core sample itself. In this context, the data sets from laboratory investigations of multiphase flow displacements at the intermediate (cm-meter) scale are rather scarce (Hofstee et al., 1998; Kueper et al., 1989). Following the definition by Lenhard et al. (1995), the length scale of an intermediate-scale experiment has to be small enough for the laboratory setting to be controlled and the dimensions of the flow domain have to be compatible with measurement techniques. We add here that the usefulness of performing immiscible displacement experiments at the meter-scale lies in the ability to quantify the relative contribution of small-scale processes to flow and transport phenomena at a larger scale. As pointed out by Oostrom et al. (2007) two-dimensional

experiments conducted in intermediate-scale flow cells represent a suitable intermediary for mimicking flow processes occurring between one-dimensional column tests and field-scale.

In a set of homogeneous experiments using unconsolidated sands in a 2-D sandpack (Trevisan et al., 2014), we have investigated the role of grain sizes on the influence of capillary forces on the displacement of a non-wetting phase (NWP) plume. Fine-grained sands increase the relative contribution of capillary forces vs. gravity and viscous forces, thus stabilizing the front and leading to larger footprints and lower average NWP saturations. Furthermore, the potential mobilization of temporarily trapped NWP at elevated saturations was demonstrated with the application of a forced wetting phase flow once the fluids had reached a complete redistribution. The addition of heterogeneous structures to those fairly simple experiments would allow extending such investigations to the study of capillary barrier phenomena on NWP plume migration and trapping. In this context, a key aspect to take into account is how such heterogeneities are correlated (Bryant et al., 2008; Han et al., 2010; Ide et al., 2007). In the present study we consider two heterogeneous scenarios characterized by different continuity of the sand zones and we compare them with a homogeneous base case conducted previously, so as to observe and quantify the effects of sand correlation on the lateral migration and entrapment of a NWP plume. As expected, correlated heterogeneities led to more pronounced horizontal propagation of the plume, whereas wider range of NWP saturations and larger amount of trapped fraction were observed in the uncorrelated experiment.

a. Medium tank homogeneous setup

Several numerical studies aimed to capture the influence of inherent heterogeneity of deep geological reservoirs on trapping of injected CO_2 have been reported in the literature (Buscheck et al., 2012; Doughty and Pruess, 2004; Flett et al., 2007; Lengler et al., 2010; Obi and Blunt, 2006). However, carrying out controlled field experiments has always involved uncertainty related to setting up and control of boundary conditions and determining the distribution of soil types. Therefore, the influence of natural heterogeneity and connectivity (i.e. spatial continuity of different permeability zones) on migration and trapping of $scCO_2$ in deep saline formations is still a challenging issue to be addressed. In order to investigate the effects of permeability field variability and to compare them to actual reservoir settings the experiments

featured in this section represent a base case homogeneous scenario and two scenarios with a geometrically similar configuration and spatially correlated and correlated heterogeneity.

The laboratory experiments were carried out in a rectangular quasi-two-dimensional flow cell with internal dimensions (L × W × H) of (91.4 × 5.6 × 61) cm^3. As shown in Figure 8, the synthetic aquifer consisted of a homogeneous medium with an inclination of 2° underlying a practically impervious layer of very fine sand consisting of a 2:1 mixture of sieve sizes #110 and #250 (U.S. Silica Company) that acted as caprock.

For each experiment, the height difference between the two reservoirs was adjusted according to the permeability of the sand to produce an injection flow rate of 0.7 ml/min. During injection, this flow rate was maintained constant throughout the three experiments corresponding to a capillary number of 1×10^{-5}. The magnitude of the capillary number for our experiments is in agreement with values reported by Bandara et al. (2011) for a high permeability reservoir. The Darcy velocity used for calculating the capillary number was estimated by dividing the volumetric flow rate of the injected fluid by the total area of the screen.

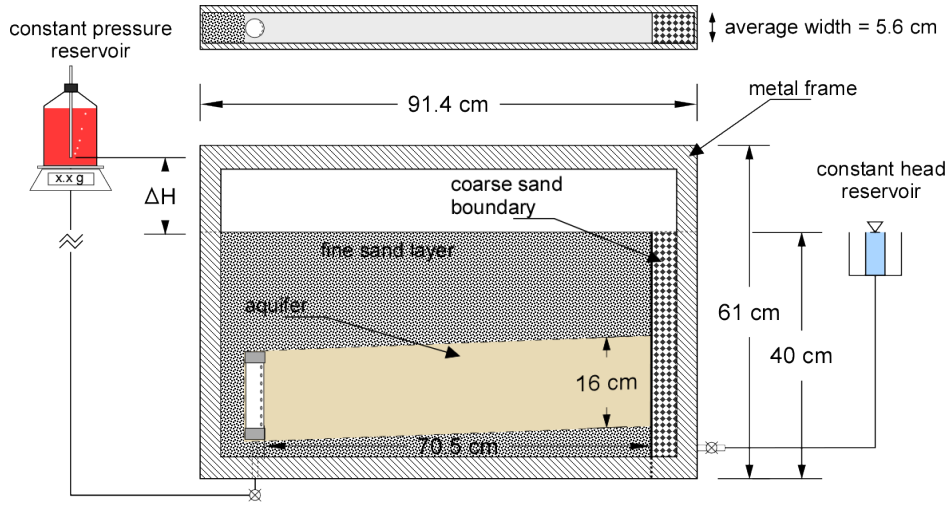

Figure 8 Sketch with dimensions of the synthetic aquifer and experimental setup.

After the injection stage, the plume was monitored through photography and x-ray attenuation measurements until no variation in Soltrol 220 saturation was detected, indicating a fully immobilized plume. Afterwards, in order to establish a wetting phase flow corresponding to a chase brine event, the Mariotte bottle previously filled with Soltrol 220 was replaced with a reservoir filled with glycerol-water. In order to prevent the wetting phase from by-passing the

NWP plume accumulating below the fine sand layer, the flow rate of this wetting phase flow event was maintained at 2 ml/min until all the mobile fraction of NWP had left the reservoir.

A set of unconsolidated porous media with variable permeability was used to study the multiphase flow behavior through a range of Bond numbers, expecting higher permeability to cause a faster vertical migration of the injected NWP due to a stronger influence of gravity over capillary forces. The corresponding Bond numbers changed from 2.61×10^{-5} (experiment #1) to 3.3×10^{-6} (experiment #3). The laboratory sands used for packing the synthetic aquifer are identified by the effective sieve numbers and consisted of hydrophilic silica sands commercialized under the brand Accusand (Unimin Corp.) with well-characterized physical properties (see Table 2).

Although the viscosity and density contrasts of the fluids used in the experiments are representative for $scCO_2$/brine at reservoir conditions, the permeability expected at field sites such as Sleipner will be more than 1-2 orders of magnitude lower than the laboratory sands.

Table 2 Properties of silica sand grades used in the displacement experiments with corresponding Bond numbers.

Exp.	Sand	k (m^2)	Φ_{avg} (-)	d_{50} (mm)	d_{60}/d_{10} (-)	$S_{nw}^{r,max}$	Bo ($x10^{-5}$)
1	#30/40	1.14×10^{-10} [a]	0.354 (0.355[a])	0.45[b]	1.22[b]	0.26	2.61
2	#40/50	6.42×10^{-11} [a]	0.39 (0.355[a])	0.28[b]	1.21[b]	0.22	1.47
3	#50/70	3.46×10^{-11} [a]	0.379 (0.372[a])	0.23[b]	1.28[b]	0.25	0.33
1-3	#8	1.55×10^{-9} [c]	0.396[c]	1.4[c]	1.6[c]	N/A	N/A
1-3	#110	5.21×10^{-12} [c]	0.34[c]	0.12[c]	1.6[c]	N/A	N/A

N/A: not available.

[a] from Zhang et al. (2008).

[b] estimated from sieve data provided by the manufacturer.

[c] from Sakaki and Illangasekare (2007).

In previous laboratory experiments conducted in the same flow cell by Fagerlund et al. (2007), the vertical Plexiglas™ walls displayed a noticeable bulging across the y-axis, which could affect the estimation of sand porosity and NWP saturation. In order to normalize the sand

and NWP path lengths at each scanning point by the variable thickness of the flume, we followed the first step in Figure 5 to determine the width variation for the whole flow domain. The contour map resulting from interpolation of x-ray attenuation data in Figure 9 revealed an increasing thickness (in cm) approaching the center of the flume. In order to reduce the noise from acquired data, before proceeding to the porosity estimation, a smooth surface was fitted to the interpolated contours and these estimates were used to represent the two-dimensional variation of flume thickness (Figure 9).

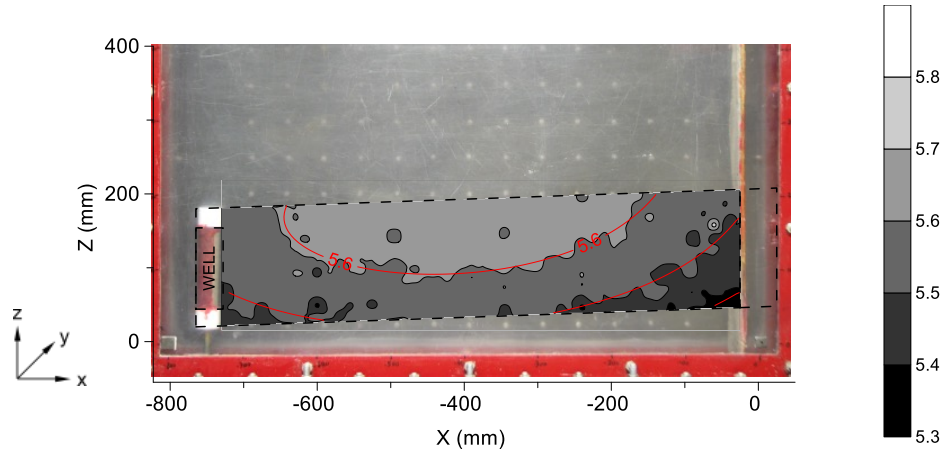

Figure 9 Empty flume with overlapped interpolated contours of flume thickness (in grey shades) and smooth surface (red lines).

After wet-packing with a known mass of sand and prior to the injection of the NWP into the synthetic reservoir, a complete x-ray scan of the flow domain was performed to characterize the spatial distribution of sand porosity. A total of 611 measuring (or scanning) points covered the flow domain with a measurement spacing of (1.5 × 1.5) cm^2. Figure 10 shows the resulting contour maps of the porosities for the three packing configurations, indicating that a certain degree of heterogeneity exists even though all attempts were made to pack the tank homogeneously. However, it was observed during each displacement experiment that there was no evidence of preferential flow pathways due to porosity changes in the sand pack.

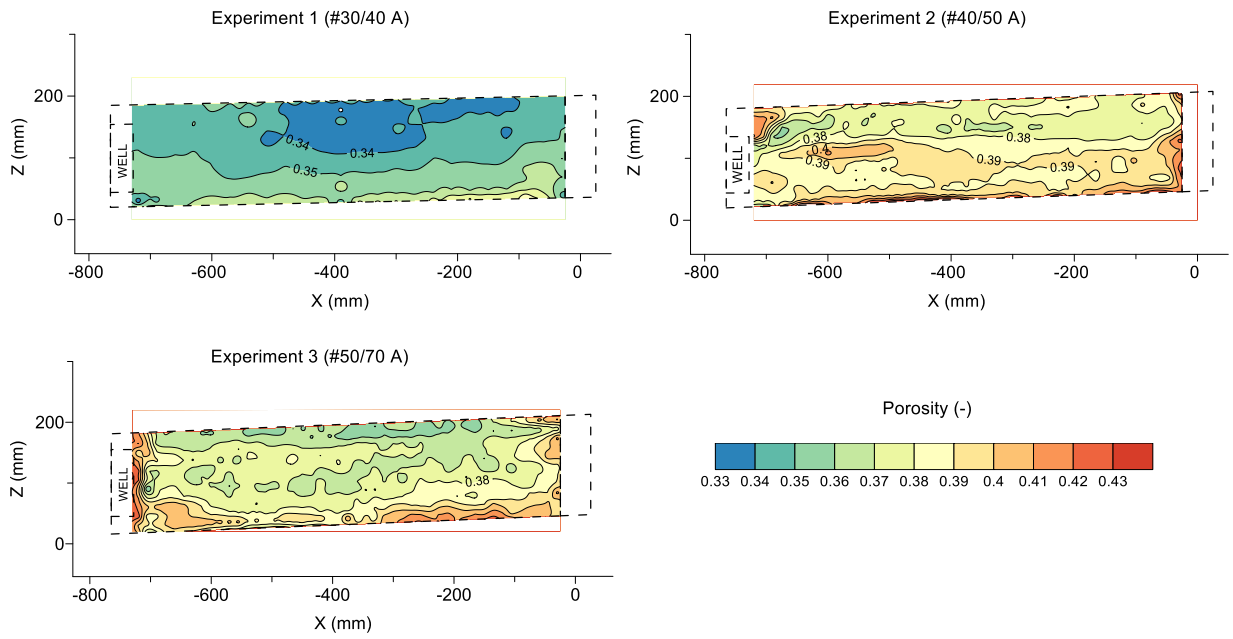

Figure 10 Contour maps of sand porosity for the three packing configurations.

These values agreed with the porosity estimated after the total mass used to pack the tank. Figure 11 shows porosity histograms from x-ray data analysis for the three packing configurations, where mean values are in good agreement with measurements from Zhang et al. (2008), as shown in Table 2.

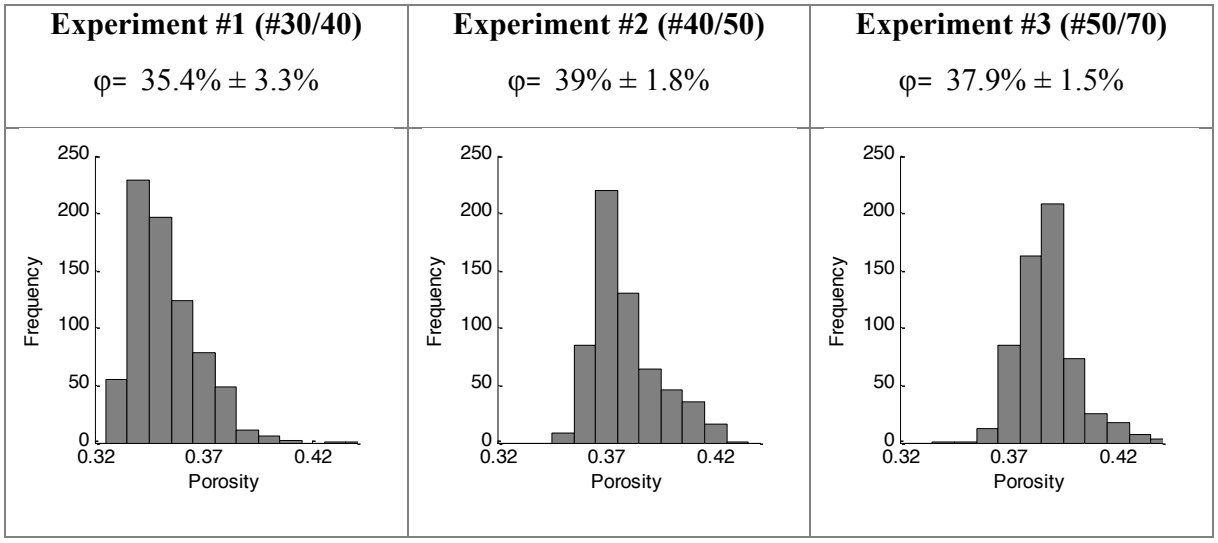

Figure 11 Histograms of porosity for the three packing configurations.

b. Medium tank heterogeneous setup

In this section of the work, two heterogeneous sand configurations (Het.1 and Het.2) with different spatial correlation of the permeability field (Figure 13) are considered. In both cases, the background material is the same sand used in the homogeneous experiment with intermediate permeability, while finer and coarser sands are distributed within the domain by following two correlation values. Each experiment involves three stages, namely drainage (5.5 hours at 0.72 ml/min), fluid redistribution (no injection for approximately two weeks), and forced imbibition stages (48 hours). Experimental parameters for the drainage and forced imbibition stages are given in Table 3.

In order to evaluate trapping effectiveness for the heterogeneous experiments, we compare the observed initial-residual NWP saturations with the Land trapping model (Land, 1968), which takes the following form:

$$S^*_{\mathrm{nw,r}} = \frac{S^*_{\mathrm{nw,i}}}{1 + \mathrm{C} S^*_{\mathrm{nw,i}}} \tag{8}$$

where $S^*_{\mathrm{nw,r}}$ is the effective residual NWP saturation, $S^*_{\mathrm{nw,i}}$ is the effective maximum (or initial) NWP saturation reached at flow reversal, and C is the Land trapping coefficient, which is a function of the effective endpoint residual NWP saturation, $S^{*\max}_{\mathrm{nw,r}}$:

$$C = \frac{1}{S^{*\max}_{\mathrm{nw,r}}} - 1 \tag{9}$$

All effective saturations are calculated by normalizing measured NWP saturations by the volume of wetting phase contributing to the flow:

$$S^*_{\mathrm{nw}} = \frac{S_{\mathrm{nw}}}{1 - S_{\mathrm{w,irr}}} \tag{10}$$

where $S_{\mathrm{w,irr}}$ is the irreducible wetting phase saturation, which takes a value of 0.07 for all the three sands.

Table 3 Summary of the experimental parameters. ΔH is the height difference between constant pressure reservoir and constant head outflow boundary; Ca is capillary number; PV is the pore volume of each aquifer measured with x-rays; PVI are the pore volumes injected during each stage.

Experiment	stage	flow rate (ml/min)	time (h)	ΔH (cm)	Ca (-)	PV (cm^3)	PVI (-)
Hom.	Drainage	0.7	5.5	35	1.0×10^{-5}	2379	0.097
	F.I.	2	48	19	3.6×10^{-4}		2.42
Het. 1	Drainage	0.72	5.5	35	1.0×10^{-5}	2164	0.109
	F.I. I	1	24	13	1.8×10^{-4}		0.665
	F.I. II	1.5	24	17	2.7×10^{-4}		0.998
Het. 2	Drainage	0.72	5.5	35	1.0×10^{-5}	2238	0.106
	F.I. I	1	24	13	1.8×10^{-4}		0.643
	F.I. II	1.5	24	17	2.7×10^{-4}		0.965

Three hydrophilic silica sands (Accusand, Unimin corp.) with effective sieve numbers #30/40, #40/50, and #50/70 were used for packing the synthetic aquifers. By using these grades, the flow domain was populated with three levels of permeability ranging from 3.5×10^{-11} to 1.1×10^{-10} m^2 (35 - 116 D). The corresponding capillary pressure-saturation relationships are shown in Figure 12 and represent Van Genuchten model (1980) fits applied on experimental data gathered using the same fluid pairs as in this study (Mori et al., 2015). Interestingly, the distinctive shape of the drainage curve for finer sand as compared to both coarse and medium sands reflects a similar pattern observed for the uniformity coefficient and porosity. Moreover, although the differences in threshold entry pressure and endpoint values (residual NWP saturation, $S^{*\max}_{\mathrm{nw,r}}$, and irreducible wetting phase saturation, $S_{\mathrm{w,irr}}$) between the three sands are minimal (~0.1 kPa), we expect that at sufficiently low flow rates, the effect of the different properties of the sands will affect the displacement and, accordingly, the saturation distribution.

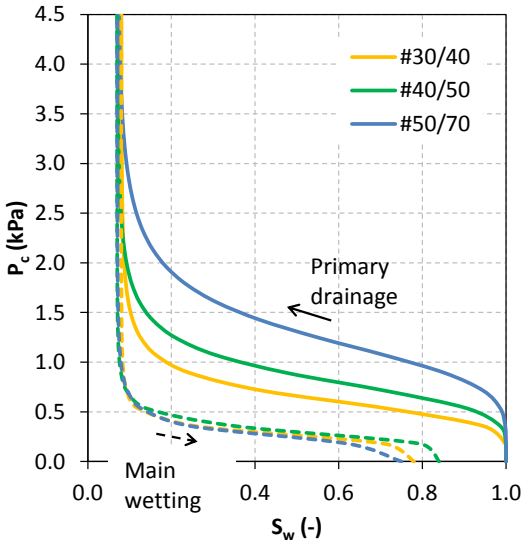

Figure 12 Capillary pressure-saturation constitutive relationships for the three sands used in the experiments. Van Genuchten model is fitted on experimental data measured by (Mori et al., 2015). Continuous and broken lines represent primary drainage and main wetting cycles, respectively.

The two heterogeneous permeability fields have the same volumetric proportions of the three sands (15%, 66%, and 19% for coarse, medium, and fine sand, respectively) and were generated to create two scenarios with different spatial correlations (Figure 13), namely poorly correlated (Het. 1, also referred to as "uncorrelated") and moderately correlated (Het. 2, also referred to as "correlated"). The packing grid consists of 224 cells (28 columns by 8 rows) and each grid block has dimensions of (2.5 × 2) cm^2.

Spatially uncorrelated (Het. 1) Spatially correlated (Het. 2)

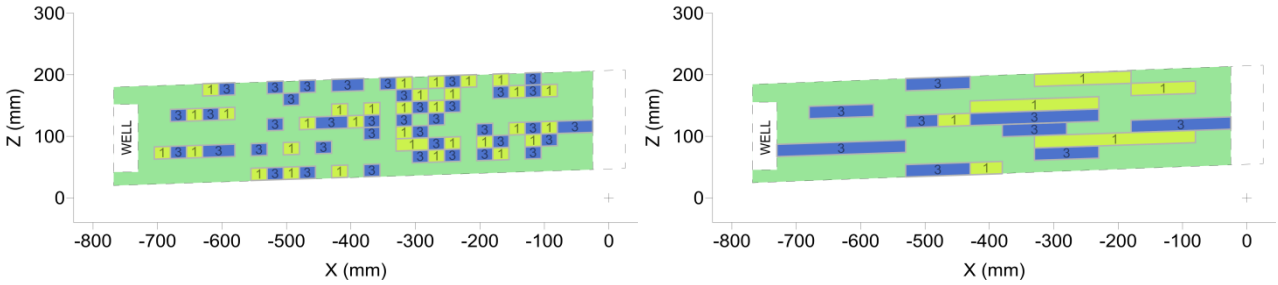

Figure 13 Spatial distribution of sand blocks with variable permeability; #30/40 (no. 1) is colored in yellow, #40/50 (no. 2) in green, and #50/70 (no. 3) in blue. Relative proportions are kept constant.

Figure 14 shows the experimental variograms along the longitudinal flow direction in terms of a semivariogram function $\gamma(h)$ plotted as a function of a lag distance h for both scenarios. In the first case (Het. 1) the maximum variability value (sill) is reached at very short distances, thus indicating poor spatial correlation, and the progression is scattered around an average value of 0.38, thus suggesting a cyclic behavior. On the contrary, the semivariogram of the second case (Het. 2) increases with distance and approaches a value of 0.38 at a distance equal to 25 cm (range). It is worth noting that the variance of both permeability fields is the same (0.38) and agrees with the variance of the normal distribution function computed on a random distribution of the three sands in the volumetric proportions used in this study.

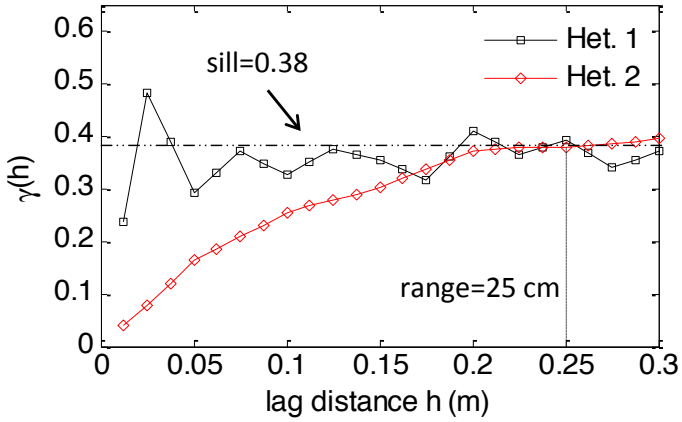

Figure 14 Experimental variograms along x-direction of the two heterogeneous cases. The vertical dashed line indicates the distance at which data are no longer autocorrelated (range) for Het. 2. The horizontal dashed line shows the variance (sill) shared by both heterogeneous scenarios.

c. Large tank setup

The experiments presented in the previous section are for fairly simple and ideal scenarios. Therefore, in an attempt to reproduce more realistic geological media, two experiments were conducted in a larger tank (8 ft. × 4 ft.), allowing for the observation of additional processes, such as increased vertical migration of the plume, effects of background hydraulic gradient on plume entrapment, and the contribution of larger spatial variability of the permeability field. The ultimate goal of these experiments is to test the implementation of optimal injection schemes to enhance storage capacity in highly heterogeneous systems and to

test the applicability of a new multiphase model developed at Lawrence Berkeley National Laboratory, namely TPFLOW. In fact, the complex, yet explicitly defined heterogeneous arrangement of laboratory sands recreated in these experiments represents a simple system to be controlled and to allow exact representation in numerical simulations.

With respect to the geometry of the medium tank experiments, large tank (8 ft. × 4 ft.) configurations allow for the observation of additional displacement and trapping phenomena. These include: a) the effects of background hydraulic gradient on the plume migration and entrapment, b) the larger effects of buoyancy forces enhanced by the larger vertical extent of the synthetic aquifer, and c) the ability to reproduce larger degrees of spatial variability of the permeability field.

Given the increased vertical extent of the NWP plume generated in this larger setup, the implementation of a confining unit able to prevent breakthrough became less trivial and led to several failed experiments. A clay layer created with different proportions of bentonite and glycerol-water in order to facilitate packing (more liquid at the bottom) was used for this purpose. As shown in Figure 15, a 5-cm thick layer of 110-250 sand was packed between the aquifer and the clay in order to achieve a straight interface between the two layers.

Three wells have been implemented in this large tank configuration in order to have the ability to simulate injection/extraction scenarios using different well arrangements. The wells consist of 10-cm-long acrylic pipes (internal diameter, I.D.=4.5 cm) open at the top and filled with #8 sand. For all the experiments conducted in the large tank, only the rightmost well was used to inject Soltrol into the reservoir.

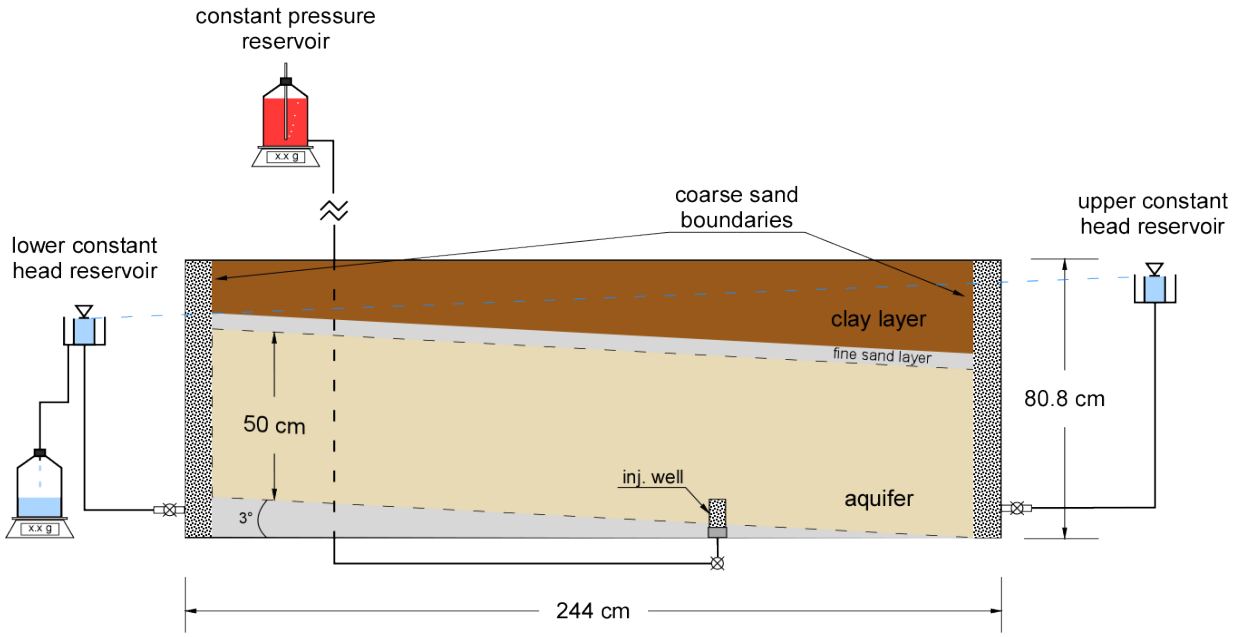

Figure 15 Experimental setup for immiscible displacement experiments in the "large" 8 ft. × 4 ft. tank. Injection takes place from the bottom right portion of the aquifer. The aquifer has a gentle slope (3º) in the direction of flow.

Two large-tank immiscible displacement experiments are presented in this section: a base case homogeneous scenario with medium-permeability sand (#50 Granusil) and a highly heterogeneous scenario with equivalent mean permeability and variance of 1.69. For each experiment, two consecutive injections of NWP are performed, separated by a fluid redistribution stage allowing for the plume to reach equilibrium. The experimental approach taken by Barth et al. (2001) and Fernandez-Garcia et al. (2004) to explicitly represent a random field site sedimentary structure in a synthetic laboratory aquifer was followed and further improved. A log-normal distribution of permeability was discretized in six categories corresponding to Granusil sands #16, #20, #30, #50, #70, and #110, from coarsest to finest (see Table 4 for physical properties of the sands). Figure 16 (left) shows the target probability of sand blocks for each category, which is used to populate the permeability field and (right) the capillary pressure – saturation drainage curves for the six sands plus the coarsest sand #8 used for packing the injection well and lateral boundaries.

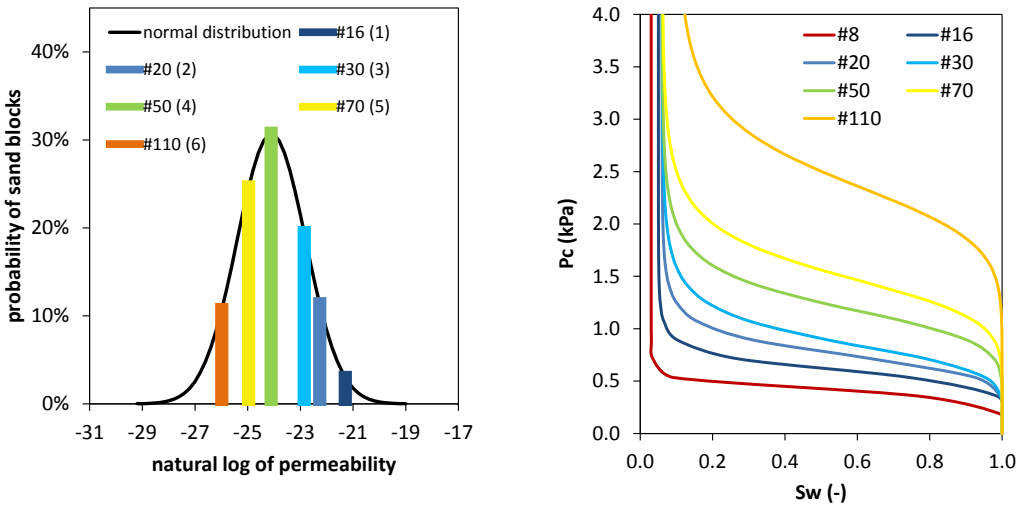

Figure 16 (left) Target histogram of the frequency for the six sands selected to discretize a log-normal distribution of permeability (in m^2) and (right) characteristic P_c-S drainage curves for each sand.

The relative volumetric proportion calculated for each sand is: 3% of #16, 11.4% of #20, 19.5% of #30, 30.8% of #50, 24.7% of #70, and 10.7% of #110. Using these proportions, the sands were distributed in a two-dimensional vertical rectangular array of 122 by 25 (XZ) cells with dimensions (2 × 2) cm^2.

In order to recreate a synthetic reservoir with a spatial variation of permeability that would agree with most of reservoir simulations focusing on permeability heterogeneity (Flett et al., 2007; Han et al., 2010; Ide et al., 2007; Saadatpoor et al., 2010), we used Sequential Indicator Simulation (SIS) algorithm from the geostatistical library GSLIB (Deutsch and Journel, 1998) coupled to the open source program SGeMS (Remy et al., 2009) to generate 20 equiprobable realizations based on an exponential semivariogram. Starting from the assumption that a layer-type heterogeneity can enhance storage capacity by counteracting buoyancy forces (Doughty et al., 2001), a long horizontal (50 cm) and a shorter vertical (4 cm) correlation length were considered to observe delayed upwards migration and enhanced spreading of the plume throughout the synthetic reservoir.

Table 4 Physical properties for the silica sand grades used in the large tank displacement experiments.

material	Sieve size	k (m^2)	lnk	φ_{avg} (-)	d_{50} (mm)	d_{60}/d_{10} (-)
1	#16	6.38×10^{-10} [a]	-21.3	0.407	0.88 [a]	1.72 [a]
2	#20	2.13×10^{-10}	-22.3	0.411		
3	#30	2.01×10^{-10} [a]	-22.9	0.433	0.49 [a]	1.50 [a]
4	#50	3.86×10^{-11} [a]	-24.1	0.426	0.30 [a]	1.94 [a]
5	#70	2.40×10^{-11} [a]	-25.0	0.418	0.19 [a]	1.86 [a]
6	#110	6.52×10^{-12} [a]	-26.0	0.334	0.10 [a]	~2.0 [a]

[a] from Barth et al. (2001)

Among the 20 equiprobable realizations simulated using SIS, we selected the three that best honored the target Gaussian distribution (Figure 17) and assured a satisfactory connectivity of the most permeable sands (#16, #30, and #50). Then, in order to evaluate the behavior of the plume through the three permeability fields, we used a continuum-based finite-volume multiphase flow model, namely TPFLOW, to simulate injection and redistribution of the Soltrol plume.

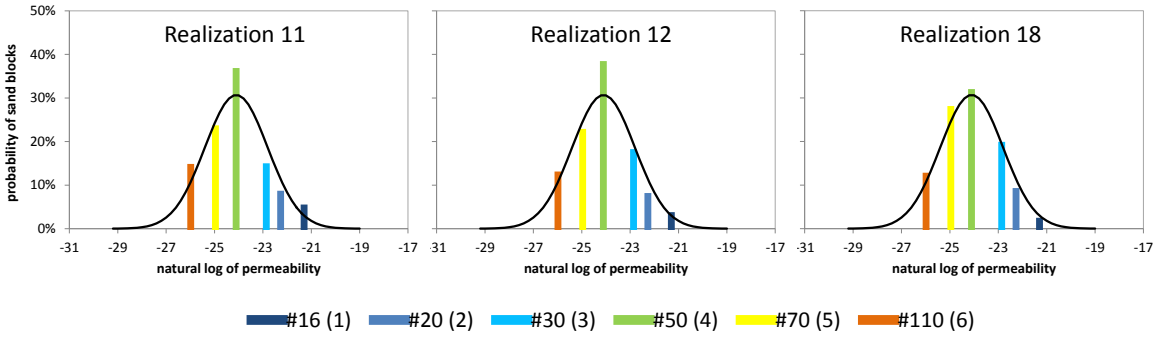

Figure 17 Histograms of the natural log of intrinsic permeability (in m^2) for the three heterogeneous packing scenarios: comparison with the target Gaussian distribution with mean μ=-24.1 (#50 sand) and variance σ^2=1.3.

Ultimately, realization no. 18 showed no early breakthrough of the plume into the constant head boundaries as well as no accumulation of bulk phase near the caprock. As a result of these conditions, realization no. 18 was selected for packing in the 8 ft. × 4 ft. tank. Figure 18 shows the spatial distribution of the six reservoir materials, where the dark red color indicates the

coarse sand (#8 Granusil) used to fill the injection well and the lateral boundaries of the tank. The color coding is maintained consisted with the previous figures.

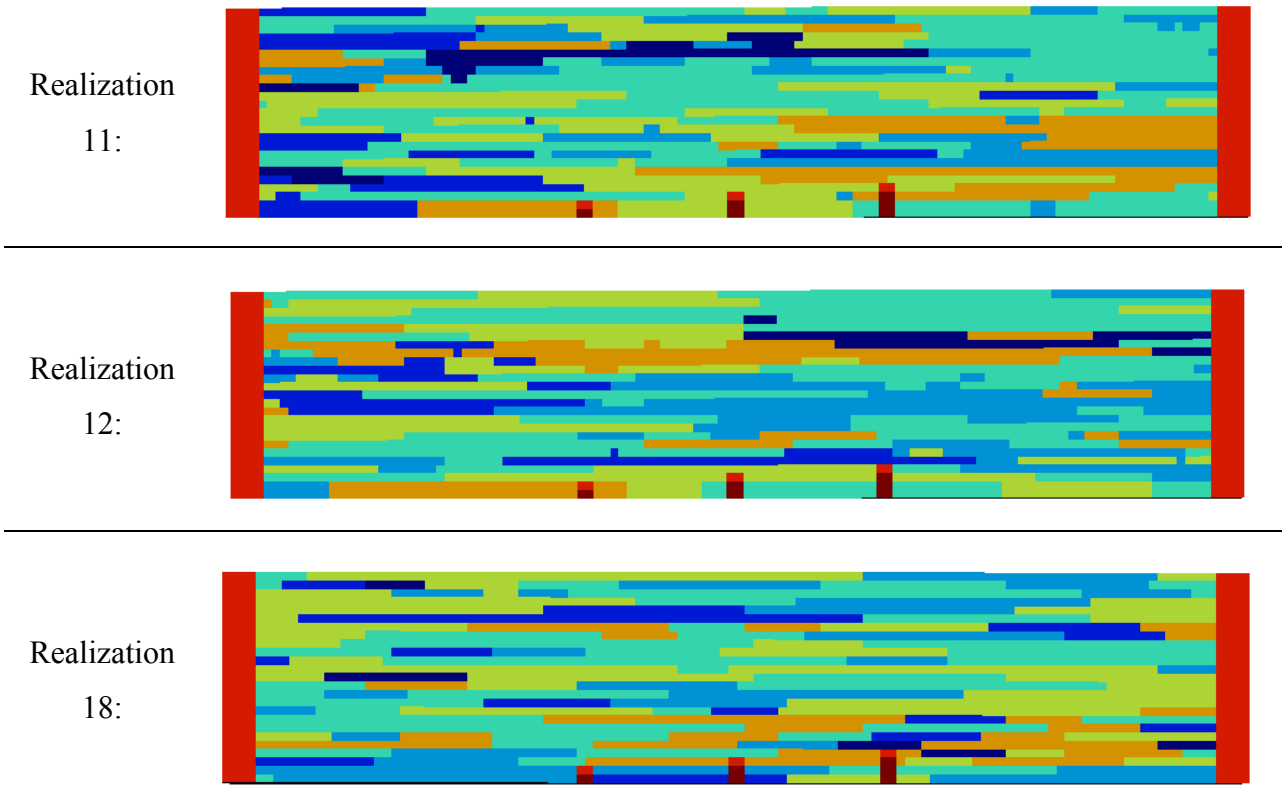

Figure 18 Stochastically equivalent realizations of permeability distribution. The 8 colors represent the 6 materials shown in Figure 17, plus #8 sand (light red) used for the injection well and boundaries and a fictitious impermeable material (dark red) used to avoid lateral migration of the plume from the injection well.

Figure 19 shows the experimental variograms along the flow direction for the three stochastic realizations. For realizations 11 and 18, the maximum variability value (sill) is approached at range equal to 0.5 m, in agreement with the input variogram parameters used to generate the realizations. As a reference, a theoretical exponential semivariogram model defined by equation (11) is also plotted.

$$\gamma(h) = c_0\left[1-\exp\left(-\frac{3h}{a_0}\right)\right] \qquad (11)$$

where c_0 is the sill, h is the lag, and a_0 is the range.

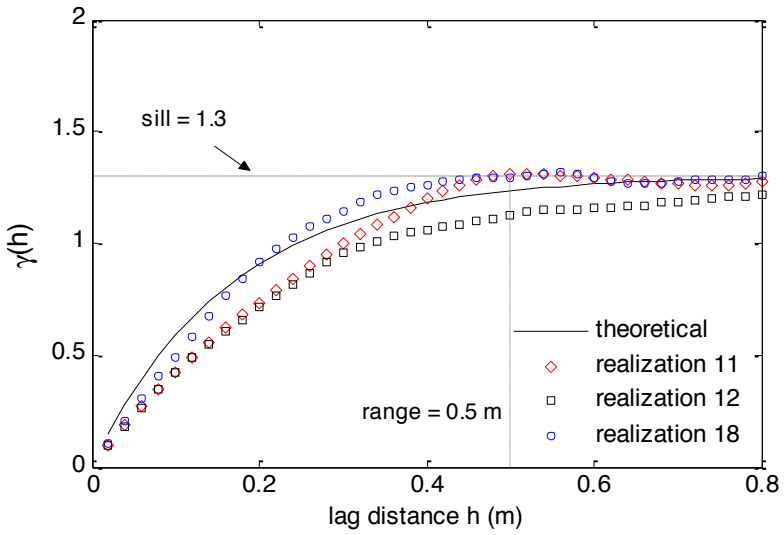

Figure 19 Experimental and theoretical semivariograms for the three stochastic realizations of the permeability field.

In order to compare the degree of heterogeneity of the synthetic reservoir with cases of practical interest, the Dykstra-Parson coefficient V_{DP} was estimated. V_{DP} is a common descriptor of reservoir heterogeneity that estimates the permeability variation (Craig, 1993) as follow:

$$V_{DP} = \frac{k_{50} - k_{84.1}}{k_{50}} \tag{12}$$

where k_{50} is the permeability mean and $k_{84.1}$ is the permeability mean plus a standard deviation; for a homogeneous reservoir V_{DP} approaches zero, while for an extremely heterogeneous reservoir V_{DP} would approach one. V_{DP} estimated from the experimental heterogeneous permeability field resulted to be 0.64, which is in agreement with values reported in the literature (Farajzadeh et al., 2011; Kumar et al., 2005; Saadatpoor et al., 2010).

Similarly to the experiments carried out in the 3 ft. × 2 ft. setup, prior to the Soltrol injection, the porosity variation of the sand pack was determined for both homogeneous and heterogeneous packing configurations by means of x-ray attenuation (Figure 20). Regarding the heterogeneous packing, due to similar porosity (~0.4) of the six sands, their spatial distribution is not distinguishable from this contour plot; however, the evidence of an inclined stratification, as well as of the clay layer confining the aquifer (porosity>0.5) is clear. The higher porosity observed in the heterogeneous case is due to the looser packing carried out to minimize the mixing of finer and coarser sands.

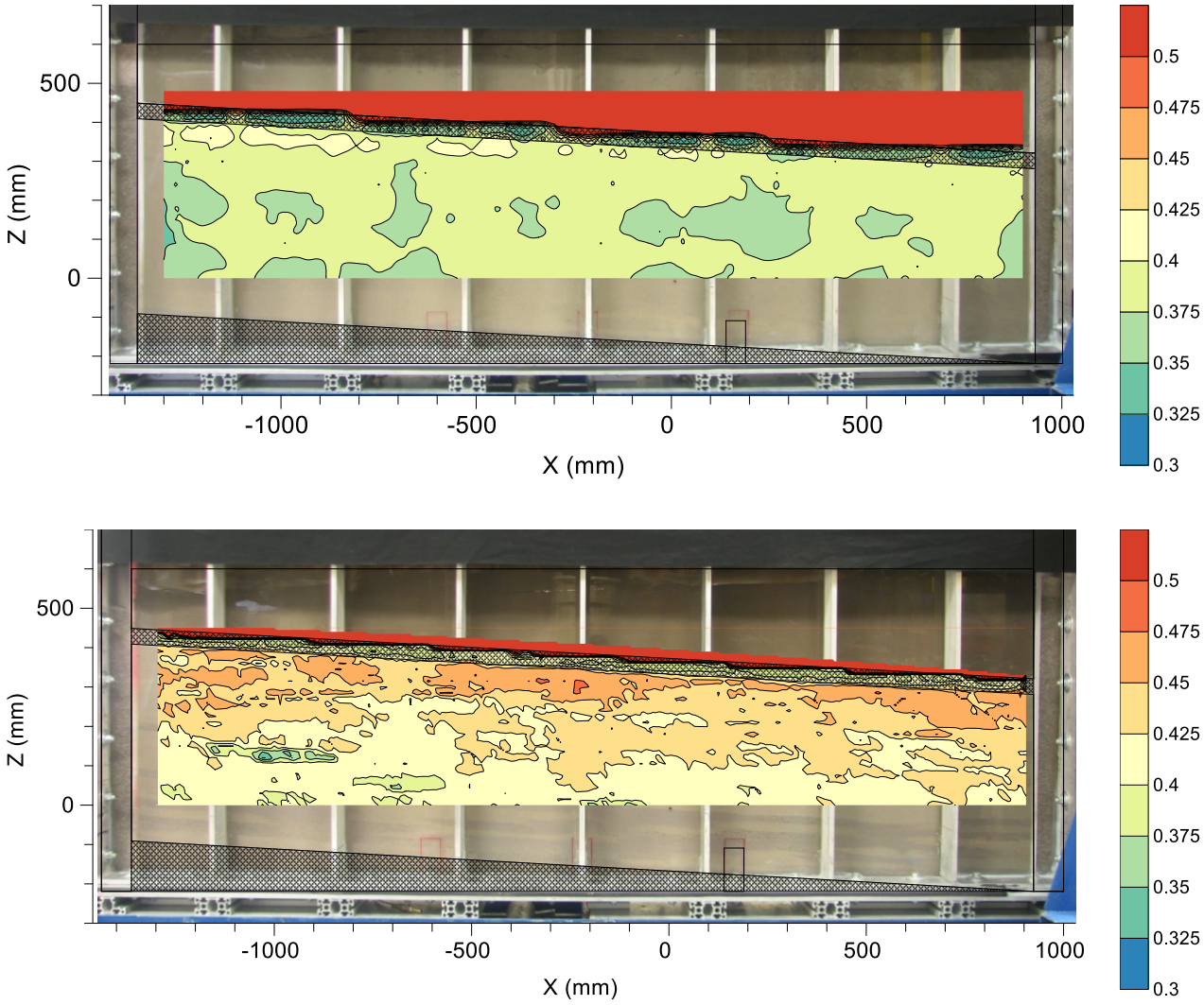

Figure 20 Sand porosity distribution for the homogeneous (top) and heterogeneous (bottom) setups.

One of the advantages of conducting experiments in 8 ft. × 4 ft. tanks is the ability to constrain a background hydraulic gradient to observe effects on NWP plume migration and trapping. Prior to the injection of Soltrol 220 into both homogeneous and heterogeneous configurations, different background hydraulic gradients were tested in order to obtain an equal discharge rate of wetting phase at the outflow boundary, as shown in Figure 21. For the heterogeneous case, a 4.5-cm height difference, corresponding to a 2% gradient, was selected, resulting in a wetting phase flow discharge of 0.56 ml/min. In order to maintain the same wetting phase flow discharge for both experiments, the hydraulic gradient through the homogenous aquifer had to be larger (4.4 %).

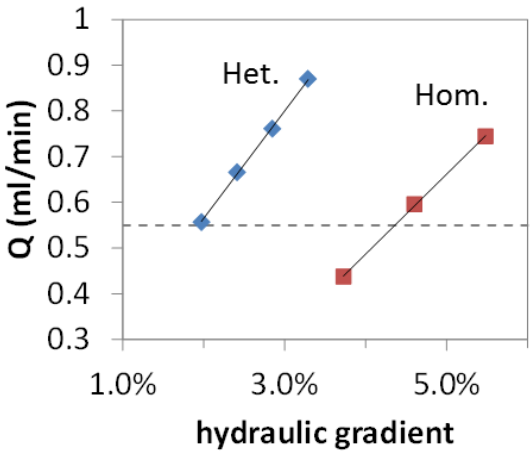

Figure 21 Correlation between outflow rate and background hydraulic gradient (dashed line represents the 0.56 ml/min wetting phase flow discharge applied to both large tank experiments).

This behavior supports the evidence of the connectivity of some high permeability layers in the heterogeneous experiment, which contribute more to the flow of the wetting phase, as illustrated by the horizontal blue bars in Figure 22, representing the relative magnitude of the harmonic mean calculated for each horizontal layer.

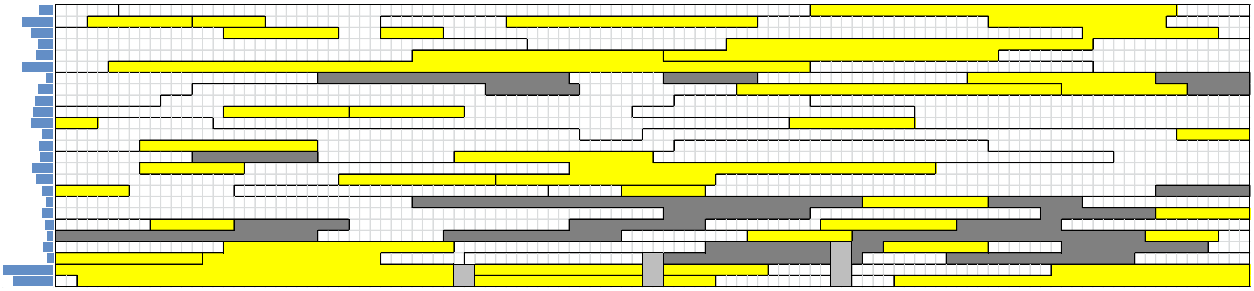

Figure 22 Packing grid of the large tank heterogeneous experiment. Yellow layers represent high permeability (#16, #20, and #30 sands), dark grey layers represent low permeability (#110 sand). Blue bars on the left symbolize the relative magnitude of the harmonic mean calculated for each horizontal layer. Highest value is 7.93×10^{-11} m^2, lowest value is 8.09×10^{-12} m^2.

3.2 Dissolution trapping (miscible displacement) experiments

In dissolution trapping studies, two-dimensional (2-D) and three-dimensional (3-D) observations provide better understanding on the processes under ambient pressure and

temperature conditions. First of all, different fluid combinations were tested in the 2-D small tank for the selection of the most appropriate surrogate fluids of $scCO_2$ and formation brine.

First, the contribution of mixing processes to the stable trapping of dissolved $scCO_2$ in deep heterogeneous geologic formations was studied. In homogeneous formations, mixing is dominated by convection, and the dissolved mass moves through the deeper parts of the formation. On the other hand, in presence of heterogeneity, the dominant mixing process (either diffusive or convection mixing) and the spatial distribution of dissolved $scCO_2$ depend on the geometry, distribution and hydraulic properties of the units in the formation, which influences the storage efficiency (Figure 23).

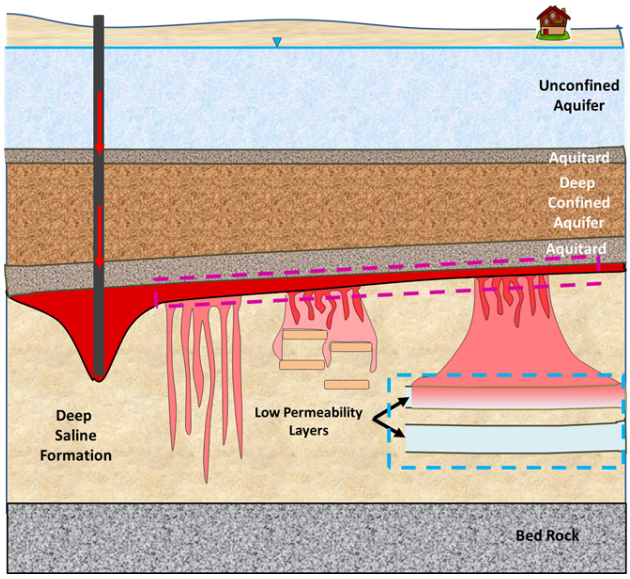

Figure 23 Conceptual model of mixing in homogeneous and heterogeneous porous media.

In the second experimental study, the large tank experiments were designed to examine the storage capacity of low permeability layers compared to homogeneous formations using the spatial moment analyses and the effects of back diffusion on the persistency of stored mass. The tank is made of Plexiglas. The back side of the tank has 448 sampling ports which allows for sampling during the experiment for the measurement of concentration variations. Periodically taking digital images from the front and back sides of the tank allow for the tracking of the plume movement. In addition, the tank is wide enough (7.7 cm) for the observation of the 3-D density-driven convective fingering. After completion of the homogeneous media experiments,

layered heterogeneous systems are examined for the storage capacity/time of the low permeability layers and the effects of back diffusion.

The findings from the first part of the study suggest that the low permeability layers are able to store dissolved $scCO_2$ through immobilization depending on their permeabilities and thicknesses. In other words, the low permeability zones in layered systems could enhance the storage of dissolved $scCO_2$. However, back diffusion, which occurs when the concentration of the reservoir becomes less than the concentration of the low permeability layer (Figure 24), reduces the amount of immobilized dissolved $scCO_2$. The storage capacity of low permeability layers and the impacts of back diffusion on the persistence of the dissolved $scCO_2$ in low permeability layers are examined in the second part of the project using large tank experiments and numerical modeling.

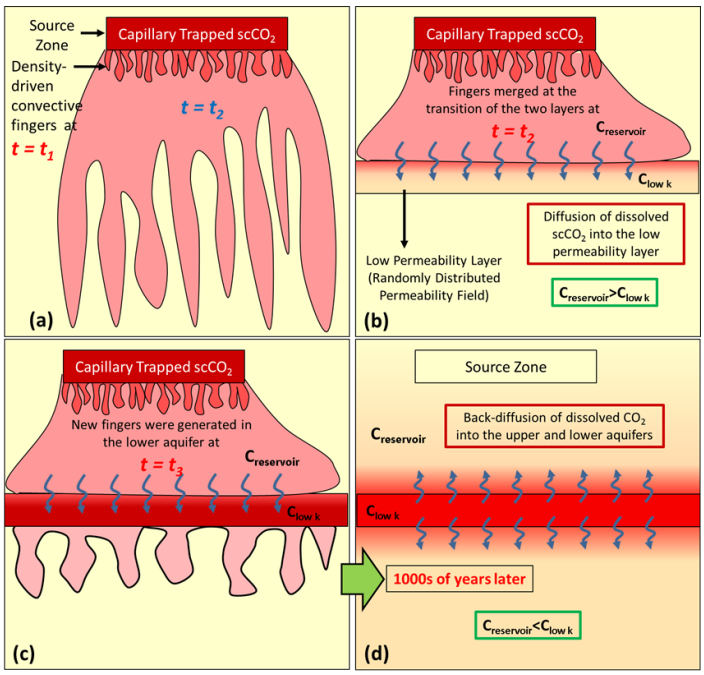

Figure 24 Conceptual model for the spreading of dissolved CO_2 in (a) homogeneous and (b-d) layered porous media, (c) the generation of convective fingering in lower aquifer, and (d) the back-diffusion from low permeability layer.

Similarly to the capillary trapping experiments, dissolution trapping experiments were performed in a 2-D test tank using surrogate fluids for $scCO_2$ and brine. However, where the former category of experiments is characterized by the immiscibility of the two fluids, the surrogate fluids used in the following experiments are partially miscible. The tank was packed

with test sands having variable permeabilities to observe the physics of the processes clearly for distinct homogeneous and heterogeneous cases.

3.2.1 Selection of surrogate fluids

The first experimental study conducted in the small-scale tank (described in the next section) was for the selection of the surrogate fluids of $scCO_2$ and formation brine because our test tanks were not designed to resist the high pressures present in deep geologic formations. For this reason, we chose to use surrogate fluids that have similar physical and chemical properties with $scCO_2$ and formation brine. Two sets of small tank experiments were carried out using the selected surrogate fluid combination (propylene glycol (PG) is for formation brine, and food dyed water is for $scCO_2$) to investigate the influences of (1) homogeneity and (2) heterogeneity on the contribution of convective mixing to the stable trapping of dissolved $scCO_2$.

For this task, two possible surrogate fluid pairs, methanol/ethylene glycol mixture (MEG) in water (Neufeld et al., 2010) and water in propylene glycol (PG) (Backhaus et al., 2011), were tested with the selected test sands. The comparison of the densities of the candidate fluid combinations, and $scCO_2$ and formation brine before and after dissolution are given in Table 5 and Figure 25, respectively. Neufeld et al. (2010) used a food dyed mixture consisting of 37% methanol and 63% ethylene glycol (MEG) by weight as surrogate $scCO_2$, and observed the spreading of dissolved MEG in water. Backhaus et al. (2011) performed experiments with water dyed with food dye and PG as surrogates of $scCO_2$ and formation brine, respectively. For both of the fluid pairs, the density of resultant fluid after dissolution was greater than the density of the surrogate brine (Figure 25). A series of porous media tests was carried out using these fluid pairs by following the experimental methodology explained in the next section. In these tests, the soil packing configuration given in Figure 31 was used, and the main domain was packed with #30/40 sand.

The results of the porous media tests given in Figure 26 demonstrate that density-driven convective mixing is observed in both of the fluid pairs (Figure 26a and b). The dyed dissolved surrogate CO_2 was outlined to compare the variations in the spreading with time. Each spreading contour represents the particular time given on Figure 26a and b. The outmost contour is for the final distribution of the dissolved fluid inside the tank. The image processing method cannot be used to determine the dissolved concentrations for the fluid selection experiments due to greater

oscillations in the light intensity during these experiments and location of the tank in the laboratory.

Table 5 Density ratios of $scCO_2$-formation brine and tested fluid combinations.

Fluid Combinations	Fluids	Density (g/cm^3)	Solubility (mole/kg)
Supercritical CO_2 in Formation Brine (Nordbotten et al., 2005)	$scCO_2$	0.266-0.733	~1.2575
	Brine	0.945-1.230	
Methanol/Ethylene Glycol (MEG) in Water (Neufeld et al., 2010)	MEG + Food Dye	0.967	Miscible
	Water	0.997	
Water in Propylene Glycol (Backhaus et al., 2011)	Water + Food Dye	0.997	Miscible
	Propylene Glycol	1.034	

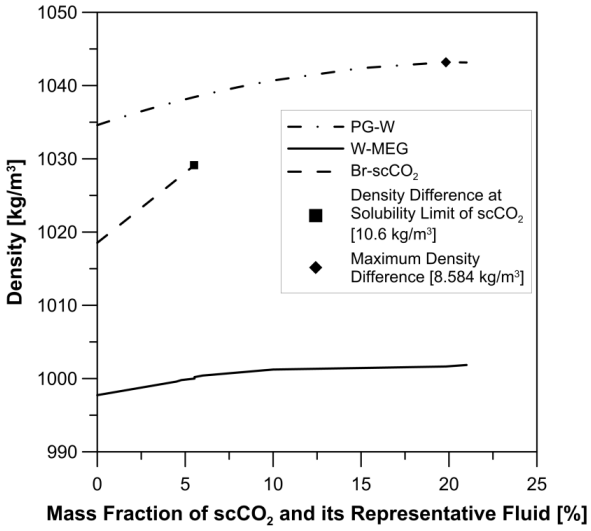

Figure 25 Variation of density of formation brine, PG solutions and water solutions with mass fraction of CO_2, water and MEG, respectively.

The spreading of dissolved MEG in water was very fast, which limits the detailed observation of the formation of density-driven fingers and mixing processes (Figure 26a). However, the dissolution of water in PG, the initiation of the density-driven fingers and the spreading of dissolved water in porous media were slow enough to track the physical processes clearly (Figure 26b). Therefore, the PG and water fluid combination was selected for small tank experiments.

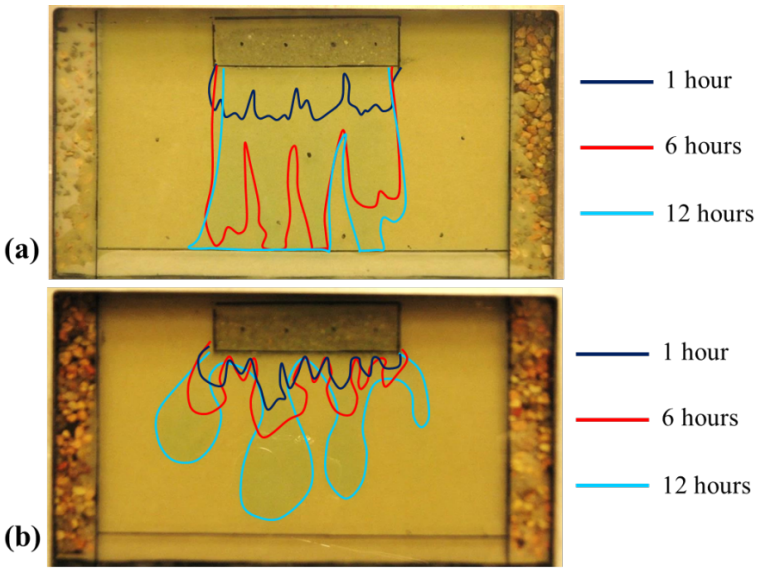

Figure 26 Results of porous media experiments for the selection of the test fluid pairs: (a) methanol/ethylene glycol in water and (b) water in propylene glycol.

PG, which is a member of the glycerol family, is a colorless, nearly odorless and clear viscous liquid. The density and viscosity of pure PG and PG solutions depend on temperature. Under ambient pressure (atmospheric) and temperature conditions (~22^{o}C), the density and viscosity of the PG solutions change linearly with water concentration for lower mass fractions of water. The relationships given in equations (13) and (14) are for the density and viscosity as a function of water mass concentration, respectively. The general density characteristics of PG solutions and CO_2 solutions are similar (Figure 25); however, the viscosity variations of these solutions are slightly different. The viscosity of the PG solutions decreases with increasing water fraction (equation (14)), which speed up the vertical motion of the dissolved water at higher concentrations. On the other hand, the viscosity of brine is assumed to be independent of the CO_2 concentration (Phillips et al., 1981).

$$\rho_{PG} = 85.935w^3 - 217.62w^2 + 88.425w + 1034.1 \tag{13}$$

$$\mu_{PG} = 4.4968\times10^{-2}\exp(-3.8613w) \tag{14}$$

where w is the water fraction.

3.2.2 Measurement Methods

a. Image Processing Method

In the small tank density-driven flow experiments, propylene glycol (PG) and water were used as surrogates of brine and $scCO_2$, respectively. In order to determine the dissolved water concentrations inside the tank, different methods were tested including gas chromatography, mass spectrometry, refraction index etc. However, none of these methods was able to measure dissolved water concentrations due to specific chemical properties of propylene glycol and low concentrations of water. Therefore, an image processing method was developed for the determination of concentration distribution inside the tank from the periodically taking digital images. The image processing method was carried out for the five sands (#50w, #50/70, #40/50. #30/40, and #12/20) that were used in the homogeneous and heterogeneous media small tank density-driven flow experiments. The sands were packed in a layered system for variable background concentrations of dissolved water in propylene glycol as seen in Figure 27. The digital images taken for each concentration were analyzed based on RGB (Red-Green-Blue) color intensities. The results of the analysis showed that Green intensity captures the concentration variations much better compared to Red and Blue. The relationship between Green color intensity and dissolved water concentration as seen in Figure 28 was formulized for each sand. By using the developed equation, the concentration distribution inside the tank for each experiment were determined.

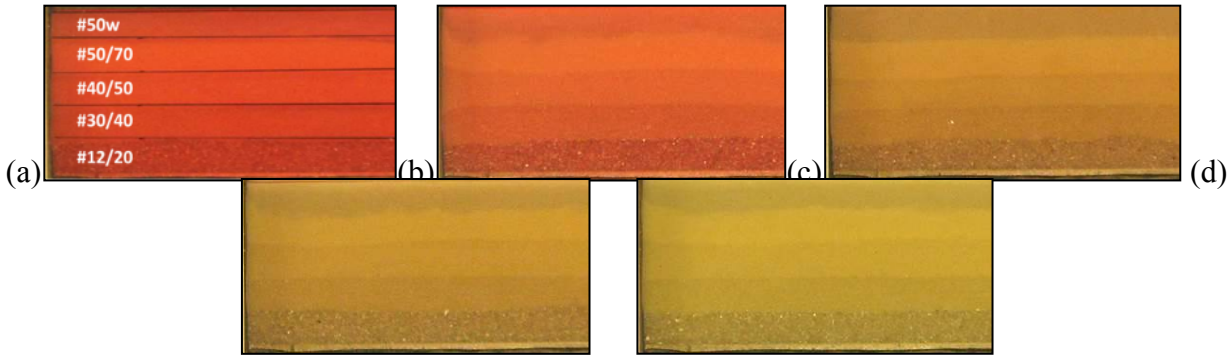

Figure 27 Five different sands having (a) 47.98 kg/m^3, (b) 23.99 kg/m^3, (c) 4.798 kg/m^3, (d) 2.399 kg/m^3, and (e) 0.4798 kg/m^3 dissolved water concentrations.

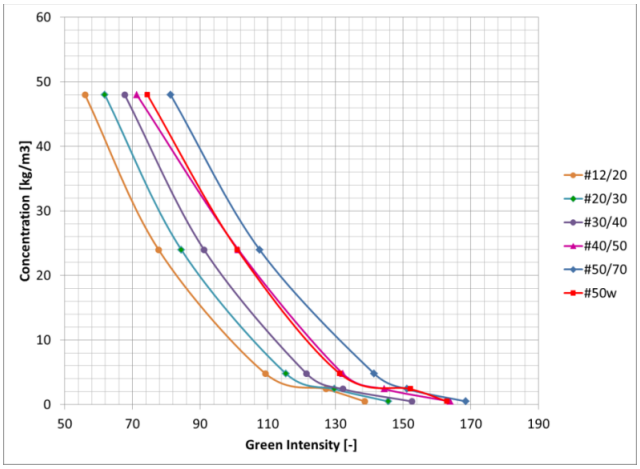

Figure 28 Concentration vs Green intensity graph for the sands.

b. Ion Chromatography

Ion chromatography (IC) is a type of liquid chromatography that quantifies concentrations of ions by using an ion exchange resin to separate different ions present within a sample. Chromatography is a separation technique where a sample containing various chemical compounds is injected instantaneously into a column, and the different compounds travel through the column at different rates based on their chemical properties. The Dionex DX-600 IC system in the Center for Experimental Study of Subsurface Environmental Processes (CESEP) laboratory has the capability of analyzing for both anions and cations, but is currently set up only for anion analysis. In IC method, each anion that shows up at different times has a unique bell shaped curve (Figure 29). This method was used in the large tank density-driven flow experiments in order to determine the Br^- concentrations (Figure 29) for calculation of the NaBr

concentrations of the unknown samples taken from the tank. In this method, the retention time of Br^- is ~6.8 minute, and the detection limit of Br^- is 0.1 mg/l.

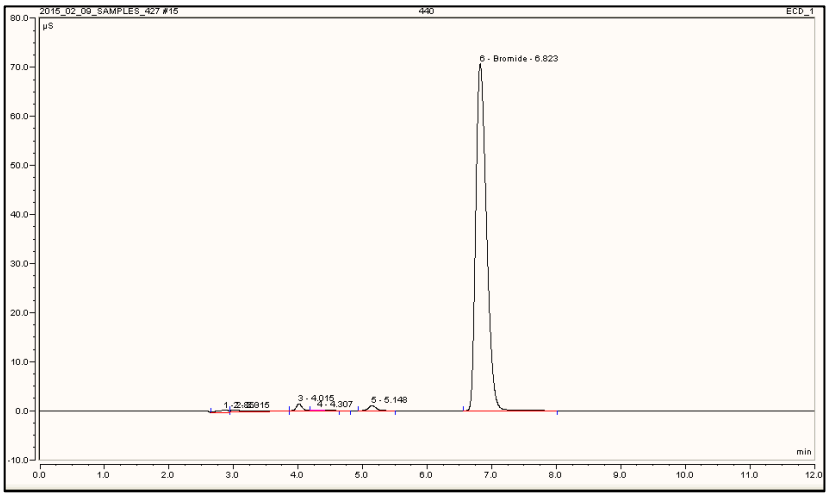

Figure 29 IC response for one of the standards: vertical axis represents conductivity in µS, while horizontal axis represents retention time in seconds.

In order to calculate the unknown concentrations accurately, it is necessary to draw calibration graph using standards. Standards are the samples with known concentrations (Table 6). When either height or area of the curve of the standards are correlated with their corresponding known concentrations, the relation between response (height/area) and the concentration is developed to calculate concentrations of the unknown samples.

Table 6 IC response for the known concentration NaBr standards.

NaBr Concentration [g/l]	Retention Time [min]	Height [µS]	Area [µS×min]
0.0513	6.86	1.919	0.330
0.1538	6.83	7.693	1.313
0.5130	6.81	23.591	4.128
1.5380	6.74	80.925	15.601
5.1300	6.61	223.646	54.090
15.3800	6.45	474.017	147.424

In Table 6, the retention time, height, and area of the known concentration standards are listed. There is a linear relationship between height/area and corresponding NaBr concentration as seen in Figure 30a and Figure 30b. However, the accuracy of the height measurements

decreases at higher concentrations (Figure 30a) because the curve might be trimmed at the top due to upper detection limit of the IC. On the other hand, the area provides more accurate results (Figure 30b). The relation between the area under the Br^- curve and the NaBr concentration is seen in Figure 30b for the listed standards in Table 6. The concentrations of the samples taken from the large were calculated using this relationship.

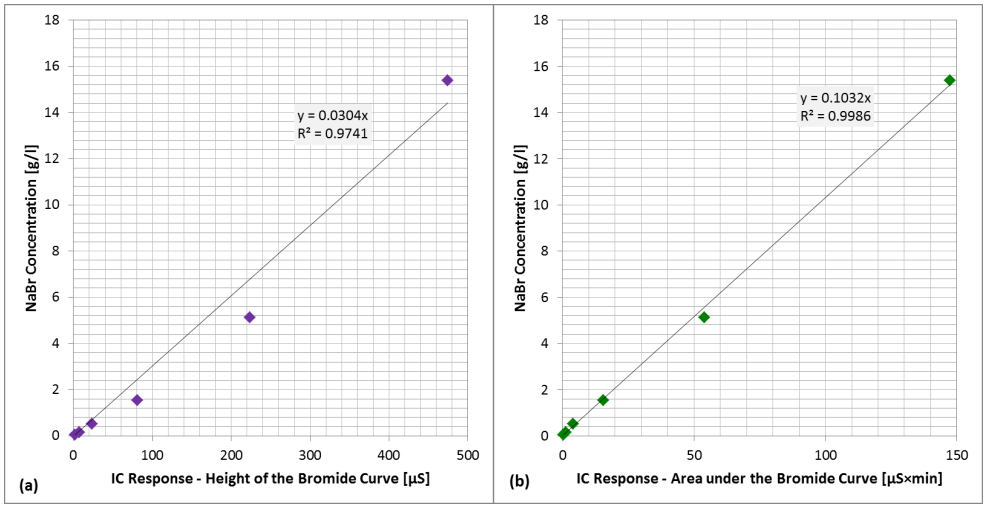

Figure 30 IC calibration curve to calculate NaBr concentrations of unknown samples using (a) height and (b) area of the Br^- curve.

c. Gas Chromatography

Gas chromatography (GC) equipped with flame ionized detector (FID) was used in the small tank mass transfer experiments to determine the dissolved hexanol concentrations in water. GC is one of the common methods used in analytical chemistry in order to separate and analyze compounds by vaporizing the samples without decomposition. For these analyses, FID was used because it is sensitive to wide range of organic compounds, concentrations, and hydrocarbons. Selection of carrier gases plays an important role for the detectors, and for different detectors, different carrier gases are needed. For GC with FID, ultra high purity helium, ultra high purity nitrogen, hydrogen, and zero air gases were used. As in IC method, each component produces a specific spectral peak at different times. The height and area of these peaks are proportional to the concentrations of the corresponding substances in the sample. In the analyses, a Hewlett Packard HP 6890 GC with FID was used.

d. X-ray Attenuation Method

The x-ray attenuation method was used to determine the spatial and temporal distribution of hexanol saturations trapped in the source zone in the small tank mass transfer experiments. The x-ray attenuation method is based on Beer-Lambert's law that describes the change in energy intensity for a beam of mono-energetic photons traveling through a material with linear attenuation coefficient α and thickness x:

$$I/I_0 = e^{-\alpha x} \tag{6}$$

where I is the intensity of photons transmitted across the material, and I_0 is the photon flux in the absence of a material or incident beam intensity (Trevisan, 2015). Volumetric fractions of any of the phases (hexanol) inside the tank are measured moving x-ray source and photon detector simultaneously along the scanning grid. The interpolation of the data gives the distribution of the scanned phases (hexanol) in the tank.

The hexanol saturations in the source zone were determined by following these steps:

(1) The empty tank (I_0) and tank filled with wetting phase (water) (I) were scanned in a row to obtain path length which is width of the tank.

(2) The tank filled with wetting phase (I_0) and wet-packed tank with the sands (I) were scanned to determine path length of the void spaces which is porosity of the sand. Interpolation of this data gives the porosity map of the sand inside the tank.

(3) The wet-packed tank (I_0) and porous medium with trapped hexanol (I) were scanned as a last step to calculate the path length of the hexanol which is hexanol saturation. Data was interpolated for determination of the saturation distributions in the source zone.

3.2.3 Small tank homogeneous setup

The 2-D test tank was made of Plexiglas and aluminum with 27.94 cm × 15.24 cm × 2.54 cm (L×H×W) internal dimensions (Figure 31). Plexiglas wall allows for the visual observation of the processes by periodically taking digital images. The sampling ports drilled on the other side of the tank were used for the creation of the source.

The tank was packed to represent a confined saline formation using the test sands. The model domain was composed of four zones: the main mixing domain, the source zone, the

impervious caprock and bedrock, and the two head reservoirs to set the boundary conditions. Each of these zones was packed with test sands with known permeabilities (Table 7).

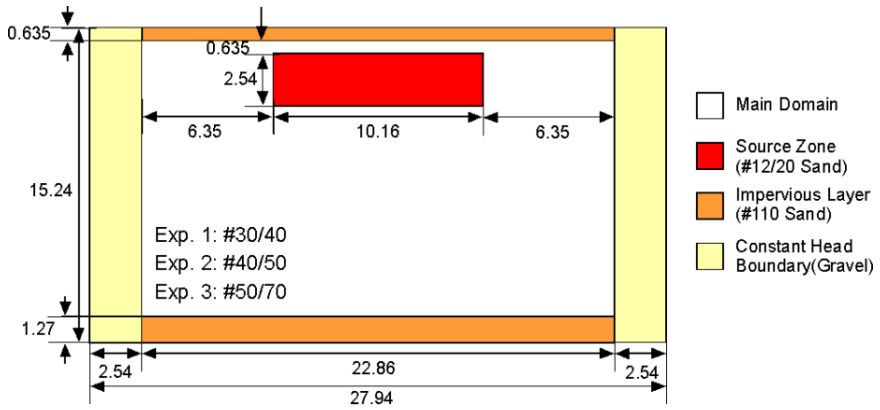

Figure 31 Two-dimensional small scale experiment (units are in cm).

The upper and lower impervious boundaries of the synthetic reservoir were achieved with very low permeability #110 sand by the creation of a hydraulic barrier. Two vertical gravel packs were placed to the left and right boundaries as optional constant head constraints. A discrete coarse sand inclusion packed with a #12/20 sand acted as a source zone to simulate an initial distribution of $scCO_2$ trapped by capillary forces. Sands in the main mixing domain varied depending on the goal of the experiment.

Table 7 The physical characteristics of the sands (Sakaki and Illangasekare, 2007).

Sand Type	Porosity (-)	Hydraulic Conductivity (cm/s)	d_{50} (mm)
#12/20	0.318	0.3760	1.040
#20/30	0.320	0.2300	0.750
#30/40	0.325	0.1060	0.524
#40/50	0.334	0.0520	0.358
#50/70	0.363	0.0359	-
#50w	0.301	0.0186	0.280
#110	0.323	0.00507	0.12

In each experiment, the tank was wet-packed with the surrogate brine (PG). All sides of the tank were closed representing no-flow boundary conditions. In these experiments, it was assumed that the trapped surrogate $scCO_2$ in the source zone was at residual saturation. The

surrogate $scCO_2$ was first dyed with 10% food dye by volume and injected from the four injection ports corresponding to the source zone using four 1 ml plastic syringes. The injected fluid was extracted immediately to represent low saturations (residual saturation). The extraction was continued until the surrogate brine was detected inside the syringes from the color changes. After the dissolution of the surrogate $scCO_2$ in the surrogate brine, the spreading of the dissolved plume inside the tank was tracked periodically through digital imaging.

3.2.4 Small tank heterogeneous setup

Two distinct packing configurations, layered and distinct rectangular blocks, were used to represent four heterogeneous porous media experiments. The first two experiments were carried out for simple (Figure 32a) and complex layering (Figure 32b) to investigate the effects of a texture transition on finger generation, mixing and trapping. In the first experiment, #50/70 sand was overlaid by #40/50 sand with a low angle (7.5^o) inclination as shown in Figure 32a. This experiment was continued for 32 days until the spreading regime in the low permeability layer was clearly identified. Following this experiment, the effects of layered heterogeneity were studied by creating alternating layers of coarse, medium and fine sands in the order of #50w, #20/30, #40/50, and #30/40 (Figure 32b). The thickness of gravel columns located at each end of the tank in the second experiment was decreased to half that of the first experiment to enlarge the main test domain. The spreading of the dissolved plume was tracked for 18 days to investigate the behavior of dissolved water in different permeabilities and at each sand transition.

In the second set of heterogeneous experiments, the distinct rectangular blocks with variable permeabilities were studied to observe the influence of connected high permeability pathways on mixing and stable trapping (Figure 32c, Figure 32d). Except for the thickness of gravel columns, the main difference between these two experiments was the permeability of the rectangular block located under the source zone. In the 3^{rd} heterogeneous experiment, it was packed with medium permeability sand (Figure 32c), whereas low permeability sand was used in the 4^{th} heterogeneous experiment (Figure 32d). These experiments were continued until the impacts of different permeability distributions on the spreading characteristics could be observed and this corresponds to 42 and 7 days, respectively.

3.3 Large tank experimental setup

Large tank experiments were carried out using NaBr solution as dissolved CO_2 and water as brine (Table 8). Among the other salts, NaBr was preferred because Br^- is not a common anion in water with respect to F^-, Cl^-, NO_3^-, SO_4^{-2}, and PO_4^{-3}. This led to the accurate measurement of Br^- concentrations using the ion chromatography method. The known concentration NaBr solution (15.38 g/l) was prepared to achieve the identical density difference (10.60 kg/m^3) with dissolved CO_2 and brine at equilibrium concentration under reservoir pressure (~9 MPa) and temperature (~36˚C) conditions. This fluid mixture allowed us to determine the dissolved concentrations NaBr in water. In addition, 10% red food dye (by volume) added into the NaBr solution enabled the visual tracking of the plume.

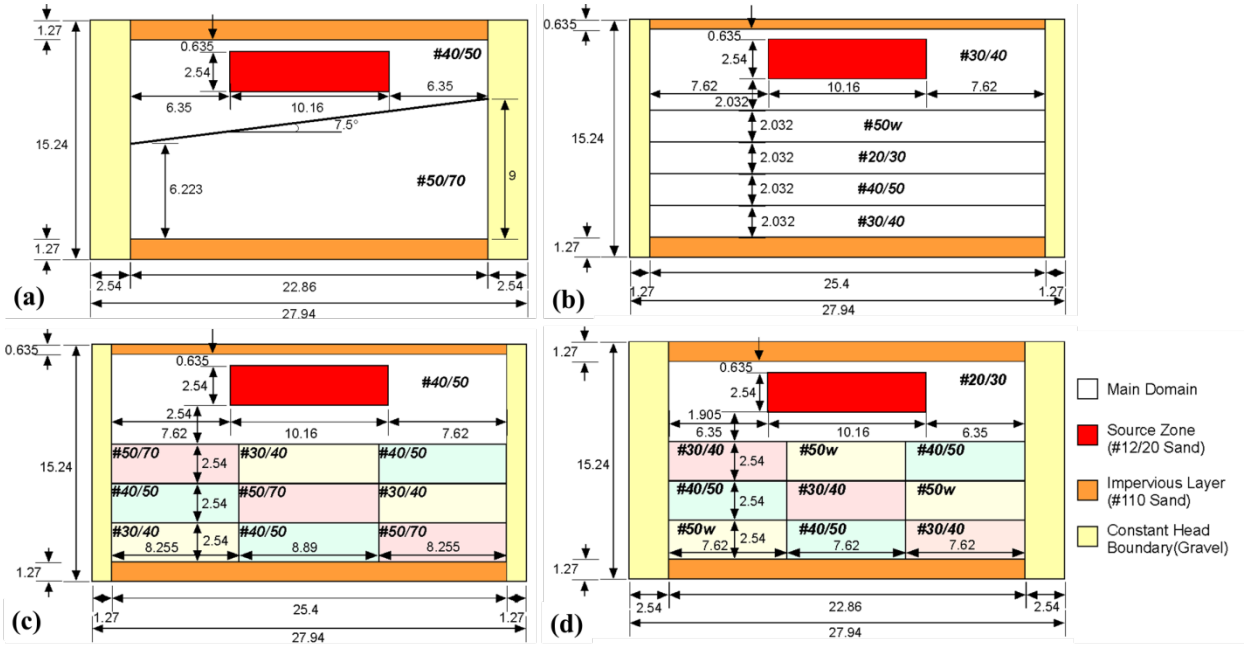

Figure 32 Packing configuration of heterogeneous media experiments (a) 1, (b) 2, (c) 3 and (d) 4 (units are in cm).

Table 8 Density ratios of $scCO_2$-formation brine and tested fluid combinations.

Experiments	Fluid Combinations	Fluids	Density (g/cm^3)	Solubility (g/kg)
-	Supercritical CO_2 in Formation Brine (Nordbotten et al., 2005)	$scCO_2$	0.2660-0.7330	~55.34
		Brine	0.9450-1.2300	
Small Tank Density-driven Flow	Methanol/Ethylene Glycol (MEG) in Water (Neufeld et al., 2010)	MEG + Food Dye	0.9670	Miscible
		Water	0.9970	
Small Tank Density-driven Flow	Water in Propylene Glycol (Backhaus et al., 2011)	Water + Food Dye	0.9970	Miscible
		Propylene Glycol	1.0340	
Large Tank Density-driven Flow /Diffusion	NaBr Solution in Water	NaBr Solution	1.007.6	~943.2 (20˚C)
		Water	0.9970	
Small Tank Mass Transfer	Hexanol in Water	Hexanol + Sudan IV	0.8140	~5.9 (20˚C)

In this section, the setup of large tank experiments and the source injection methodology are explained. Two homogeneous and one heterogeneous media experiments were carried out under ambient temperature and pressure conditions. The heterogeneous large tank experiment was designed to investigate the contribution of convective mixing, diffusion controlled trapping, and back diffusion processes to the long-term storage of dissolved CO_2 in multilayered systems with respect to the homogeneous formations. The intermediate-scale experiments were performed in the plexiglas tank with 243.84 cm x 121.92 cm x 7.7 cm (L x H x W) internal dimensions as seen in Figure 33. The plexiglas material of the tank allowed for taking the periodical digital images from both front and back walls of the tank. This provided us to observe the effects of 7.7 cm thickness of the tank on density-driven fingering process. At the back wall of the tank, 448 sampling ports were drilled to be used to take samples during the experiments to measure concentration variations. The sampling grid can be seen in Figure 33.

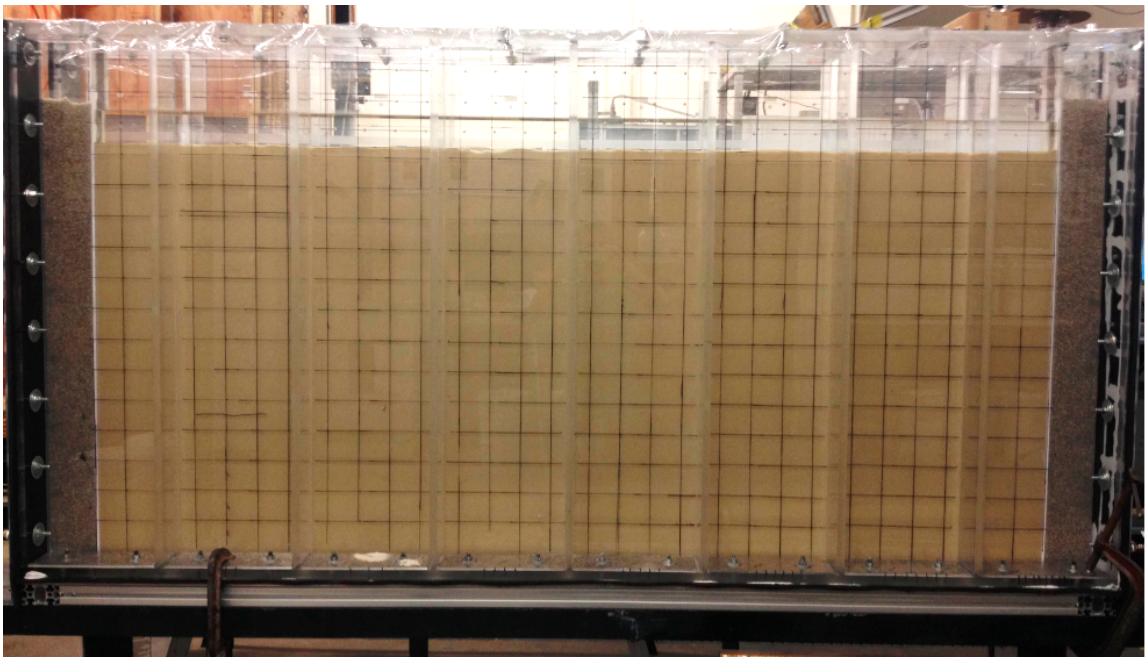

Figure 33 Homogeneous large tank experimental setup showing the sampling grid.

3.3.1 Source Injection Methodology

In the small tank experiments, Agartan et al. (2015a) created the source using the sampling ports corresponding to the source zone. However, the same method could not be applied to the large tank experiments because the sparsely spaced sampling ports (7 cm) led to the generation of individual sources at this scale instead of creating a rectangular source as in the small tank experiments. These individual sources could artificially trigger the fingers. To avoid this, the tube made up of porous material was used to achieve the homogeneous distribution of NaBr solution in the source zone.

The two 50 cm long porous tubes were placed in the middle of the 7.62 cm thick source zone. We assumed that the capillary trapped CO_2 under the caprock was completely dissolved after a certain period of time (in 100s of years). Therefore, the source injection was achieved in two stages. In the first stage, 560 ml food dyed NaBr solution having 15.38 g/l concentration was injected into the source zone with 10 ml/min flow rate using a Harvard Apparatus syringe pump in order to fill the source zone in a shorter time frame without forcing the generation of density-driven fingers. Then, the additional 620 ml NaBr solution was injected with 1 ml/min flow rate to keep the source zone full without applying excessive pressure to trigger the fingers.

3.3.2 Setup of Homogeneous Large Tank Experiment

Two homogeneous porous media experiments (Figure 34) were performed under the same boundary conditions, initial conditions, and source injection scheme. All sides of the tank were closed representing no-flow boundary conditions. The denser food dyed NaBr solution was injected into the source zone to mimic the transport of dissolved CO_2 trapped under the caprock. After the first experiment, the NaBr solution was completely flushed away from the tank. When the NaBr concentrations in the tank dropped down to zero, the second experiment was conducted using the same packing in order to examine the effects of pore-scale heterogeneity present in the homogeneous formations on density-driven flow. The spreading of the dissolved fluid was tracked for 4 days by taking fluid samples from the sampling ports and taking digital images from both front and back walls of the tank.

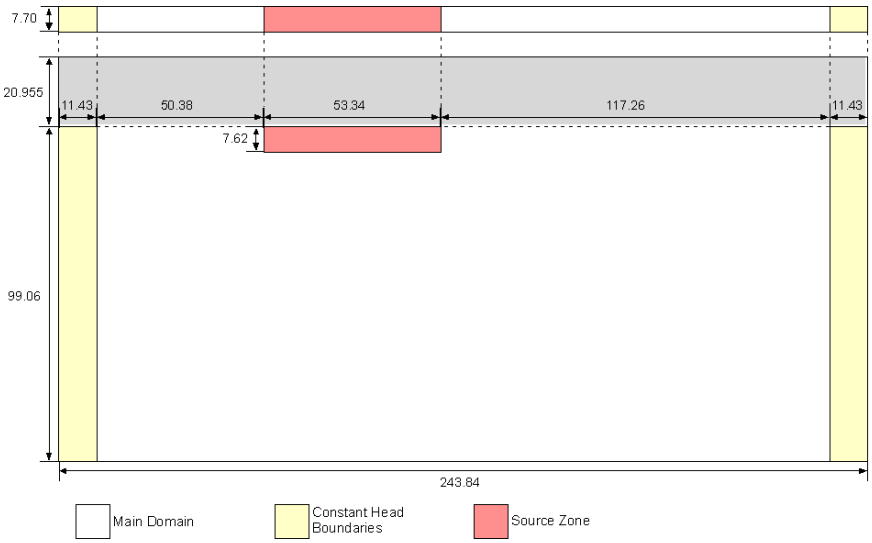

Figure 34 Homogeneous large tank experimental setup (units are in cm).

3.3.3 Setup of Heterogeneous Large Tank Experiment

With respect to homogeneous experiments, the continuous 9.525 cm thick low-permeability layer was added in the middle of the main mixing domain packed with #40/50 sand (Figure 35). The low-permeability layer was composed of #110 sand and silt. The geometry and the sands of the vertical two head reservoirs and the source zone were same with the homogeneous experiments. The same source injection scheme was applied with the homogeneous media experiments. Unlike the homogeneous experiments, the background

hydraulic gradient (i = 0.0008, analogues value to Gulf Coast from Hubbert, 1953) was applied to both of the aquifers (1st period). After 8 days, the background water flow was stopped in order to understand fundamentals of the observed processes (2nd period). The second background water flow was initiated on 19th day (3rd period). At this time, the higher hydraulic gradient was applied to flush away the mass in the aquifer in order to estimate the percentage of stored mass in the low-permeability materials.

The low-permeability layer was composed of randomly distributed #110 sand (in red color) and silt (in blue color). The relative volumetric proportions for each material is: 50% of #110 sand and 50% of silt. The low-permeability materials were distributed in a 2-D vertical rectangular array of 128 (x) by 5 (z) cells with 1.905 cm × 1.905 cm dimensions. Sequential Indicator Simulator (SIS) algorithm from the geostatistical library GSLIB (Deutsch and Journel, 1998) in Stanford Geostatistical Modeling Software (SGeMS) was used to generate 10 realizations. In order to investigate the behavior of dissolved mass in relatively higher permeability connected pathways present in low-permeability layers, the long horizontal (50 cm) and medium vertical (3.81 cm) correlation lengths were chosen. The realization that honored the target material ratios (50% sand and 50% silt) and showed adequate #110 sand connectivity in both x and z directions was selected (Figure 35) to be studied in the large tank experiment.

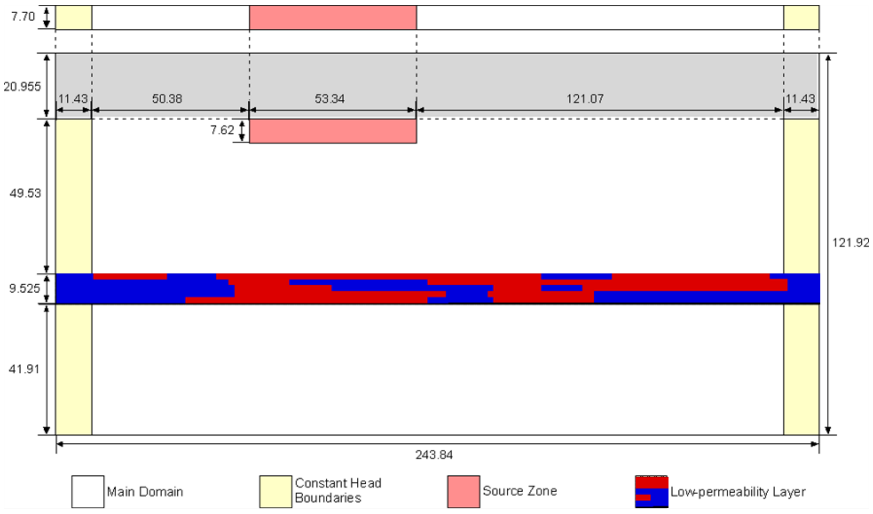

Figure 35 Heterogeneous large tank experimental setup showing low-permeability zone packing. Red and blue colors represent #110 sand and silt, respectively (units are in cm).

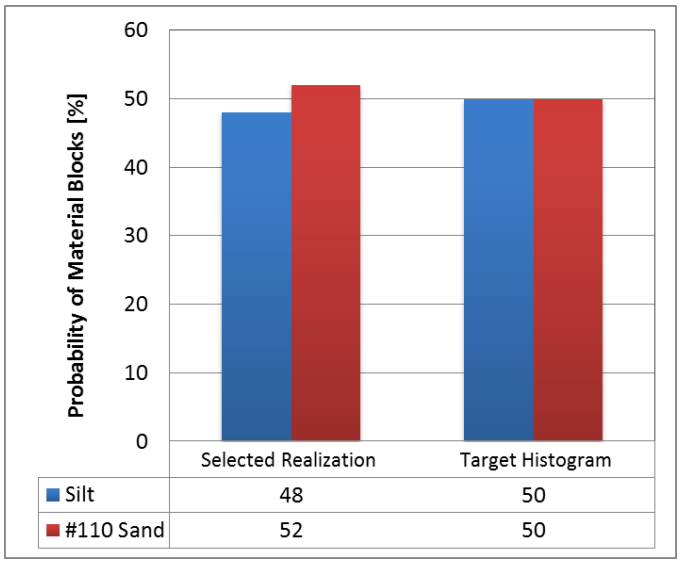

Figure 36 Comparison of histogram of the selected realization with the target material ratios.

3.3.4 Column experiments to obtain constitutive models

Constitutive relationships of $P_c - S_w$ and $k_r - S_w$ of multiphase flow systems are needed as inputs for models that could be used for improved understanding of behavior of $scCO_2$ and brine in geologic systems. In this section we present the development of constitutive models for the surrogate fluids of $scCO_2$ and brine used in the tank experiments.

3.3.5 Pc – Sw curve measurements

Experimental methods for to obtain the P_C –S_W and k_r – S_W relationship for the surrogate fluids and test sands were investigated. First, various methods for measuring the P_C –S_W relationships were examined. As the use of $scCO_2$ as the non-wetting fluid under ambient laboratory conditions are not feasible, use of surrogate fluid pair in the laboratory to obtain these relationship was tested. As will be presented in the next sub-section, a scaling method referred to as Leverett scaling can be used to obtain the P_C – S_W relationship for a second fluid combination using the P_C – S_W relationship of another fluid pair. However, this scaling method does not consider changes in the irreducible saturation and residual saturation that are specific to the fluid types used. Therefore, two other methods were developed to evaluate the differences in these two saturations. This research compares the P_C – S_W relationships derived from Leverett scaling and the two new methods developed in this research that scales the entry pressure, and use dielectric sensors to mesure the differences in irreducible saturation and residual saturation. Also, hysteresis behaviors of P_C –S_W relationships were investigated.

a. Leverett scaling method

Leverett (1941) found that a dimensionless shape function $J(S_w)$ defined in Equation (15) allows for the determination of the P_c – S_w relationship for one fluid pair in a porous medium (e.g. $scCO_2$-brine or the surrogate fluid pair) from that of another two-phase porous medium system (e.g., air and water).

$$J_{(S_x)} = \frac{P_{c,1}}{\sigma_1}\left(\frac{k_1}{\phi_1}\right)^{1/2} = \frac{P_{c,2}}{\sigma_2}\left(\frac{k_2}{\phi_2}\right)^{1/2} \tag{15}$$

Where, P_c = capillary pressure [F/L^2], ϕ = porosity (-), subscript 1 and 2 corresponds to fluid pair 1 and 2.

When scaling in the same porous medium where the porosity and intrinsic permeability are the same, P_c for fluid pair 2 calculated in terms of fluid pair 1 is given by;

$$P_{c,1} = \frac{\sigma_1}{\sigma_2} P_{c,2} \tag{16}$$

Equation (16) shows that with Leverett scaling, the P_c – S_w relationship for a second fluid pair can be estimated from the known P_c – S_w relationship for a different fluid pair using the ratio

of interfacial tension values of each of the two fluid pairs. Therefore, the P_c for the $scCO_2$-brine system is expected to be lower by a factor of ~0.27-0.82 compared to the $P_c - S_w$ relationships of air-water system reported by Sakaki et al. (2013).

b. Entry pressure scaling method

A primary limitation of the Leverett scaling method described above is that the scaling factor is solely determined based on the interfacial tension between the two fluids and it does not factor in the effect of possible differences in the contact angle affecting the $Pc - S_w$ relationship for the two fluid pairs. Richardson (1961) included the contact angle into the Levertt scaling method, although measurement of contact angle of two phases is not always easy. We found that forming a bubble of Soltrol (surrogate for $scCO_2$) in glycerol/water (surrogate for brine) to measure the contact angle was difficult as Soltrol was lower in density compared with glycerol/water. As an alternative to a method that relies on the measurement of the contact angle, we proposed a scaling method based on entry pressure, which would include the effect of both contact angle and interfacial tension. However, we are aware that measurements will be affected by sand packing conditions and it takes significant amount of time compared to the Leverett scaling. The scaling was performed using Equation (16) but substituting ratio of entry pressures in place of ratio of interfacial tension. To measure the entry pressure head of the Soltrol-glycerol/water system, an experimental set up shown in Figure 37 was constructed with three identical columns placed on the same platform. Three columns were used to verify the reproducibility of the results. The test sand was first tightly wet-packed in the glycerol/water mixture (with a wetting surrogate fluid height of 15 cm in each column). An external constant head device filled with glycerol/water, which is connected at the bottom of each column, was positioned at the same elevations as the surface of the glycerol/water-saturated sand (15 cm elevation) to maintain the glycerol/water head at the same value. A Mariotte bottle filled with Soltrol was connected to the top part of all three columns to supply Soltrol above the glycerol/water saturated sand with a certain pressure head. The pressure of Soltrol was increased in a stepwise manner by elevating the Mariotte bottle at constant intervals of 0.5 cm (as shown in Figure 37). Once a new pressure head is applied with the raised Mariotte bottle, a sufficient time (typically 12 hours) was allowed for the system to reach equilibrium. When there was no

glycerol/water outflow or no Soltrol inflow indicating static conditions, the Mariotte bottle was raised by another 0.5 cm.

The pressure at which Soltrol entered the sand was determined when a sharp change of outflow of the displaced glycerol/water was observed. In addition, the entry pressure was also checked visually using digital photographs taken every 12 hours. Observation of sudden entry of the dyed Soltrol indicated that the capillary pressure has reached the entry value. All experiments were performed at room temperature (approximately 20 ˚C) and required about a week to complete each.

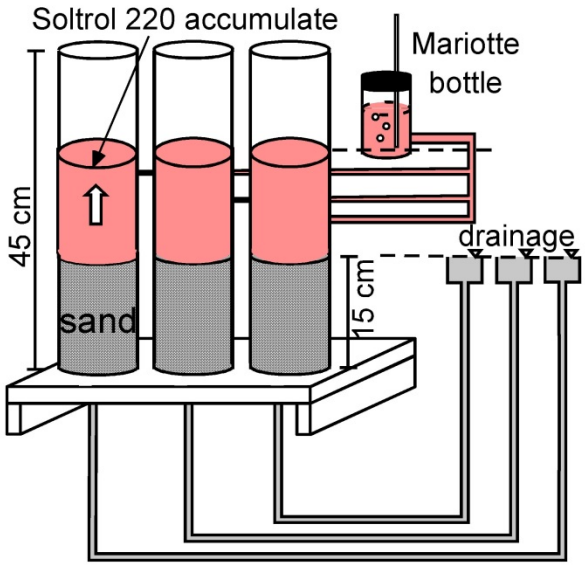

Figure 37 Experimental setup for the determination of entry pressures. Sand was saturated with glycerol/water in advance. The Mariotte bottle was raised to increase capillary pressure and drainage of glycerol/water was monitored at the drainage boundary fixed at the sand surface.

c. Dielectric sensor method

Both the Leverett scaling and entry pressure methods assume that the initial (S_i) and residual (S_r) saturations of different fluid pairs are the same. However, Tokunaga et al. (2013) pointed out that these values could vary for different fluid pairs. The dielectric sensor method used in this study allows for the direct measurement of S_i and S_r during the generation of data for the $P_c - S_w$ relationships. This measurement method first requires the calibration of the dielectric

sensor for the surrogate fluids before conducting the one-dimensional column experiments to obtain $P_c - S_w$ relationships.

The dielectric sensor used to monitor the saturation of the glycerol/water was an ECH_2O EC-5 soil moisture sensor (5.5 cm long, operation frequency 70 MHz, Decagon Devices, Pullman WA). EC-5 sensors measure capacitance of the surrounding soil. The sensor readings are sensitive to the volumetric fraction of Soltrol as its dielectric constant is sufficiently smaller than that of the glycerol/water. Calibration of the EC-5 sensors was based on the two-point α-mixing model developed for the air-water system (Sakaki et al., 2008; 2011), which was extended to surrogate fluids.

For the calibration of sensors, the readings in several soil samples with known but different phase saturations were needed. Unlike the air-water system, we found that it was very difficult to mix the two surrogate fluids in sand (without entrapping air) so that the two phases distribute uniformly within the sand sample. This was largely because lighter Soltrol in the form of bubbles and ganglia tended to flow upward quickly due to buoyancy. After a trial-and-error process, we found EC-5 sensor output showed a good sensitivity to the fraction of the thickness of the sensor, which was placed in the Soltrol and glycerol/water saturated sand. Therefore, saturations were measured having a denser glycerol/water-saturated layer at the bottom and a Soltrol-saturated layer on the top and inserting an EC-5 sensor vertically (perpendicular to the initial fluid layers) at different fraction of the sand layers. The sensor reading (ADC) was recorded at 6 different saturations. A mixing model (Equation (17)) was then fitted to the measured ADC data and the coefficient ε was determined for the Soltrol-glycerol/water system. Note that the ε is a sensor and fluid specific coefficient.

$$S_w = \frac{X^{\varepsilon} - X_{Soltrol}^{\varepsilon}}{X_{Glycerol}^{\varepsilon} - X_{Soltrol}^{\varepsilon}} \tag{17}$$

where, X is the sensor ADC reading, subscript $_{Soltrol}$ and $_{Glycerol}$ are sensor reading in Soltrol saturated soil and the glycerol/water mixture saturated soil, respectively, and ε is the fitting parameter (Sakaki et al., 2008; 2013). The best-fit value of ε was found to be 2.5, which is the same value by Sakaki et al. (2008; 2011) for the air-water system. The measured calibration data points and the fitted mixing model are shown in Figure 38.

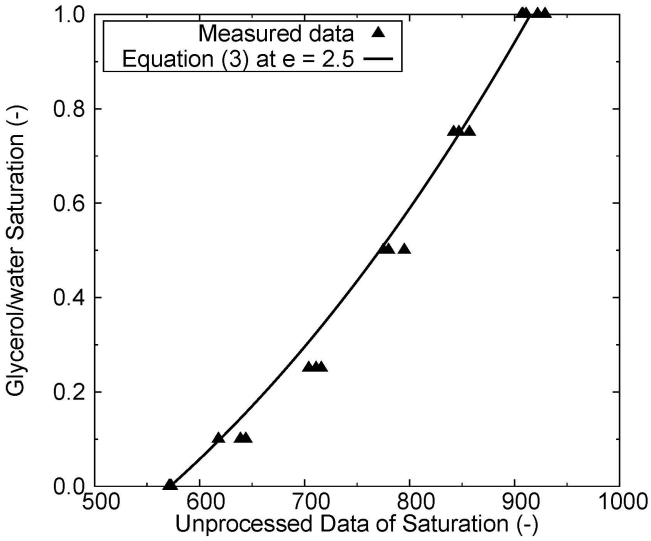

Figure 38 Calibration of EC-5 sensor. The symbols are measured raw sensor outputs at different saturations and the line was obtained by fitting the mixing model (equation (17) with ε = 2.5).

For the direct measurement of $P_c - S_w$ relationships, the one-dimensional column shown in Figure 39 was developed. The saturation of the glycerol/water mixture was measured using two dielectric soil moisture sensors installed at 5 and 10 cm depths from the top of the 50 cm tall column. The size of the sensor is 8.9×1.8×0.7 cm^3. The sampling volume of the sensor is known to be 18 cm^3 (Sakaki et al., 2008), thus, under the configuration shown in Figure 39, the sensors measure phase saturations that are averaged horizontally over the length of the electrodes (~5.5 cm).

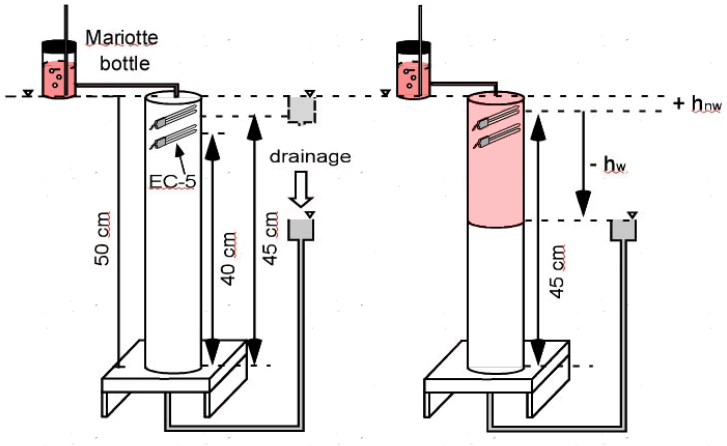

Figure 39 Experimental setup of the dielectric sensor method. (Left) The initial condition of the experimental setup. (Right) After the drainage process has started, by lowering the constant head device.

For each column experiment, glycerol/water saturated sand was tightly wet-packed in the column in accordance with the methodology presented in Sakaki and Illangasekare (2007). An external glycerol/water constant-head reservoir was connected to the bottom of the column, with which the pressure of glycerol/water was controlled. A Mariotte bottle filled with Soltrol was connected to the top of the column. The elevations of the glycerol/water constant-head tank and the Soltrol filled Mariotte bottle were initially set at the same level. By lowering the glycerol/water constant-head reservoir in a stepwise (Figure 39 right), the pressure of Soltrol was increased at the top surface of the sand. The constant-head reservoir was lowered in 2-4 cm height increments, every 12 hours. The outflow of the glycerol/water mixture and Soltrol inflow was continuously monitored. When the capillary pressure at the sand surface exceeded the entry pressure, Soltrol started to penetrate into the column and simultaneously the same volume of the glycerol/water mixture spilled out of the constant-head reservoir. When the outflow ceased, it was assumed that the pressure distribution in both fluids had equilibrated and reached static conditions. Figure 40 illustrates the pressure distributions in the two fluids at a certain state (Mori, 2013). This approach allowed calculation of the capillary pressure in the surrogate fluids without measuring pressures in the two phases separately, as this can be very challenging (Equation (18).

$$P_c = P_{nw} - P_w = \rho_{nw} g L - \rho_w g H \quad (18)$$

Here, g refers to gravitational acceleration [L/T^2], L and H corresponds to the height [L] indicated in Figure 40.

As the drainage proceeded, Soltrol seeped into the sand further and the EC-5 sensor at the top starts to register a decrease that was converted into phase saturation S_w using the calibration (Equation (17)). The $P_c - S_w$ relationship was developed by obtaining the capillary pressure P_c (as in Figure 40) and S_w at each step. When the glycerol/water constant head reservoir was sufficiently low that there was no change in S_w observed, this indicated that S_w has reached the S_r. The wetting cycle was then initiated by elevating the glycerol/water reservoir in a stepwise manner.

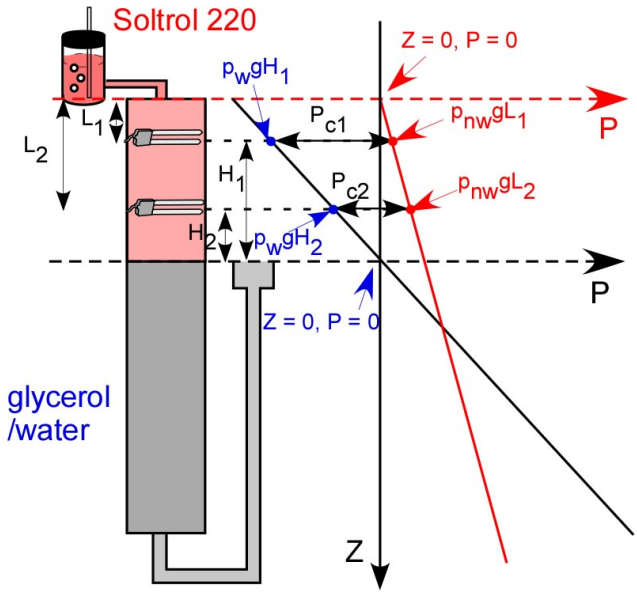

Figure 40 Calculation of capillary pressure P_c based on hydrostatic pressure distributions in both fluids at equilibrium. Red line refers to non-wetting phase such as Soltrol and blue line is wetting phase, glycerol/water.

3.3.6 Measurement of $k_r - S_w$ relationships

In this section, methods for measuring the $k_r - S_w$ relationships are described to obtain both wetting phase and non-wetting phase relative permeabilities. In multiphase flow applications dealing with air – water systems with air as a non-wetting phase with low viscosity, normally only the relative permeability of the wetting phase is measured (Irmay 1954; Corey 1994). As Soltrol, a high viscosity was used as a surrogate fluid for $scCO_2$, it is necessary to

determine its relative permeability. The two different measurement techniques that were used to measure the wetting phase and non-wetting phase relative permeabilities are presented next.

a. Wetting Phase Relative Permeability Measurement: Long Column Method

The long column method presented by Corey (1994) to measure the $k_r - S_w$ relationship of the wetting phase for the air-water system was modified for the surrogate fluid system used in this study. The left side of **0** shows the setup of the long column experiment. This setup consists of a 95-cm-long acrylic pipe, oriented vertically, installed with two ECH_2O EC-5 soil moisture sensors and two tensiometers to measure the phase saturation and head gradient of the wetting phase. The EC-5 soil moisture sensors were located 35 cm and 75 cm from the bottom of the pipe, while tensiometers were placed 30 cm and 80 cm from the bottom. The top of the column was open to the atmosphere and the bottom was connected to a constant-head reservoir which maintained the wetting fluid head level at the same elevation as the bottom of the column. The saturated with glycerol solution column was packed tightly and uniformly throughout the column with sand except for the top and bottom 5 cm of the column which contained a gravel layer to equally distribute the fluids across the column section before entering and leaving the test sand. Both glycerol solution and Soltrol were injected from the top of the column using Mariotte's bottles and the injection rates were adjusted by changing the size of needles connected to outlet of the bottles.

b. Wetting Phase Relative Permeability Measurement: Long Column Method

The long column method presented by Corey (1994) to measure the $k_r - S_w$ relationship of the wetting phase for the air-water system was modified for the surrogate fluid system used in this study. The left side of **0** shows the setup of the long column experiment. This setup consists of a 95-cm-long acrylic pipe, oriented vertically, installed with two ECH_2O EC-5 soil moisture sensors and two tensiometers to measure the phase saturation and head gradient of the wetting phase. The EC-5 soil moisture sensors were located 35 cm and 75 cm from the bottom of the pipe, while tensiometers were placed 30 cm and 80 cm from the bottom. The top of the column was open to the atmosphere and the bottom was connected to a constant-head reservoir which maintained the wetting fluid head level at the same elevation as the bottom of the column. The

saturated with glycerol solution column was packed tightly and uniformly throughout the column with sand except for the top and bottom 5 cm of the column which contained a gravel layer to equally distribute the fluids across the column section before entering and leaving the test sand. Both glycerol solution and Soltrol were injected from the top of the column using Mariotte's bottles and the injection rates were adjusted by changing the size of needles connected to outlet of the bottles.

The long column method presented by Corey (1994) to measure the $k_r - S_w$ relationship of the wetting phase for the air-water system was modified for the surrogate fluid system used in this study. The left side of **0** shows the setup of the long column experiment. This setup consists of a 95-cm-long acrylic pipe, oriented vertically, installed with two ECH_2O EC-5 soil moisture sensors and two tensiometers to measure the phase saturation and head gradient of the wetting phase. The EC-5 soil moisture sensors were located 35 cm and 75 cm from the bottom of the pipe, while tensiometers were placed 30 cm and 80 cm from the bottom. The top of the column was open to the atmosphere and the bottom was connected to a constant-head reservoir which maintained the wetting fluid head level at the same elevation as the bottom of the column. The saturated with glycerol solution column was packed tightly and uniformly throughout the column with sand except for the top and bottom 5 cm of the column which contained a gravel layer to equally distribute the fluids across the column section before entering and leaving the test sand. Both glycerol solution and Soltrol were injected from the top of the column using Mariotte's bottles and the injection rates were adjusted by changing the size of needles connected to outlet of the bottles.

c. Non-Wetting Phase Relative Permeability Measurement: Hydrostatic Method

The non-wetting phase relative permeability (k_{rnw}) was measured using the hydrostatic method presented by Dane et al. (1998). The experimental setup shown on the right side of **0** consisted of two concentric cylinders, the inner made of ceramic and the outer made of Teflon, that were glued to two circular Teflon plates at each end. The length of the double walled cylindrical annulus was 6.5 cm. The diameter of the ceramic and Teflon cylinder were of the same size as the inner and outer radii of the annulus. The ceramic cylinder was hydrophilic and impermeable to Soltrol, the non-wetting fluid. The two cylinders and the end plates sealed with O-rings were assembled and tightened with threaded rods and wing nuts. The sample was

contained between two 200 mm steel meshes to prevent the sand from clogging the fluid supply tubing. The annulus between the Teflon and ceramic cylinders were filled with glycerol solution. When the fluid level in the constant-head device is at the same elevation as the top of the Teflon cylinder, the saturation in the soil is 1.0 (fully saturated). Lowering the height of the constant-head device then can changes the saturation in the sample. The sand was wet packed inside the ceramic cylinder with glycerol solution to avoid trapping air inside the sample. Under hydrostatic conditions, the capillary pressure (P_c) is constant everywhere with in the sample.

In this experiment, we fixed the elevation of the outlet Soltrol reservoir level (indicated as drainage on Fig.1) at 1.5 cm from the top of the cylinder. Since P_c is constant in the sample, the elevation of the Soltrol reservoir was determined to be 4.3 to provide the appropriate injection pressure to allow the Soltrol to flow into the sample (Dane et al., 1998).

During the experiment, the Soltrol outflow rate (q_{nw}) was measured as a function of time and the effective permeability of the sand was calculated using the following equation derived by applying Darcy's law for two-phase flow(Dane et al,. 1998):

$$k_{nw} = -\frac{q_{nw} \times \mu_{nw}}{(\rho_{nw} - \rho_w)g} \qquad (2)$$

where $\boldsymbol{k_{nw}}$ is non-wetting phase effective permeability (L^2).

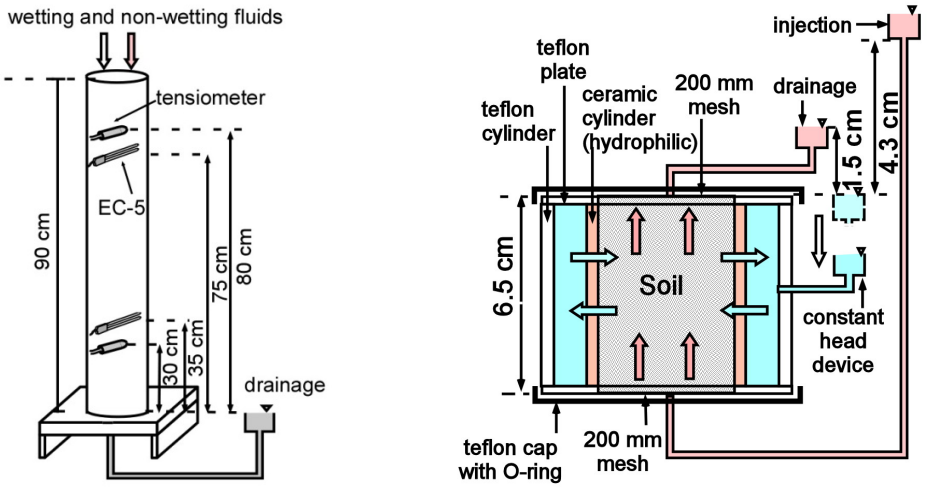

Figure 41 Experimental setup for the long column method (left), and for the hydrostatic method (right).

4 ANALYSIS OF EXPERIMENTAL DATA AND DEVELOPMENT OF CONSTITUTIVE MODELS

Given the large variability in time scale characterizing capillary and dissolution trapping mechanisms (see Figure 1), we investigated these phenomena separately. The following sections describe the sets of experiments carried out in different tank setups and porous media configurations to observe a variety of displacement and trapping processes.

4.1 Capillary trapping experiments

The first set of capillary trapping experiments (Trevisan et al., 2014) was aimed at developing an approach to translate the results from meter-scale laboratory experiments to the scale relevant to actual field storage scenarios. By selecting a combination of analog fluids and appropriate flow rates and unconsolidated porous media, the interplay of governing forces at deep reservoir conditions was mimicked in the synthetic reservoir at laboratory conditions. Then, a series of immiscible displacement experiments through homogenous sand-packs with variable permeability was performed to gain insight into the influence of buoyancy forces on the propagation of the displacing phase.

The second set of capillary trapping experiments shows the impact of heterogeneity variability and correlation on capillary barrier effects that enhances trapping. These heterogeneities were created in the form of either barriers or high-permeability connected pathways and their regular geometry allowed for a systematic investigation of the contribution of capillary phenomena to the trapping and migration of the displacing phase. In this section, two scenarios are presented that differ in the spatial configuration (or correlation) of the heterogeneities, and a comparison is made with results from an immiscible displacement experiment performed in a homogeneously packed tank.

The experiments in the medium tank represent fairly simplified and ideal scenarios. Therefore, in an attempt of reproducing more realistic geological media, two experiments were conducted in a larger tank, allowing for the observation of additional processes, such as increased vertical migration of the plume, effects of background hydraulic gradient on plume entrapment, and the contribution of larger spatial variability of the permeability field. The ultimate goal of these larger experiments was to test optimal injection schemes that can enhance storage capacity in naturally heterogeneous systems and to test the applicability of a new multiphase model developed at Lawrence Berkeley National Laboratory (LBNL).

4.1.1 Medium tank homogeneous experiments

Two approaches were used to visualize the evolution of NWP saturation during the plume migration: 1) a qualitative comparison between digital photography and linear interpolation of NWP saturation measurements via x-ray attenuation, and 2) a temporal series of saturation observed at selected locations. In the latter approach, we omitted the plots corresponding to those locations that did not show saturation changes above the detection limit. Highly spatially refined x-ray measurements provided saturation data for quantitative analysis and allowed for spatial moment analysis to estimate the total NWP volume present in the plume and also quantify the spatial architecture. For this purpose the zeroth order spatial moment as reported by Freyberg (1986) and Fagerlund et al. (2007) was used to match the injected volume of Soltrol 220 tracked via electronic scale on which the supply reservoir was placed. In Figure 42 shows a comparison of cumulative NWP volume measured by electronic scale versus volume estimated from zeroth moment calculation. Figure 42 shows a 30 ml-mismatch (12.7% of the total volume injected) in volume estimation between zeroth moment and NWP weight

measurements from the electronic scale. This is attributed to the unavailability of x-ray data at the well location, causing the NWP volume around the well to remain out of reach for spatial moment calculations.

$$V_{NWP} = M_{00} = \iint \varphi(x,z) S_{NWP}(x,z) dx dz \tag{19}$$

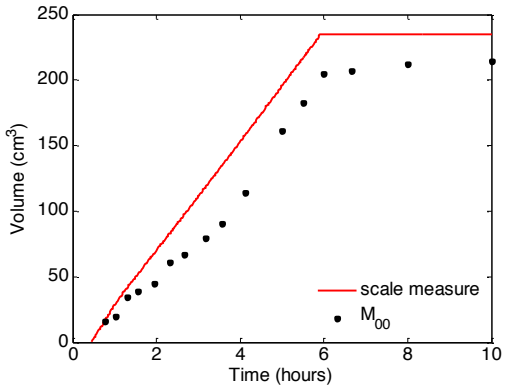

Figure 42 Cumulative NWP volume measured via electronic scale (red line) and derived from zeroth moment calculation (black circles).

Figure 43 shows the distribution of 25 observation points that were selected to compare temporal plots of saturation measured using x-ray attenuation for different Bond number scenarios in all three experiments. The vertical spacing between each point is 1.5 cm. The variable horizontal spacing between the vertical arrays was intended to better capture the evolution of plume saturations in the proximity of the injection location.

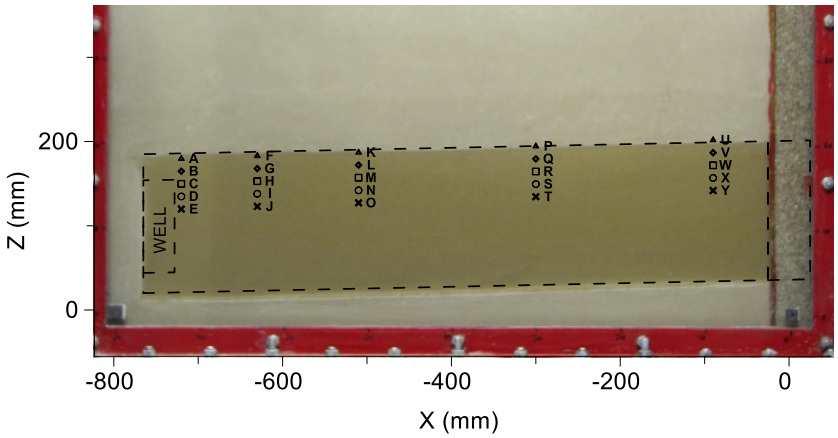

Figure 43 Experimental flume after wet-packing with location of the 25 observation points; broken lines delineate flow domain, injection well, coarse sand boundary.

The highest Bond number scenario corresponds to experiment #1, where the synthetic reservoir was packed with #30/40 Accusand (see Figure 44). By interpolating the saturation data acquired via x-ray attenuation throughout the whole flow domain, contour maps of the NWP saturation were generated, allowing identification of regions with mobile and disconnected phases. The larger influence of buoyancy versus capillary forces produced by the higher permeability of this sand pack led to strong gravity segregation between the two phases, as well as NWP plume propagation at the very top of the flow domain, along the caprock interface. As a result, poor volumetric sweep efficiency and rapid NWP build-up near the injection well were observed (Figure 44a). This behavior has been shown in previous studies presented in the literature (e.g. Ide et al. (2007); Tchelepi and Orr (1994)), however this experiment represents an attempt to demonstrate the validity of some of these previous predictions made using numerical simulations, in the laboratory. A total volume of 231 ml of Soltrol 220, corresponding to approximately 10% of the reservoir pore volume, was injected during 5.5 hours. This injection scenario resulted in NWP saturations greater than 0.9 near the injection well at the end of injection (Figure 44a). Once the plume had completely redistributed as driven by buoyancy after about 590 hours (Figure 44b), a forced imbibition event was created with the intent of displacing any mobile fraction of the plume away from the well and maximizing the contact area between the plume and the reservoir, which is known to affect the final sweep efficiency (Figure 44c). Even though there is a definite boundary effect at the right end of the reservoir, we focused on

the near-well area, where NWP saturations measured at the onset of forced imbibition still had values higher than the expected residual value of 0.26 of the test sand #30/40.

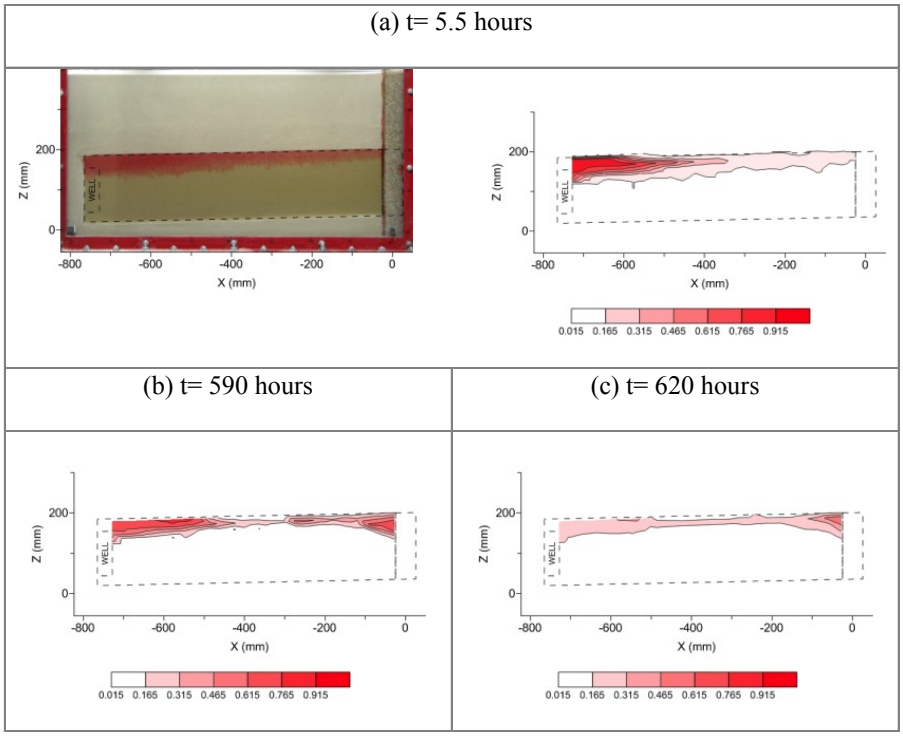

Figure 44 Image and saturation contours of NWP plume at different times during experiment #1 (#30/40 Accusand): at the end of the injection stage (a), and before and after the forced imbibition stage respectively b, c).

The buildup of NWP saturations that are higher than residuals near the injection well for an extended period of time of was confirmed by analyzing the time series shown in Figure 45.

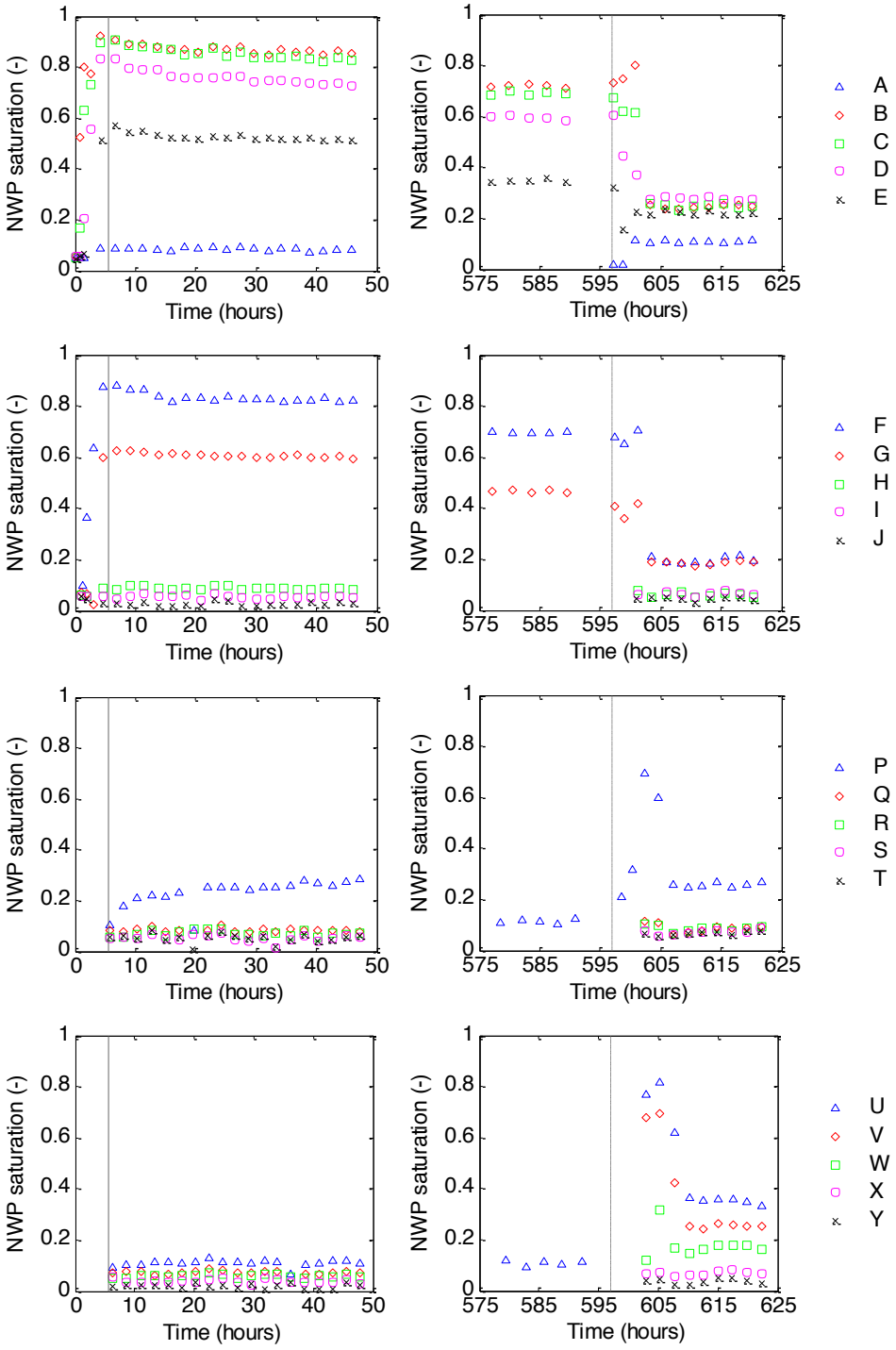

Figure 45 Experiment #1: temporal series of NWP saturation at the observation points shown in Fig. 8 throughout the injection and recovery stages (left column) and forced imbibition stage (right column). The solid and dotted vertical lines highlight the end of the injection stage and the beginning of the forced imbibition event, respectively.

Even though NWP saturation slowly decreased between 40 and 590 hours, all the saturations near the injection well (at observation points A, B, C, D, E) remained above residual values before the impact of forced imbibition. Faster vertical migration, together with a local smoothing of the caprock inclination near the well and a lower porosity at the middle top of the reservoir (see Figure 10) due to a tighter packing of the sand may have limited further migration of the plume in the updip direction. Except for point A, which lays above the interface between the reservoir sand and the caprock sand, the other 24 points recorded increasing saturation values at higher vertical locations, as a proof of the presence of a saturation transition zone produced by capillary forces.

Saturations higher than 0.3 were detected at the two uppermost points of the left half of the reservoir (F, G), suggesting the presence of continuous phase in variable amounts, possibly due to the lower porosity at near the caprock. The persistence of high saturations at those locations was observed during two days after the injection. Hence the plume was left to redistribute for longer times (>3 weeks), before starting forced imbibition.. All these points, as well as those nearby the well (B, C, D, E), indicated that a residual saturation had been reached (see Table 2). Some locations, especially in the upper part of the aquifer, exhibited a rapid spike in NWP saturation after the onset of the glycerol-water injection (i.e., forced imbibition), due to the piston-like displacement of mobile NWP phase from left to right. The most important result from the observations in the right half of the reservoir (P through Y) is the increase in NWP residual saturation achieved after the forced imbibition event. This behavior represents an effect of a secondary drainage/imbibition cycle and it can be translated to field-scale, where such an injection strategy can eventually lead to enhanced storage of CO_2 at locations far from the injection well. Experiment #2 was conducted in a sand with low permeability to reduce the relative magnitude of buoyancy versus capillary forces to decrease the Bond number (1.47x10-5). In this case, the sand pack consisted of #40/50 Accusand, with permeability 40% lower than #30/40 sand. Examination of the digital images and contour maps of measured NWP saturation (Figure 57), shows that saturation of Soltrol 220.

After the ceasing injection, the NWP was fully immobilized as a result of capillary trapping. Completed wetting cycle resulted in residual saturations at these locations representing the endpoint $S_{nwr,max}$, or the maximum historical NWP saturation. This represents a critical parameter in multiphase flow simulations that use the Land's trapping model (Land, 1968).

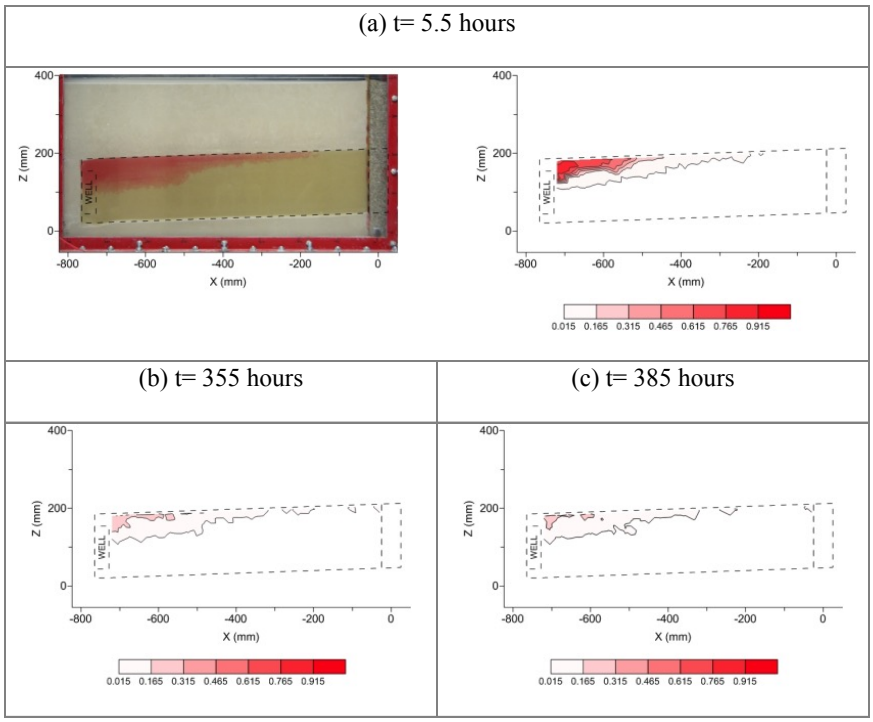

Figure 46 Image and saturation contours of the NWP plume at different times during experiment #2 (#40/50 Accusand): at the end of the injection stage (a), and before and after the forced imbibition stage respectively (b, c).

In experiment #2 there was no evidence of the strong gravity segregation observed in the previous case. For this reason, the forced imbibition stage did not lead to the marked effect on residual saturation that had arisen from the piston-like displacement of the mobile NWP accumulating on the left section of the reservoir during experiment #1. However, a feature that can be readily observed from the temporal series in Figure 47 is the different depletion rates in NWP saturation at observation points at different vertical locations during the 240 hour natural imbibition or the recovery stage. Also, a delayed response in saturation depletion at downstream points represents an effect of the updip migration of mobile NWP from the well area. This behavior is expected to be more pronounced in higher permeability reservoirs where the effect of buoyancy forces is stronger. In field sequestration scenarios, these outcomes are relevant to the reliability of capillary trapping at deeper regions, where $scCO_2$ at the trailing edge of the plume may become immobile with a faster rate compared to regions underlying the caprock.

In order to provide an injection scenario characterized by a lower influence of buoyancy compared to capillary forces, we performed a third experiment in a geometrically similar setting

with sand of even lower permeability. In this case, we wet-packed the reservoir with #50/70 Accusand, which has a permeability 47% lower than #40/50 Accusand used in experiment #2.

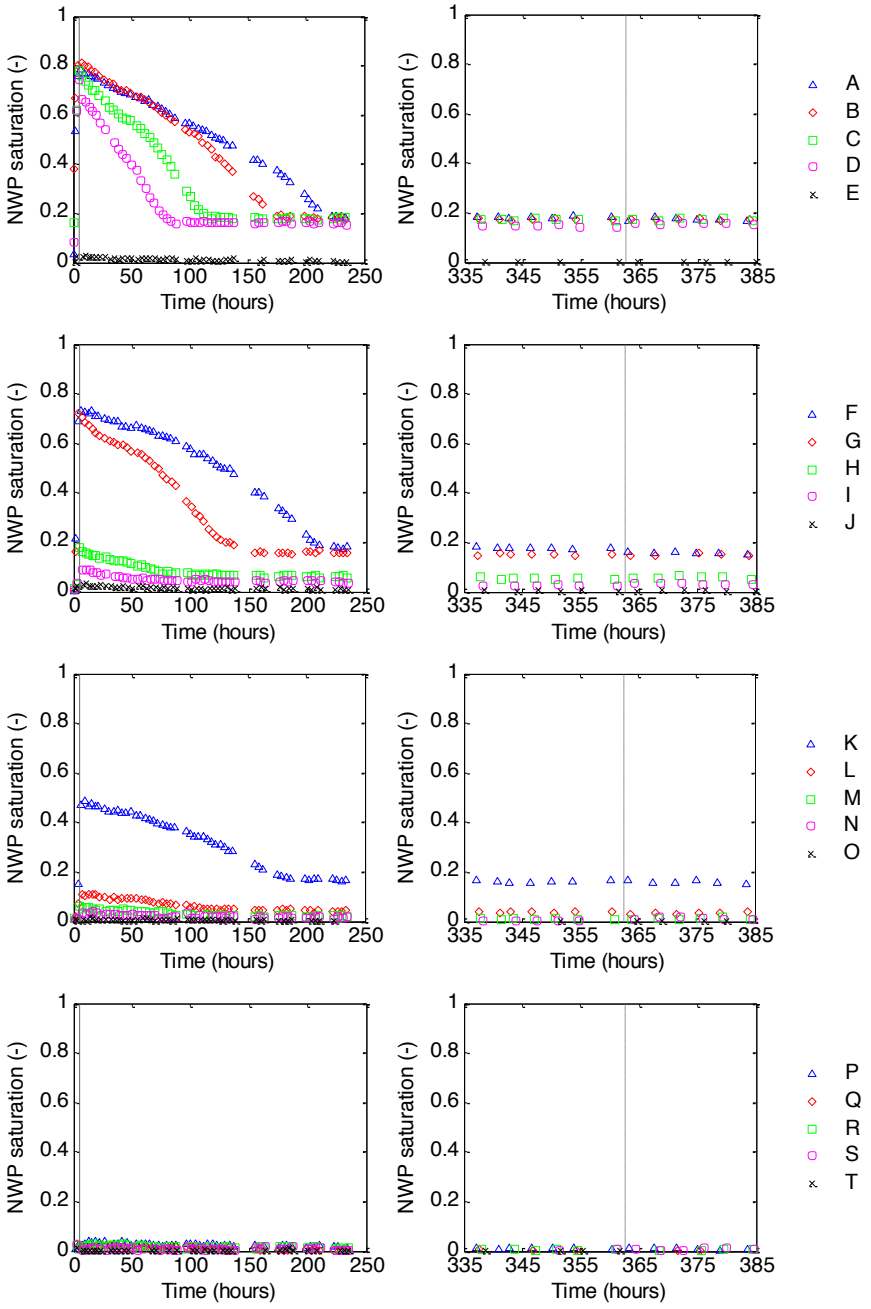

Figure 47 Experiment #2: temporal series of NWP saturation at the observation points shown in Fig. 8 throughout the injection and recovery stages (left column) and forced imbibition stage (right column). The solid and dotted vertical lines highlight the end of the injection stage and the beginning of the forced imbibition event, respectively.

Once the Soltrol injection was stopped, the plume configuration appeared more compact compared to experiments #1 and #2, as evidence of increased sweep efficiency (Figure 48a). This process can eventually affect the storage capacity of a given reservoir (Cinar et al., 2009). Similarly to what was observed in experiment #2, NWP saturations measured at higher locations were characterized by slower depletion rates. Particularly, some tendency to plume accumulation was observed at point A, although a residual saturation of 0.25 was achieved after leaving the fluids to redistribute spontaneously during approximately one week (Figure 49).

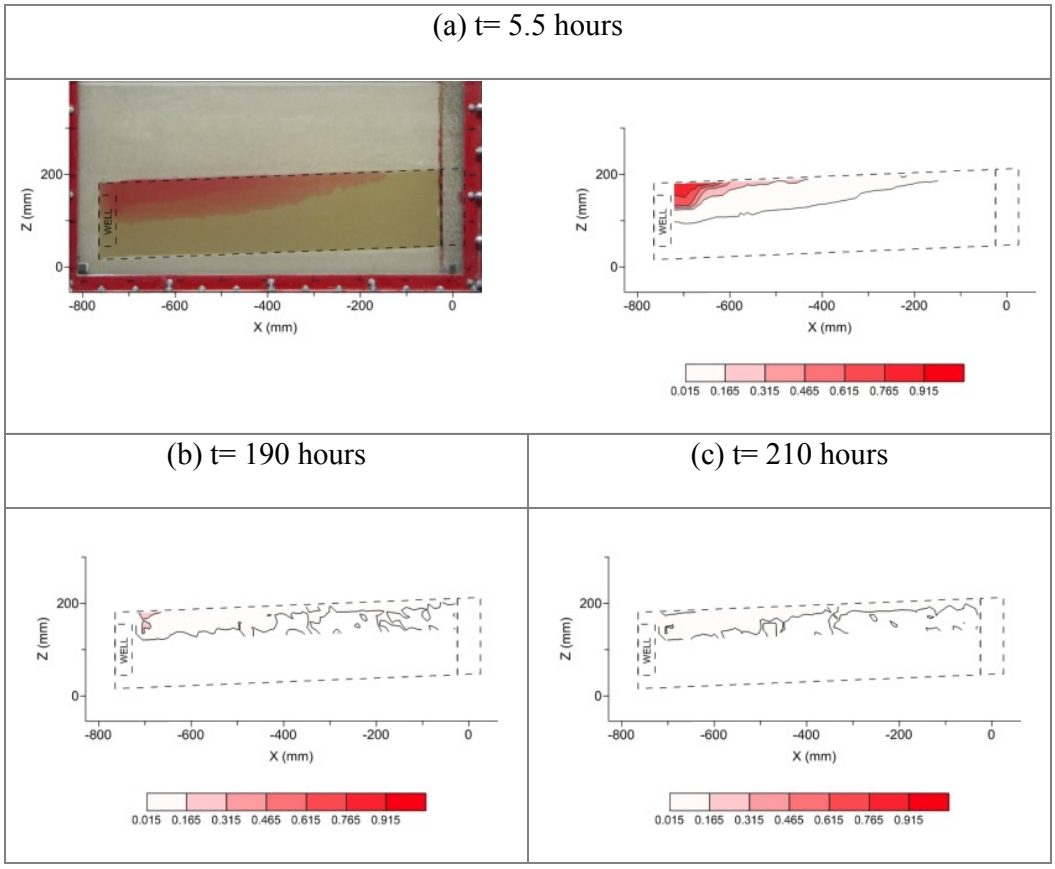

Figure 48 Image and saturation contours of NWP plume at different times during experiment #3 (#50/70 Accusand): at the end of the injection stage (a), and before and after the forced imbibition stage respectively (b, c).

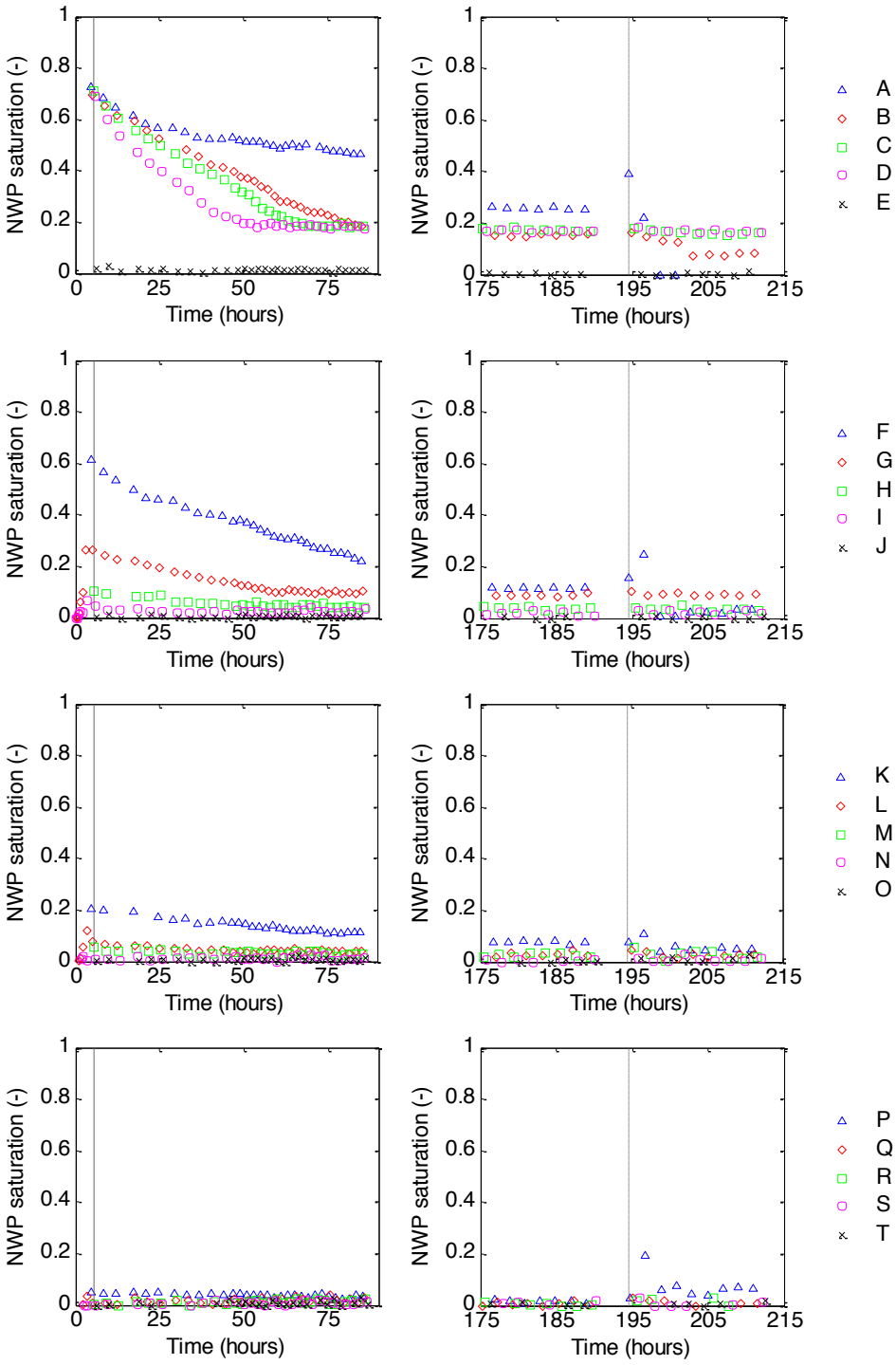

Figure 49 Experiment #3: temporal series of NWP saturation at the observation points shown in Fig. 8 throughout the injection and recovery stages (left column) and forced imbibition stage (right column). The solid and dotted vertical lines highlight the end of the injection stage and the beginning of the forced imbibition event, respectively.

To evaluate the ability of a number of trapping models to fit our experimental data, we followed the analysis by Pentland et al. (2010) and compared four trapping models from the literature (Jerauld, 1997; Land, 1968; Ma and Youngren, 1994; Spiteri et al., 2005). A comparison between the mentioned trapping models and the correlation for the maximum NWP saturation reached at flow reversal (S_{nw}^{i}) and the residual NWP saturation (S_{nw}^{r}) for the three experiments is shown in Figure 50.

Experiment #1 (#30/40 Accusand)

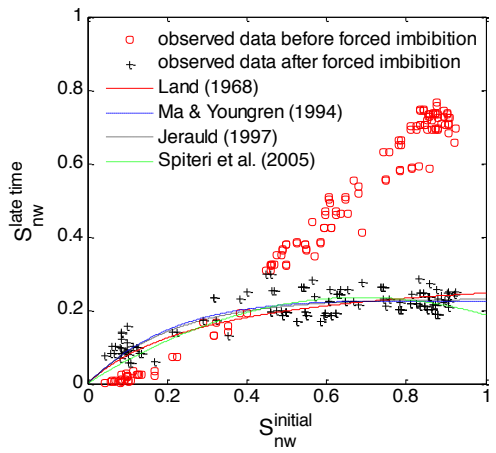

Experiment #2 (#40/50 Accusand)

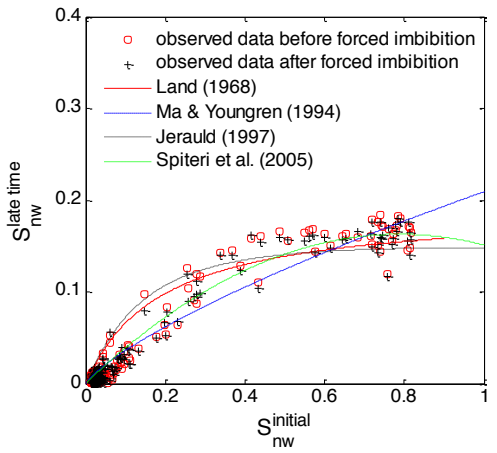

Experiment #3 (#50/70 Accusand)

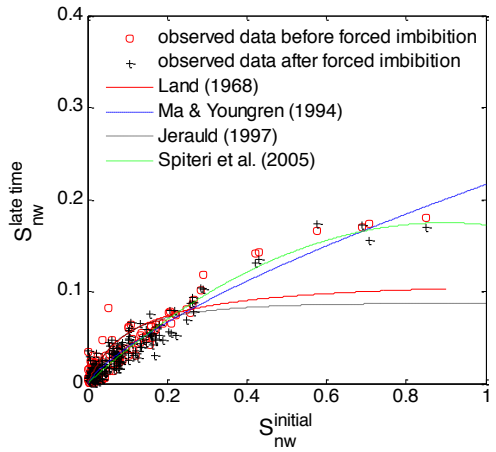

Regression analysis of Land's fitting coefficient

experiment (sand)	C	R^2
1 (#30/40)	3	0.63
2 (#40/50)	5.4	0.87
3 (#50/70)	8.6	0.67

Figure 50 Initial-Residual saturation data observed before and after forced imbibition compared with four different trapping models. Regression analysis of Land's trapping coefficient performed on data observed after forced imbibition.

A common feature among these plots is the higher occurrence of measurements at initial saturations that are lower than 0.2, suggesting that most of the NWP is residually trapped at low

saturations. Also, as previously observed by Krevor et al. (2012) from core-flood experiments with $scCO_2$ in several sandstones, the Land's fitting coefficient C increases (reducing the capillary trapping) as the permeability of the porous medium decreases. Our displacement experiments conducted in unconsolidated sands indicate values of C varying from 3 (for #30/40 sand) to 5.4 (for #40/50) to 8.6 (for #50/70). However, the fitting of Land's model to the data of experiment #3 was significantly biased by the larger occurrence of measurements at small initial saturations.

The red dots in the initial-residual saturation plots denote NWP saturations detected prior to the onset of glycerol-water injection, while the black dots indicate NWP saturations achieved once the forced imbibition stage had been completed. In the case of experiment #1, where an accumulation of Soltrol 220 was observed underneath the confining layer, the red dots follow a linear trend that is typical for 100% trapping (Stegemeier, 1977) or pooling of NWP due to capillary barrier effect (Fagerlund et al., 2007; Krevor et al., 2011).

Table 9 Summary of the displacement experiments with assessments of NWP mass balance, vertical sweeping efficiency, and plume propagation.

	Experiment #1	Experiment #2	Experiment #3
NWP left before forced imb. / Total NWP injected	76 %	37 %	30 %
NWP left after forced imb. / Total NWP injected	40 %	35 %	28 %
vertical sweep efficiency	25 %	25 %	35 %
$\frac{\max x_{tip}}{x_{reservoir}}$	100 %	84 %	84 %

Except for experiment #1, where a considerable fraction of the injected fluid (76%) remained in the reservoir before the onset of forced imbibition, the rest of the experiments exhibited a depletion of the NWP plume during the fluid redistribution stage. Consequently, the forced imbibition stage had a minor effect on the entrapped plume for experiments #2 and #3, displacing only 2% of the NWP remaining in the reservoir.

As a further comparison of displacement efficiency between the three experiments, we calculated the ratios between the tip position of the plume at the end of the injection stage (max

x_{tip}) and the total length of the reservoir. While for the largest permeability scenario (experiment #1) the plume spanned the whole length of the reservoir, 'leaking' faster through the right boundary, the distance traveled by the plume during experiments #2 and #3 was 16% shorter.

Investigating the correlation between initial and residual NWP saturation for three experiments conducted with variable sand permeability, we were able to show the effect of structural versus residual trapping based on the inclination of the confining sand. We showed that single two-dimensional displacement experiments allow for the observation and measurement of a range of initial NWP saturations that would be otherwise acquired through a series of one-dimensional core flooding experiments at different injection flow rates, as reported by Pentland et al. (2010) or Akbarabadi and Piri (2013) among others. Four trapping models from the literature were able to reproduce reasonably well ($R^2 > 0.6$) the initial-residual NWP saturation correlation for the experiments, as shown in Figure 50.

4.1.2 Medium tank heterogeneous experiments

In order to identify the displacement and trapping mechanisms associated with drainage and forced imbibition, these two stages are described separately in the following sections.

a. Drainage and fluid redistribution

Digital photographs of the injected plume provide an effective method to track plume movement over time and to qualitatively detect distinctive displacement patterns among the different packing configurations (Figure 51). As an example of general validity, Figure 51 shows for the three scenarios snapshots of the plume taken just after injection has ceased and at the end of the fluid redistribution period (about 2 weeks), i.e. prior to starting the forced imbibition campaign. In the former case (left column), it can be readily seen that the plume has advanced less for the case of uncorrelated permeability field (Het. 1) compared to the other two cases, where its leading edge has already reached about ¾ of the length of the aquifer. Interestingly, the front of the plume in the homogeneous case shows a characteristic profile, which has been referred to as 'capillary pinning' (Zhao et al., 2013) , which manifested by the sharp change in the slope of the plume front that is visible half way through its leading edge. For the heterogeneous scenarios, the spreading of the plume is highly controlled by the arrangement of low- and high-permeability zones that characterize these systems: in the case of poorly correlated

heterogeneity (Het. 1), a more compact plume is observed, in contrast to a channeling behavior exhibited in the spatially correlated heterogeneous experiment (Het. 2). As expected, during those experiments only the coarse and medium permeability sands were invaded by the NWP, since the pressure drop driving the NWP injection during the heterogeneous experiments was kept at the exact same constant level.

Comparison of the left and right column in Figure 51 allows for the appreciation of the role of buoyancy and capillary forces within the aquifer on NWP plume redistribution once injection has ceased. Here, the striking difference among the three experiments is that NWP breakthrough at the outflow boundary was observed for both the homogenous and the spatially correlated experiment, while the plume movement stopped and remained entirely trapped in the aquifer for the uncorrelated experiment. Moreover, the intensity of the colors in those snapshots further suggests that in this latter case (Het. 1) the NWP is trapped at relatively large saturations as compared to the other two scenarios. We anticipate that this phenomenon may have important implications in the potential remobilization of the plume.

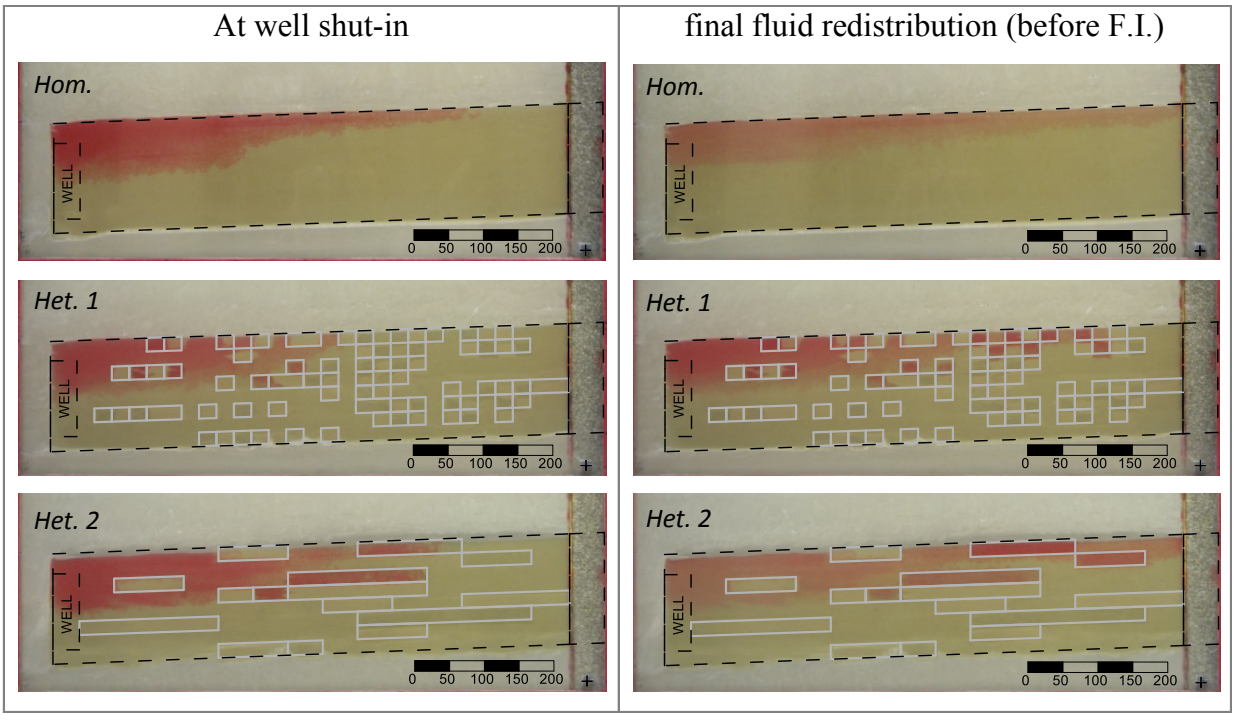

Figure 51 Digital photographs showing plume distribution for homogeneous, heterogeneous uncorrelated, and heterogeneous correlated configurations after injection (left) and fluid redistribution (right) stages (scale bar in mm).

A more quantitative assessment on the evolutions just described is achieved by comparing the coordinates of the center of mass of the plume for the three experiments, as given by Eqs. (3)-(5) and shown in Figure 52. In particular, the temporal evolution of the center of mass along the x-direction (Figure 52, left) suggests that (1) the spatially uncorrelated (Het. 1) and the homogeneous (Hom.) experiments exhibit a common displacement speed during the fluid redistribution period, and that (2) the plume migrates significantly faster through the spatially correlated heterogeneous aquifer (Het. 2). Note that the former observation does not contradict the conclusions drawn from the analysis of the photo images shown in Figure 51, but rather hints towards a different aspect ratio of the plume. In other words, the extended tongue that characterizes the homogeneous plume carries less weight into the estimation of the center of mass in the horizontal direction. The analysis of the vertical position of the plume's center of mass (Figure 52, right) supports this conclusion with the height of the center of mass decreasing in the direction Hom. > Het. 2 > Het. 1. Generally, a fairly stable evolution is observed in each experiment, with the total variation over time being less than 1 cm. Interestingly, a common feature shared by experiments Hom. and Het. 2 is the downward movement of the center of mass as the plume breaks through the outflow boundary (filled symbols in Figure 52). This behavior is not observed in Het. 1 (the slower and more compact plume), where the vertical position of the center of mass has stabilized at about 200 hours. The fluid redistribution stage was considered to be over when the center of mass reached equilibrium and no further movement occurred along horizontal and vertical directions. This period lasted slightly less than two weeks for both homogeneous and heterogeneous experiments.

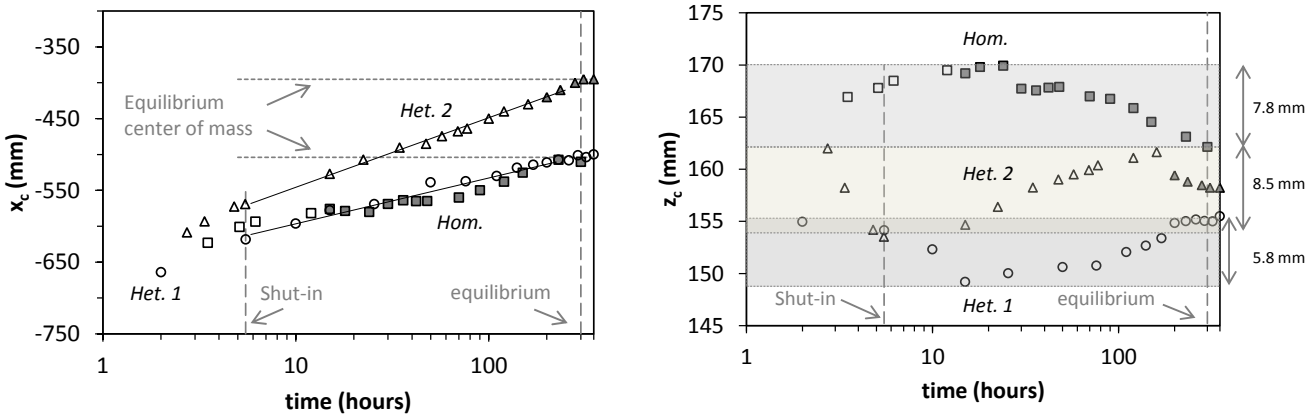

Figure 52 Temporal evolution of the horizontal (left) and vertical (right) coordinates of the plume's center of mass. Filled symbols represent measurements taken after plume breakthrough into outflow boundary. Horizontal coordinate of well's center is -750 mm**.**

b. Forced imbibition

At the conclusion of the fluid redistribution period, glycerol-water (the wetting phase) was allowed to flow throughout the aquifer, thus mimicking a "chase-brine" type of event (Juanes et al., 2006; Qi et al., 2009; Rahunanthan et al., 2014). This forced imbibition consisted of two consecutive 24-hour periods of different flow rates to trigger the mobilization of NWP that has accumulated behind capillary barriers. The first stage was carried out at 1 ml/min (Q_1), i.e. injecting 0.67 pore volumes, and it was followed by the injection of 1 pore volume of wetting phase at 1.5 ml/min (Q_2). For the sake of completeness, we include in the discussion results obtained for the homogeneous experiment, where the forced imbibition was carried out in one stage and by applying a constant flow rate of 2 ml/min.

Figure 53 provides an overview of the three experiments in terms of box plots that illustrate the range of NWP saturations measured before and after forced imbibition events from the x-ray scanning; larger boxes, enclosed by 1st and 3rd quartiles, represent plumes with a wide range of NWP saturations, in contrast with narrow boxes denoting plume saturations constrained to a limited range of values.

In the figures, the dashed horizontal lines represent the endpoint residual NWP saturation $S_{\mathrm{nw,r}}^{\max}$ for the background sand as obtained from laboratory measurements of P_c-S relationships for the pair of fluids used in this study (Mori et al., 2015). In other words, any value of residual

saturation measured below this line can in principle be described by a trapping model, such as the one proposed by Land (1968) introduced in chapter b.

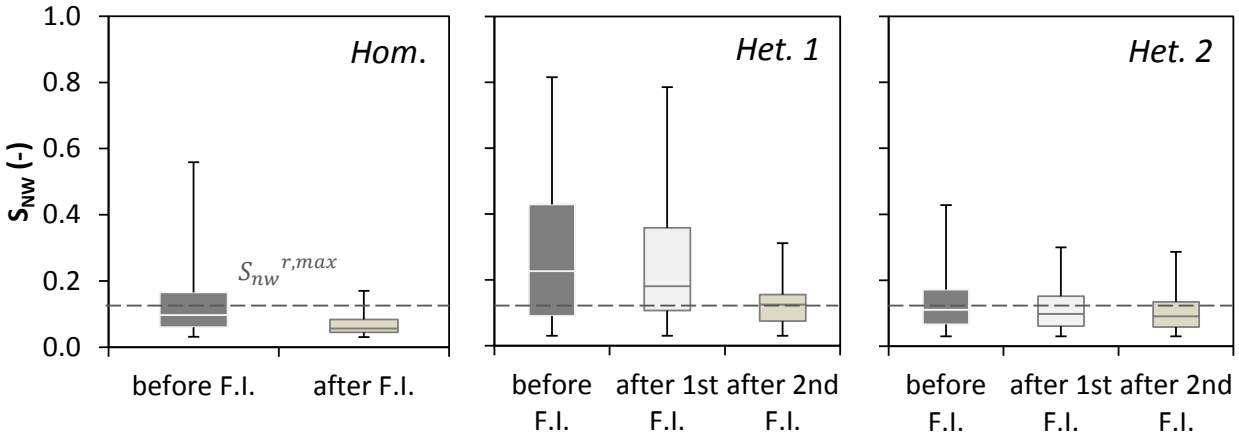

Figure 53 Box plots showing NWP saturation distribution before and after forced imbibition (F.I.) events. Middle lines represent the median of the distributions, upper and lower edges represent first and third quartile, respectively, while 'whiskers' above and below each box represent maximum and minimum values observed, respectively. Dashed line represents the endpoint residual NWP saturation of #40/50 sand.

Several observations can be made from the results shown on these figures. In the homogeneous scenario (left panel), most of the plume is found at saturations below the maximum residual saturation limit already achieved after the fluid redistribution period is over. Accordingly, a forced imbibition event has the effect of further reducing the NWP saturations, thus leading to a situation where the *entire* plume is trapped with a very narrow distribution of saturations around a mean value of 0.08. On the contrary, distinct responses to the forced imbibition are observed when the two heterogeneous configurations are considered.

For the Het. 1 case (center), most of the plume still contains saturations significantly larger than $S_{\mathrm{nw,r}}^{\mathrm{max}}$ after the first event, with about 20% of the distribution found within a range of saturation values 0.4 - 0.8. As expected, the second event performed at a larger flow rate is more effective and leads to a narrower range of saturation values that are mostly found below and just above the residual limit, $S_{\mathrm{nw,r}}^{\mathrm{max}}$. Interestingly, a similar final distribution is observed for the Het. 2 case (right panel), although in this case the latter was attained already after the first event. Het. 2 shows a similar spread of saturation values prior to the wetting phase injection as for the homogeneous case. In both heterogeneous cases, however, the presence of NWP saturation

higher than residual, represented by the top 'whiskers', is evidence of capillary barrier effect still holding part of the plume in a continuous phase. As described below, more insights on this phenomenon are obtained by considering the spatial distribution of the plume at various stages of the process.

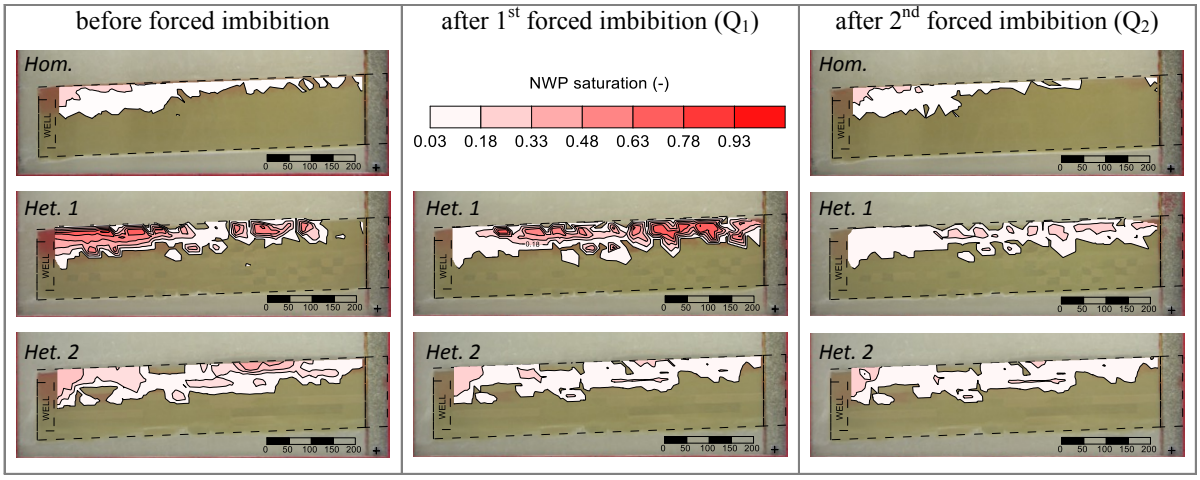

Figure 54 Comparison of 2-D NWP saturation distribution measured via x-ray attenuation for homogeneous (top), spatially uncorrelated (middle row), and correlated (bottom row) heterogeneous experiments prior and subsequently to forced imbibition events at different flow rates.

2-D plume saturations distributions measured via x-ray attenuation after these forced imbibition events are shown in Figure 54 and are compared to images taken just prior to the injection of the wetting phase. It can be seen that in all three cases the forced imbibition has indeed mobilized the plume, though with different effectiveness. Although the injection of wetting phase into the homogenous aquifer did not result in an effective mobilization of the plume, it can be seen that the region of trapped NWP left behind is fairly homogeneous and has maximum non-wetting phase residual saturation levels that would be expected from the residual saturation captured in the capillary pressure curve alone (about 0.15). This region is located near the injection well, being the same region where most NWP was present prior to later injection of the wetting phase, as a result of the interplay between viscous and buoyant forces in a sloping aquifer. This picture is very different when the heterogeneous scenarios are considered. After the first imbibition event in both cases, the plume occupies almost entirely the top half of the aquifer; however, while for Het. 1 trapped saturations are locally still very high (up to 0.80), most of the plume in Het. 2 contains NWP at saturations close to the residual limit observed for

the homogeneous case. In this context, therefore, capillary forces help distribute the plume more homogeneously throughout the entire aquifer, thus counteracting the effect of buoyancy; at the same time, the spatial distribution of potential capillary barriers is key in controlling the actual saturation of the trapped plume, this being very different when Het. 1 and Het. 2 are compared. In fact, once the bulk fraction of the plume has been swept by the second (and stronger) forced imbibition event, the plume in both heterogeneous cases are practically indistinguishable, these having very similar footprint *and* saturation distribution. It is worth noting that despite the high saturations occurring after the first forced imbibition event in the Het.1 case, the plume advancement is still significantly hindered by several capillary barriers it encountered; this behavior cannot be captured if relative permeability alone is considered as an indicator of fluid mobility in the aquifer.

The present study consists of an experimentally driven analysis on migration and entrapment under capillary-dominated flow conditions of a $scCO_2$/brine-surrogate fluid pair in an unconsolidated sand reservoir that is embedded with structurally well-defined heterogeneities. The characteristic length of the heterogeneities considered in this study (from about (2.5×2) cm^2 to (15×2) cm^2) is of the same order in size as the "synthetic" aquifer, that is (16×70) cm^2, and can therefore be associated with bed-form type of heterogeneities encountered in sedimentary formations (Ringrose et al., 1993). These heterogeneities are implemented in the form of either barriers or high-permeability streaks and their regular geometry allows for a systematic investigation on the contribution of capillary phenomena to the trapping and migration of the NWP. Two scenarios were presented that differ in the spatial configuration (or correlation) of the heterogeneities and a comparison has been made with results from an immiscible displacement experiment performed in a homogeneous aquifer (base-case). X-ray imaging has been applied to quantify the temporal and spatial distribution of fluids' saturations throughout the various stages of the experiments, which in each case included a period of injection, fluids' redistribution and forced imbibition. The latter represents a "chase-brine" type of event that is often considered in the design of field-scale injection operations in saline aquifer as a strategy to maximize CO_2 storage, both through capillary trapping and dissolution (Hassanzadeh et al., 2009; Qi et al., 2009; Saeedi et al., 2011).

c. Displacement and trapping mechanisms

As shown in Figure 55 for the Het. 1 configuration, a more detailed analysis of the mechanisms associated with capillary barriers and forced imbibition driving the trapping and mobilization of NWP can be carried out by observing the evolution of the NWP saturation at selected locations. Generally, the presence of heterogeneities leads to abrupt variations in NWP saturation at contiguous locations, and depending on the relative position of the capillary barrier (upstream vs. downstream and distance from the injection well) distinct trends in the temporal evolution of the saturation are observed. In particular, the following mechanisms have been identified as a response to a forced imbibition event: (1) invasion of NWP into previously inaccessible sands (e.g. points A, D, and E); (2) increase in NWP saturation (e.g. all points in (1) with addition of F); (3) 'wave' effect reflecting the transit of mobile NWP characterized by the attainment of a maximum NWP saturation followed by a decrease; the magnitude of this 'wave' increases at locations farther from the injection well, facilitated by larger volumes of NWP accumulating at near-well regions; (4) rapid decrease of NWP saturation as a consequence of wetting phase flow mobilizing the accumulated bulk NWP from coarse sands (e.g. point B). It is worth noting that the uncorrelated nature of the distribution of heterogeneities in the Het.1 experiment has the effect of increasing the frequency of these mechanisms. Most importantly, not only a forced imbibition event results into the immobilization of NWP into a residual phase (as it would also happen in a homogeneous aquifer), but it leads to a local increase of NWP saturation and in some instances it can even force NWP into zones of the aquifer previously not accessible. The latter observation suggests that room exists for optimizing CO_2 storage through a combination of NWP *and* wetting phase injection into the aquifer. The mechanisms mentioned above are responsible for the different NWP trapping performance exhibited by the three configurations, as reported in Table 10.

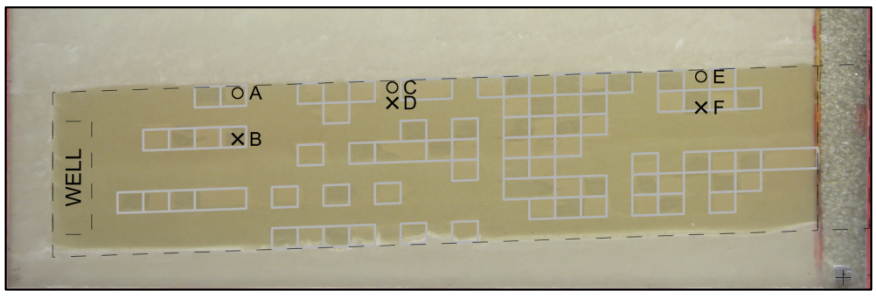

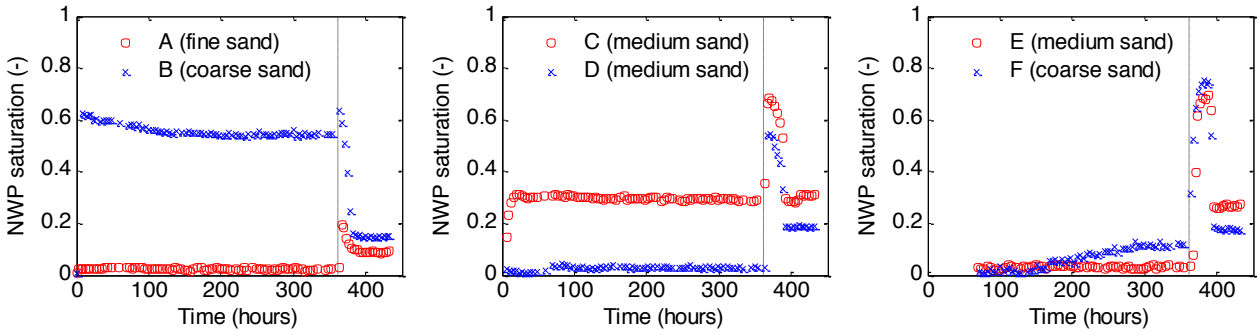

Figure 55 NWP saturation evolution observed at six selected locations in the uncorrelated heterogeneous scenario (Het. 1). Vertical dashed lines indicate the onset of the forced imbibition phase.

d. Trapping performance

A simple material balance calculation (NWP injected versus NWP collected at outflow) provides estimates of NWP volumes retained in the aquifer and allows assessing the trapping performance of each experiment throughout the three stages described above (an overview is given in Table 10). As anticipated, residual NWP saturations (about 0.16 for these sands) could be already attained within most part of the plume after the fluids' redistribution period (no injection) in the homogeneous case (35 vol.% of the injected volume retained in the aquifer); accordingly, a weak effect of forced imbibition on saturation distribution was observed and about 5 vol.% of the plume was mobilized and produced. While the implementation of correlated heterogeneities (Het. 2) enhanced the retention of the plume behind capillary barriers (with NWP saturations up to 0.5 and a trapping of 47 vol.%), once the first forced imbibition was put in place 17 vol.% of the plume's volume was remobilized and a total of 21 vol.% has left the aquifer after completion of the second stage (similarly to the homogeneous case, 37 vol.% of the injected volume is retained in the aquifer).

Table 10 Trapped NWP normalized by the total NWP volume injected for the two heterogeneous configurations as compared to the homogeneous case.

	Hom.*	**Het. 1**	**Het. 2**
Trapped NWP fraction before onset of forced imbibition	37%	100%	47%
Trapped NWP fraction after 1st forced	N/A	94%	39%

imbibition			
Trapped NWP fraction after 2nd forced imbibition	35%	42%	37%

N/A: not applicable.

* Only one forced imbibition event performed.

The uncorrelated heterogeneity in Het. 1 represents the most desirable arrangement of capillary barriers, since the plume was retained entirely in the aquifer before the onset of forced imbibition and only 6 vol.% of its volume was mobilized and produced after the first stage of wetting phase injection. After completion of the second stage, however, the final trapped NWP volume showed a value similar to the other two experiments, with 42 % of the plume's volume being trapped.

In a so-called 'Initial-Residual' saturation plots (Figure 56), the effective residual saturation observed after a waterflood ($S^*_{\mathrm{nw,r}}$) is plotted as a function of the corresponding effective maximum NWP saturation reached at flow reversal ($S^*_{\mathrm{nw,i}}$). This type of plot enables the development of several parametric models that describe this correlation (Jerauld, 1997; Land, 1968; Ma and Youngren, 1994; Spiteri et al., 2008), known under the general name of "trapping models". When applied to the experiments presented in this study, such plot can be quite useful as it can be populated with saturation values measured at different spatial locations before and after a forced imbibition event, thus including the possibility to distinguish among different types of sands.

Figure 56 provides a comparison between results from the two heterogeneous cases (shown as symbols for both coarse (#30/40) and medium (#40/50) sands) together with predictions of the Land trapping model (shown as solid lines) applied to results from two homogeneous scenarios using the same sands and that were published in a previous paper. As reported in a previous publication (Trevisan et al., 2014), these curves were generated from equation (8), while Land's coefficients for the two sands were calculated from equation (9) by using the corresponding effective endpoint residual saturation, $S^{*\max}_{\mathrm{nw,r}}$. For the Het.1 case and prior to the forced imbibition event, all saturation points lie close to the identity (1:1) line that represents a scenario with essentially no mobilization (C=0 in Equation (8)).

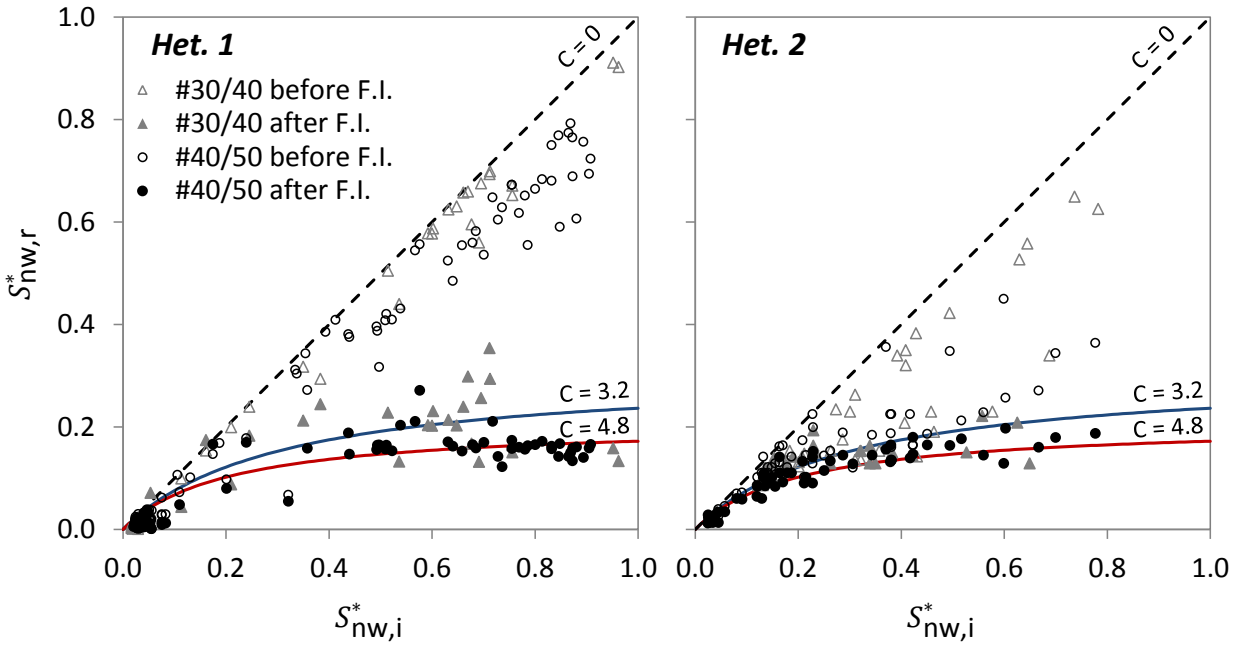

Figure 56 Trapped NWP saturations measured in the coarse (triangles) and medium (circles) sands before (empty symbols) and after (filled symbols) forced imbibition as a function of the maximum NWP saturation reached at flow reversal. The dashed line shows the 100% trapping (Land coefficient C=0), while blue and red lines represent Land trapping models derived from endpoint residual NWP saturations observed in P_c-S relationships of coarse and medium sands, respectively.

For coarser sands this effect is the strongest due to the higher probability for the latter of being located behind a sand with higher entry pressure. A similar pattern can be observed for the Het. 2 case, where both sands lie now underneath the identity line, but with the medium sand showing significant mobilization already during the fluids' redistribution stage. The stronger trapping effectiveness seen in the Het. 1 case as compared to the Het. 2 case is expected due to the higher occurrence of capillary barriers. Interestingly, when the situations are compared *after* the forced imbibition events, residual saturations have significantly dropped and occupy a region bounded by the Land's trapping model curves that represent coarse and medium sands. This is clearly evident in the Het. 2 case, while trapped saturation values above residual are still present at some locations within the coarser sand zones of the Het. 1 case. This behavior supports the usefulness of Land's trapping model for predicting residual NWP saturations as a function of maximum initial NWP saturations also in heterogeneous scenarios, when a forced wetting phase flow has swept the bulk of NWP accumulating at above-residual saturations behind capillary barriers. This observation is indeed very important as it suggests that a *heterogeneous* system can

eventually be treated as *homogeneous* when the ultimate (long-term) trapping behavior is considered. It is worth noting, however, that although the experimental points lie on the same curves, the *ranges* of saturations among the different scenarios are quite different, with the cloud of points moving towards the left-hand side of the plot in the direction Het.1 < Het. 2 < Hom. This trend reflects the fact that much larger local saturation values can be reached in the presence of heterogeneities. Moreover, those saturations have a stronger potential of being mobilized when the system is subject to forced imbibition, as a larger saturation implies a larger relative permeability.

As a final remark, it is worthwhile to analyze these results in the context of large-scale field's operation. As anticipated above, the forced imbibition applied in this study can be related to a "chase brine" scheme that is adopted to enhance the displacement efficiency and trapping capacity in a reservoir (Juanes et al., 2006; Qi et al., 2009). Accordingly, we can ask ourselves when the mobilization of part of the plume's volume trapped behind capillary barriers will eventually stabilize into a Land-type of behavior. For a simplified scenario of a 1-D reservoir, such estimate can be readily obtained as:

$$t = \frac{PV}{Q} = \frac{L \cdot \varphi}{u} \tag{20}$$

where L is the longitudinal extension of the reservoir, ϕ is its porosity and u is the Darcy velocity of the waterflood. The latter is often assumed to take a value of about 0.3 m/day (Ringrose et al., 1993); for a reservoir with a 10-50 km longitudinal extension and an arbitrary porosity of 0.2 it would take 20 to 100 years to reach injection of 1 Pore Volume, i.e. the forced imbibition scheme adopted in this experimental study.

4.1.3 Large tank experiments

The results of the immiscible displacement experiments conducted in the 8 ft. × 4 ft. tank are presented in the following sections by means of examination of digital photographs and a quantitative analysis of NWP saturation measurements gathered via x-ray attenuation.

a. Homogeneous scenario

The main goal of this experiment is to represent a base case scenario that can be compared to a geometrically similar domain characterized by a stochastically generated permeability field.

Figure 57 and Figure 58 illustrate the evolution of two injection events carried out under the same constant injection pressure in a homogeneous sand aquifer. Although the Mariotte bottle connected to the injection well was maintained at a constant elevation throughout the experiment, thus fixing the injection pressure, the flow rate rose gradually during the experiment. This behavior could be explained by the growth of the plume and the consequent increase in flow pathways available for the NWP. As a consequence of a larger average saturation, an increase in NWP relative permeability followed. Consequently, the injection flow rate evolved from 0.31 ml/min to 1.16 ml/min during both injection events. During the first injection, the early evolution of the plume is controlled by buoyancy forces, showing a rapid vertical migration, while around 14 hours from the onset of the injection, the plume begins to move laterally migrating preferentially along the direction of the background flow of wetting phase (from right to left). After stopping the first injection (Figure 57 top), the plume was allowed to redistribute for10 days during which it showed a clear tendency of gravity segregation, until it had reached equilibrium (Figure 57, bottom). During the early stages of the second injection,, the plume followed the path established by the invasion zone of the non-wetting fluid in the previous injection. Afterwards, the lateral spreading of the plume increased visibly with respect to the plume extent at the end of the first fluid redistribution. As an effect of this plume expansion a spike in NWP saturation was observed at locations nearby the well (Figure 64, points A, B, and D), leading to higher residual saturations once the wetting phase had imbibed back the trail of the plume. Similarly to the first injection event, once the flow rate began to increase during the second injection, the plume expanded further, occupying areas previously un-invaded and leading to a larger plume invasion zone (Figure 58, bottom).

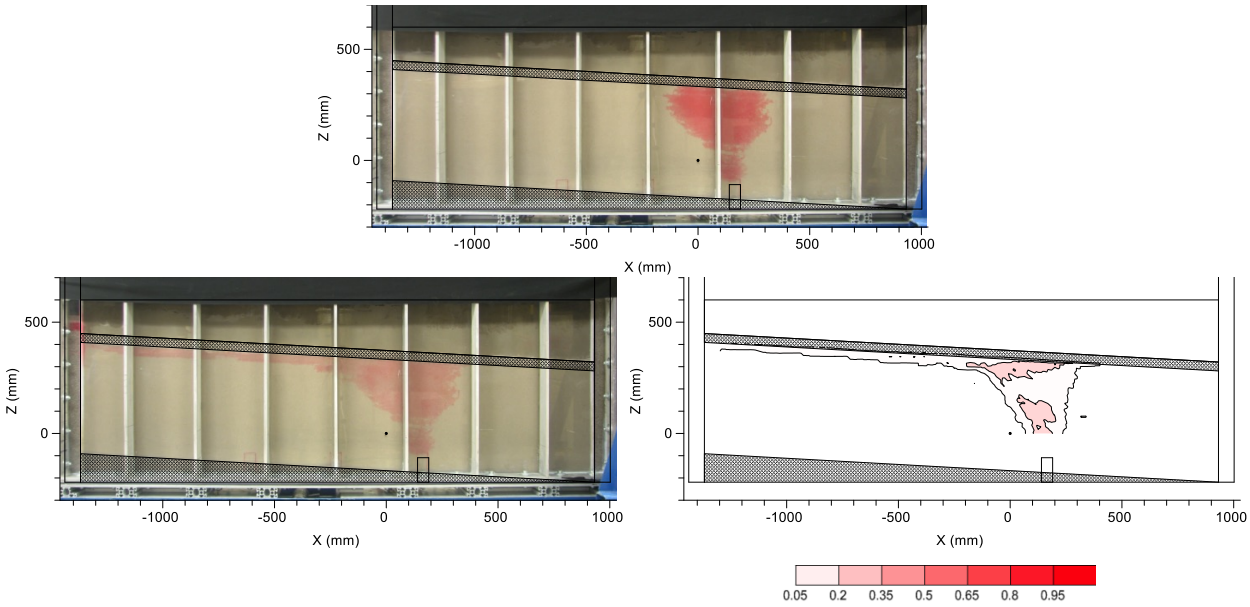

Figure 57 Plume shapshot at the end of the first injection (top) and after fluid redistribution (bottom). Digital photography (left), and NWP saturation contours measured via x-ray attenuation (right).

As shown in Figure 57 and Figure 58, the area of the reservoir occupied by the plume once the NWP has completely redistributed after the 2nd injection is visibly larger than the area occupied after the 1st injection (23% larger). However, assuming that the outflow boundary of the tank represents a leakage pathway (e.g. fault in the caprock), this scenario shows that a large fraction of the injected NWP has bypassed a significant portion of the reservoir, migrating along a thin tongue beneath the caprock.

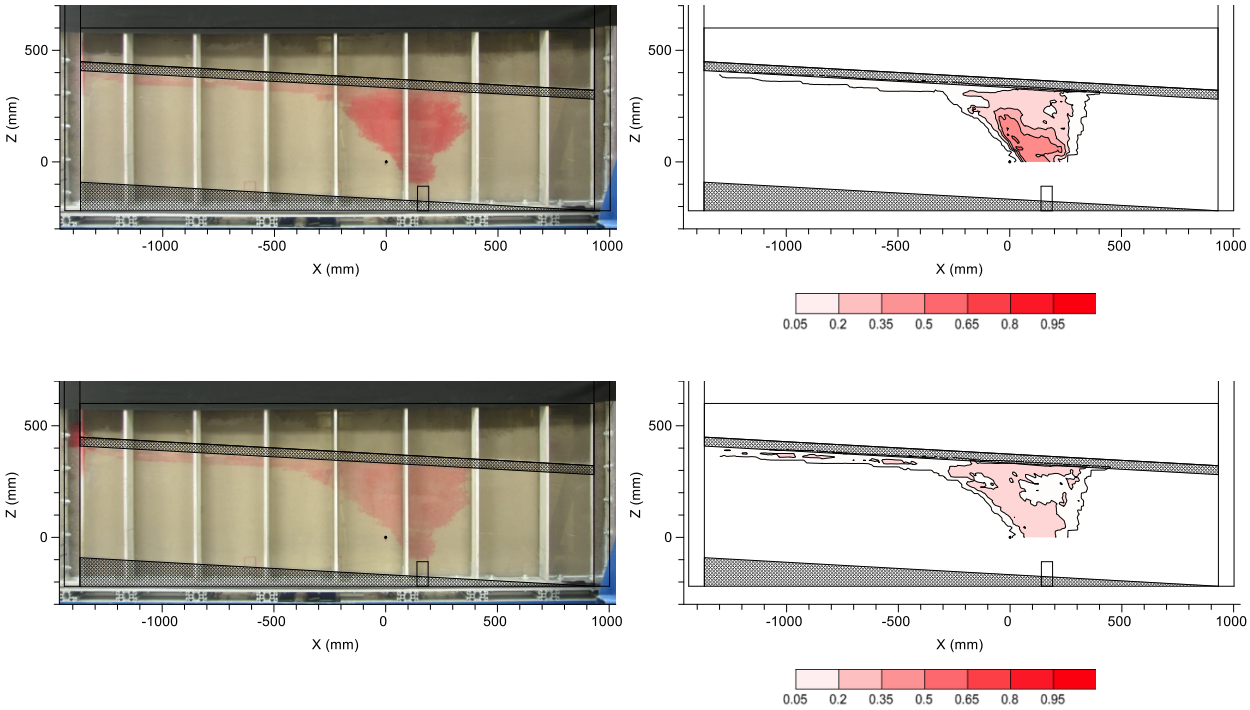

Figure 58 Plume shapshot at the end of the second injection (top) and after fluid redistribution (bottom). Digital photography (left), and NWP saturation contours measured via x-ray attenuation (right).

From the analysis of the zeroth spatial moment expressing the total amount of NWP present in the experimental domain covered by the x-ray scanning grid (Figure 59), some observations can be made.

First, the maximum NWP volume detected after the 1st injection event (730 ml) does not correspond to the actual volume injected into the reservoir (1000 ml); this is due to the fact that it was not able to make x-ray measurements below z=0 due to space limitations. Secondly, the residually trapped volume can be determined from the plateau reached once the fluid redistribution phase is completed. From this observation, we estimated that the stored volume of NWP is 60% higher after the second injection. On the other hand, the fraction of the plume that has escaped through the leakage pathway is also 60% higher.

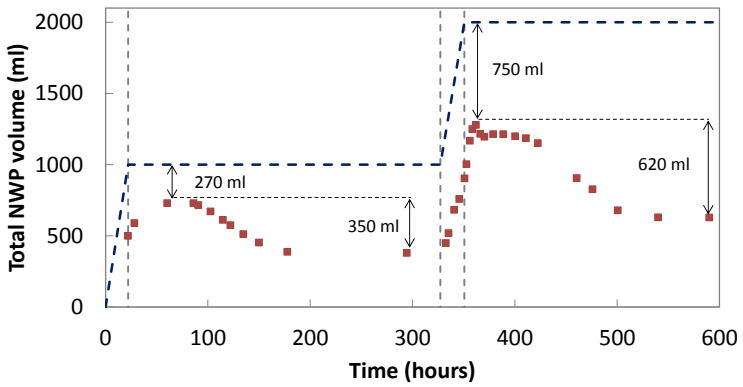

Figure 59 Zeroth moment evolution of NWP plume (covered by scanning grid).

The visualization of the temporal variation of the first moments in the horizontal and vertical directions (Figure 60) helps understanding how the location of the plume center of mass is affected by the breakthrough of the plume into the outflow boundary, occurring at 94 and 417 hours, following the two injection events. When the plume reaches the outflow boundary, the center of mass reverses its original migration direction (both horizontally and vertically) and starts moving countercurrent with respect to the dipping angle of the aquifer and the background flow. A similar behavior is observed during the second injection event, when the addition of NWP volume made the center of mass move closer to the injection location. An analysis of the horizontal and vertical variance of the plume reveals a trend similar to the migration of the center of mass. The lateral and vertical spread of the plume increase until the plume reaches the outflow boundary, and then it quickly decreases to an equilibrium state characterized by a uniform residual saturation value. During the second injection, the horizontal variance decreases whereas the vertical variance increases, due to the addition of NWP close to the well.

During the homogeneous experiment, the injection flow rate of Soltrol 220 increased monotonically with time in a similar fashion for both injection events, as shown in Figure 62. Since the pressure was maintained constant at the injection well, the variation in flow rate had to depend on other factors, such as the increase in available flow pathways for the NWP as the plume became bigger. For a real case this behavior may represent an advantage, since a constant pressure below the fracturing pressure can be constrained while the injectivity of the reservoir increases with time.

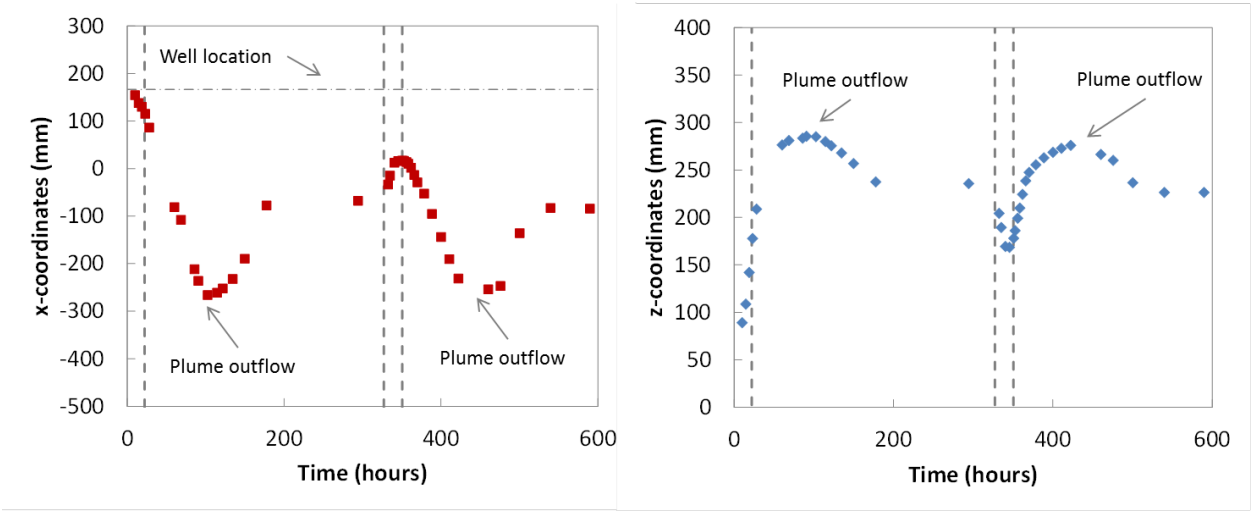

Figure 60 Temporal evolution of the horizontal (left) and vertical (right) coordinates of the plume center of mass during the homogenous experiment. The intervals shown by the vertical dashed lines represent the duration of the injection events. X-coordinates decrease towards the left (outflow) boundary of the domain.

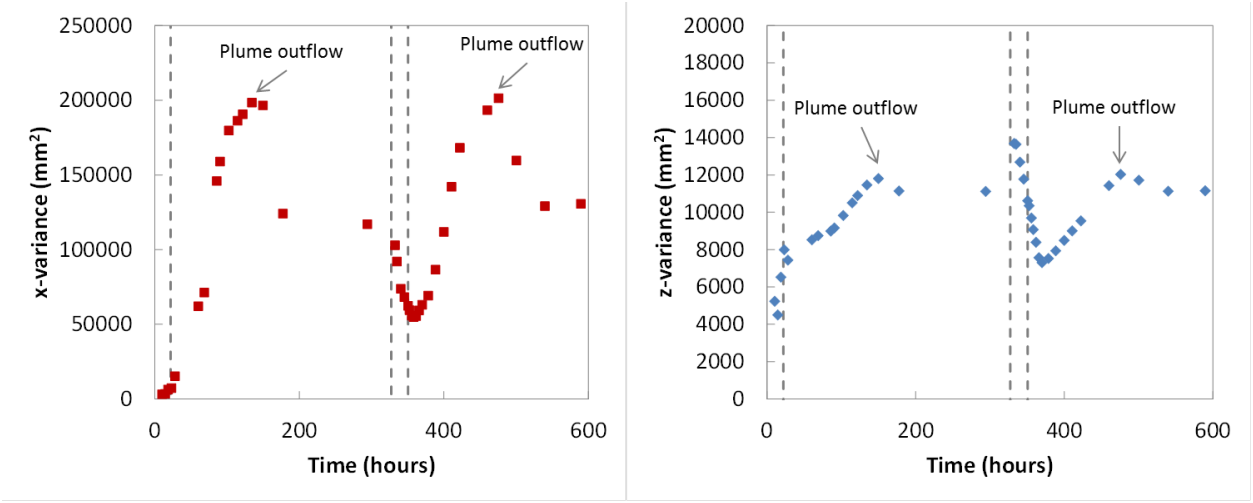

Figure 61 Temporal evolution of the horizontal (left) and vertical (right) variance of the plume.

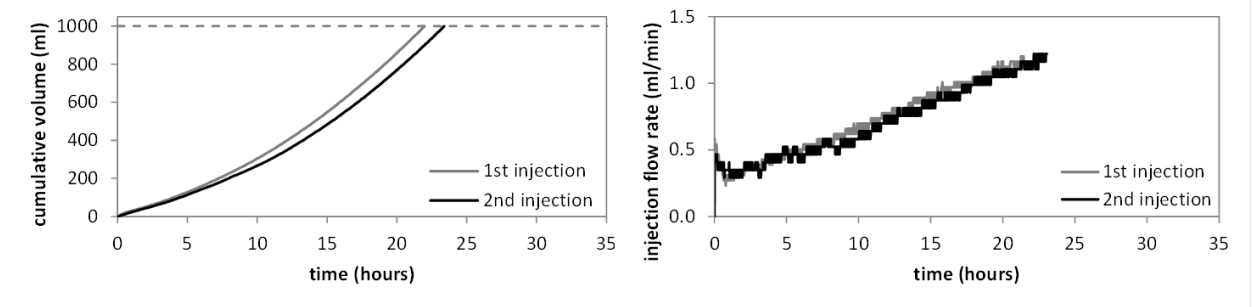

Figure 62 Cumulative volume injected and flow rate variation of Soltrol 220 for the homogeneous experiment.

A similar increasing trend in injection rate has been observed at Sleipner, as shown in Figure 63.

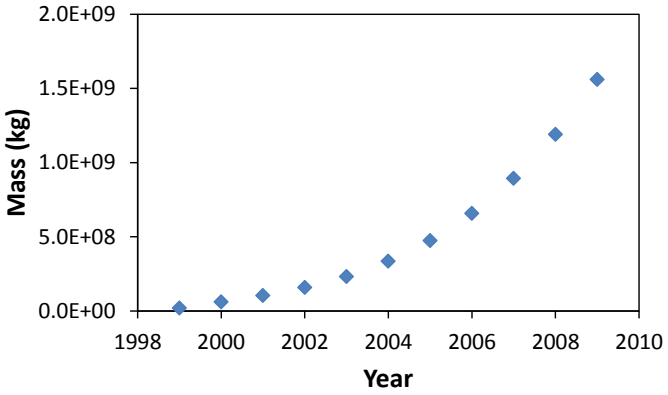

Figure 63 Yearly injected mass of CO_2 at Sleipner (Singh et al., 2010).

Plots of NWP saturation evolution at six selected observation points (Figure 64) allows to recognize some features that are not readily detectable in two-dimensional contour maps. For example, at locations near the injection well (A, B) the second injection event is characterized by larger initial NWP saturations, leading to larger residual saturations once the *spontaneous* imbibition of the wetting phase (i.e. glycerol-water) has occurred. This effect has been observed already at locations far away from the injection well in the small tank experiments, as a consequence of a *forced* imbibition event, which pushed any bulk phase away accumulated upstream. In this case, however, the second NWP saturation peak is due to a second injection event that, even though carried out at the same pressure potential, it is able to displace more wetting phase, invading an increased number of pores.

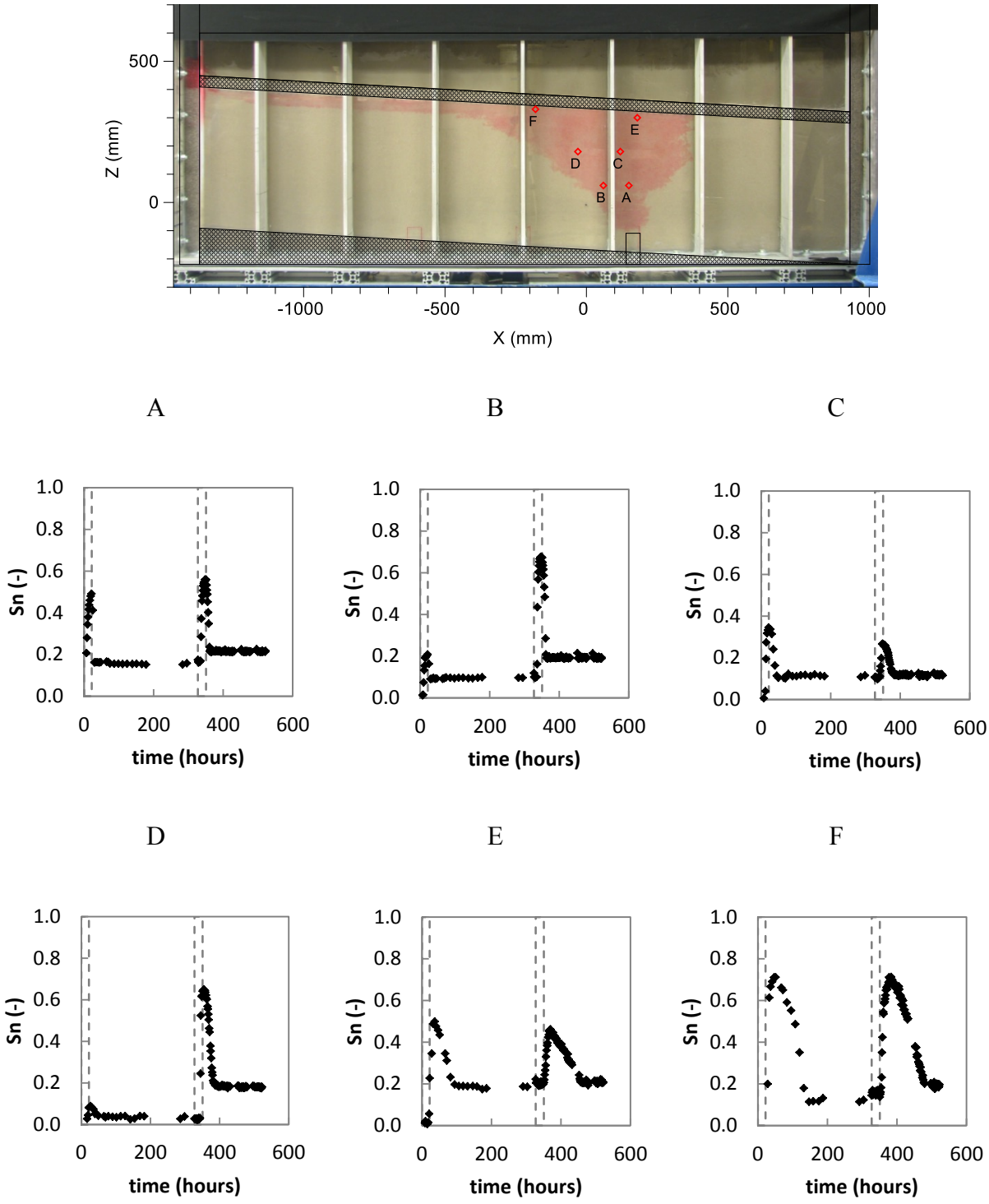

Figure 64 NWP saturation evolution for the homogeneous case at 6 observation points.

b. Heterogeneous scenario

By means of injecting the same volume of NWP following a comparable procedure through a permeability field with mean permeability equivalent to the homogeneous scenario, the influence of aquifer heterogeneity on plume propagation and trapping was studied. The high saturation contours observed in Figure 65 (bottom row) indicate that once the fluids have reached equilibrium after the first injection, high NWP trapped saturations remain immobilized inside high permeable layers juxtaposed to sands with lower entry pressure. While the second injection event during the homogeneous experiment slightly increased the plume extension, the same secondary injection into the heterogeneous domain produced a much larger increment in plume distribution.

Despite the compact area occupied by the plume at the end of the second injection event (Figure 66, bottom row), the NWP volume accumulating at capillary barriers is sufficient to eventually break into sands with higher entry pressure, leading to a slow migration dominated by capillary and gravity forces.

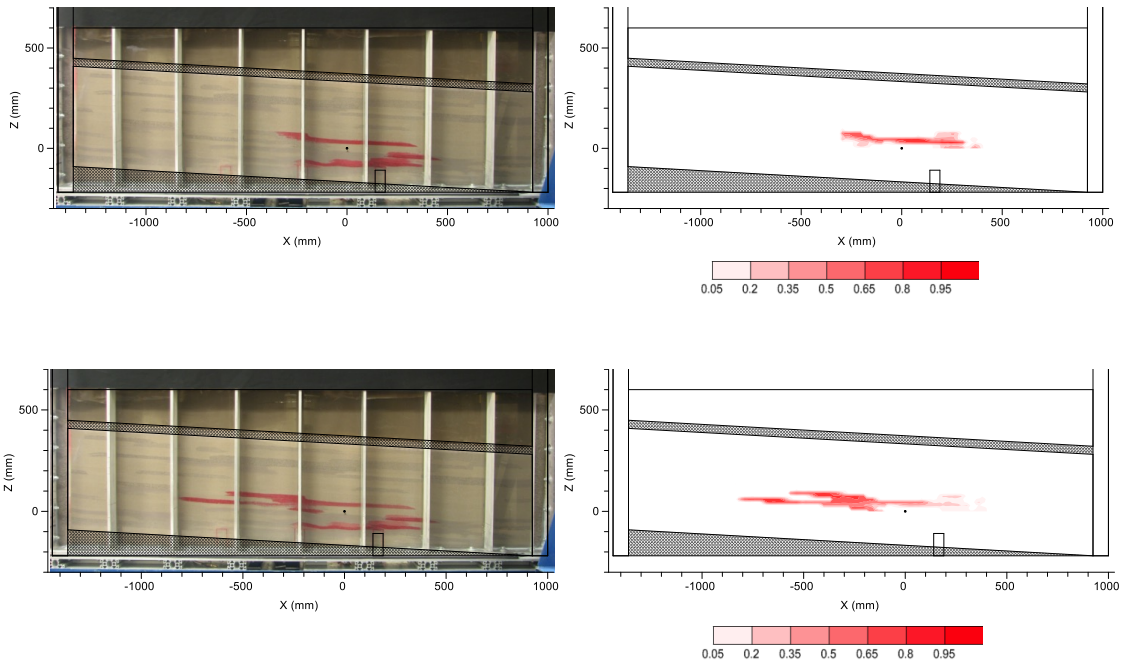

Figure 65 Plume shapshot at the end of the first injection (top) and after fluid redistribution (bottom). Digital photography (left), and NWP saturation contours measured via x-ray attenuation (right).

Similarly to the homogeneous experiment, due to spatial limitations of the x-ray gantry positioning system, the NWP volume residing below the origin of the coordinates (black dot in

digital images and contour plots) cannot be covered by x-ray measurements. However, since the entire plume remained in the aquifer, the volume of the undetected region can be quantified by subtracting the volume identified with the zeroth moment from the total injected volume, as shown in Figure 65.

As shown in Figure 68, an equilibrium situation is quickly attained after the first injection, both horizontally and vertically. Once the second injection event stops, however, the added volume of NWP is enough to trigger a stable movement of the plume's center of mass that has been ongoing during the last two months.

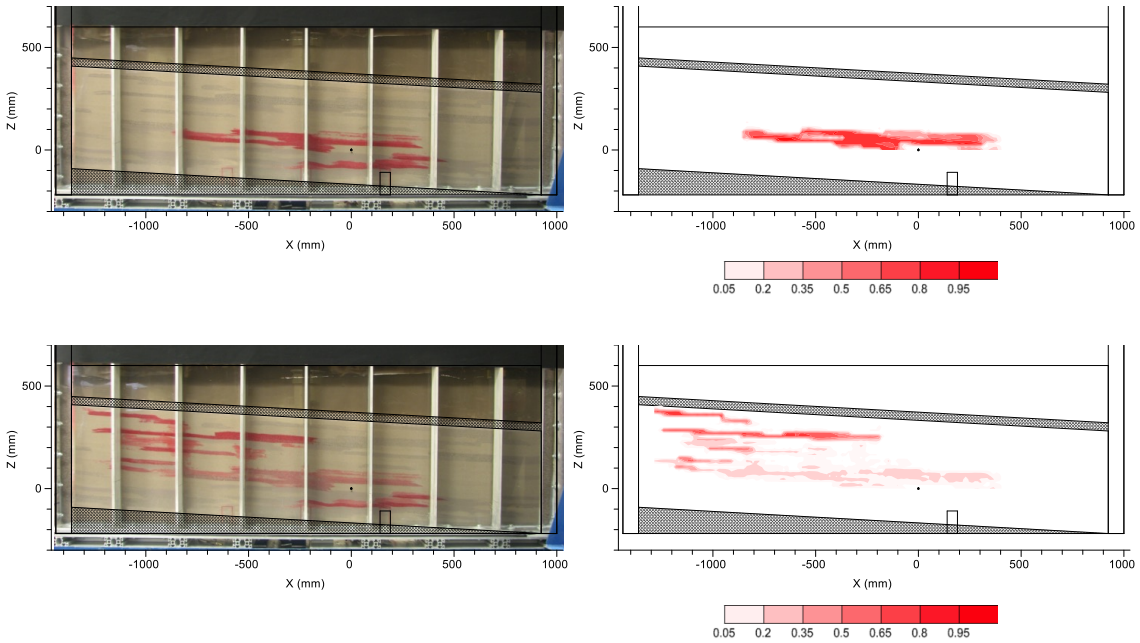

Figure 66 Plume shapshot at the end of the second injection (top) and late time (bottom). Digital photography (left), and NWP saturation contours measured via x-ray attenuation (right).

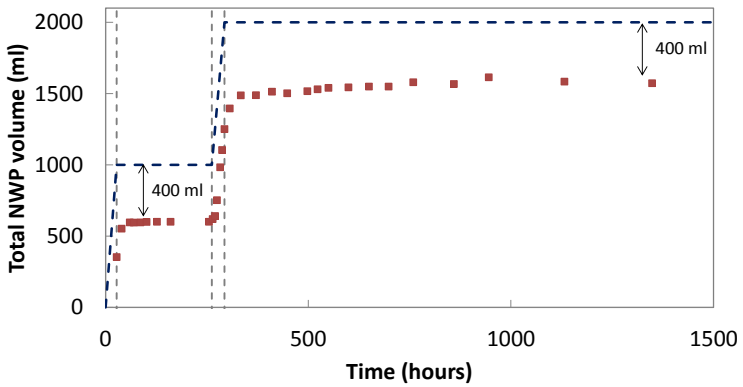

Figure 67 Zeroth moment evolution of NWP plume (covered by scanning grid). Dashed line represents the total NWP volume injected throughout the two injection events (1000 ml each).

With respect to the variance evolution observed during the homogeneous experiment (Figure 61), the trend observed in the heterogeneous one (Figure 69) indicated a rapid increase after a period of apparent equilibrium. This behavior was confirmed by photographic images, which showed the NWP invasion into layers apparently disconnected from the bulk of the plume. Hydrodynamic instabilities, such as fingering, caused this anomalous progression of the plume, which quickly increased its spread through the aquifer.

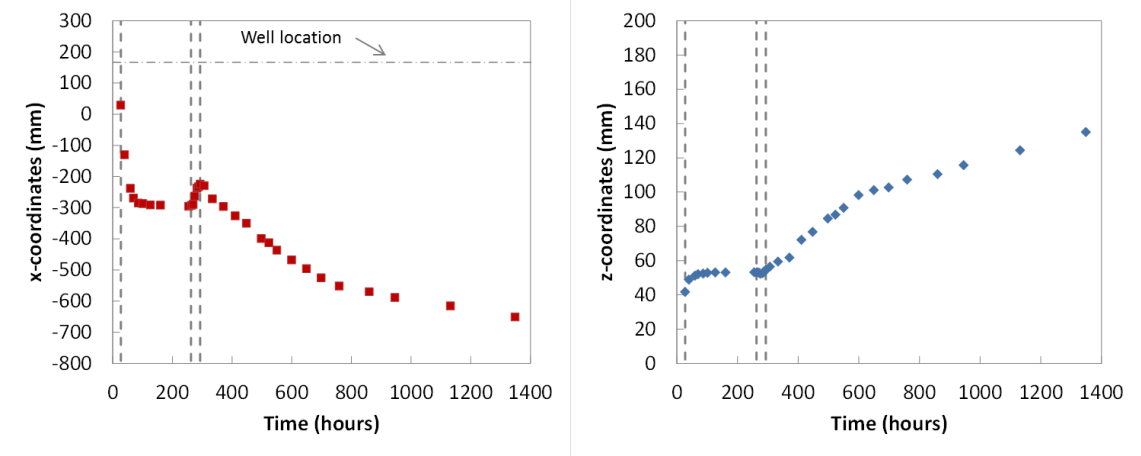

Figure 68 Temporal evolution of the horizontal (left) and vertical (right) coordinates of the plume center of mass during the heterogeneous experiment. The intervals shown by the vertical dashed lines represent the duration of the injection events. X-coordinates decrease towards the left (outflow) boundary of the domain.

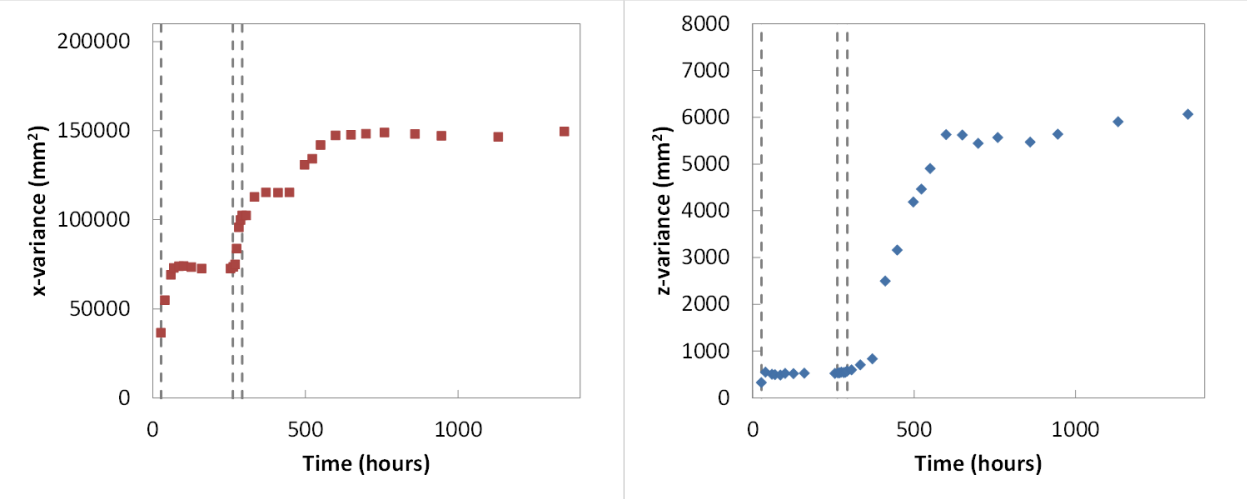

Figure 69 Temporal evolution of the horizontal (left) and vertical (right) variance of the plume.

Reminding that the same pressure of NWP was constrained to the well, the injection flow rate evolved in a different way with respect to the homogeneous experiment. Also, some differences were observed between the two injection events. From Figure 70 it can be noticed that the first liter of Soltrol was injected in a shorter period (27.2 hours) than the second injection (30.85 hours). Besides, compared to the injection duration of the homogeneous experiment (22 and 23 hours for the first and second injection, respectively), this heterogeneous configuration contributed to slow down considerably the injection process.

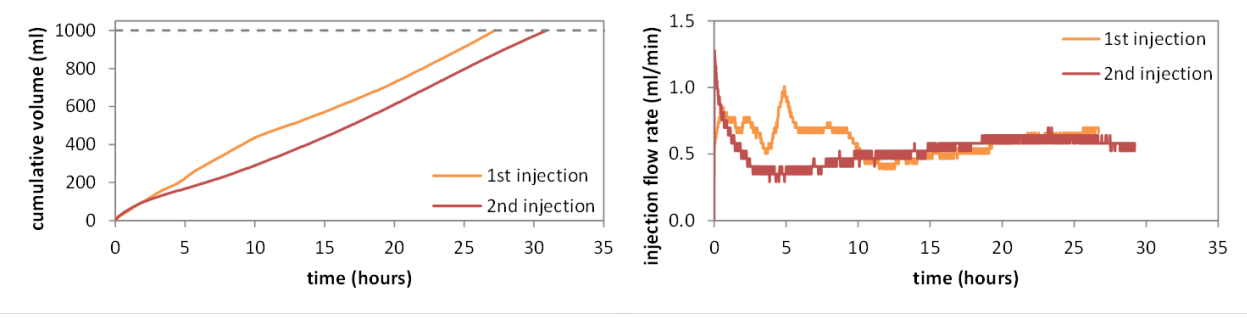

Figure 70 Cumulative volume injected and flow rate variation of Soltrol 220 for the heterogeneous experiment.

Similarly to the homogeneous experiment, a monotonic increase in flow rate was observed during the injection events; however, some rapid variations were observed during the first injection. Such behavior was observed when the plume did not have available space to invade at the current pressure potential (decrease in flow rate) and when high permeable zones

were reached by the plume (increase in flow rate), promoting a fast propagation until those layers were filled.

From the experimental observations of the displacement and immobilization mechanisms occurring in the large tank configurations presented above it was possible to determine the trapping efficiency of an ideal homogeneous scenario as opposed to a more realistic heterogeneous permeability field. While a significant part of the plume (35%) left the homogeneous domain after the 1st fluid redistribution stage, 100% of the injected volume was retained in a small area of the heterogeneous domain. Once reached final equilibrium in the homogeneous case, the NWP plume exhibited a 23% larger area with respect to the previous footprint, compared to the 45% larger area occupied by the plume in the heterogeneous case. While 51.5% of the total injected volume (2 L) had been retained by only residual trapping in the homogeneous aquifer, 79% of the plume was immobilized in the heterogeneous by the concomitant effect of residual trapping and capillary barriers.

4.2 Dissolution trapping experiments

4.2.1 Small tank homogeneous experiments

The results of homogeneous media experiments for #30/40, #40/50, and #50/70 sands are given in Figure 69, Figure 72, and Figure 73, respectively. The calculated Ra values for these experiments in Table 11, which are greater than the critical value (~40), support the experimental observation of generation of density-driven convective finger development in all the experiments.

Table 11 Rayleigh numbers for homogenous experiments.

Sands	Permeability (m^2)	Ra (-)
#30/40	1.08×10^{-10}	647
#40/50	5.30×10^{-11}	309
#50/70	3.66×10^{-11}	196

The *Ra* values were calculated for these experiments using equation (1) where D is 8×10^{-11} m^2/s, μ_{PG} is 5.5×10^{-2} Pa.s and *H* is 0.1016 m. $\Delta\rho$ (8.594 kg/m^3) for the final distribution of dissolved water in the source zone prior to the onset of convection. The injected water in the source zone was assumed to be fully mixed with PG. The dissolved water sank in the lower one

third of the 2.54 cm thick source zone along the boundary between the high (#12/20 sand) and medium or low (#20/30, #30/40, #40/50, and #50/70 sands) permeability sands. The concentration of dissolved water in the specified zone was assumed to be uniform. The mass fraction of water was calculated as 0.194. Then, by using equation (13), the density of PG with dissolved water was determined for the calculation of $\Delta\rho$.

The propagation of the longest finger (Figure 74a) versus time graph of these experiments was plotted using the periodically taken digital images. The length of the longest finger was measured from the bottom of the source zone. The results of image processing analysis were examined for each experiment. The first (Figure 74b) and second (Figure 74c) spatial moments in z-direction versus time graphs were generated using the data from image processing analysis to compare the experimental results quantitatively. The bottom of the source zone locates at 0.1143 m, which is the highest value for the first moment observed in the beginning of the experiment. The long fingers, small center of mass values, and large spreading values were observed in high permeability sand experiments.

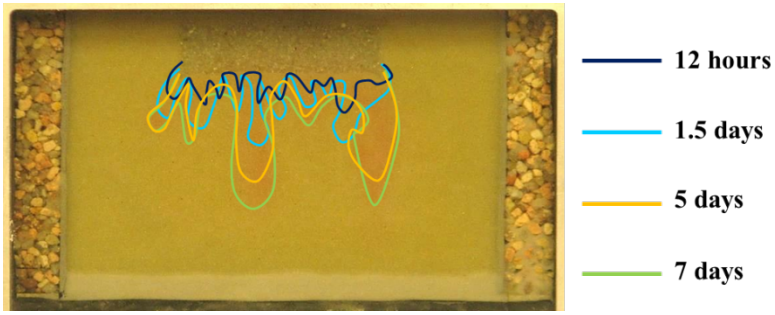

Figure 71 Results of 1st homogeneous media experiment for #30/40 sand.

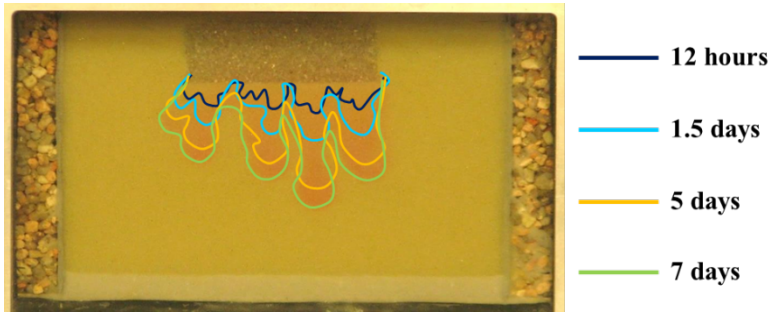

Figure 72 Results of 2nd homogeneous media experiment for #40/50 sand.

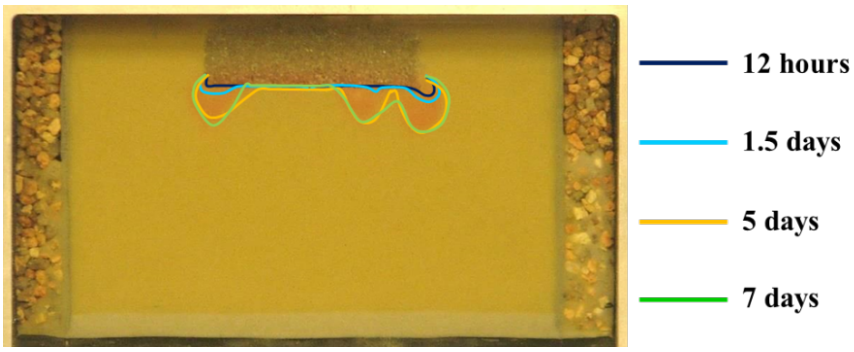

Figure 73 Results of 3rd homogeneous media experiment for #50/70 sand.

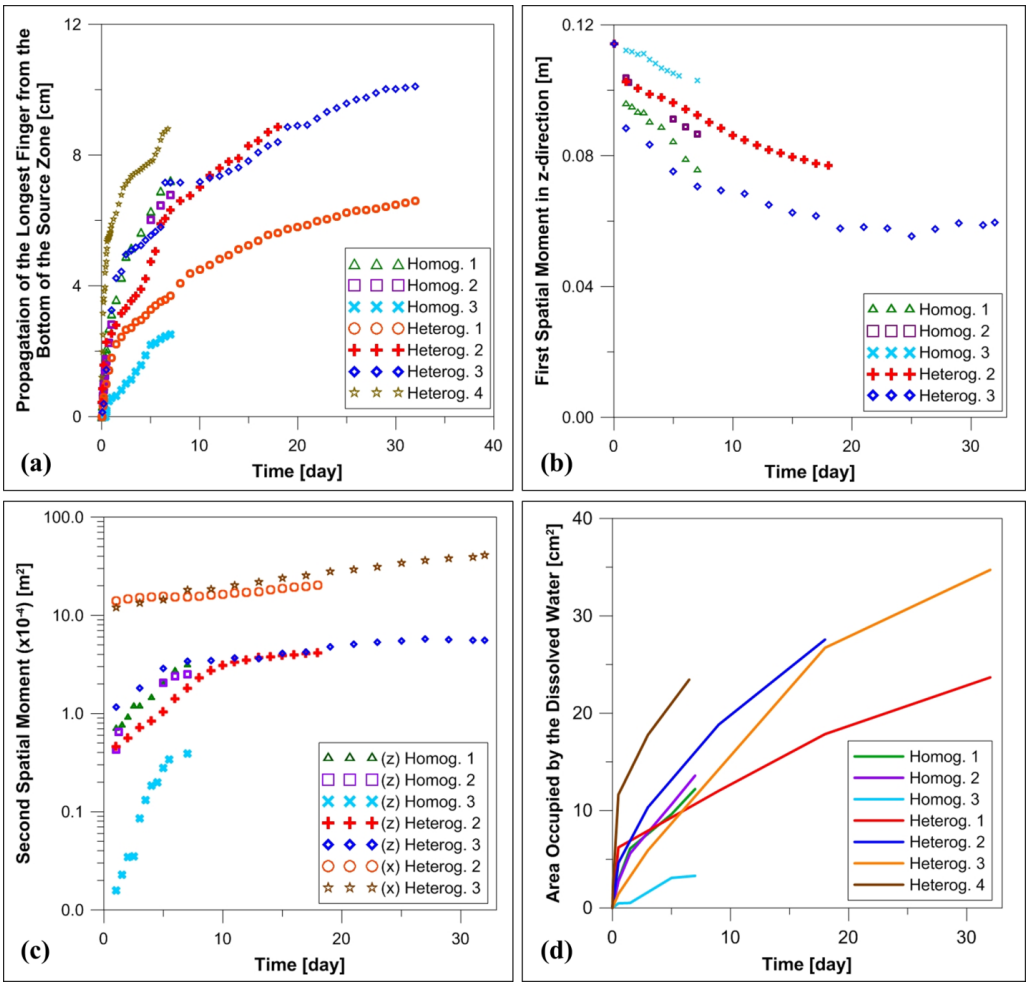

Figure 74 (a) Fingertip propagation, (b) first and (c) second spatial moments of dissolved water plume, and (d) area occupied by dissolved water versus time graphs for all experiments.

4.2.2 Small tank heterogeneous experiments

For the 1st heterogeneity experiment with the inclined lithological interface, the density-driven convective fingers generated into medium permeability #40/50 sand reached to the boundary between medium and low (#50/70) sands, where the fingers merged (Figure 75). This slowed down the vertical spreading, but enhanced the lateral spreading as can be seen from the area occupied by the dissolved plume graph in Figure 74d. The interface inclination led the dissolved water plume move through the down slope. Although the inclination contributes to the spreading in vertical direction, the low permeability #50/70 sand blocks the movement due to slow diffusion rates. Therefore, the plume propagates slowly in the vertical direction as seen in Figure 74a. The result of 2nd heterogeneous medium experiment with alternating layers of high,

medium, and low permeability sands is given in Figure 76. In addition to the finger propagation (Figure 74a) and area occupied by dissolved water (Figure 74d) graphs, the variations in first (z-direction in Figure 74b) and second (x and z directions in Figure 74c) spatial moments with time were determined using the data from image processing analysis. This experiment highlights the changes in the flow at the sand transitions due to the boundary between high/medium and low permeability sands, which impacts the stable trapping. The low permeability layers in the system slowed down the vertical spreading due to slow diffusion rates (Figure 74a, b, and c). Fingers merged, and dissolved water spread in lateral direction along the boundary (Figure 76) as can be seen in the increasing second spatial moment in x-direction with time in Figure 74c. This increases the diffusion area along the sand transition. The results also highlight the storage capacity of low permeability layers compared to high permeability ones.

The results of 3rd and 4th heterogeneous media experiments with rectangular blocks are presented in Figure 77 and Figure 78, respectively. In the presence of rectangular blocks of low, medium and high permeability sands, the density-driven convective fingers were formed in the high permeability layer under the source zone (Figure 77, Figure 78), and the convective mixing is controlled by density driven sinking through high and medium permeability connected pathways. The difference observed on the spreading of two experiments is a result of the permeability distribution of the rectangular blocks. The propagation of the longest finger (Figure 74a) and the area occupied by dissolved water (Figure 74d) graphs showed the effect of this distribution on the results. In Figure 74a, the fingertips reached to 8 cm depth from the bottom of the source zone at 15.8 and 5 days, respectively. In addition, the image processing analysis was performed for 3rd heterogeneous media experiment, and the results of first and second spatial moments are given in Figure 74b and c.

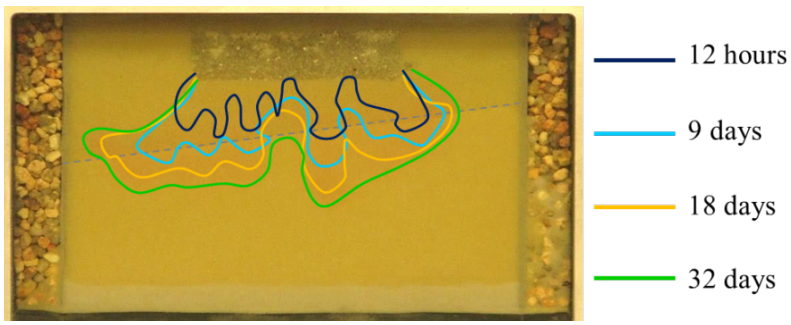

Figure 75 Results of heterogeneous media experiment 1.

Figure 76 Results of heterogeneous media experiment 2.

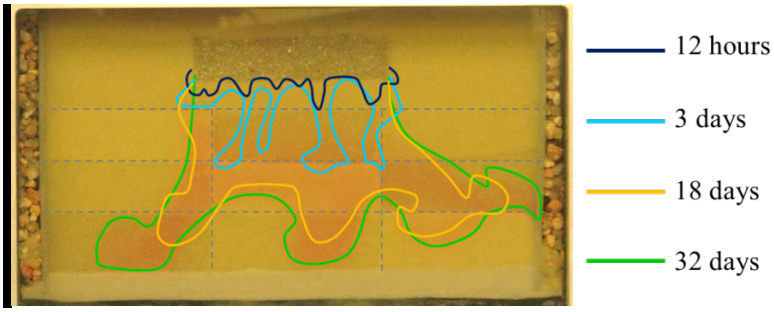

Figure 77 Results of heterogeneous media experiment 3.

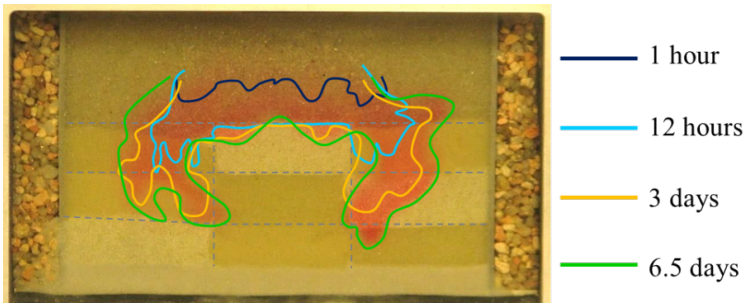

Figure 78 Results of heterogeneous media experiment 4.

For homogeneous systems, the stable trapping is to get more dissolved mass into the system and spread the mass over a larger aquifer zone to increase the potential for more mineralization that contributes to the permanence of the dissolved plume in the formation. Convective mixing enhances the trapping of the dissolved fluid in the deeper parts of the formation. The magnitude of convective mixing depends on the permeability of the medium. From higher (#30/40) to lower permeability sands (#50/70), the onset time of convection and trapping of dissolved CO_2 increase (Figure 69, Figure 72, Figure 73). The deeper center of mass

(Figure 74b), and greater spreading in z-direction (Figure 74c) observed at early times are indicators of the faster onset of convection as observed in #30/40 sand homogeneous medium experiment. From lower permeability (#50/70) to higher permeability (#30/40) homogeneous experiments, the finger width decreases (Figure 69, Figure 72, Figure 73), the finger length increases (Figure 74a), the center of mass moves to the deeper parts (Figure 74b), and the vertical spreading from center of mass enhances (Figure 74c). These indicators also point out the faster mass depletion from the source zone for higher permeability formations compared to lower permeability ones. Therefore, the effectiveness of convective mixing increases with increasing permeability of the formation.

The earlier onset time, the higher mass depletion rates, and the faster vertical motion observed in the higher permeability formations enhance the stable (secure and long term) storage of dissolved CO_2 in deeper parts of the formation, which reduces the risk of leakage. This vertical spreading also contributes to the potential for mineralization due to increase in contact area between dissolved CO_2 and the host rock.

The lower permeability layer (#50/70) in the 1st heterogeneous experiment with inclination slowed down the mass depletion rates, and the vertical flow of the dissolved water. In order to evaluate the effects of additional inclined low permeability layer on the results, this experiment was compared with the 2nd homogeneous experiment. The same sand (#40/50) was used to packed the 2nd homogeneous experiment and the upper layer of the 1st heterogeneous experiment. The #50/70 sand has a significant influence on the spreading characteristics. The longest finger in the second homogeneous experiment reached 7 cm in 5 days; however, the same depth was reached after 30 days in the 1st heterogeneous experiment. Moreover, the visual observations indicates that the density-driven convective flow observed in the 2nd homogeneous experiment was replaced with more diffusive transport by the addition of #50/70 sand in the medium, which led fingers to merge at the sand transition. Slow diffusion rates in that layer might enhance the storage of dissolved fluid through immobilization. Therefore, the low permeability sands have a significant effect on the spreading and storage of the dissolved fluid.

In the presence of multi-layer heterogeneity (Figure 76), it was observed that the density-driven convective mixing was replaced by diffusive mixing in low permeability layers. These experimental results confirm that permeability has a noticeable impact on the fate of instabilities, and the spreading and trapping of dissolved mass. At the transition of the high/medium to low

permeability layers, the fingers merge and spread along the boundary between layers. The results of the layered media experiments show that the sequence in which the variable permeability layers are arranged is another factor influencing overall spreading behavior. Under reverse conditions (movement from low- to high-permeability medium), the fingers were immediately generated in the high-permeability zone, and density-driven convective mixing became the dominant mechanism (Figure 76).

The propagation of the longest finger versus time graph clearly showed the influence of different permeability layers on the spreading. The stepwise propagation was observed due to the alternation of low and high permeability sands in the sequence. The first (Figure 74b) and second (Figure 74c) spatial moments, which were determined using image processing method, also highlight the effects of the layers on spreading. In order to determine the influence of alternating layers on the spreading and storage, the result of the 2^{nd} heterogeneous experiment was compared with the 1^{st} homogeneous medium experiment because in both cases, the same sand (#30/40) was used to pack the layer under the source zone. In 2^{nd} heterogeneous experiment, the upper #30/40 sand later was followed by low, high, and medium permeability sands, respectively. These additional layers slow down the vertical movement of the plume as can be seen in Figure 74a and b, and also limit the vertical spreading due to low diffusion rates into #50w low permeability sand layer (Figure 74c). The center of mass in the 1^{st} homogeneous experiment spread around 0.075 m depth after 1 week; however, in the 2^{nd} heterogeneous experiment, it reached the same location in 18 days.

On the other hand, during the movement from high to low permeability media, the lateral spreading due to the accumulation of dissolved water mass along the boundary between sands increased the contact area between the dissolved fluid and the low permeability layer as observed in Figure 76. As a result, the total amount of diffused dissolved water mass in the low permeability layer increased, which led to the stable trapping of more mass. The stable trapping in layered formations depends on the storage capacity of low permeability layers because the dissolved CO_2 can be trapped in low permeability layers through immobilization. This is a secure and long term storage of dissolved CO_2. The loading capacity of these layers depends on their hydraulic and geometric properties.

In the presence of rectangular blocks with different permeabilities, density-driven convective fingers were controlled by higher permeability connected pathways. The hydraulic

boundaries in the system significantly modified the spreading characteristics. Farajzadeh et al. (2011) called this process channeling. Although finger like features were observed in the tests, they occurred as a result of the movement of dissolved mass through connected pathways. Contrary to the layered systems, low permeability zones behaved more like impervious discrete layers as clearly seen in the results of the small tank experiments with rectangular blocks heterogeneity (Figure 77, Figure 78). Green and Ennis-King (2010) numerically observed a similar behavior for discrete shale layers. They found that the plume motion depends on the permeability in vertical and horizontal directions and the shale layers speed up the vertical spreading compared to the homogeneous formation with same effective vertical and horizontal permeability. In both of the cases, the higher permeability connected pathways controlled convective mixing.

Figure 77 and Figure 78 show an obvious difference in the mixing behavior between these two experiments, which was caused by the lower permeability of the upper rectangular block located under the source zone in the 4th heterogeneous experiment (Figure 78). It can be said that the low permeability block split the paths, accelerated the spreading of dissolved water into deeper parts of the domain, and also decreased the spreading time. In addition, the splitting of the paths enhanced the lateral spreading. The accumulation of the dissolved water mass on top of the low permeability block in the 4th heterogeneous experiment increased the concentration and density gradients, which speed up the vertical motion of the plume under the effect of gravitational forces (Figure 78). However, in the 3rd experiment, the fingers spread through the medium permeability upper block (Figure 77), which diluted the dissolved water concentration and decreased the density gradients. The spreading in the 4th experiment was faster than the 3rd one due to greater density gradient. This regime decreases the time to reach the deeper parts of the formation.

As a result, the spreading time variations observed in the 3rd and 4th heterogeneous experiments influence the stable trapping. More dissolved plume got in touch with host rock in a short time in the 4th experiment compared to 3rd experiment as seen in Figure 74d. In the 4th heterogeneous experiment, 23 cm^2 spreading area was observed at 6.5 days; however, the same area reached at 15th day in the 3rd heterogeneous experiment. The potential mineralization in the 4th heterogeneous porous media experiment is expected to occur in a shorter time compared to the 3rd experiment. Therefore, these findings indicate the importance of the distribution and

hydraulic properties of the rectangular blocks in the formation on the spreading and storage of dissolved plume.

The comparison of the 3rd heterogeneous experiment with the 2nd homogeneous experiment, which have the same #40/50 sand layer located under the source zone, emphasize the importance of rectangular blocks heterogeneity with variable permeabilities in the system. In Figure 74a, the similar finger lengths were observed in the beginning of the experiments. However, when the dissolved plume in the 3rd heterogeneous experiment reached to the higher permeability sand block (#30/40), the vertical spreading enhanced. In the center of mass versus time graph in Figure 74b, the effects of #30/40 sand on spreading is more clear. Instead of higher permeability #30/40 sand, the lower permeability #50/70 was placed in the same location. The vertical spreading could be paused at the sand boundary; however, due to accumulation of the higher density dissolved water, the faster spreading would be observed in vertical direction.

In the experiments that were reported, source strength and boundary conditions are important factors that influence forces driving convective mixing. They might have considerable impacts on flow of dissolved water that was used as the surrogate for CO_2. For example, the gravel packs located on each side of the small tank to control the boundary heads enhance convective mixing because they may act as channels for upward flow in the convective cells. In the absence of gravel columns, vertical spreading of dissolved water might be slower, whereas the wider gravel packs might speed up convective flow. On the other hand, the instantaneous release of source (water) slows down the vertical spreading due to dilution of dissolved water concentrations at the deeper parts of the medium as observed in the small tank experiments. This reduces the density of the solution, and hence the effects of gravitational forces acting on it. However, the continuous source of water might decrease the impacts of dilution. In other words, concentration and density of solution will not be significantly reduced during the flow. This might contribute to convective flow. For example, in the 2nd heterogeneous medium experiment with alternating layers of fine, medium, and coarse sands, the continuous water source might enhance diffusion into low permeability layers due to greater concentration gradients while contributing to convective mixing in the relatively higher permeability sands.

4.2.3 Large tank homogeneous experiments

The two homogeneous experiments were conducted using the same sand packing to investigate the effects of pore-scale heterogeneity and packing imperfections on density-driven flow. The digital images periodically taken from the front wall of the tank shown in Figure 79 compares the evolution of the fingers in both of the experiments. After the release of the source, heterogeneity at the sand transition and pore-scale heterogeneity triggered the density-driven fingers in an hour. The fingers reached to the bottom of the tank in two days and started to pool. The pooling stopped the convective flux and led merging of the fingers. Thus, the dissolved mass concentrations started to get homogenized in the tank.

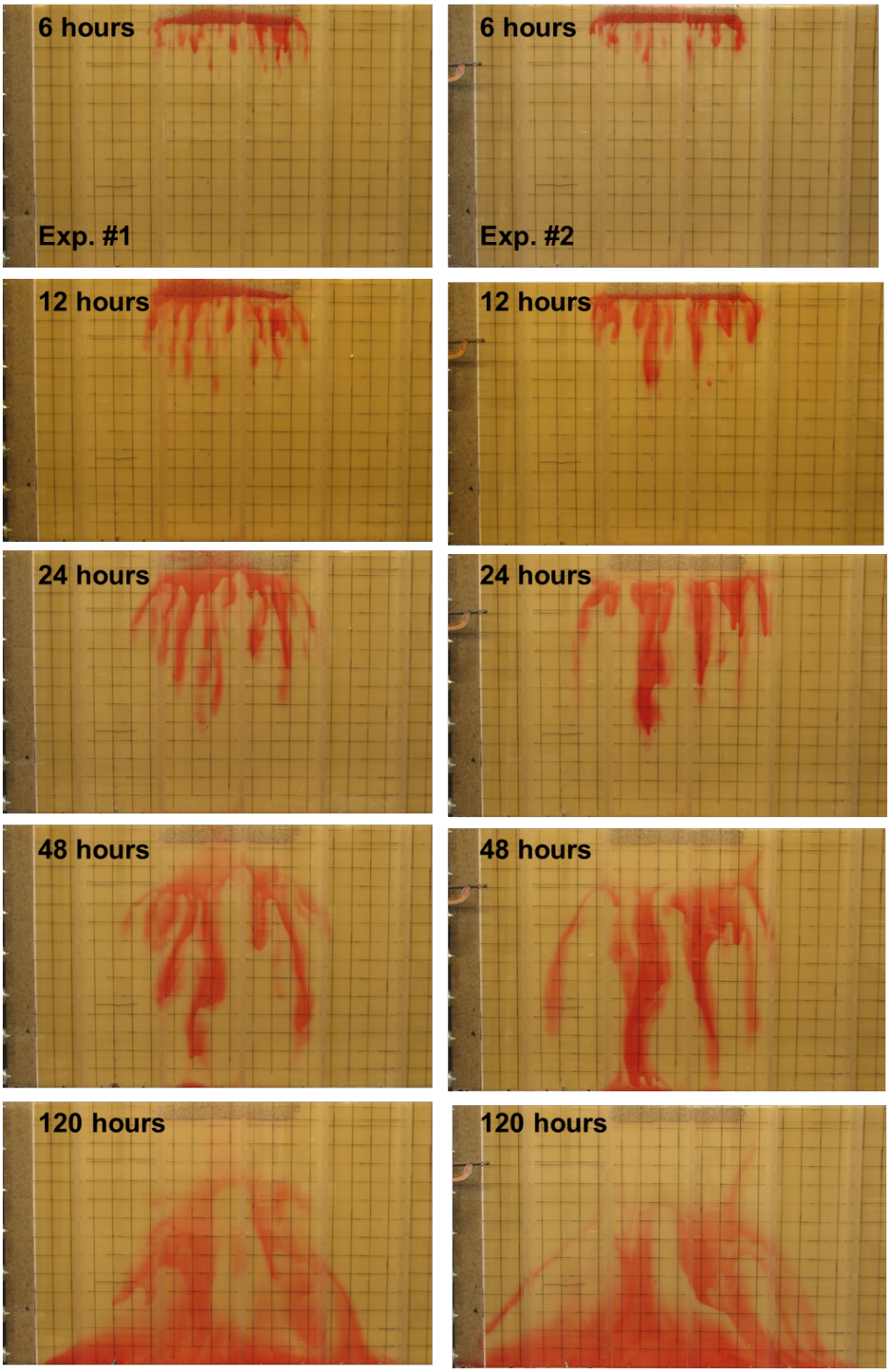

Figure 79 Spreading of density-driven fingers from the front wall for experiment 1 and 2 at (a) 4 hours, (b) 12 hours, (c) 24 hours, (d) 48, and (e) 120 hours after the source release.

Figure 80 highlights the differences in spreading observed on the front and back walls at 37th hour for both of the experiments. This was a result of 3-D nature of the fingers that cannot

be fully characterized through visual observations from the walls. This tank has enough thickness (7.7 cm) for the 3-D fingers to develop without moving towards the walls to be visible through the plexiglas. This phenomenon was not observed in the small tank experiments due to relatively small thickness of the tank (2.54 cm). The types of fingers generated in this tank were analyzed in detail in the heterogeneous experiment section during the comparison of the results from the two types of experiments.

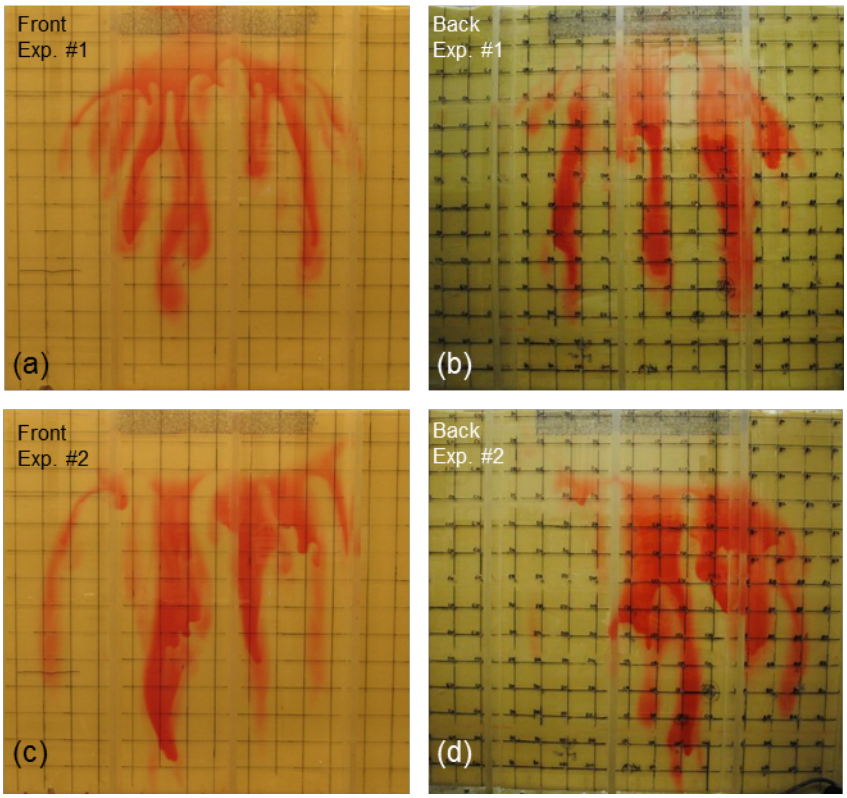

Figure 80 Comparison of spreading in front and back walls of the tank at 37 hours after injection: Experiment #1 (a) front wall and (b) back wall, and Experiment #2 (c) front wall and (d) back wall.

The pore-scale heterogeneities and packing imperfections resulted in different spreading patterns of the dissolved mass in these experiments (shown in Figure 79 and Figure 80). The aqueous samples taken during these experiments were analyzed to determine the spatial moments of the plume. The analysis of center of mass in the z-direction in Figure 81a shows that the migration of dissolved mass in the second experiment was faster than the first experiment under the same source injection scheme. In the x-direction, the spreading from the center of mass is similar for both of the experiments (Figure 81c); however, the dissolved mass in the first

experiment moved towards the right side of the tank while the second one moved through the left (Figure 81b).

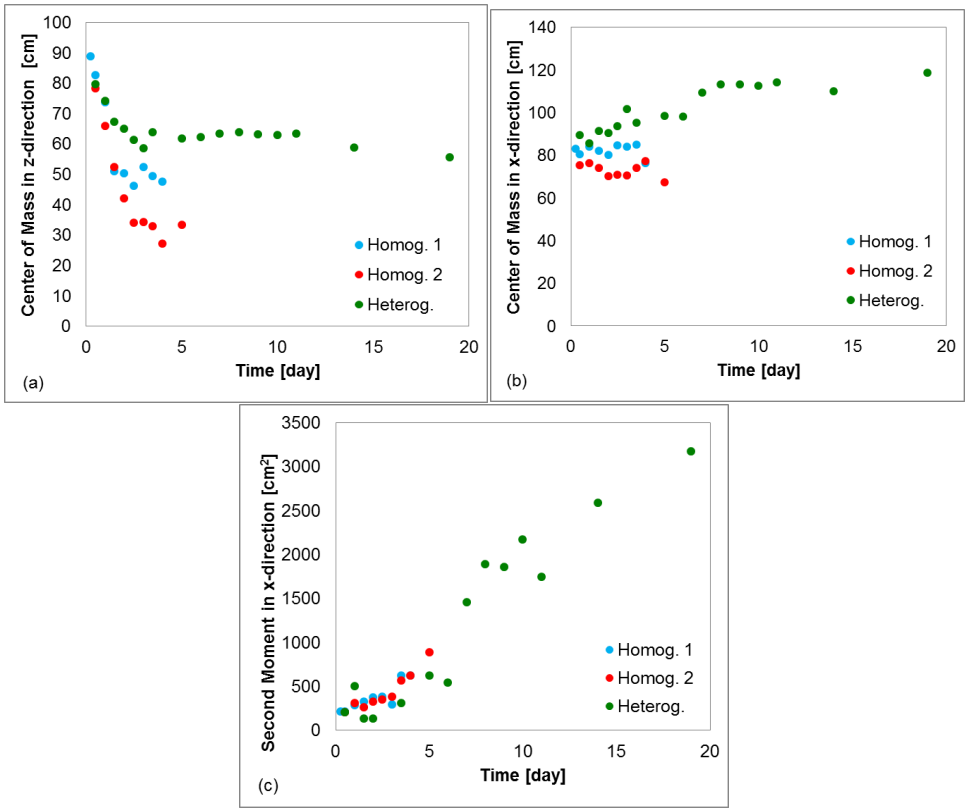

Figure 81 Comparison of the moments of the homogeneous and heterogeneous experiment: (a) center of mass in z-direction, (b) center of mass in x-direction, and (c) spreading from center of mass in x-direction.

4.2.4 Large tank heterogeneous experiments

The fractures and/or the deposition environment of the particles present in clay and shale layers cause heterogeneity (Neuzil, 1994), which has a considerable influence on the flow dynamics (Shi, 2005). This experiment was conducted with the goal of investigating the role of the vertical connectivity present in the low-permeability layer on mixing and long-term storage of dissolved CO_2 in multilayered systems. Unlike in the homogeneous experiments, a very slow background hydraulic gradient was maintained to best capture field-scale phenomena with reasonable accurately. The source was created using the same injection scheme as of the homogeneous experiments. This experiment was completed in three periods that include: (1) the

initial slow background water flow and source injection, (2) no background water flow, and (3) relatively higher background water flow.

The results of the first 4 days were compared with the homogeneous experiments to analyze the effects of the low-permeability layer on spreading of the dissolved mass. The onset time of the density-driven fingers and the spreading in x-direction (second moment) were similar to the homogeneous cases at the initial times (Figure 81c). In 12 hours, the dissolved mass reached the low-permeability layer and started to pool (Figure 84). The fingers got merged at the high and low-permeability layer transition. This low-permeability layer limited the vertical flow whereas enhanced the lateral spreading (seen in Figure 81a and Figure 81c). Due to slow diffusion rates into the low-permeability layer, the center of mass in z-direction did not move much until the onset of convection in the second layer. In addition, the fresh water leakage into the upper aquifer contributed to the lateral spreading (Figure 81c).

The same type of density-driven fingers was observed as in the homogeneous media experiments. The distribution of dissolved mass at 12 and 24 hours (Figure 82a and Figure 82b, respectively) was analyzed to identify these fingers. Three vertical locations were selected. In the first location, no fingers were observed though the front and back walls of the tank (Figure 82a). However, the fluid samples taken from the middle of the tank showed variations in NaBr concentrations with depth as seen in Figure 81a. This was a consequence of the finger not visible through the tanks walls. In the second location in Figure 82a, the red color was observed on the front wall as a proof of the concentrations higher than zero, whereas no color variation was seen on the back wall. The concentrations measured in the middle of the tank identified the finger that spread from the front wall through the middle of the tank (Figure 81a). The third location showed one large finger that covered the total thickness of the tank. On the front and back walls, some portion of the finger was observed, and the higher NaBr concentrations measured in the middle of the tank (Figure 81a) indicated its size. . The results at 24 hours (Figure 82b and Figure 81b) illustrated the merging and pooling of these fingers. The dissolved mass concentrations at locations closer to the source zone decreased due to depletion of the mass, and the higher concentrations were observed either in the middle or bottom of the tank.

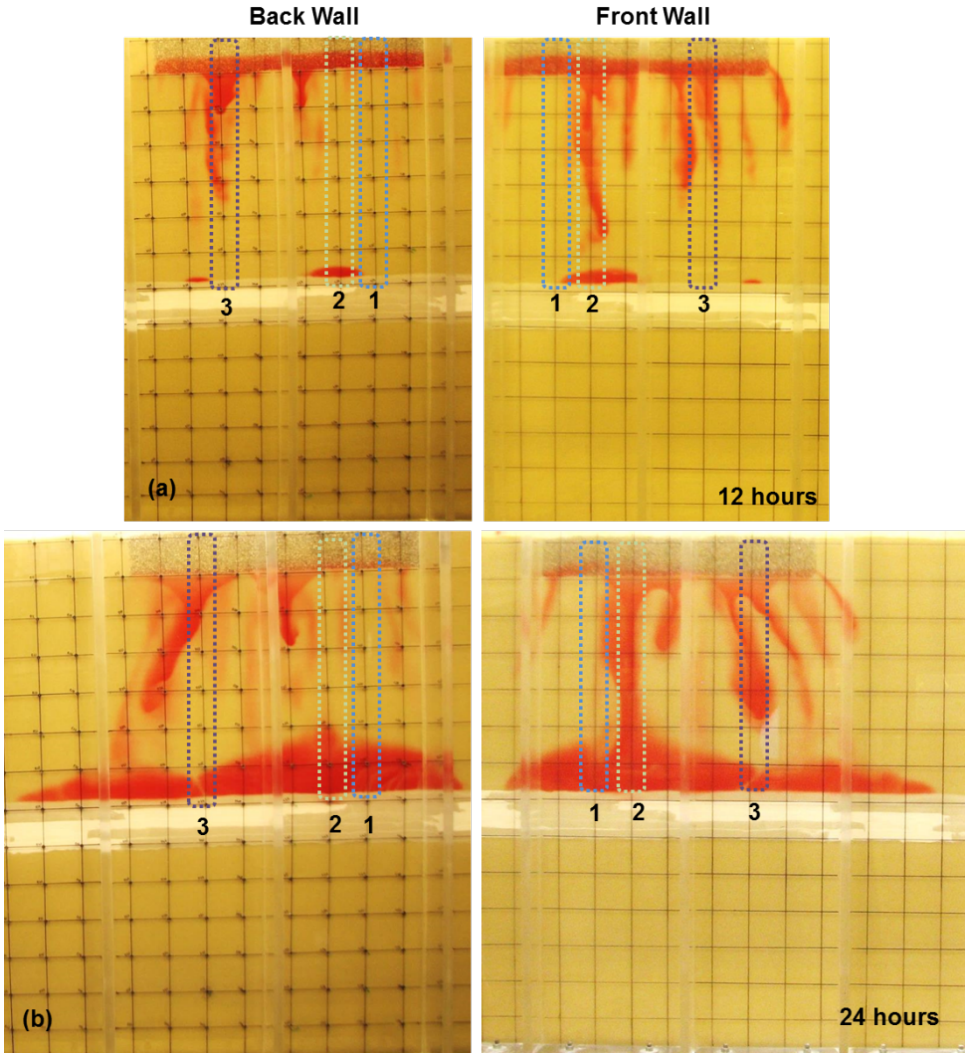

Figure 82 Three different fingering observed in the tank. The digital images taken from front and back walls of the tank showing the spreading at (a) 12th hour and (b) 24th hour.

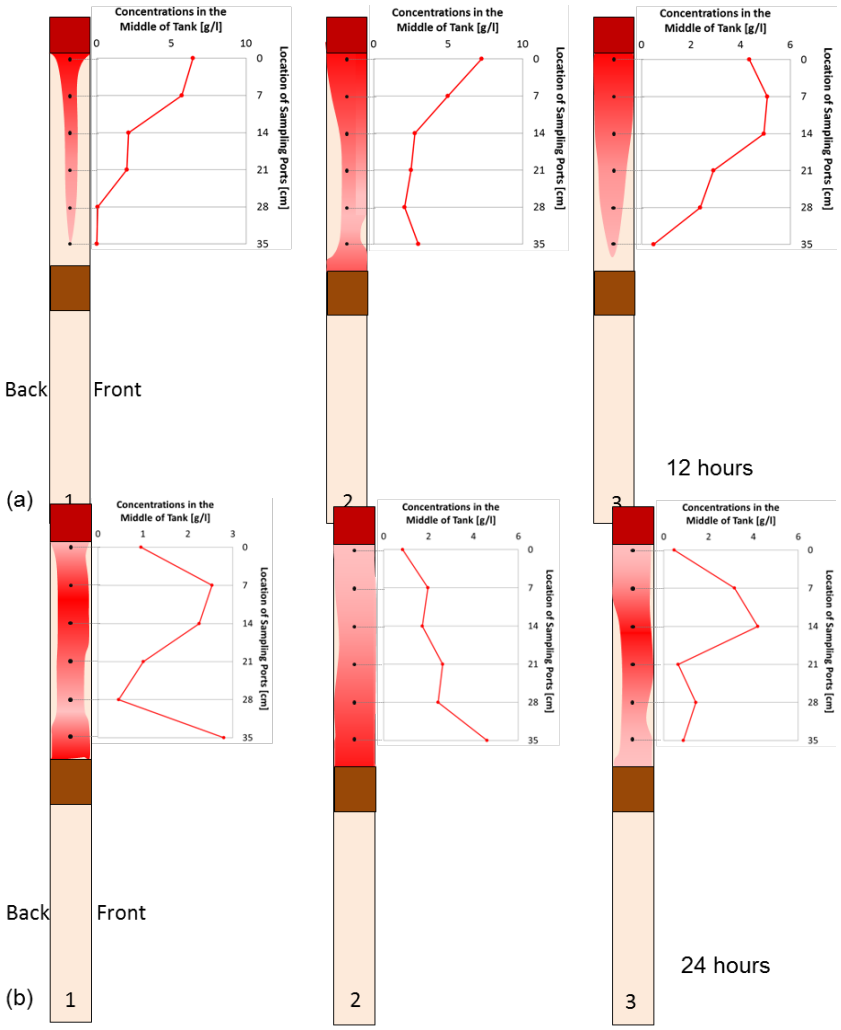

Figure 83 The cross-section from the side wall showing three types of fingering observed in the tank at the location specified in Figure 82 at 12th hour (a), and merging of the fingers at the same locations at 24th hour (b).

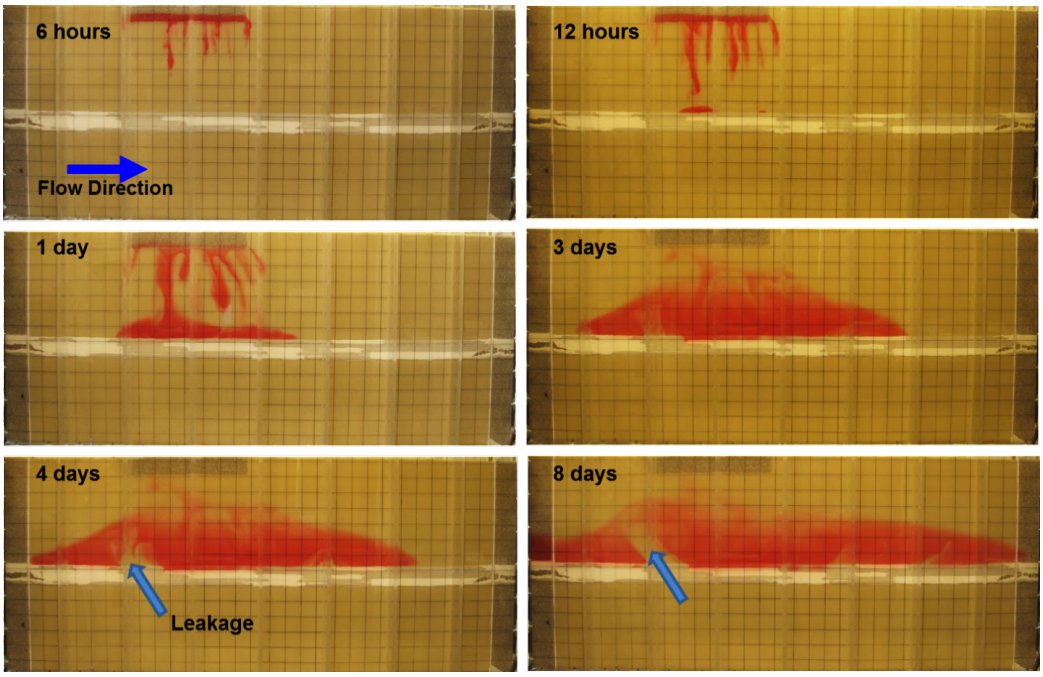

Figure 84 Evolution of the density-driven fingers in the heterogeneous experiment.

The same constant head boundary conditions were applied to both aquifers. However, the slightly higher pressures (1 mm difference) measured in the lower aquifer contributed to leakage of fresh water into the upper one. Under the selected boundary conditions, the fresh water leakage limited the diffusion of dissolved mass into the low-permeability layer at some locations (Figure 84) and prevented the flow of dissolved mass through connected pathways of #110 sand into the lower aquifer. This mechanism that was introduced as reversed convection contributed to the mixing of dissolved mass with fresh water.

Fractures and/or the distribution of the particles might contribute to the leakage through confining layers. In addition, the injection of CO_2 at higher pressures might trigger the leakage of brine. For some of the formations, the water/brine flow created through shale is comparable to that in the sandstone (Neuzil, 1986). For example, in the Frio formation of the Texas Gulf Coast basin, the calculated permeability of the shale fractures are similar with that of the Frio sandstones so that these shale producedflow comparable to the sandstones (Capuano, 1993).

The fresh water leakage observed in this experiment limited the vertical spreading of the dissolved mass through vertical connected pathways of #110 sand whereas it enhanced the lateral spreading, and contributed to the diffusion into silt zones. On the other hand, under the static conditions, the denser mass flowed along the connected #110 sand pathways into the lower

aquifer by replacing with the fresh water as seen in Figure 85, and eventually convective mixing in the second aquifer was observed on 12th day (Figure 85). The higher permeability connected pathways of #110 sand contributed to the fingering at two locations in the lower aquifer. The replacement of dissolved mass in the upper aquifer with fresh water in the lower aquifer triggered the third convective mixing mechanism in the upper layer. These processes enhanced (1) the diffusion area between dissolved mass and silt zones for the storage in silt zones, (2) the contact area between dissolved mass and the host rock for potential mineralization, and (3) the storage of dissolved mass in the deeper parts of the formation.

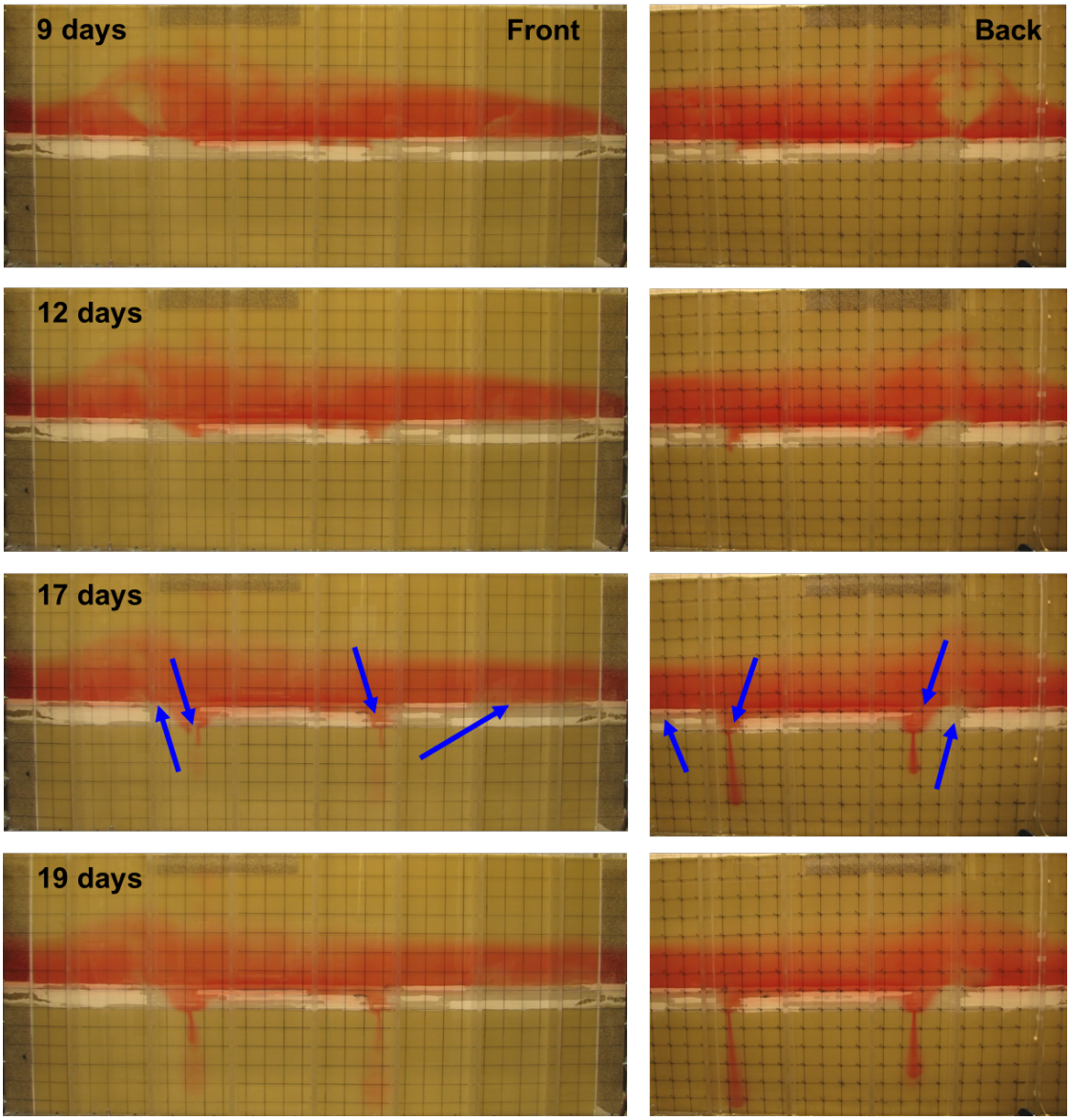

Figure 85 Spreading of dissolved under the static conditions and the onset of convection in the lower aquifer from front and back walls.

The background hydraulic gradients was started again on 19th day in order to flush the mass in the aquifers and estimate the amount stored mass in the silt zones. The higher flow rate was applied to flush away the mass in a shorter time. Following the initiation of the flow, fresh water in the lower aquifer began to leak into the upper aquifer. This fresh water flow through #110 sand reversed the concentration gradient between the silt zones and #110 sand, and led to the back diffusion of more mass from the higher concentration silt zones. In this experiment, due to clogging of the outlet valves in the upper aquifer, the flow rates gradually declined with time as seen in Figure 85b. The increased the pressures in the upper aquifer forced fluid to leak into the lower aquifer through the connected pathways of #110 sand. The flow rate of the lower aquifer increased due to this leakage. During the second background water flow period, the aqueous outflow samples collected from the upper and lower aquifers were used to plot breakthrough curves in Figure 85a and Figure 85c, respectively. The NaBr concentrations in the upper aquifer created a tailing as a result of the back diffusion from the silt zones. The two early peaks in Figure 85c belong to the two fingers generated in this layer. The concentration increase observed after 24th day in Figure 85c was a result of the mass leaked from the upper aquifer. The tailing of the breakthrough curve was caused by the back diffusion from the silt zones. By the end of the 35th day, the amount of dissolved mass stored in the low-permeability layer was calculated as 12.50% (

Figure 88).

In this experimental study, the effects of the vertical higher permeability connected pathways in the low-permeability layer on mixing and trapping of the dissolved CO_2 were investigated. The results of the experiment showed that the heterogeneity of shale layers is very important while investigating the behavior of dissolved CO_2 in the storage formation. The vertical connected pathways changed the flow characteristics of dissolved plume. The cross-flow occurred between the aquifers enhanced mixing by introducing two mechanisms as (1) the fresh water leakage from the lower aquifer which created reversed convection in the upper aquifer and (2) replacement of the denser mass with the fresh water under static conditions which led to the onset of convection in the lower aquifer. These pathways contributed to the storage of dissolved mass both in the deeper aquifers by generating convective fingering and in the silt zones due to

increasing diffusion area. However, in the long-term, these connected pathways enhanced the back diffusion from the silt zones due to increase in concentration gradient along the #110 sand and silt contact. These results have significant implications for understanding the role of shale heterogeneity on flow and long-term storage of the dissolved CO_2. However, this finding was limited to one experiment. Based on this conceptualization of enhanced mixing due to the connetvity, a numerical modeling study was carried out to investigate the mixing and storage of dissolved mass in different distributions of silt and #110 sand with the same material ratios in volume, and the results were compared with the pure silt packing.

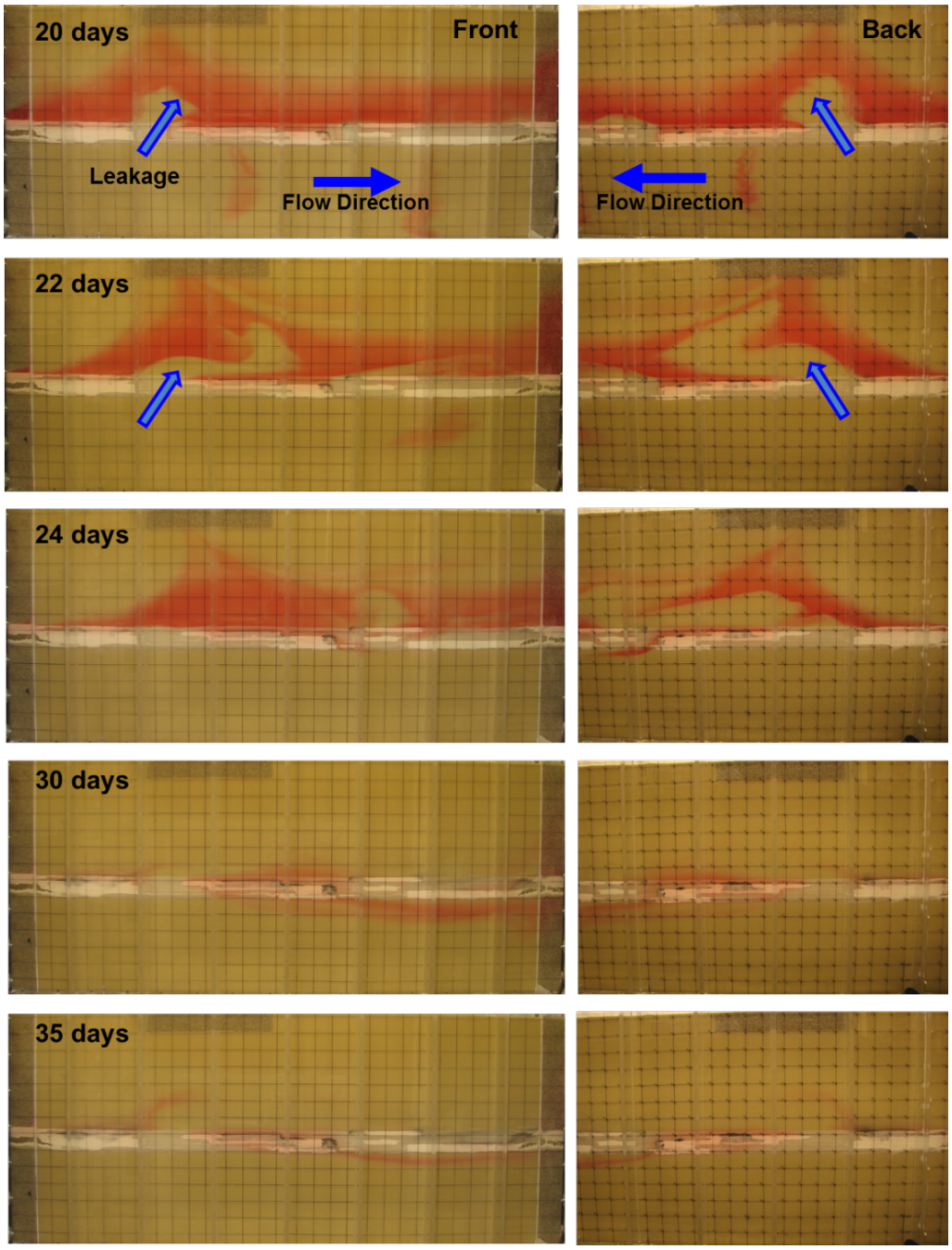
20 days
Front
Leakage
Flow Direction
Back
Flow Direction
22 days
24 days
30 days
35 days

Figure 86 The second background flow initiated on19th day. Flushing of the mass in the aquifers from front and back walls.

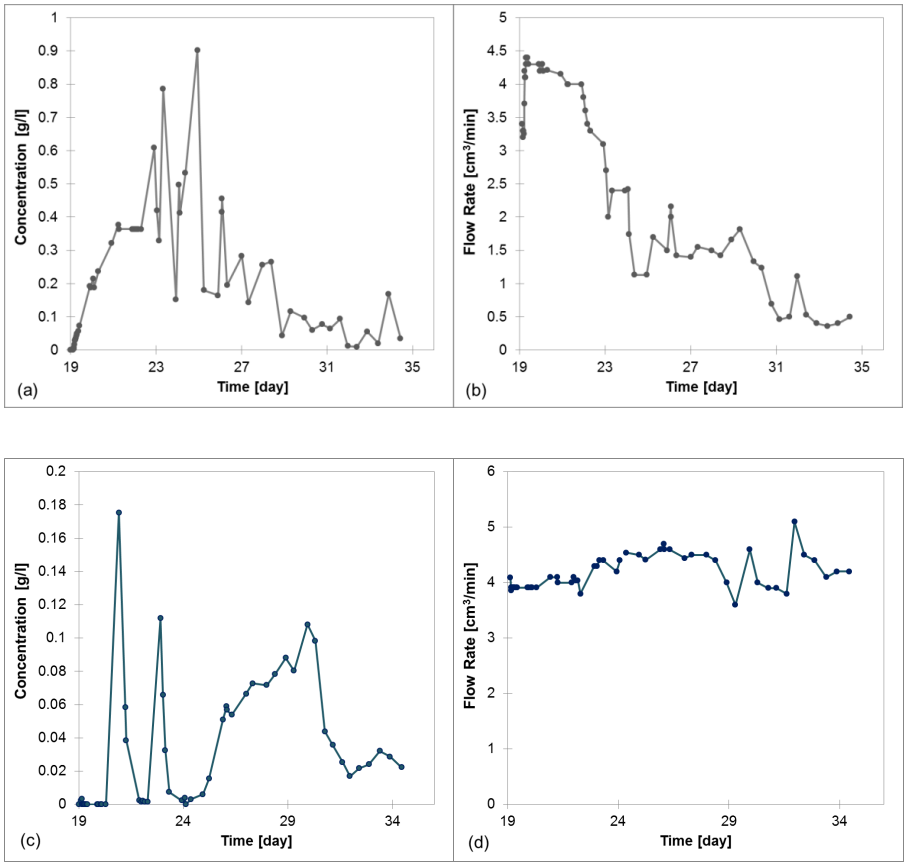

Figure 87 Breakthrough curves and flow rate graphs of (a, b) upper aquifer and (c, d) lower aquifer.

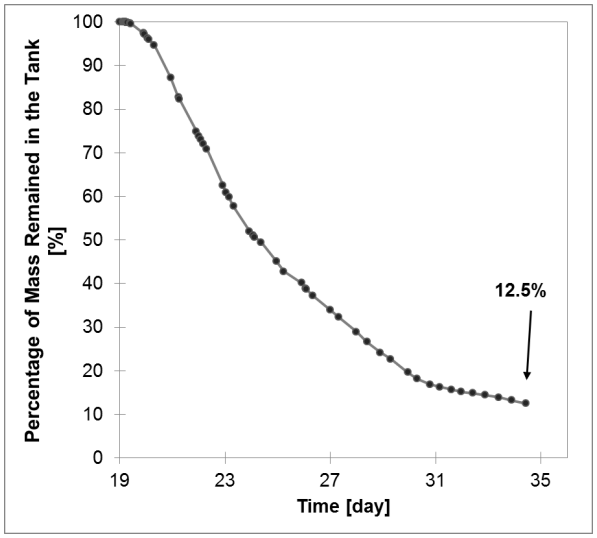

Figure 88 Mass remained in the tank with time.

4.3 Experimental results for constitutive modeling

4.3.1 Leverett Scaling

The average value of the three repeated interfacial tension measurements is summarized in Table 3. Adding Sudan IV to Soltrol did not significantly affect the interfacial tension. The measured interfacial tension was 17.3 with Sudan IV and 16.7 dyne/cm without it. The Leverett scaling factor was calculated to be 0.24 from the interfacial tension values of air-water (73 dyne/cm) and Soltrol-glycerol/water (17.3 dyne/cm). Figure 87 shows the predicted $P_c - S_w$ relationships for the Soltrol-glycerol/water system for each sand size based on Leverett scaling of the air-water system (Equation 2) as well as the original $P_c - S_w$ relationships for the air-water system.

Table 12 Interfacial Tensions of different combination of fluids and the Leverett scaling factors.

Fluid combination	σ [dyne/cm]	Temperature [°C]	$\frac{\sigma}{\sigma_{air/water}}$
Overview of literature [1)]			
Soltrol (without sudan IV)-water	36.4	20.0	0.50
Independently measured by Cenco-DuNoüy tensiometer *			
Air-water	73.0	17.6	1.00
Glycerol/water-Soltrol (without sudanIV)	16.7	17.7	0.23
Glycerol/water –Soltrol	17.3	19.0	0.24

[1)] Schroth et al. (1995), * mean of three measurements, the measured values were almost identical

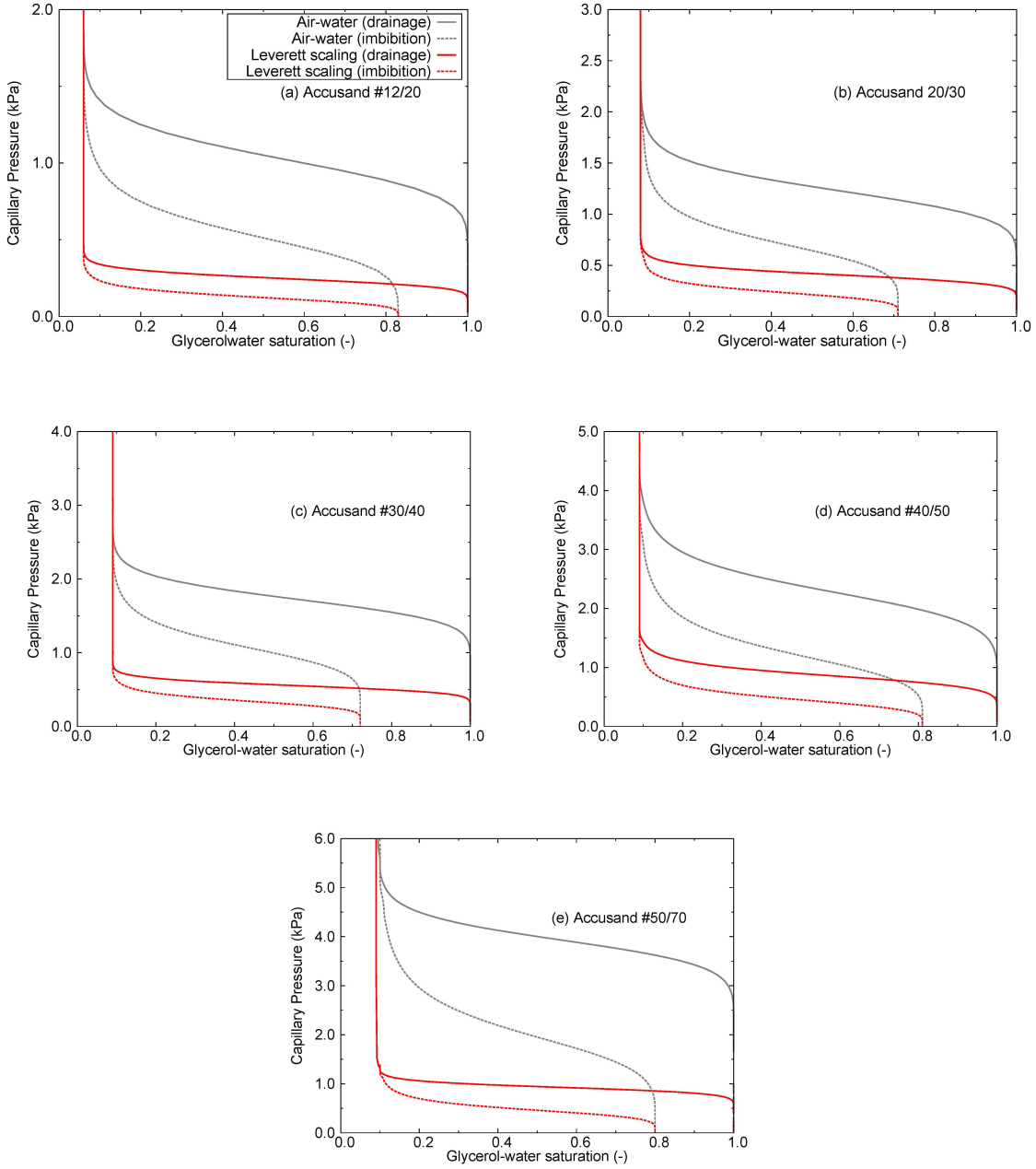

Figure 89 Scaled $P_c - S_w$ relationships for the surrogate fluids in five Accusands using Leverett scaling factor (red). Unscaled reference $P_c - S_w$ relationships for air-water are also shown for comparison. Note that S_i and S_r are assumed to remain unchanged.

4.3.2 Entry Pressure Scaling

Entry pressure heads (h_d) for Soltrol added to sand saturated with the glycerol/water mixture were obtained for each of the test sands. These values are compared to the air-water system pressure heads of Sakaki et al. (2013a) in **Table 4**. The scaling factors obtained for each of the five Accusand samples were in the range of 0.24-0.38. The entry-pressure scaled $P_c - S_w$ relationships for each sand size are plotted in **Figure 6**. Each sand sample had somewhat higher scaling factors using entry-pressure scaling than factors calculated through Leverett scaling, except for the #12/20 and #50/70 sands, which yielded similar values using both scaling methods. The results from the entry pressure method are likely more representative of the actual $P_c - S_w$ relationship than those inferred from Leverett scaling because the entry pressure method includes the effects of contact angle while Leverett scaling does not.

Table 13 Measured entry pressure and entry-pressure scaling factors.

Sand no.	Measured h_d of Soltrol-glycerol/water system (cm of water)			h_d of visual entry at wall (cm of water)	Average h_d of glycerol-Soltrol system (cm of water)	h_d of air-water system (cm of water)*	Scaling factor (-)
	Column 1	Column 2	Column 3				
#12/20	1.9	1.9	1.9	0.8	1.9	7.9	0.24
#20/30	3.9	4.0	4.1	1.9	4.0	12.0	0.33
#30/40	5.2	5.2	5.2	4.4	5.2	16.1	0.32
#40/50	7.3	7.5	7.0	4.8	7.3	19.4	0.38
#50/70	11.1	-	11.1	4.0-4.8	11.1	34.0	0.24

*Values taken from Sakaki et al. (2013a)

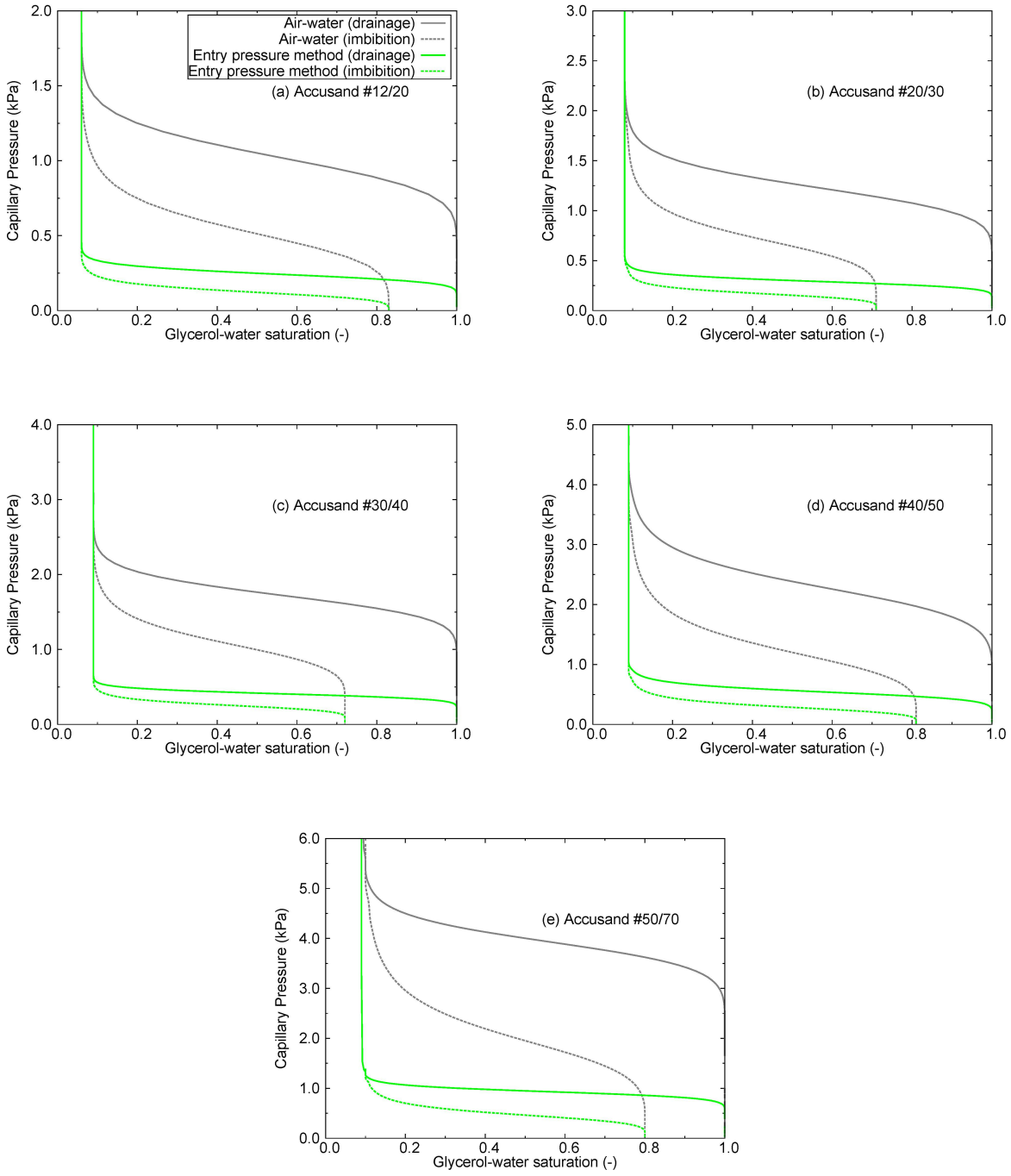

Figure 90 Scaled $P_c - S_w$ relationships for the surrogate fluids in five Accusands using entry pressure scaling (green). Unscaled reference $P_c - S_w$ relationships for air-water are also shown for comparison. Note that S_i and S_r are assumed to remain unchanged.

Visual observations showed that the red-dyed Soltrol started to penetrate the sand pack somewhat before a significant outflow of glycerol/water was observed. When this "visually observed" entry was seen, only small outflow rates of glycerol/water were confirmed. This was then followed by a more distinct outflow (as well as an inflow of Soltrol), after the Soltrol pressure increased. Therefore, the entry pressure values determined based on the significant mass inflow/outflow were larger than those visually determined (values given in columns 4 and 5 of Table 13).

It has to be emphasized here that visual observations of the column wall only show what is happening at the interface of column wall and sand. Unless other methods such as light transmission are used, no information on what is occurring "in" the sand column is obtainable from the images. It is well known that at the column-grain interface, the grains are forced to align along the column wall and the grain pattern is no longer random. This leads to the porosity along the column wall being locally higher (i.e., wall effects). This thin layer along the column wall with a larger porosity (or equivalently larger pore) allows glycerol/water to drain and Soltrol to enter at a lower entry pressure. A similar observation was reported by Culligan et al. (2006). We believe that this is what is seen in the photographs, which led to apparently smaller entry pressure values. Figure 91 shows photographs after Soltrol penetration along the wall was observed. This artifact can be a pitfall if the entry pressure measurement relies only on visual observation. Therefore, it is highly recommended to measure entry pressure based on monitoring outflow mass rather than using visual observation.

Figure 91 Soltrol penetration along the column wall-sand grain interface at pressures below the entry pressure. No penetration was observed in the bulk of the sand even when Soltrol had penetrated along the interface.

4.3.3 Dielectric sensor results

Measured P_c - S_w values for each sand sample were plotted and fitted to the van Genuchten model (Figure 92). The fitted van Genuchten parameters are summarized in Table 5. The S_i and S_r observed in the measurements (also shown in Table 14) with Soltrol-glycerol/water were used to estimate the fitting parameters. Because of the uniform grain size distribution of the test sands used in this study, a rapid change in S_w with a small change in P_c was observed, leading to flat P_c - S_w curves. Although the number of data points for the coarsest #12/20 sand was somewhat limited, measurements were repeated twice for each of the test sands, and the results showed reasonable repeatability. The saturation values measured with the dielectric sensors were unaffected by the wall effect and consequently accurately reflected the actual drainage/wetting behavior in the test sands. The uncertainty in the estimated saturation resulting from the scatter in the calibration data was estimated to be ±0.03~0.07.

Table 14 Van Genuchten model parameters fitted to the Pc – Sw data for the Soltrol-glycerol/water system obtained with the dielectric sensors. Note that Sr and Si are the actual measured values for Soltrol-glycerol/water.

	van Genuchten parameters	van Genuchten parameters

				(drainage)		**(imbibition)**	
Sand no.	Measured S_r (-)	Measured S_i (-)	Soltrol Entry pressure in water head (cm)	α (1/cm)	n (-)	α (1/cm)	n (-)
#12/20	0.857	0.104	1.9	0.29	20.24	0.85	15.54
#20/30	0.734	0.056	4.0	0.29	6.61	2.03	2.45
#30/40	0.739	0.076	5.2	0.21	6.56	0.60	4.59
#40/50	0.836	0.040	7.3	0.17	4.47	0.36	3.50
#50/70	0.703	0.088	8.0	0.10	5.05	0.54	3.03

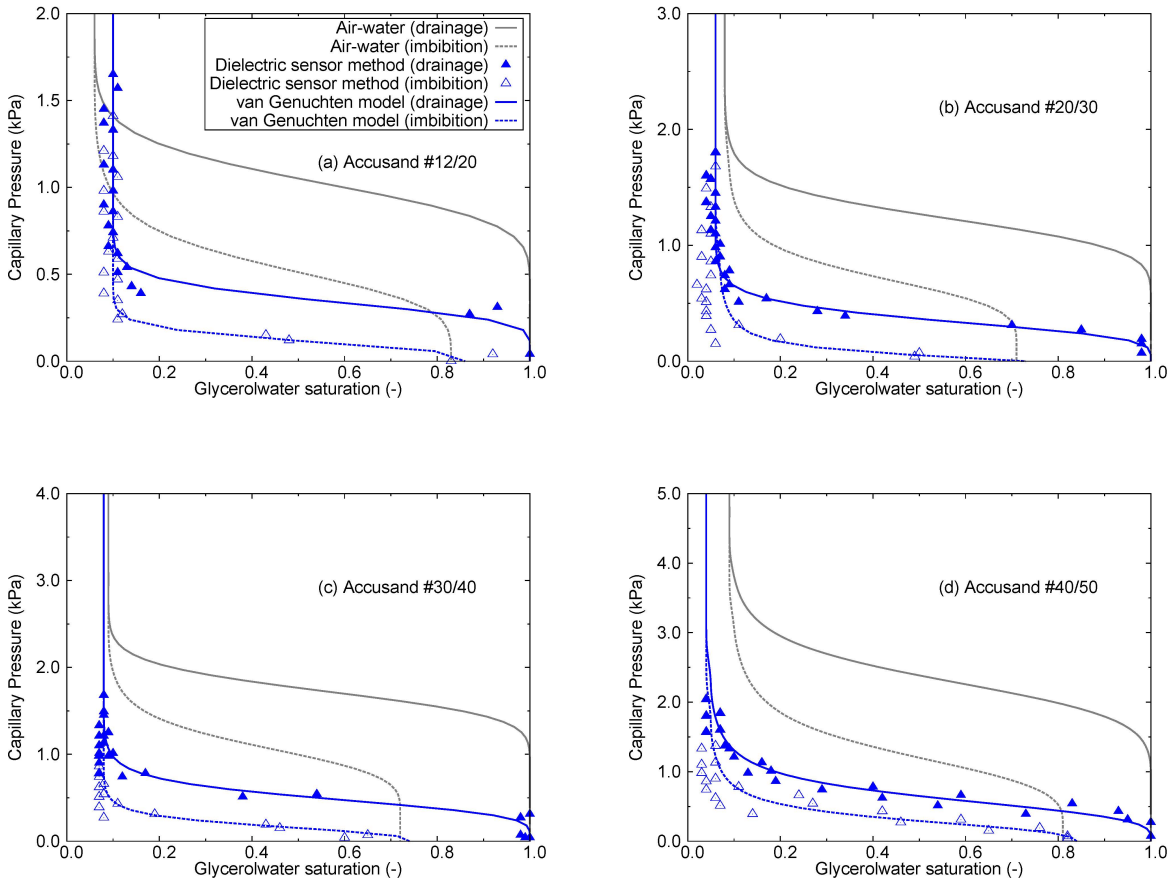

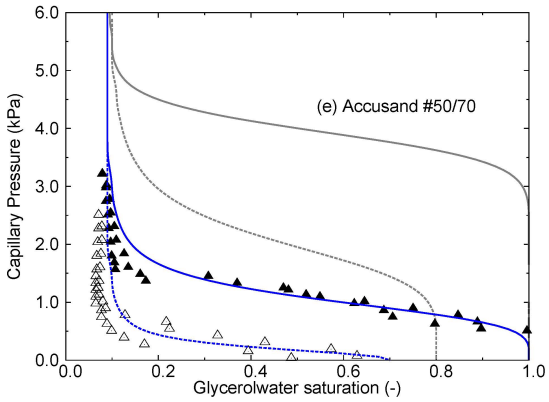

Figure 92 Measured $P_c - S_w$ relationships for the surrogate fluids in five Accusands using dielectric sensor method (open and closed triangles). Unscaled reference $P_c - S_w$ relationships for air-water are shown for comparison. Also shown in blue are the best-fit van Genuchten models.

4.3.4 Comparison of the Three Methods

Although Leverett scaling is the easiest method of the three tested here, higher capillary pressures were calculated using Leverett scaling than with entry pressure scaling or the dielectric sensor method, both of which rely more on physical data than Leverett scaling (Significant differences in entry pressure did not result in large changes in interfacial tension (Table 15). Tokunaga et al. (2013) measured $scCO_2$ – brine interfacial tensions under two different pressures and showed that Leverett scaling was insufficient to scale the capillary pressure for different reservoir conditions.

Table 15 Comparison of fluid dependent systems.

	#40/50	#50/70	Tokunaga et al. (2013) at 8.5 MPa	Tokunaga et al. (2013) at 12.0 MPa
Grain size (mm)	0.360[1)]	0.270[2)]	0.250-0.355	0.250-0.355
Porosity (-)	0.34[1)]	0.34[2)]	0.381	0.381
μ_{nw}/μ_w (-)	0.064	0.064	0.033[3)]	0.075[3)]
ρ_{nw}/ρ_w (-)	0.65	0.65	0.27	0.636
σ (dyne/cm)	17.3	17.3	33.1	30.1
Capillary	$10^{-6} - 10^{-7}$	$10^{-6} - 10^{-7}$	$10^{-8} - 10^{-9}$	$10^{-8} - 10^{-9}$

Number (-)				
Bond Number (-)	$10^{-5} – 10^{-6}$	$10^{-5} – 10^{-6}$	10^{-5}	10^{-5}
Entry pressure (kPa)	0.712*	0.787*	0.8**	0.5**
S_i	0.040	0.088	0.04-0.05	0.03-0.05
S_r	0.812	0.703	0.92-0.93	0.66-0.81

[1)]Sakaki et al. (2013a), [2)] measured as part of this study, [3)] El-Dessouky and Ettouney (2002), *surrogate fluids, **$scCO_2$-brine, Tokunaga et al. (2013) sieved 40-60 mesh Unimin round quartz sand to obtain the grain size range listed above. Their sand hydraulic conductivity was 3.9×10^{-4} m/s.

All three methods captured the hysteretic behavior well. In most of the sands, the scaling methods resulted in higher calculated capillary pressures during imbibition than were calculated using the dielectric sensor method. This is consistent with the $P_c – S_w$ relationship measured for $scCO_2$ and brine under high pressure by Tokunaga et al. (2013). This suggests that the scaling factors may need to be determined separately for drainage and imbibition cycles; this is perhaps because the interfacial tensions are different at advancing and retreating fronts.

For some of the test sands, S_r was poorly defined due to the shape of the $P_c – S_w$ data; in those cases, we carefully selected S_r by choosing a value where the capillary pressure is slightly below zero. However, there were distinct differences in both S_i and S_r compared with those for the air-water system (Table 16). These differences between the air-water and glycerol/water values highlight the advantage of using the dielectric sensor method over the scaling methods. There was no clear trend in the differences among S_i and S_r with respect to the different sands.

Table 16 Comparison of S_i and S_r values between air-water and Soltrol-glycerol/water systems

Sand no.		air-water[1)]	Soltrol-glycerol/water
#12/20	S_i	0.055	0.104
	S_r	0.827	0.857
#20/30	S_i	0.082	0.056
	S_r	0.712	0.734

#30/40	S_i	0.085	0.076
	S_r	0.725	0.739
#40/50	S_i	0.085	0.040
	S_r	0.812	0.836
#50/70	S_i	0.093	0.088
	S_r	0.703	0.703

[1)] Values taken from Sakaki et al. (2013a)

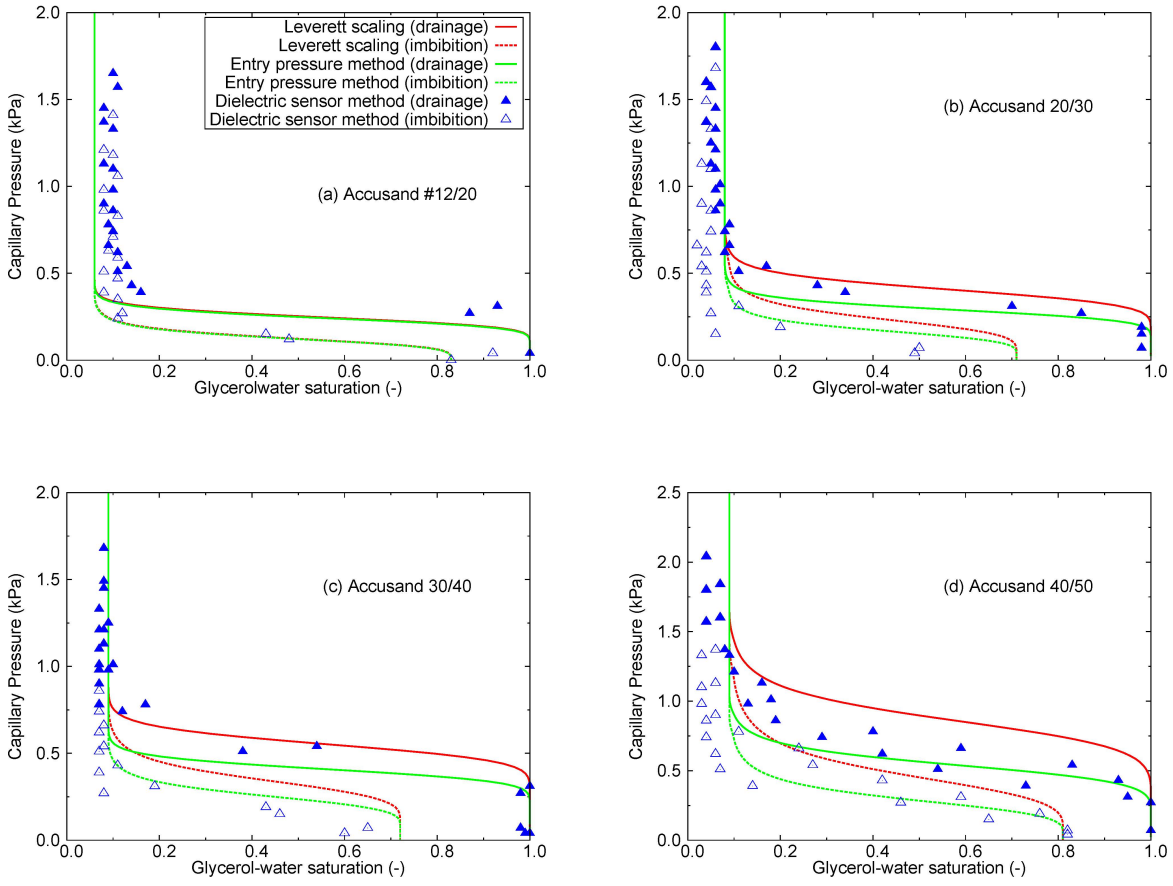

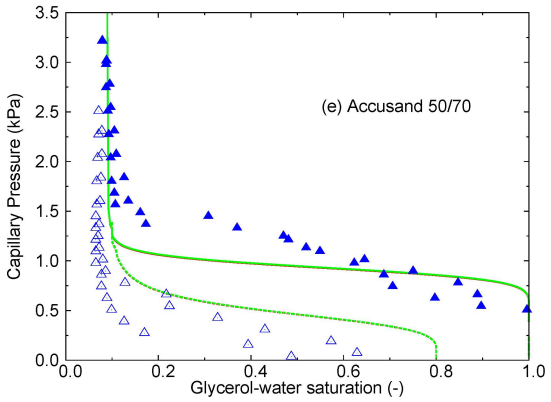

Figure 93 Comparison of $P_c - S_w$ curves for the surrogate fluid pair obtained using the Leverett scaling method, the entry pressure scaling method, and the dielectric sensor method.

4.3.5 Comparison with $scCO_2$/brine data

Although Tokunaga et al. (2013) measured $scCO_2$-brine capillary pressure in unconsolidated sand under two different high pressure/temperature test conditions, there were some similarities between the observed $P_c - S_w$ curves for the #40/50 and #50/70 Accusands used in this study and the $P_c - S_w$ curves for Tokunaga et al. (2013). .Low S_i values were observed in both $scCO_2$-brine and Soltrol-glycerol/water, the Soltrol-glycerol/water fluid properties were relatively close to those in the Tokunaga et al. (2013) measurements at 12 MPa (Table 16), and the S_i and S_r values for Accusand #40/50 were similar to those in their 12 MPa system. However, the entry pressure in their 12 MPa was distinctly different from our results, and this could be explained from the wettability changes with exposure time because high wettability lowers the entry pressure value.

Nonetheless, the surrogate fluids and actual $scCO_2$ and brine displayed qualitatively similar capillary pressure behavior and reasonable quantitative agreement with allowances for differences in the sand properties. This similarity in $P_c - S_w$ behavior between the surrogate fluids and $scCO_2$/brine demonstrates that surrogate fluids are applicable to studies of $scCO_2$/brine system behavior.

4.3.6 Verification of the relative permeability of surrogate fluids

In section 2.1, we showed that 50 % glycerol can be used to measure the relative permeability instead of using 80 % glycerol to expedite the experiment. To verify this assumption, the relative permeabilities for both glycerol/water mixtures were measured for Accusand #30/40. There were no distinct differences observed between the relative permeabilities of 80 % and 50 % glycerol. Therefore, it is valid to use the modified surrogate fluids to measure the relative permeability and the argument that was made for the relative permeability measurements to replace the less viscous wetting fluid was reasonable. Once this assumption was verified, the hydrostatic experiment was conducted only with 50 % glycerol.

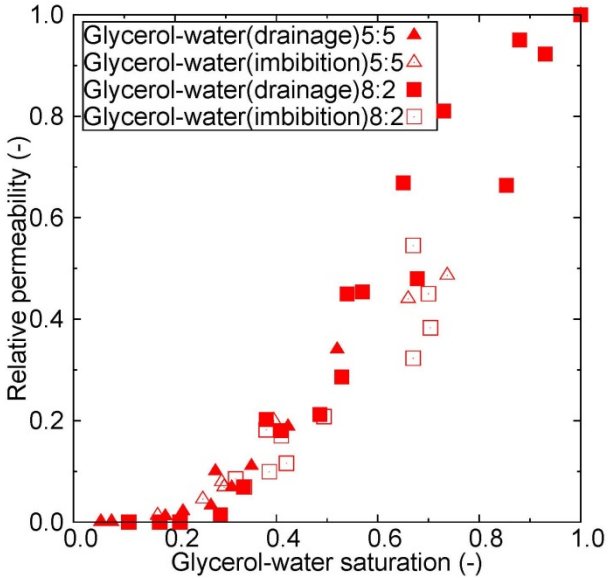

Figure 94 Comparison between the wetting phase relative permeability of 80 % and 50 % glycerol for Accusand #30/40.

4.3.7 Comparison of experimentally and derived relative permeability

0 presents the relative permeability derived using the van Genuchten – Mualem model from capillary pressure – saturation measurements and the directly measured relative permeability data for Accusand #30/40. The van Genuchten – Mualem model used the van Genuchten parameters given earlier. No noticeable hysteresis was observed in either the wetting or non-wetting phase relative permeability when comparing the drainage and imbibition data as suggested by Corey (1994). The measured relative permeability values differed greatly from those derived using the van Genuchten – Mualem model. The difference between van Genuchten

derived permeability values and the measured values was greatest for the non-wetting phase. This difference suggests that for the sand test, the van Genuchten – Mualem model is not suitable. This result is not completely unexpected because the van Genuchten – Mualem model was originally developed for agricultural field soils, not for uniform pore-size sand grains such as the ones used in this study (Irmary, 1954; Hausenberg and Zaslavsky, 1963; Ruan and Illangasekare, 1999).

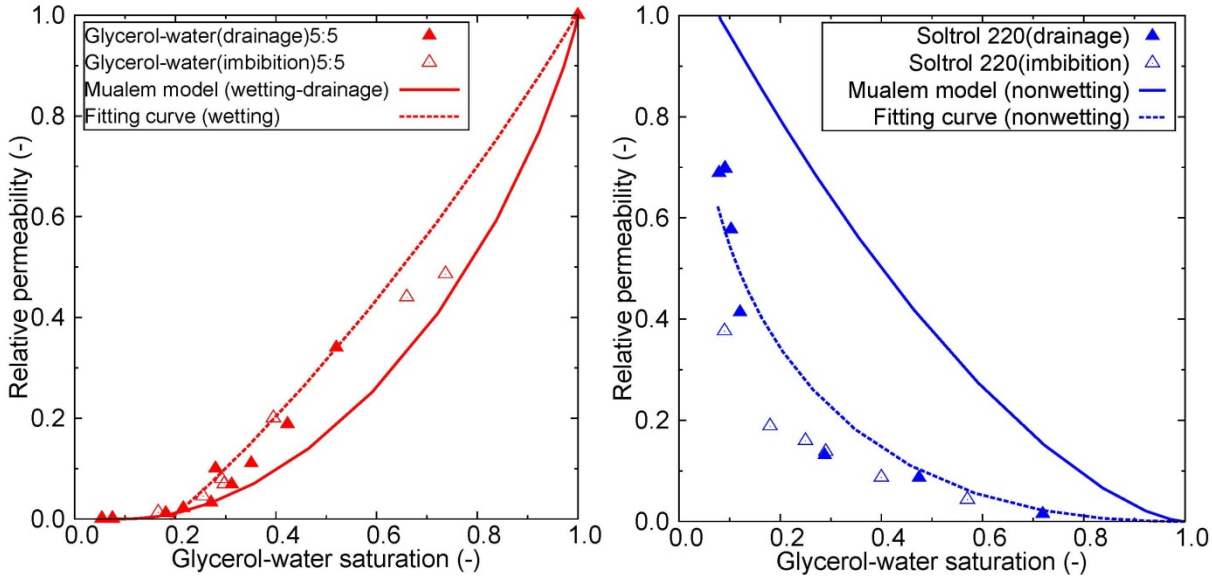

Figure 95 Comparison between experimental data and the constitutive model (van Genuchten – Mualem model) of k_r – S_w relationships. Left: Drainage and imbibition process of relative permeability experimental data for glycerol/water 50 wt%. Right: Drainage and imbibition process of relative permeability experiments data for Soltrol.

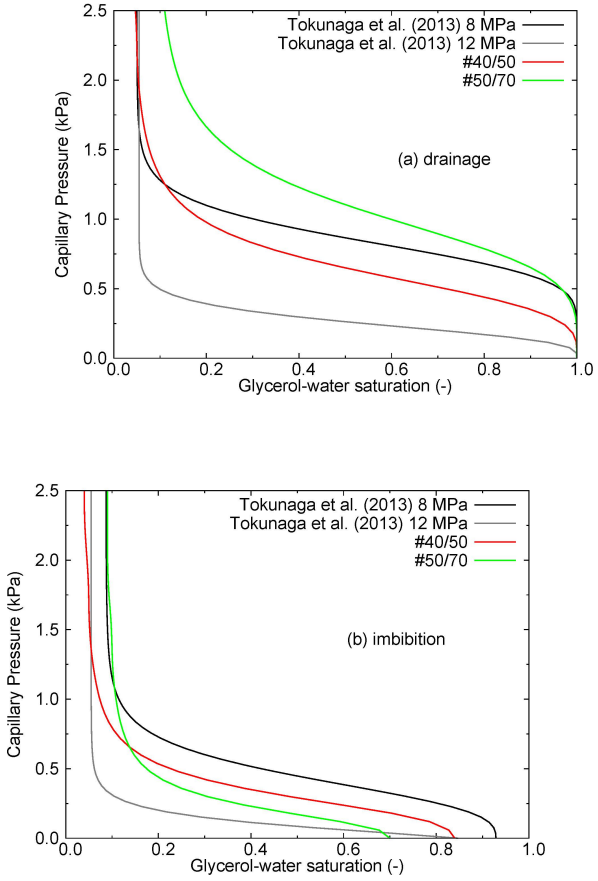

Figure 94: Comparison of $P_c - S_w$ relationships by Tokunaga et al. (2013) with those for Accusand #40/50 and #50/70; (a) drainage cycle, and (b) imbibition cycle.

4.4 Constitutive Model Development for Hysteretic Two-Phase Flow Parameters

During CO_2 injection and storage in deep reservoirs, the injected CO_2 enters into an initially brine saturated porous medium, and after the injection stops, natural groundwater flow eventually displaces the injected mobile-phase CO_2, leaving behind residual non-wetting fluid. In such applications, primary drainage and subsequent wetting behaviour are critical for securing safe storage through entrapment of injected mobile phase CO_2. During the primary drainage process, the maximum injected-phase fluid saturation may vary spatially, and the entrapped non-wetting fluid saturation at the end of imbibition (main wetting) is typically a function of the maximum saturation at the end of injection. Hysteretic constitutive relationships among macroscopic variables (such as capillary pressure, saturation and relative permeability functions) are needed for traditional two-phase flow models predicting spatial and temporal distribution of fluids in porous media.

In a two-phase system, as drainage occurs, pores or voids with wetting fluid can drain when the non-wetting fluid entry pressure is lower than the local capillary pressure, with the largest voids typically draining first. However, not all of these voids drain because of poor pore connectivity or due to blockage from surrounding smaller sized voids. As a result, the wetting fluid in some portion of these voids becomes trapped. During imbibition, smaller voids tend to fill first with the wetting phase (invaded fluid) as the capillary pressure decreases, but the wetting phase may never imbibe into all voids of a given size as a result of entrapment of the non-wetting phase. These fundamental differences in pore-scale processes result in macroscopic hysteretic relationship among capillary pressure, saturation and relative permeability (Haines, 1930; Miller and Miller, 1956). In addition to contact angle hysteresis, distribution and connectivity of void space controls the macroscopic hysteresis behavior and capillary entrapment of wetting and non-wetting fluids in porous media

Both empirical (e.g., Scott et al., 1983) and non-empirical approaches (e.g., Topp and Miller, 1966; Poulovassilis and Childs, 1971; Mualem, 1974) have been developed to mathematically describe the hysteresis phenomenon during multiphase flow in porous media. As shown by several experimental studies (e.g., Pentland et al., 2010), under capillary-dominated flow conditions, the entrapped or residual saturation of a fluid phase is a function of its maximum saturation at the end of the flow reversal (changing from drainage to wetting or vice versa). However, this dependence is often ignored in constitutive relationships; either the residual fluid saturations are assumed to be constant or simple empirical relationships are employed to estimate the residual fluid saturations (Land, 1968).

We developed an approach for mathematical representation of macroscopic hysteretic capillary-pressure saturation relationships with capillary entrapment (Cihan et al., 2014a). The model presented in (Cihan et al., 2014a) requires knowledge of a void-volume distribution function and two connectivity functions characterizing distinct paths of fluids during drainage and wetting. Based on the same connectivity-based approach, we also developed new models for hysteretic relative permeability functions (Cihan et al., 2014b). It is demonstrated through invasion percolation simulations for 3D computer-constructed porous media and measured data sets that this new approach is promising to successfully represent macroscopic hysteresis behavior observed during successively occurring drainage and imbibition processes. The developed hysteretic constitutive models have been incorporated into a numerical two-phase flow simulator (TPFLOW_HYST), and in section 6.2.4, the numerical model results are compared against the small tank experimental results to show the ability of the model and constitutive models to predict motion and capillary trapping of two immiscible fluids in macroscopically homogeneous and heterogeneous porous media.

5.4.1. Model for hysteretic saturation- capillary pressure relationship

The fundamental supposition behind the following model development is that the drainage and imbibition paths of the fluids are independent from each other and that the connectivity of different sized voids in space controls the displacement processes at the macroscopic scale in any stage of the drainage and wetting processes. The cumulative connectivity function for drainage, $\mathbf{P}^d$, and the cumulative connectivity function for wetting, $\mathbf{P}^w$, are introduced as to be characteristic properties of the porous medium and fluid phases, which represent quantitative measure of how the fluids are distributed in connected void space during drainage and imbibition. The drainage connectivity function characterizes connection of void space starting from larger voids toward the smaller voids where the non-wetting fluid invades through as the capillary pressure increases. The wetting connectivity function characterizes connection of void space starting from smaller voids toward the larger voids where the wetting phase invades through as the capillary pressure decreases. Considering a continuous void emptying/filling process and assuming a continuous void volume fraction distribution $f(r)$ as a function of void size r, the primary drainage curve for saturation-capillary pressure (S_w-P_c) relation is given by:

$$S_w(P_c) = 1 - \int_{r(P_c)}^{r_{\max}} \mathbf{P}^d(x, P_c) f(x) dx \tag{21}$$

Based on the assumption of independence of drainage and imbibition paths of the fluids, a S_w-P_c function representing a wetting process following a drainage event can be represented by:

$$S_w(P_c) = S_w(P_{c,\mathrm{d}}) + \int_{r(P_{c,d})}^{r(P_c)} \mathbf{P}^d(x, P_{c,d}) \mathbf{P}^w(x, P_c) f(x) dx \tag{22}$$

Likewise, for any order of drainage following an imbibition event, saturation can be expressed as

$$S_w(P_c) = S_w(P_{c,\mathrm{w}}) - \int_{r(P_c)}^{r(P_{c,w})} \mathbf{P}^d(x, P_c) \mathbf{P}^w(x, P_{c,w}) f(x) dx \tag{23}$$

During drainage and imbibition, the voids with sizes between $r(P_c)$- $r(P_{c,w})$ or $r(P_{c,d})$- $r(P_c)$ can be invaded as a function of P_c. $r(P_c)$ may differ for drainage and wetting as a result of changing contact angle from drainage to wetting and vice versa. The Young-Laplace equation can be used to obtain the relationship between $r(P_c)$ and P_c as $r \propto 1/P_c$ by scaling with the minimum entry pressures ($P_{d\min}, P_{w\min}$). Assuming the voids have similar shapes, we can express $r(P_c) = r_{\max} P_{d\min} / P_c$ for drainage and $r(P_c) = r_{\max} P_{w\min} / P_c$ for wetting. $r(P_{c,w})$ and $r(P_{c,d})$ are the last values during wetting and drainage, respectively, before a flow reversal (drainage or wetting) occurs.

The connectivity functions $\mathbf{P}^d$ and $\mathbf{P}^w$ can be estimated from pore-scale simulations, or measured primary drainage and main wetting curves can be used to inversely estimate $\mathbf{P}^d$ and $\mathbf{P}^w$. Cihan et al.

(2014a) computed $\mathbf{P}^d$ and $\mathbf{P}^w$ for multiple realizations of computer-generated porous media with bimodal lognormal and lognormal void-volume fraction distribution using the invasion percolation algorithm, and proposed that the following nonlinear Gaussian cumulative functions could represent the cumulative connectivity functions reasonably well:

$$\mathbf{P^d}\left(r,P_c\right)=a_d\,0.25\left[1+\mathrm{erf}\left(\frac{P_c-b_d}{\sqrt{2}\,c_d}\right)\right]\left[1+\mathrm{erf}\left(\frac{r/r_{\max}-d_d}{\sqrt{2}\,e_d}\right)\right]\Phi\left[P_c-P_d\left(r\right)\right] \qquad \textbf{(24)}$$

where Φ [ ] is the unit step function, and

$$\mathbf{P^w}\left(r,P_c\right)=a_w\,0.25\left[1-\mathrm{erf}\left(\frac{P_c-b_w}{\sqrt{2}\,c_w}\right)\right]\left[1-\mathrm{erf}\left(\frac{r/r_{\max}-d_w}{\sqrt{2}\,e_w}\right)\right]\Phi\left[-P_c+P_w\left(r\right)\right] \qquad (25)$$

where a,b,c,d,e are constants with subscripts (*d, w*) for drainage and wetting. P_d(r) and P_w(r) represent the entry capillary pressures for invasion of fluids into voids during drainage and imbibition (or wetting), respectively. The estimated cumulative connectivity functions from one realization of the Berea sandstone example are presented in Figure 96 as contour maps. The horizontal axis is the void size normalized by maximum void size, and the vertical axis represents the capillary pressure. In Figure 96a, at lower values of the capillary pressure where large voids might drain, $\mathbf{P}^d$ values approach zero indicating that there are no or very few large voids connected to the inlet of the injected fluid, while at very high capillary pressures, there are no or very few connected small voids that could drain (because they include trapped wetting fluid separated from the cluster of the displaced fluid connected to the outlet). For the wetting process shown in Figure 96b, the $\mathbf{P}^w$ values approach zero at large voids that entrap most of the non-wetting fluid, while the probability goes to 1 for very small voids that can become wet first if they are connected to the inlet of the displacing fluid. Note that these results are based on the assumption that both invading fluid and displaced fluid are incompressible. Without the entrapment (e.g., for displacement of compressible fluids), $\mathbf{P}^d$ and $\mathbf{P}^w$ functions approach 1 as the volumetric content of invading fluid (wetting or nonwetting) becomes equal to or greater than the percolation threshold value of the porous domain.

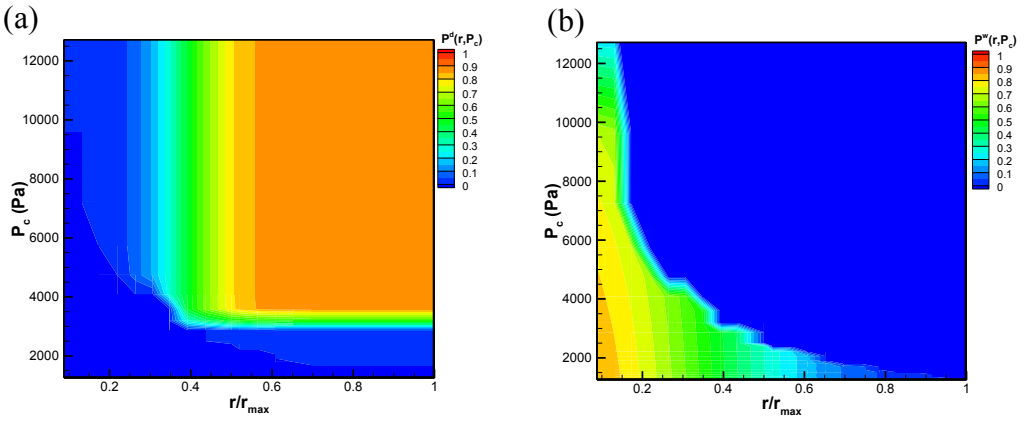

Figure 96: The cumulative connectivity functions for (a) drainage and (b) wetting for one realization of the synthetic 3D porous medium with Berea sandstone void-size distribution. The horizontal axis represents void size (non-dimensionalized by maximum void size), and the vertical axis represents capillary pressure. Estimated parameter values for drainage equal to *a*=0.88, *b*=3143.78, *c*=165.57, *d*=0.39 and *e*=0.08, and for wetting equal to *a*=1.0, *b*=17279.20, *c*=9797.76, *d*=0.38, *e*=0.24. (Adapted from Cihan et al., 2014a)

5.4.2. Model for hysteretic relative permeability functions

The mathematical models of drainage and wetting connectivity functions presented above and in Sections 2.1 and 2.2 of Cihan et al. (2014a) constitute a framework for representing the hysteretic relationships for relative permeability functions for a porous medium involving displacement of two fluid phases at any stage of drainage and imbibition. Following an approach similar to Marshall (1958) (note that similar approach later was adapted by Cihan et al., 2009, and Mualem, 1976), two surfaces from a cross-sectional cut through a random porous medium are re-joined randomly (Figure 97a). The surfaces are connected through pore necks, and the permeability is proportional to an average value of the intersection areas between pairs of contacting voids and inversely proportional to the tortuosity, assuming the validity of Poiseuille's equation for flow through pore channels and analogously the validity of the Darcy's law at a macroscopic scale of the porous medium. We also further assume that distribution of void areal fractions in a cross-section is equivalent the distribution of void volume fractions based on the results obtained by Cihan et al. (2009) in a random isotropic porous medium. As a result of the fully random matching approach, the probability of having fluid-conducting voids with sizes between r and $r+dr$ can be expressed as $\sim f(r)\mathrm{d}r\ f(r')\mathrm{d}r'$, and the intrinsic permeability, k, is proportional to : $(\int_{r_{min}}^{r_{max}} f(x)xdx)^2$. In this work, we extend this approach to represent relative permeability under two-phase flow conditions, where the intersected void areas at a cross-section are filled with different fluids.

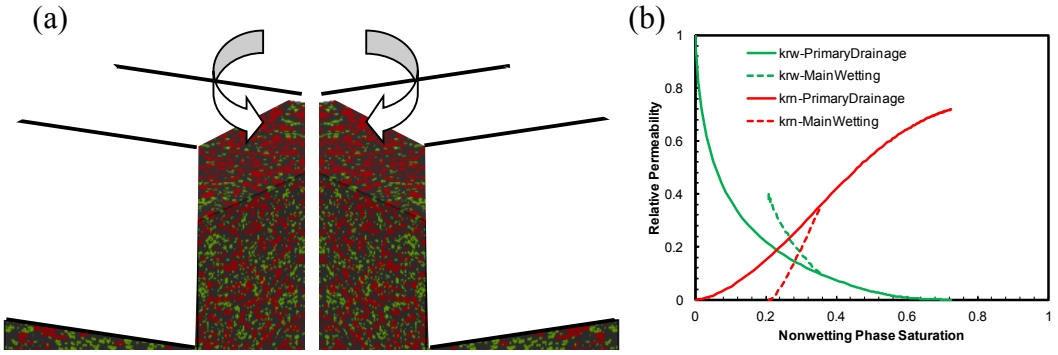

Figure 97: (a) Matching of two random porous surfaces based on Marshall (1958) probabilistic approach for modeling relative permeability functions in a random porous medium. Red color represents the non-wetting fluid, green represents the wetting fluid, and dark grey represents the solid phase (adapted from Cihan et al., 2014a); (b) Demonstration of the relative permeability models generated by equations (5.4.6-8) for an arbitrarily chosen material experiencing primary drainage and main wetting processes.

Considering the primary drainage process, probability of having non-wetting fluid-filled voids with sizes between r and $r+dr$ can be expressed as $\sim \mathbf{P}^d(r,P_c)f(r)\mathrm{d}r\,\mathbf{P}^d(r',P_c)f(r')\mathrm{d}r'$, and then permeability of the non-wetting fluid at a capillary pressure P_c, k_{nw}, is proportional to : $(\int_{r(P_c)}^{r_{\max}}\mathbf{P}^{\mathbf{d}}(x,P_c)f(x)xdx)^2\Phi[S_n-S_c]$, where S_c is the percolation threshold of the porous medium. $\Phi[S_n-S_c]$ indicates that the nonwetting fluid will have nonzero permeability in a direction only if it percolates in that direction from one end to the other end of the domain. Likewise, permeability of the wetting fluid at a capillary pressure P_c, k_w, can be expressed to be proportional to : $(\int_{r_{\min}}^{r(P_c)}[1-\mathbf{P}^{\mathbf{d}}(x,P_c)]f(x)xdx)^2\Phi[S_w-S_c]$. Note that wetting film flow is neglected in this formulation. The modeling approach here can be generalized to representation of relative permeability functions for any successive drainage and imbibition processes. The hysteretic relative permeability ($k_{rw}=k_w/k$, $k_{rn}=k_n/k$) functions for non-wetting and wetting fluids can be expressed as

$$k_{rn}(P_c)=\tau_{rn}\frac{\left(\int_{r(P_c)}^{r_{\max}}g_n(x,P_{c1},\mathrm{K}\ ,P_{cn},P_c)f(x)xdx\right)^2}{\left(\int_{r_{\min}}^{r_{\max}}f(x)xdx\right)^2}\Phi[S_n-S_c] \qquad \textbf{(26)}$$

$$k_{rw}\left(P_c\right)=\tau_{rw}\frac{\left\{\int_{r_{\min}}^{r(P_c)}\left[1-g_n\left(x,P_{c1},\mathrm{K}\ ,P_{cn},P_c\right)\right]f(x)xdx\right\}^2}{\left(\int_{r_{\min}}^{r_{\max}}f(x)xdx\right)^2}\Phi\left[S_w-S_c\right] \tag{27}$$

where g_n function represents the areal fraction of voids filled with non-wetting fluid after the nth flow reversal from drainage to imbibition or vice versa. The sub index n indicates the number of flow reversals and whether imbibition or drainage is occurring, with odd numbers for imbibition events and even numbers for drainage events. A generalized formulation for g function is given by

$$\begin{aligned}
&g_0\left(x,P_c\right)=\mathbf{P}^d\left(x,P_c\right)\\
&g_1\left(x,P_{c1},P_c\right)=g_0\left(x,P_c\right)-\mathbf{P}^d\left(x,P_{c1}\right)\mathbf{P}^w\left(x,P_c\right)\\
&g_2\left(x,P_{c1},P_{c2},P_c\right)=g_1\left(x,P_{c1},P_{c2}\right)+\mathbf{P}^d\left(x,P_c\right)\mathbf{P}^w\left(x,P_{c2}\right)\\
&g_3\left(x,P_{c1},P_{c2},P_{c3},P_c\right)=g_2\left(x,P_{c1},P_{c2}\right)-\mathbf{P}^d\left(x,P_{c3}\right)\mathbf{P}^w\left(x,P_c\right)\\
&\mathrm{M}
\end{aligned} \tag{28}$$

1. τ_{rw} and τ_{rw} are relative tortuosity factors for wetting and nonwetting fluid phases, respectively, and they are represented by:

$$\tau_{rn}=\left[\frac{S_n-S_c}{1-S_c}\right]^{\beta_n},\quad \tau_{rw}=\left[\frac{S_w-S_c}{1-S_c}\right]^{\beta_w} \tag{29}$$

where the percolation-theory based value for the exponents β is approximately equal to 0.38 for idealized porous media (Ghanbarian et al., 2013). Although this can be a good representative for the nonwetting phase relative permeability, as it will be shown later, the value for the wetting phase relative permeability in sandstone cores may be quite different from 0.38.

Equations (21-23) and (26-28) require numerical integrations. A FORTRAN code was developed for computations of the developed constitutive models. Figure 97b presents an example demonstration of the relative permeability models generated for an arbitrarily chosen material property. The model requires storing of the capillary pressure values at all flow reversal points. Testing of the new saturation-capillary pressure- relative permeability is shown partially in the next section with comparisons against laboratory experiment results at core-scale. A more comphrensive testing for dynamic flow conditions will be shown in section 5.2.4

5.4.3. Testing the hysteretic constitutive models with core-scale experimental results

Figure 98 presents a prediction of the residual non-wetting fluid as a function of varying initial non-wetting saturation using the model in Equations (21-23). The cumulative connectivity functions for drainage and wetting were estimated from computer-generated percolation models in Cihan et al. (2014a) and Raeesi and Piri (2009). The figure also shows a comparison with experimental results using different fluid pairs, the data taken from Krevor et al. (2012). The model using both computer-generated data appears to overlap with decane/water (Pentland et al., 2011) and CO_2/water (Krevor et al., 2012) experiments in Berea sandstone cores, while the other data sets fall lower. The model was also tested in comparison with two laboratory column experiments packed with two natural sand samples from (Poulovassilis, 1970). Figure 99 presents an example application of the model to predict the scanning curves in one of the sand samples. For both sand samples, lognormal distribution of void volume fractions was assumed and the model (Eqs. 21-22) was fitted to the primary drainage and main wetting data only (shown by filled circles and solid lines in Figure 99) for estimating parameters of the lognormal distribution and the drainage and wetting connectivity functions (Eqs. 24-25). The scanning curves were then calculated using the model (dashed lines) and compared to the measured data (open circles).

For testing of the developed hysteretic relative permeability models, we used the experimental data for scCO2/brine in Berea sandstone cores generated by *Akbarabadi and Piri* (2013). The model parameters were obtained from the computer-generated capillary pressure-saturation curves for primary drainage and main imbibition (Figure 100a). As demonstrated in Figure 100b, the new hysteretic relative permeability model represent the experimental measurement very well, given the fact that connectivity parameters in the model are obtained from a computer-generated porous medium. However, for a better representation, the exponents in the relative tortuosity factors need to be adjusted to some degree, especially for representing the portions of the measured curves at relatively lower wetting fluid saturations. The adjustment needed for the wetting phase relative permeability appears to be much more pronounced than the one for the nonwetting phase relative permeability. The results obtained with the new hysteresis modeling approach demonstrates that the models are promising for further testing and to predict spatial and temporal changes in residual saturations in application to geologic carbon sequestration (GCS) and other applications involving two-phase flow in porous media.

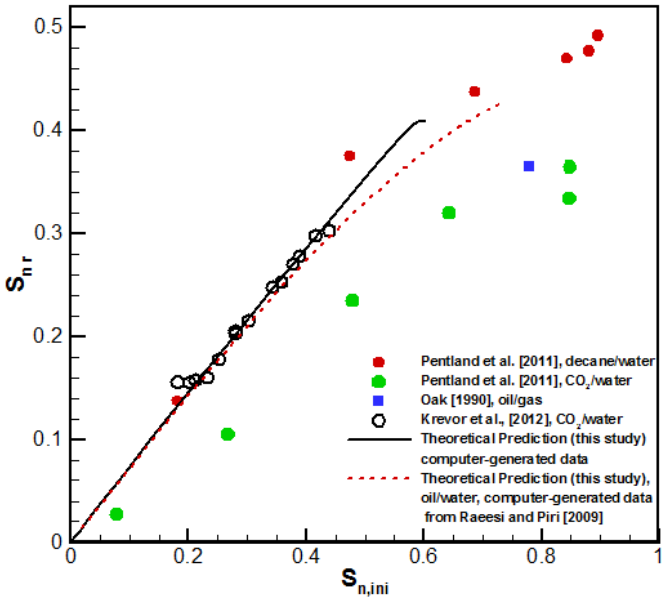

Figure 98: The predicted residual saturations of non-wetting fluid as a function of the initial saturation at the end of drainage for computer-generated Berea sandstone samples, compared with the laboratory data in the literature for different fluid-pairs in different fluid-pairs in different Berea sandstone cores (Printed after Cihan et al., 2014a)

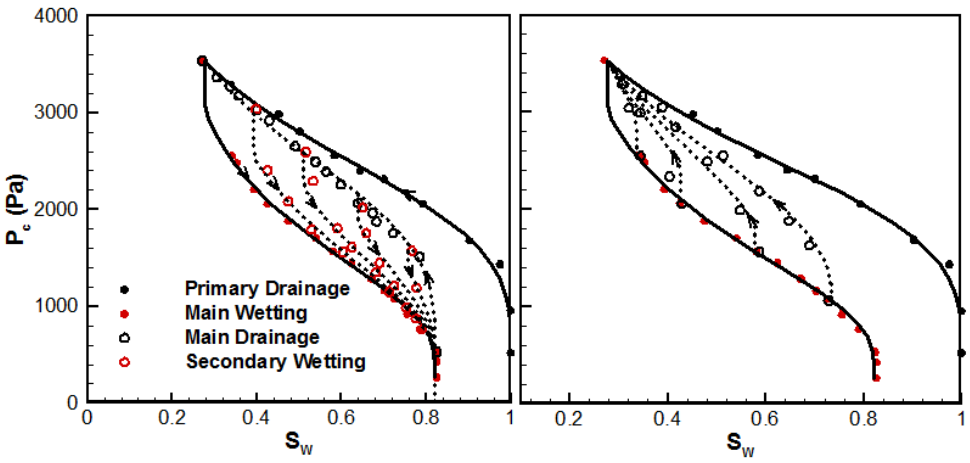

Figure 99: Comparison of the predicted wetting and drainage curves with the experimental data (Sand I) from Poulovassilis (1970). (Printed after Cihan et al., 2014a).

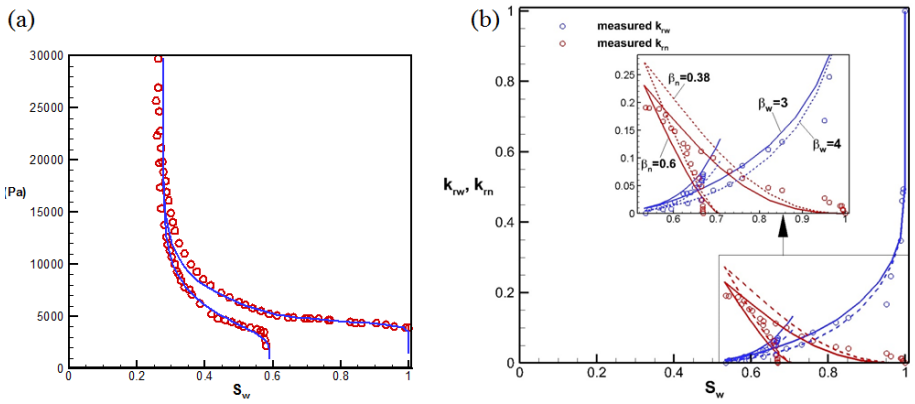

Figure 100: (a) Pc-S model functions fitted to calculated primary drainage and imbibition in the computer-generated porous medium. (b) Comparison of the predicted and measured (open circles) relative permeability curves. Experimental data in (b) were generated by *Akbarabadi and Piri* (2013).

5 NUMERICAL SIMULATION OF MIGRATION AND TRAPPING

The experimental data generated in the study allowed obtaining new insights to the basic processes of trapping. The data was also used to conduct limited model analysis with the goal of identifying possible improvements to existing DOE models. The models used for capillary trapping and dissolution trappings are fundamentally different. Capillary trapping issues are investigated using multiphase flow models, where as dissolution trapping is investigated using solute transport models that have the capability to simulate convective mixing. The model studies on capillary trapping and dissolution trapping are presented separately.

5.1 Modeling with experimentally determined constitutive models

An integrated finite difference multi-purpose simulation code, TOUGH2 T2VOC (Falta et al., 1995), was used to simulate two-phase flow in the two dimensional tank. The model was modified in order to simulate the glycerol/water mixture for wetting phase and Soltrol for the non-wetting phase. Separate simulations were performed employing either experimentally obtained $k_r - S_w$ relationships (Simulation 1) or $k_r - S_w$ relationships obtained from the van Genuchten – Mualem model (Simulation 2). To develop a continuous $k_r - S_w$ relationships for Simulation 1, curves were fit to the data resulting in equation (30) and (31) below. instead of point data; therefore, experimentally obtained data were fitted to trend lines ..

$$k_r = 0.6436 \times {S_w}^2 + 0.48416 \times S_w - 0.12353 \quad \textbf{(30)}$$

$$k_{rn} = \frac{\left(\frac{1 - S_w}{1 - 0.076}\right)^{5.3}}{1.6} \quad (31)$$

The values for k_r and k_{rn} were constrained so that they would not be negative. Simulation 2 used the van Genuchten parameters obtained from Mori et al. (2014).

Since the #110 sand that surrounded the synthetic aquifer acted as a flow barrier for the non-wetting phase, the model domain was defined only to the extent of the #30/40 Accusand. A two-dimensional rectangular mesh with constant width corresponding to the thickness of the sample in the tank was used to discretize the fluid flow domain. The cap rock interface was defined as a no-flow boundary. The grid mesh consisted of 1276 elements and the mesh size was about 1cm^3.

First, the model was used to simulate the steady-state conditions for single phase glycerol/water 80 wt% flow prior to Soltrol injection. After the steady-state condition that defines the initial conditions was obtained, Soltrol was injected at 1.17×10^{-8} m^3/s (0.7ml/min) for 5.5 hours. Even though the well was fully screened, because Soltrol is less dense than the glycerol/water 80 wt%, Soltrol was observed to flow out only from the top of the well. Hence, defining a source in the grid that is at the top of the well screen best simulated the injection.

To verify the accuracy of the x-ray method, the total mass of injected Soltrol was compared with the mass estimated using the measured saturations. The total mass injected as measured by tracking the weight change of the Soltrol in the Mariotte's bottle using a precision electronic balance was 0.1825 kg. On the other hand, the total mass of Soltrol in the sand estimated using the saturation measured by the x-ray method was 0.1877 kg, suggesting that the x-ray saturation data can be used to give an accurate estimate of the mass of Soltrol.

The plots compare the saturation level of the Soltrol observed in the tank experiment at 5 tank locations, (A, B, C, D, and E as labeled in the photograph) with the saturation values predicted using TOUGH2 T2VOC incorporating the directly measured relative permeabilites (Simulation 1) and the van Genuchten model derived relative permeabilities (Simulation 2). The tank observations do not match exactly either simulation, but at points A and B, Simulation 1

shows better agreement with the observed saturations. Furthermore, Simulation 2 overestimates the saturation as time proceeds.

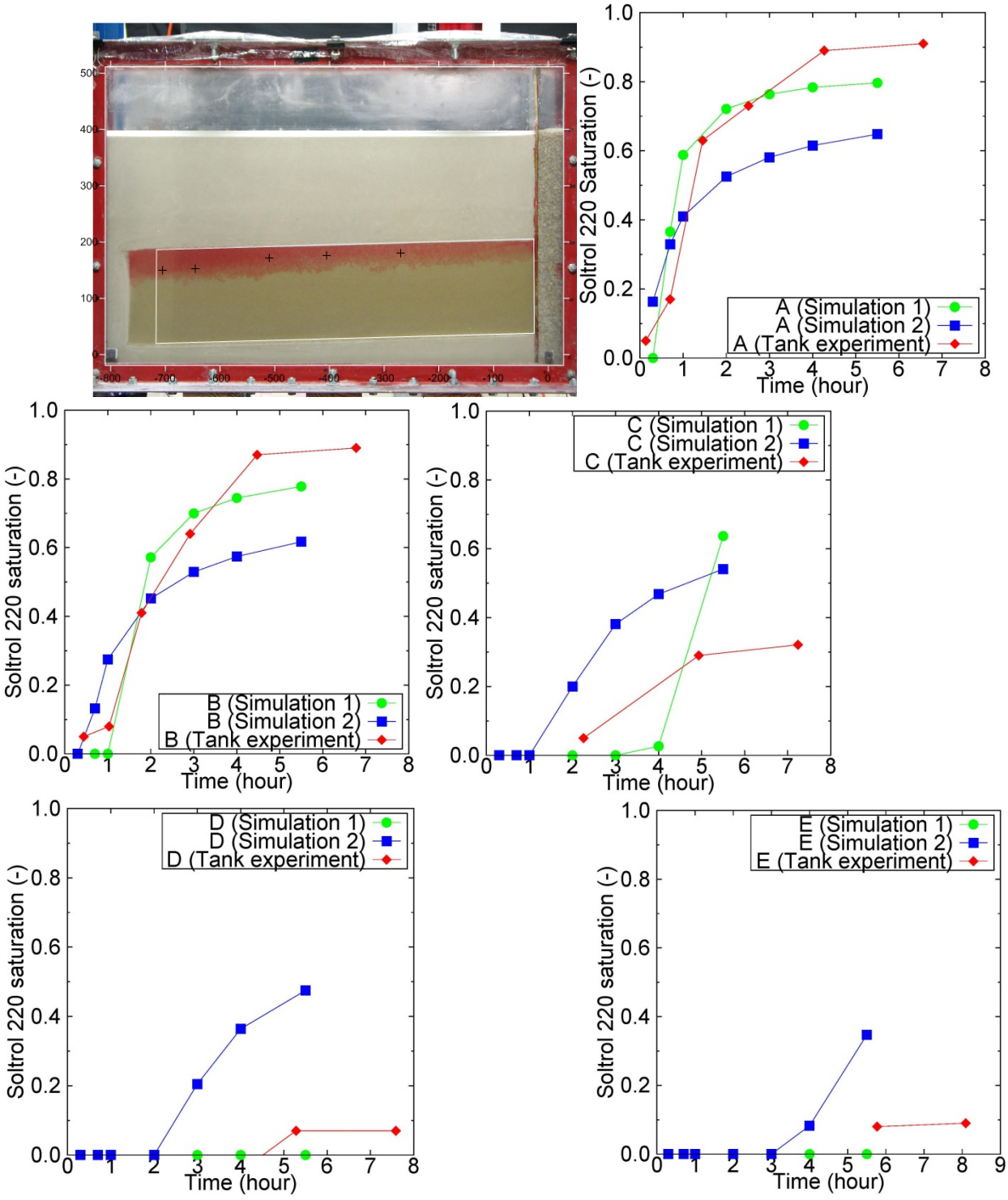

Figure 95: Saturation of Soltrol at Points A-E (labeled in the photograph) observed in the tank experiment using x-ray tomography and simulated using TOUGH T2VOC (Simulations 1 and 2). Simulation 1 uses experimentally obtained relative permeability, while Simulation 2 uses van Genuchten- Mualem derived relative permeability

To evaluate the ability of the relative permeabilities to simulate non-wetting fluid propagation, the experimental results generated by Trevisan et al. (2014) that monitored a plume in a 2-d tank with homogenous packing were used. To compare the experimental data with the model simulations using the two relative permeability function types, the saturation measurements that were made using the x-ray system at selected scanning grid was used to calculate the total Soltrol mass in vertical sections at 1.5 cm length intervals along the length of the plume. Fig. 134 shows these vertically integrated mass of Soltrol when the time the injection ceased (5.5 hours). On the same plot, the model simulated mass estimates are plotted. Overall, neither of the two simulations predicted accurately the plume distribution at the end of the injection period. In fact, while the computed saturations in Simulation 1 better matched the mass of Soltrol observed close to the injection well, the front position was underestimated. On the other hand, simulation 2 predicted a plume reaching the right end of the tank at 5.5 hours similarly to the observed experimental result but could not predict the sharp change in Soltrol mass within 30 cm from the injection well.

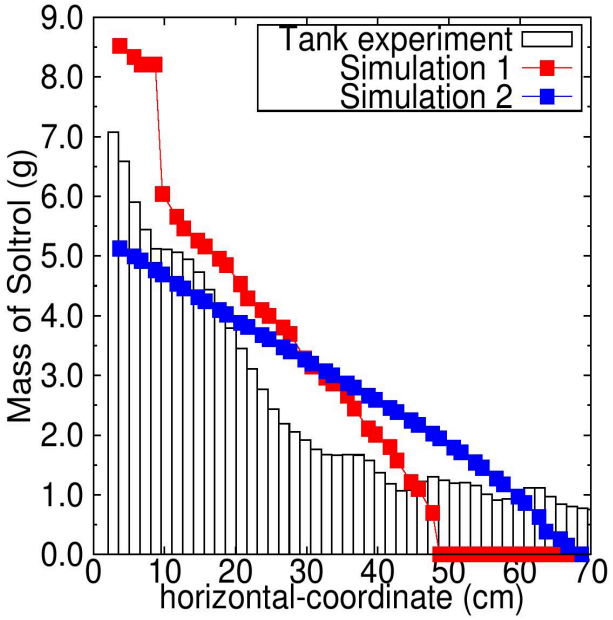

Figure 96. Cumulative mass of Soltrol 220 from the simulation model and tank experiment conducted by Trevisan et al. (2014) at 5.5 hours from the start of the experiment

5.2 Capillary trapping

The objectives of the model analysis on capillary trapping include:

1. Testing the general capabilities of the multiphase flow simulator based on the continuum approach and the influence of permeability heterogeneity on the estimation of plume migration and trapping;
2. Testing the applicability of the selected analog fluid combination to mimic the $scCO_2$/brine system at reservoir conditions;
3. Assessing the significance of capillary heterogeneity by comparing the statistical properties of the plume distribution;
4. Testing the new hysteretic constitutive models and assessing the effects of hysteresis on plume migration and capillary trapping
5. Comparing the surrogate plume behavior simulated at laboratory conditions at the meter-scale with a typical $scCO_2$ injection scenario at the kilometer-scale.

The modeling was conducted in a two-dimensional, vertical cross-sectional domain with the dimensions of the experimental specific setup (small or large tank). Overall, two multiphase flow simulators developed by DOE were used, namely TOUGH2 (Pruess et al., 1999) and TPFLOW, to simulate both small and large tank geometries. Similarly to TOUGH2, TPFLOW is a Finite Volume-based numerical simulator based on the traditional two-phase flow theory and has been developed by at Lawrence Berkeley National Laboratory as a part of this project. TPFLOW is a simplified multiphase flow model that simulates immiscible flow of incompressible fluids. Therefore, it is slightly more efficient than TOUGH2. One advantage of this new numerical code is that it allows for more straight forward implementation of drainage and imbibition (both spontaneous and forced) events in one simulation run and include new models for hysteretic two-phase flow parameters, compared to the existing TOUGH2. The TPFLOW code and new constitutive models built in it are still in the development and testing phase. A recent version of the code with hysteresis, referred as TPFLOW_HYST, has been tested successfully for modeling capillary trapping in a heterogeneous small tank experiment, which is demonstrated in section 6.4.2. .

5.2.1 Model setup for small and large tank simulations

In order to make the computational mesh small, only the flow domain was modeled, assigning no-flow conditions to the boundaries with the impervious layers, as, for the small and large tank configuration, respectively (shown in Figure 96 and Figure 97). Implementing impermeable top and bottom layers for both phases seems to be a reasonable assumption, given the very low permeability of the caprock compared to the aquifer sand. The model area is rotated counterclockwise around the lower left corner with a 2º dip angle for the small tank geometry Figure 96) and clockwise around the lower right corner with a 3º dip angle for the large tank geometry (Figure 102). In both small and large tank simulations, a constant flow rate was imposed to the uppermost grid blocks of the well zone in order to generate a plume injection scenario mimicking the experimental observation.. In the case of the small tank simulations, the injection well was modeled by a numerical block consisting of a highly permeable material (with same permeability as #30/40 Accusand) with porosity 0.6, taking into account the void fraction of the PVC pipe and the porosity of the surrounding sand. Two different mesh discretizations were tested for the small tank simulations; specifically a 5056-cell mesh with (0.5 × 0.5) cm^2 grid blocks, and a 1264-cell mesh with (1 × 1) cm^2 grid blocks. Since no substantial difference was observed in the homogeneous model predictions, the coarsest refinement was employed throughout these simulations in order to minimize computational time. However, when heterogeneity was taken into account, a more refined mesh was required to represent with adequate accuracy the sharp permeability transitions in the sands and therefore the large NWP saturation contrasts.

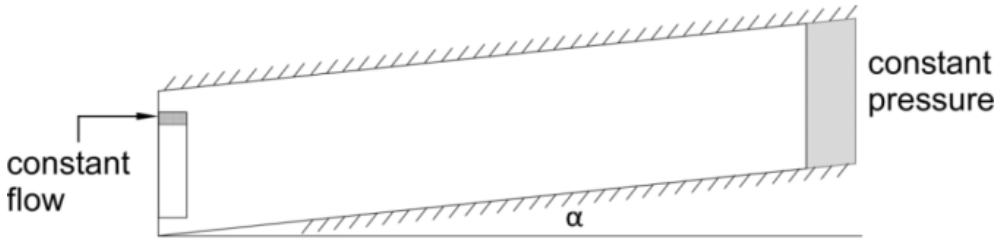

Figure 101 Schematic representation of the model domain and boundary conditions for the small tank geometry.

Large tank experiments were modeled in a similar fashion, taking into account the differences with the small tank geometry, such as the difference in constant pressure at the lateral boundaries to constrain a steady-state background wetting phase flow and the treatment of the uppermost grid blocks of the injection well as a coarse sand #8 zone. The lateral limits of the numerical domain were extended one meter away from the actual tank walls. This was to create the *semi-closed* boundary term, in order to provide a larger available volume for the outflowing plume to accumulate inside the coarse sand boundaries, without triggering secondary plumes back into the reservoir. With the same purpose, very low permeability was assigned to the grid blocks underlying the constant flow rate zone, in order to avoid unrealistic lateral development of the plume from the lateral boundaries of the well (Figure 102). An average flow rate of 0.76 ml/min was used in the numerical simulations (1 L injected during 22 hours). The computational mesh of the large tank model was discretized in 122 columns by 25 rows with (2 × 2) cm^2 grid blocks, maintaining the same refinement of the heterogeneous permeability field (see chapter c).

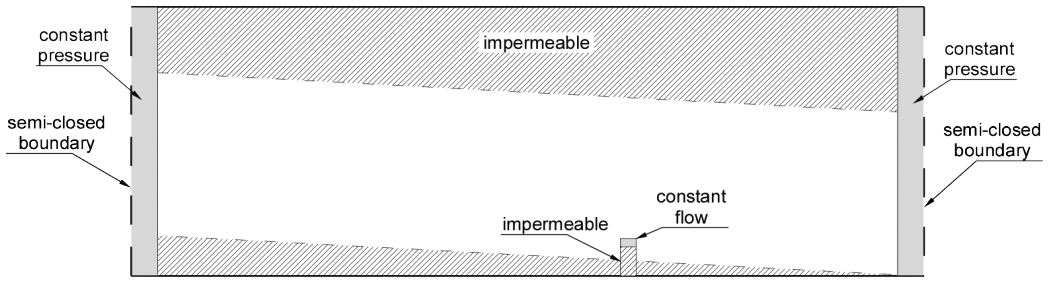

Figure 102 Boundary conditions and numerical artifacts applied to the large tank model domain.

The Van Genuchten capillary pressure–saturation model (van Genuchten, 1980) was used for the retention function:

$$S_e(P_c) = \left[1 + (\alpha P_c)^n\right]^{-m} \tag{32}$$

where the wetting phase saturation is a function of the effective saturation S_e and the maximum and irreducible wetting phase saturation, $S_w^{\max}$ and S_w^{irr}, respectively:

$$S_{\mathrm{w}}(P_c) = \left[S_e(P_c) \times \left(S_{\mathrm{w}}^{\max} - S_{\mathrm{w}}^{irr}\right)\right] + S_{\mathrm{w}}^{irr} \tag{33}$$

The Van Genuchten-Mualem (Mualem, 1976) constitutive model used for the relative permeability relations is given as:

$$k_{r,\mathrm{w}} = S_e^{L_{\mathrm{w}}} \left[1 - \left(1 - S_e^{1/m}\right)^m\right]^2 \tag{34}$$

$$k_{r,\mathrm{nw}} = \left(1 - S_e\right)^{L_{nw}} \left(1 - S_e^{1/m}\right)^{2m} \tag{35}$$

5.2.2 Representation of actual reservoir fluids by analog fluids

In order to test the applicability of the selected analog fluid combination to mimic the $scCO_2$/brine system at reservoir conditions, plume propagation observed in one small tank homogeneous experiment (no.1, chapter 3.1.4) was qualitatively compared with simulations carried out with TOUGH2. Figure 103 shows simulations with analog fluids using T2VOC code (Falta et al., 1995), while Figure 104 shows numerical predictions with $scCO_2$ and brine using ECO2N module (Pruess and Spycher, 2007). The analog-fluids and reservoir-fluids scenarios have the same injection flow rate (0.7 ml/min) as well as injection duration (5.5 hours) and total volume (231 ml). In order to achieve comparable density and viscosity ratios, the *pressure, temperature* conditions of the reservoir-fluids scenario have been constrained to 11 MPa and 37°C, respectively. These conditions can be found at depths of approximately 1500 meters (Pruess and Garcia, 2002), where CO_2 exists at the supercritical state. On the other hand, the simulation of the displacement experiment in the laboratory is carried out at 0.1 MPa and 20°C. As the multiphase flow equations and constitutive relationships being implemented are the same for both modules and the density and viscosity contrasts are similar for both scenarios, one would expect comparable simulated contours. Although neither of the simulations could match exactly the observed evolution of the plume, as we can observe in Figure 103 and Figure 104, the plume distribution predicted by ECO2N show the best-matching results.

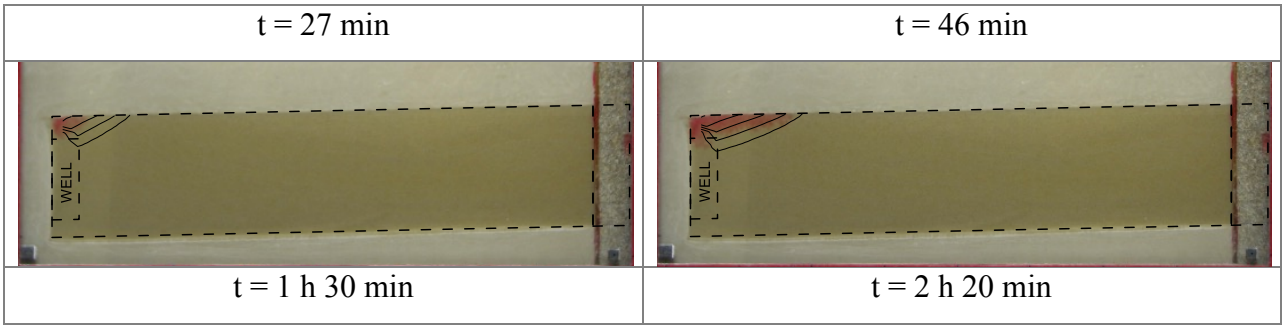

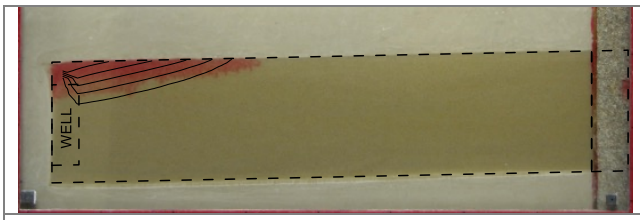

t = 3 h 30 min

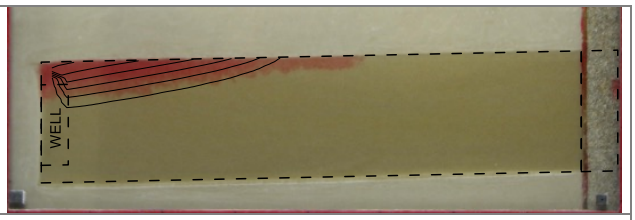

t = 4 h

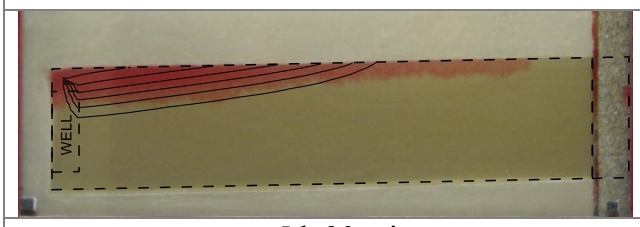

t = 5 h 30 min

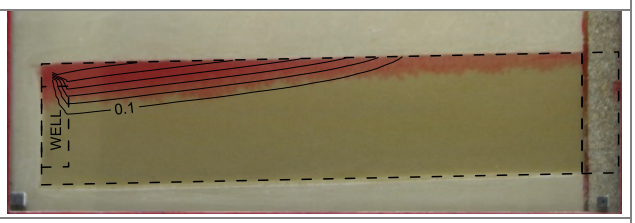

T2VOC simulation

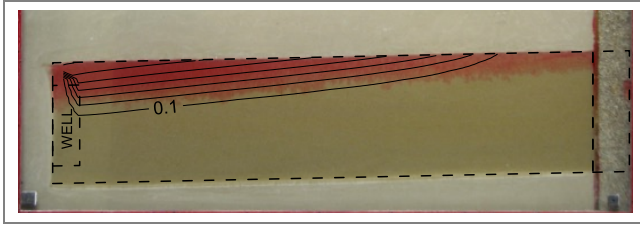

T = 20°C

P = 0.1 MPa

$\rho_{nw}/\rho_w = 0.71$

$\mu_{nw}/\mu_w = 0.08$

Figure 103 TOUGH2-T2VOC simulation's results of experiment no. 1 (chapter 3.1.4) with analog fluids at ambient conditions.

Perhaps the most striking difference between T2VOC and ECO2N models is the implementation of phase miscibility in the latter code, which hinders a full comparison between the two simulations. Despite this important dissimilarity, the better prediction of the observed plume distribution by ECO2N suggests the occurrence of some mechanism not being accounted for in the immiscible displacement simulated with T2VOC.

t = 27 min

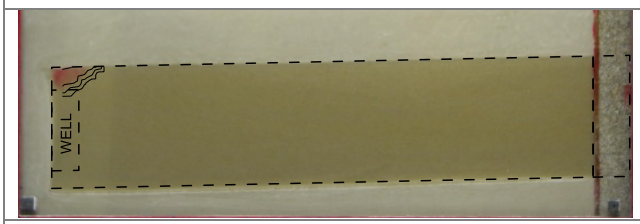

t = 1 h 30 min

t = 46 min

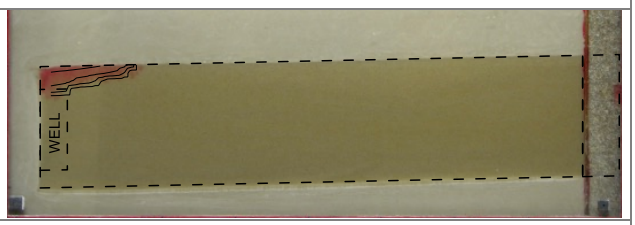

t = 2 h 20 min

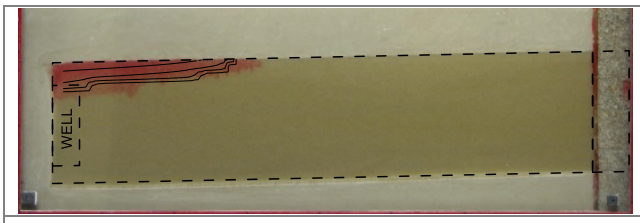

t = 3 h 30 min

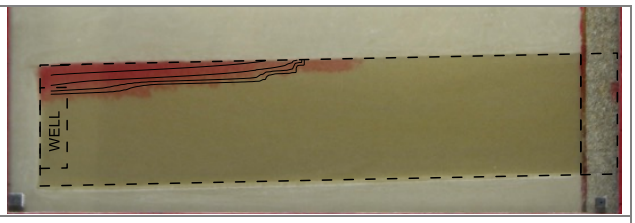

t = 4 h

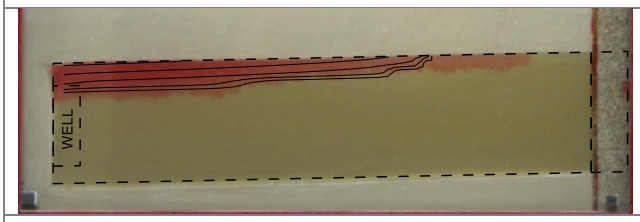

t = 5 h 30 min

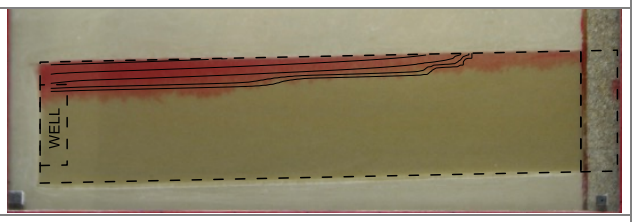

ECO2N simulation

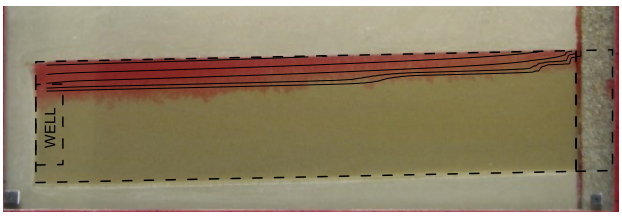

T = 37°C

P = 11 MPa

X_{NACL} = 3.2 %

ρ_{nw}/ρ_w = 0.71

μ_{nw}/μ_w = 0.08

Figure 104 TOUGH2-ECO2N simulation's results of experiment no. 1 (chapter 3.1.4) with actual fluids at reservoir conditions.

5.2.3 Effect of capillary heterogeneity in small tank

In most reservoir models, fine-scale heterogeneities are often neglected due to incomplete knowledge of the subsurface systems at such fine scales and limitations of computational resources. Small tank heterogeneous experiments presented in section 5 allow for direct observation of fine-scale heterogeneity and the influence of entry pressure contrasts on plume propagation and entrapment, hence the opportunity to assess via numerical analysis the significance of capillary heterogeneity by comparing the statistical properties of the plume distribution. Figure 105 shows the simulated NWP saturation contours for the permeability field implemented in the uncorrelated heterogeneous experiment carried out in the small tank (Het. 1, chapter 5).

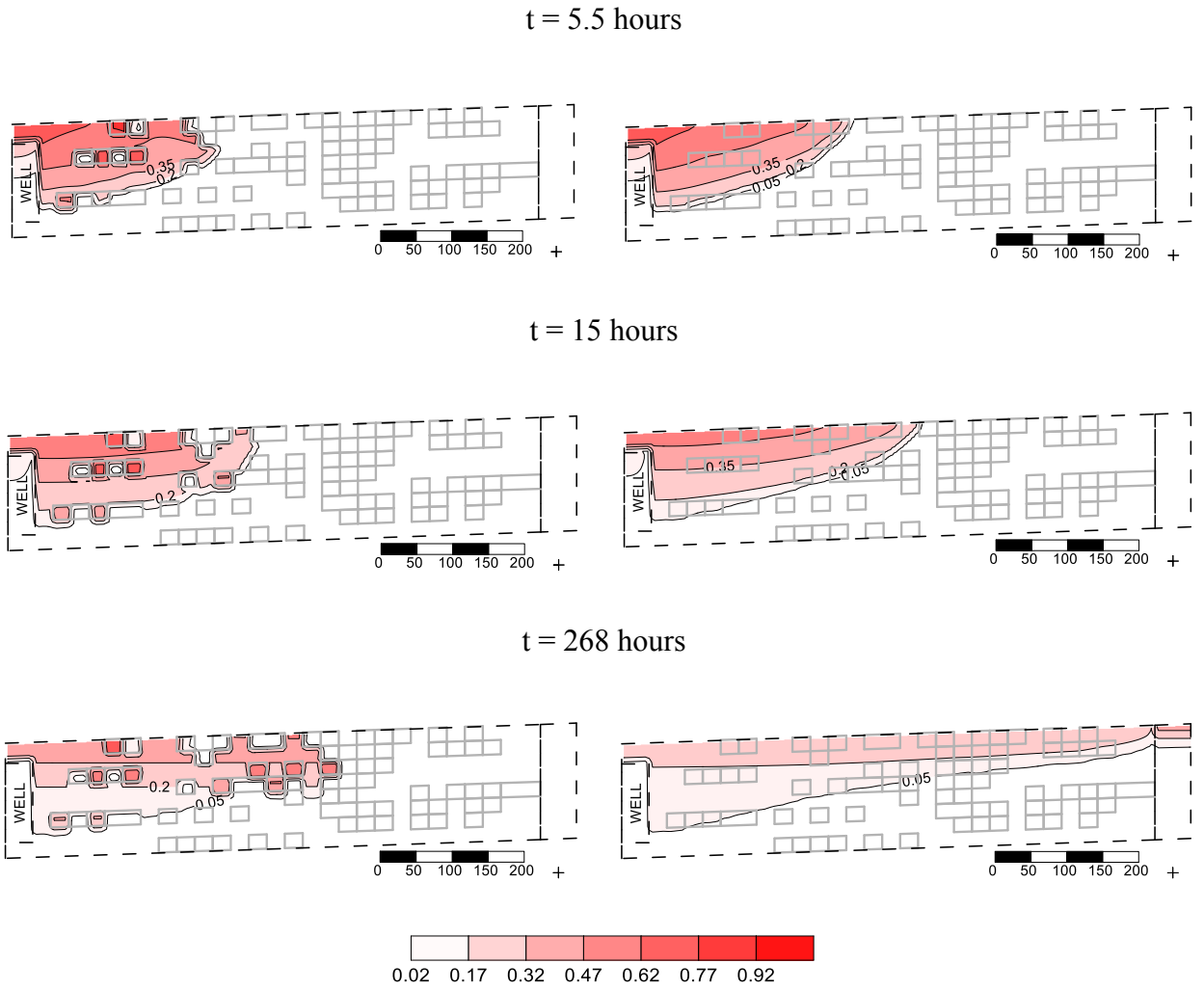

Figure 105 Simulated NWP plumes for the small tank experiment with uncorrelated heterogeneous permeability field: (left) taking into account heterogeneity of the P_c-S function and (right) using P_c-S properties of the background sand only. Scale bars in millimeters.

As expected, the uniformity in capillary entry pressure throughout the aquifer (Figure 105, right) leads to a homogeneous plume propagation, concealing the heterogeneity effect of the permeability field. These observations agree with simulation results previously reported by Saadatpoor et al. (2010), where buoyant displacement of CO_2 through a capillary heterogeneous

formation led to larger amounts of immobilized NWP than the capillary homogenous scenario via accumulation of above-residual saturations of CO_2 as a bulk phase behind local capillary barriers.

Regarding the first spatial moments of the plume along the horizontal and vertical directions, it is worth noting that the observed behavior of the plume measured by x-ray attenuation falls in between the evolution predicted by the capillary homogeneous and capillary heterogeneous scenarios. Interestingly enough, predictions from the capillary homogeneous simulation seem to better reproduce the experimental observations, at least for the initial evolution of the plume's center of mass along horizontal direction, suggesting a reduced influence of capillary heterogeneity at early times. At late times, however, the slower plume advancement rate appears to be better predicted by the capillary heterogeneous model. In the next section, a hysteresis numerical simulator is employed to understand the effects of hysteresis on apparent differences in the comparisons.

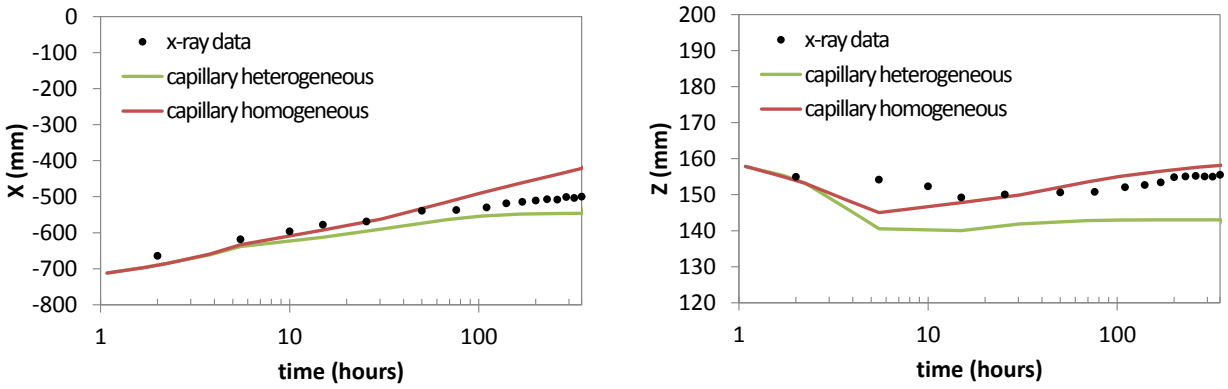

Figure 106 Temporal evolution of plume's center of mass (1st moment) along the horizontal (left) and vertical (right) axes for the observed (dots) and simulated plumes with (green line) and without (red line) accounting for capillary heterogeneity.

5.2.4 Numerical simulations of small tank experiments using a new hysteretic two-phase flow model

The developed hysteretic constitutive models have been incorporated into a Finite Volume-based numerical simulator (TPFLOW_HYST) based on the traditional two-phase flow theory. The numerical model is compared against laboratory experiments to test the ability of the theory and constitutive models to predict motion and capillary trapping of two immiscible fluids in macroscopically homogeneous and heterogeneous porous media. Table 6.2.4 presents the

hysteresis model parameters used in the numerical simulations. Note that the parameter values were obtained by fitting the hysteretic Pc-S model to measured primary drainage and main wetting curves for the glycerol-water and soltrol fluid pair system in the sands. For the void-volume distribution function, we assumed a log-normal distribution, which was shown to be a good fit for representation of both grain and void size distribution of porous media (*Diamond and Dolch,* 1972; *Hwang and Powers*, 2003). The generalized lognormal distribution used in the simulations is presented as

$$f(r)=\frac{1}{\sqrt{2\pi}\ln\sigma}\exp\left[-\left(\frac{\ln(r'/\mu)}{\sqrt{2}\ln\sigma}\right)^2\right] \qquad \textbf{(36)}$$

where $r'=(r-r_{\min})(r_{\max}-r_{\min})/(r_{\max}-r)$, and σ and μ are the distribution parameters characterizing the distribution properties of r'. The cumulative distribution function can be expressed as

$$F(r)=\frac{1}{\sqrt{2\pi}\ln\sigma}\int_{r}^{r_{\max}}\exp\left[-\left(\frac{\ln r'(x)-\ln\mu}{\sqrt{2}\ln\sigma}\right)^2\right]\frac{(r_{\max}-r_{\min})}{(r_{\max}-x)(x-r_{\min})}dx \qquad \textbf{(37)}$$

where $F(r)$ is the percent volume of voids with effective radii larger than r.

Results comparing the model predicted fluid displacements for the heterogeneous system in the previous section are presented in Figure 107a-c. The hysteretic numerical model appears to capture the plume migration reasonably well for both homogeneous (sand 40/50) and heterogeneous (Het. 1, section 5.1.2) conditions. Redistribution of non-wetting fluid during post-injection estimated by the model without hysteresis is much more rapid than those obtained by the model with hysteresis and the laboratory experiment. This indicates that the numerical simulators with the hysteresis effects included may lead to more accurate prediction of fluid distributions at field-scale geological systems. However, computational efficiency of the model with hysteresis is relatively low compared to the models without hysteresis. Further computational research would be needed to find more efficient algorithms for solving nonlinear hysteretic partial differential equations. The model results also indicate that discontinuous high permeability zones that are traversed by an injected CO_2 plume in a reservoir can contribute to long-term trapping of CO_2, but the numerical studies conducted here will need to be extended to field-scale for evaluating the effects of hysteresis at field-scale under realistic CO2 storage conditions.

Table 17: Hysteresis model parameters used in the numerical simulations. Note that the parameter values are obtained by fitting the hysteretic Pc-S model to measured primary drainage and main wetting curves for the glycerol-water and soltrol fluid pair system. ($a_d=a_w=1$, and $P_{dmin}=P_{wmin}$)

Parameters	Sand #30/40	Sand #40/50	Sand #50/70
Void-Volume Fraction Distribution			
r_{min}	0.000E+00	0.000E+00	0.000E+00
r_{max}	8.224E-05	5.000E-05	5.000E-05
μ	7.919E-05	4.351E-05	3.997E-05
σ	1.212E+00	1.846E+00	2.321E+00
Drainage Connectivity Function			
P_{dmin}	2.816E+02	3.596E+02	4.200E+02
b_d	3.621E+01	1.109E+01	9.978E+02
c_d	6.377E+02	2.507E+02	4.525E+02
d_d	8.710E-02	2.103E-01	2.045E-01
e_d	2.763E-01	9.046E-02	3.955E-02
Wetting Connectivity Function			
b_w	2.048E+02	3.938E+02	3.069E+02
c_w	1.222E+02	3.300E+02	3.436E+02
d_w	9.999E-01	9.805E-01	9.994E-01
e_w	6.620E-01	1.951E-01	6.182E-01

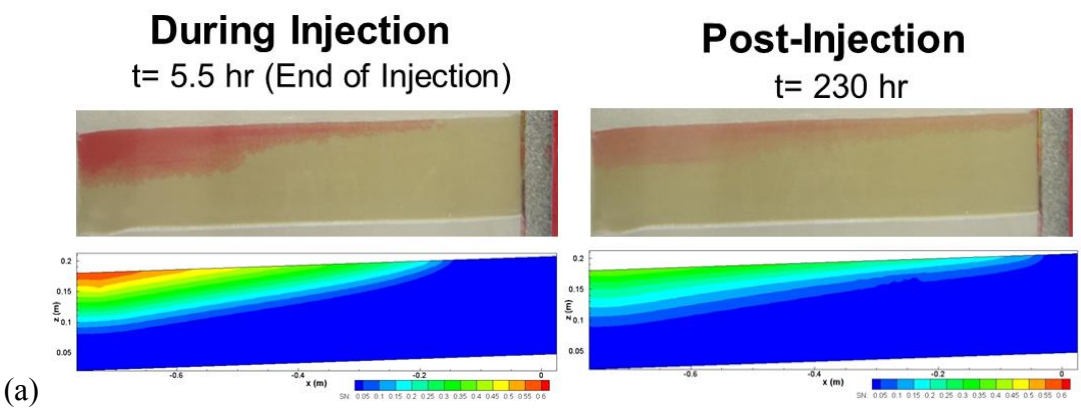
During Injection
t= 5.5 hr (End of Injection)
Post-Injection
t= 230 hr
z (m)
x (m)

(a)

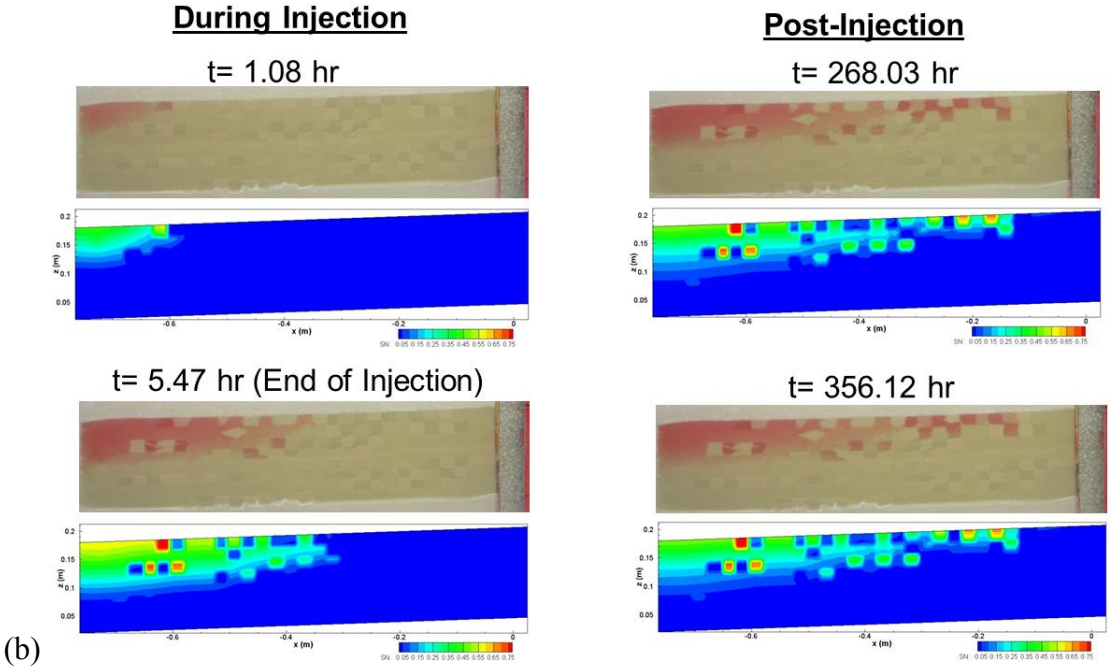
During Injection
t= 1.08 hr
Post-Injection
t= 268.03 hr
t= 5.47 hr (End of Injection)
t= 356.12 hr
z (m)
x (m)

(b)

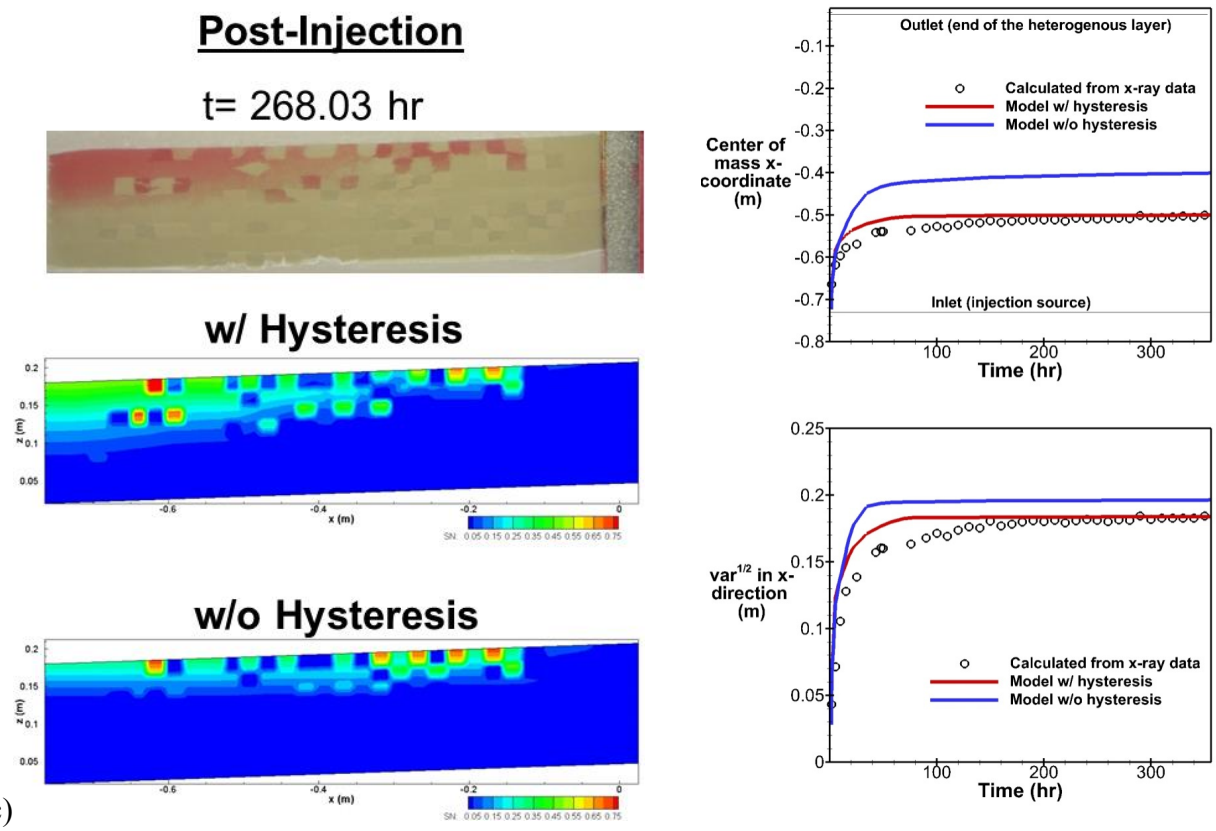

(c)

Figure 107: (a) Comparison of model-predicted nonwetting phase fluid distributions with observed migration at 5.5 hr (end of injection) and 230 hr for a homogeneous packing condition (sand type 40/50), (b) Comparison of model-predicted nonwetting phase fluid distributions with observed migration during injection and post-injection for heterogeneous packing (includes 3 different sand types as sand# 30/40, 40/50 and 50/70, see section 5 for detailed hydraulic properties), and (c) Comparison of the models with and without hysteresis against experimental data for a heterogeneous packing condition

5.2.5 Numerical simulation of large tank and field experiments

Translating the practically significant experimental laboratory scale observations to the field is a complex task that can be carried out by means of numerical simulations. In this section, the homogeneous large tank experiment and a geometrically similar homogeneous field-scale scenario are simulated using TPFLOW (without hysteresis). The geometry of the reservoir in terms of dipping angle and aspect ratio, the viscosity and density ratios, as well as the flow

boundary conditions constraining background brine flow and total $scCO_2$ injected were matched between the laboratory and field simulations.

The physical properties of the actual fluids and rock are selected to be representative of deep geological reservoirs. Similarly to the large tank model, the computational mesh of the field-scale model was discretized in 122 columns by 25 rows with (100 × 100) m^2 grid blocks.

Table 18 Model parameters used in the numerical simulations of the homogeneous laboratory experiments and a synthetic field problem with identical geometry. The highlighted rows represent the values that were matched between the two models.

Parameter	Symbol (unit)	Laboratory simulation	Field simulation
Aquifer thickness	H (m)	0.5 m	2500 m
Aquifer length	L (m)	2.44 m	12200 m
Aspect ratio	H/L (-)	4.88	4.88
Dipping angle	θ (degrees)	3	3 [a]
Initial pressure	P_i (MPa)	0.106	11
Temperature	T (ºC)	20	37
Non-wetting phase density	ρ_{nw} (kg/m^3)	860	722 [b]
Wetting phase density	ρ_w (kg/m^3)	1210	1020 [b]
Non-wetting phase viscosity	μ_{nw} (mPa·s)	4.9	0.059 [b]
Wetting phase viscosity	μ_w (mPa·s)	61	0.74 [b]
Density ratio	ρ_{nw}/ρ_w (-)	0.71	0.71 [a,b]
Viscosity ratio	μ_{nw}/μ_w (-)	0.08	0.08 [a,b]
Porosity	φ (-)	0.426	0.2 [a,c]
Permeability	k (m^2)	3.39×10^{-11}	3.0×10^{-13} [c]
Injection flow rate	Q (m^3/s)	1.26×10^{-8}	1.7×10^{-2} [d]
Injection duration	t	22 hours	5 years [d]
Horizontal hydraulic gradient	i (-)	0.044	0.044 [e]
Pore volumes injected	PVI (-)	0.04	0.04

[a] analogous value to the Median case in Kopp et al. (2009).
[b] analogous value to Gasda et al. (2013).
[c] analogous value to Birkholzer et al. (2009).
[d] corresponding to 0.39 Mt/year, analogous to the Midale project (Whittaker et al., 2011).
[e] analogous value to intermontane basins, from Hubbert (1953).

For the constitutive models for the field-scale simulations, experimental data measured in a Berea sandstone core with $scCO_2$/brine at 50°C from Pini et al. (2012) and Pini and Benson (2013b) were fitted to Van Genuchten (P_c-S) and Van-Genuchten-Mualem models (k_r-S).

Table 19 Fitting parameters for Van Genuchten and Van Genuchten-Mualem constitutive models for #50 sand and the reservoir rock used in the homogeneous field-scale simulation.

cycle	Parameter	#50	Rock
	S_w^{max}	0.83	0.85
	$S_{nw,r}^{max}$	0.17	0.15
	S_w^{irr}	0.07	0.32
	L_w	0.2	1.5
	L_{nw}	1.5	2.0
primary drainage	α (1/m)	10.0	1.6
	n	7.0	5.0
	m	0.86	0.8
main wetting	α (1/m)	30.0	4.0
	n	4.5	3.0
	m	0.78	0.67

These constitutive relationships are used in the synthetic field simulation under the assumption that they are valid at the P,T conditions constrained in the model. The corresponding parameters and fitted curves are shown in Table 19 and Figure 108.

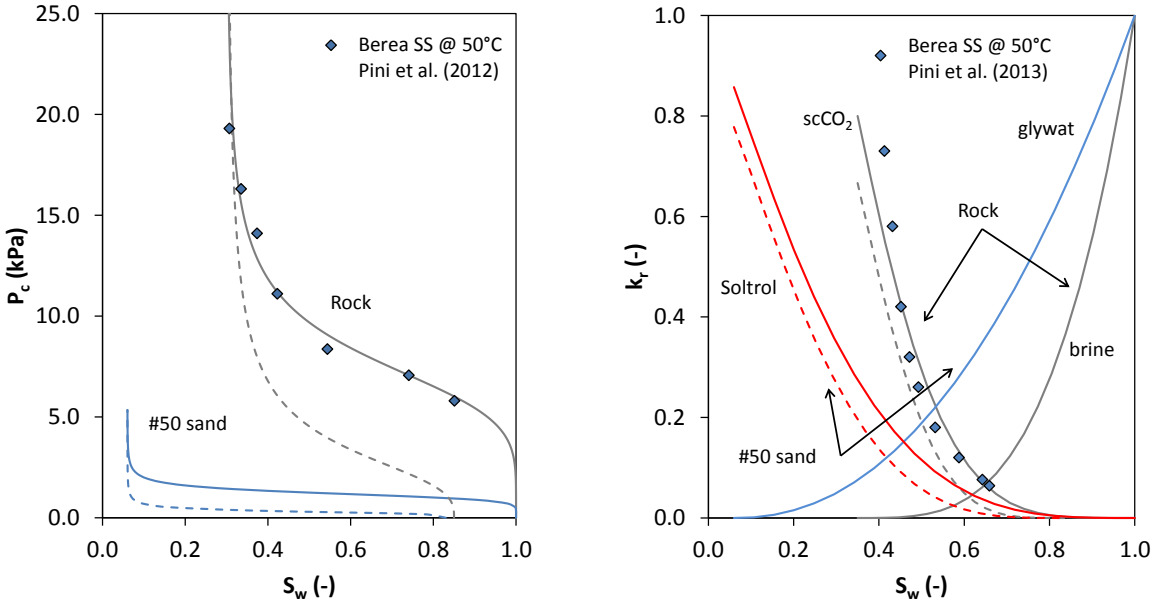

Figure 108 Capillary pressure (left) and relative permeability (right) dependence on wetting phase saturation. Values measured on a Berea sandstone (SS) with $scCO_2$/brine are fitted to the Van Genuchten and Van Genuchten-Mualem models and compared with the #50 sand curves corresponding to the fluids used in the laboratory experiments. Continuous and dotted lines represent drainage and wetting cycles respectively.

Figure 109 shows a qualitative comparison of the numerical simulation predictions of the homogenous large tank experiment with the observed plume evolution recorded by digital photography. It can be seen that some of the features observed in the homogeneous experiments are captured reasonably well by the model, while other characteristics of the plume are not reproduced. Specifically, the sharp pinning of the interface, the effect of background hydraulic gradient, and the increase in plume size as a consequence of the second injection can be observed in both experimental and numerical results. On the other hand, the breakthrough of the plume into the left boundary at the end of the first fluid redistribution, as well as the front instability during the first injection are not reproduced by the model. The latter is a clear consequence of the inability of conventional two-phase flow approach based on macroscopic (Darcian) to model the unstable flow patterns observed in real cases.

Once tested the general applicability of the multiphase flow model to reproduce the experimental observations at the laboratory scale, injection of $scCO_2$ is simulated in a geometrically similar, field-scale homogeneous reservoir using representative parameters from real cases (Table 12). The resulting plume distribution at four representative times is illustrated

in Figure 110. At first sight, the plume displacement behavior in the field simulations shows the same features of the laboratory simulations; this is expected since the physics that are simulated are identical in both models. Yet, it is worth noting the similarity of the plumes observed at the two scales, considering the significant differences existing between the constitutive relationships of the porous media (e.g. unconsolidated sand vs. Berea sandstone) and the boundary conditions applied to both scenarios.

End of 1st injection (22 hours)

End of 1st fluid redistribution (327 hours)

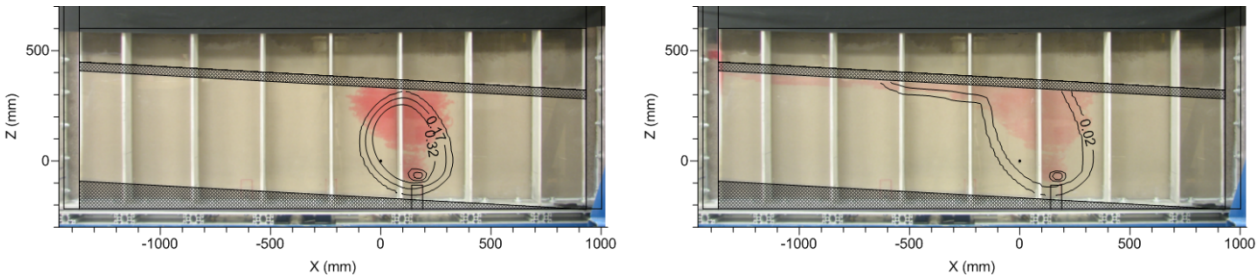

End of 2nd injection (350 hours)

End of 2nd fluid redistribution (590 hours)

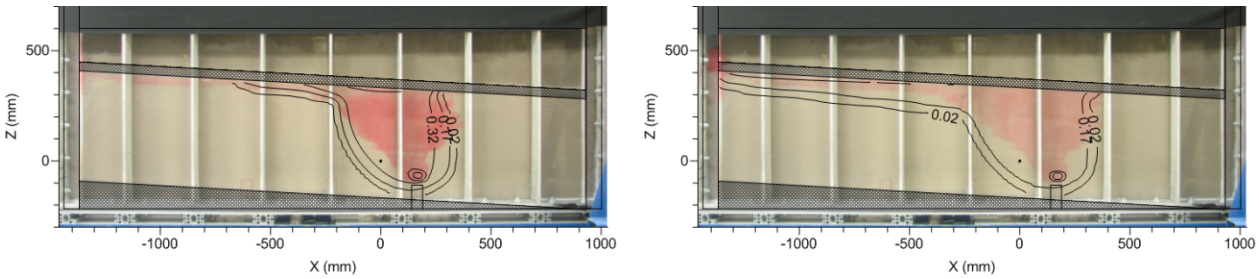

Figure 109 Saturation contours of Soltrol plume for the large tank homogeneous experiment compared to the photographs at four representative times.

Similarly to the approach taken to evaluate the influence of capillary heterogeneity on the overall distribution of the NWP plume in small tank setups, spatial moment analysis was extended to the large tank experiments to compare the performance of model predictions with the experimental outcomes.

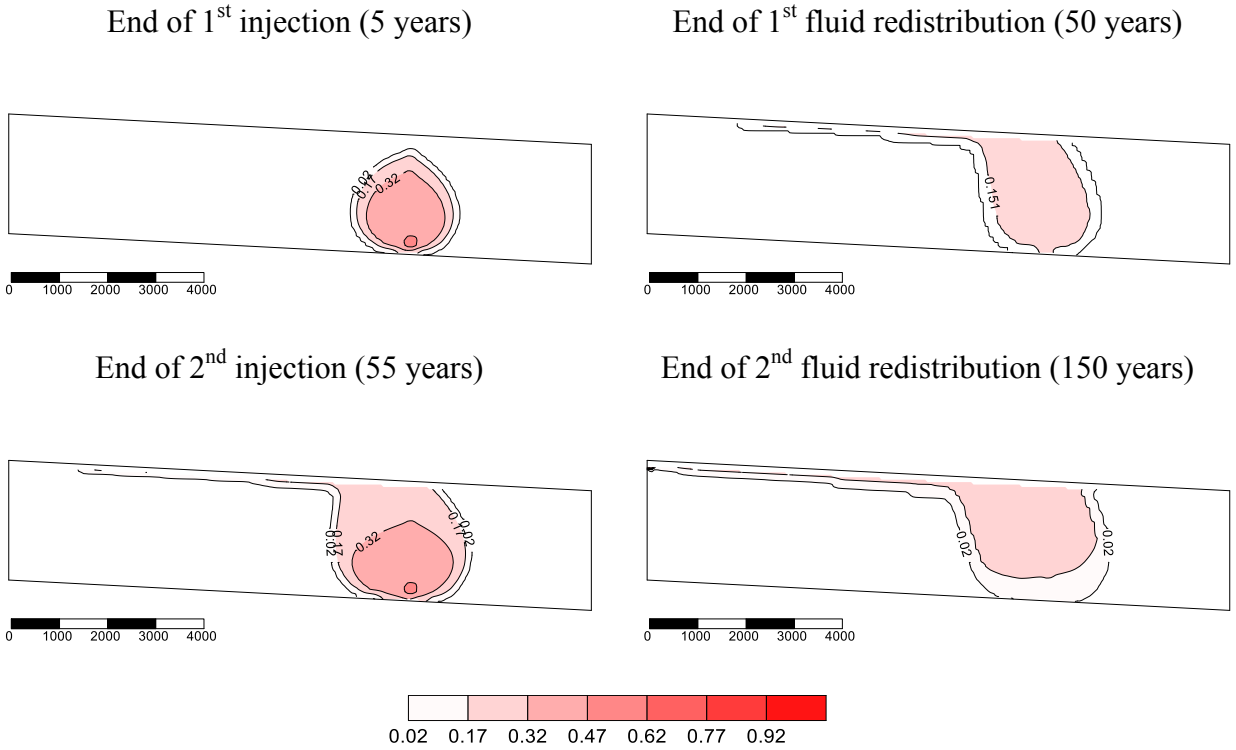

Figure 110 Field-scale simulation results showing saturation contours of $scCO_2$ plume at four representative times. Scale bars are in meters.

In addition to the evolution of the first moment presented above, the 0th and second moments were also considered. Figure 111 (left) shows the 0th moment estimated from x-ray measurements, compared to TPFLOW model predictions, whereas Figure 111 (right) shows evolution of 0th moment in field-scale model predictions. As explained in section 5, the underestimation of NWP plume volume from 0th moment analysis was affected by the partial coverage of x-ray measurement. Nevertheless, this method is convenient to evaluate the temporal evolution of the plume, as well as the fraction of trapped NWP compared to the total injected volume. Zeroth moment analysis confirms the observations from Figure 109 and Figure 110, showing plume breakthrough after cease of the second injection. Likewise, first spatial moment analysis was carried out to compare observed and simulated migration of the plume's center of

mass for the homogeneous laboratory experiment and to evaluate the general behavior of the field-scale plume compared to the laboratory scale.

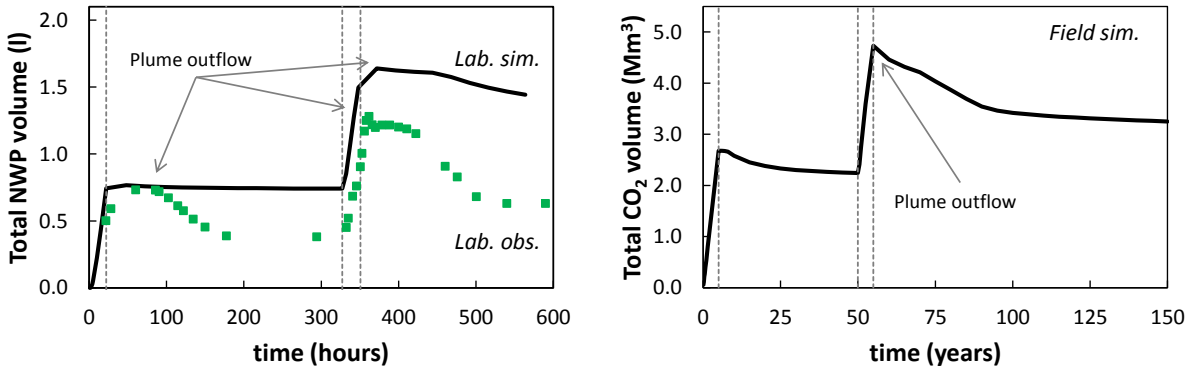

Figure 111 Zeroth moment evolution estimated from observed and simulated Soltrol plume in the laboratory scale (left) and from simulated $scCO_2$ plume in the field scale.

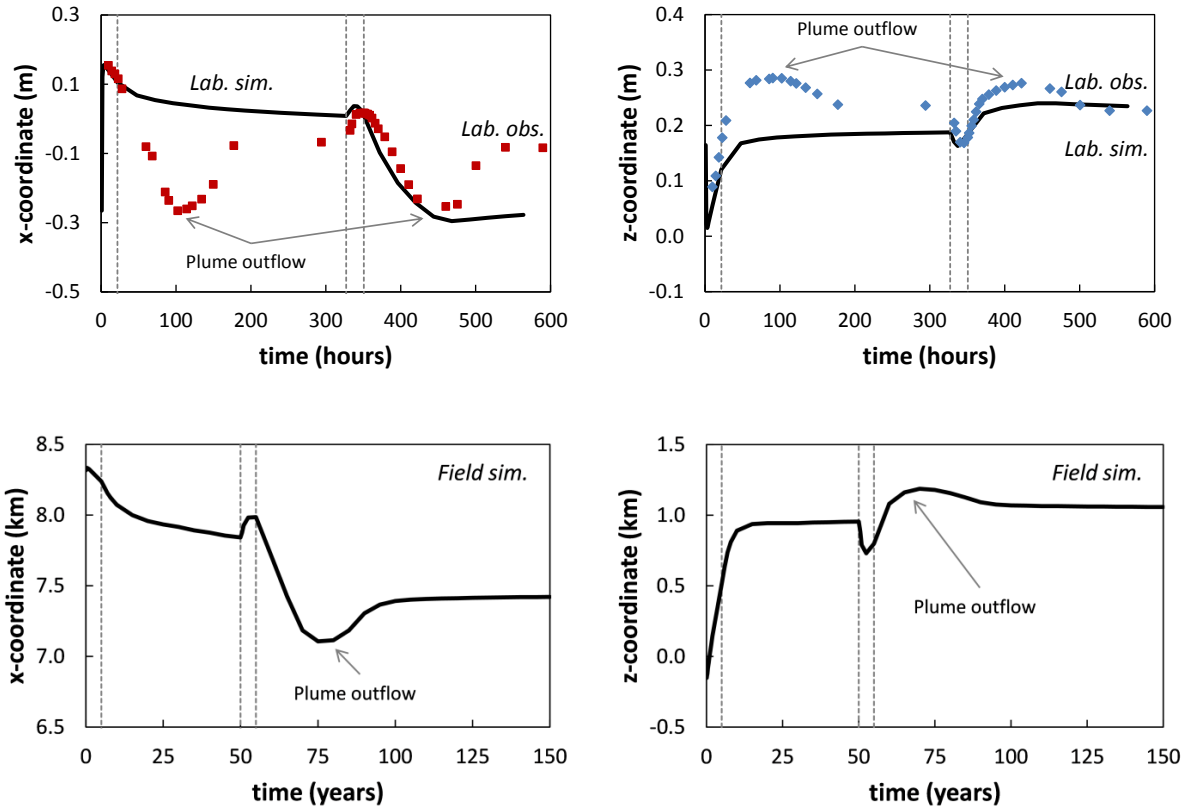

Figure 112 Horizontal (left) and vertical (right) coordinate of the plume's center of mass estimated by the first spatial moment observed and simulated in the large tank homogeneous experiment (top) and in the field-scale homogeneous simulations (bottom).

Vertical lines at first injection cease (22 hours; 5 years), and second injection onset and cease (327-350 hours; 50-55 years) for laboratory and field cases.

It can be seen from Figure 112 (top left) a discrepancy exists between observations and simulations during the first fluid redistribution phase; this behavior is caused by the failed reproduction of plume breakthrough observed in the experiments shortly after cease of the first injection event, as shown in Figure 109. An analogous trend is observed in the predictions at the field scale (bottom left). However, the counter-current displacement of the center of mass observed during the second injection is correctly reproduced by the model at both laboratory and field scales. Furthermore, the simulated rate at which the plume redistributes after the second injection is in agreement with the laboratory observation.

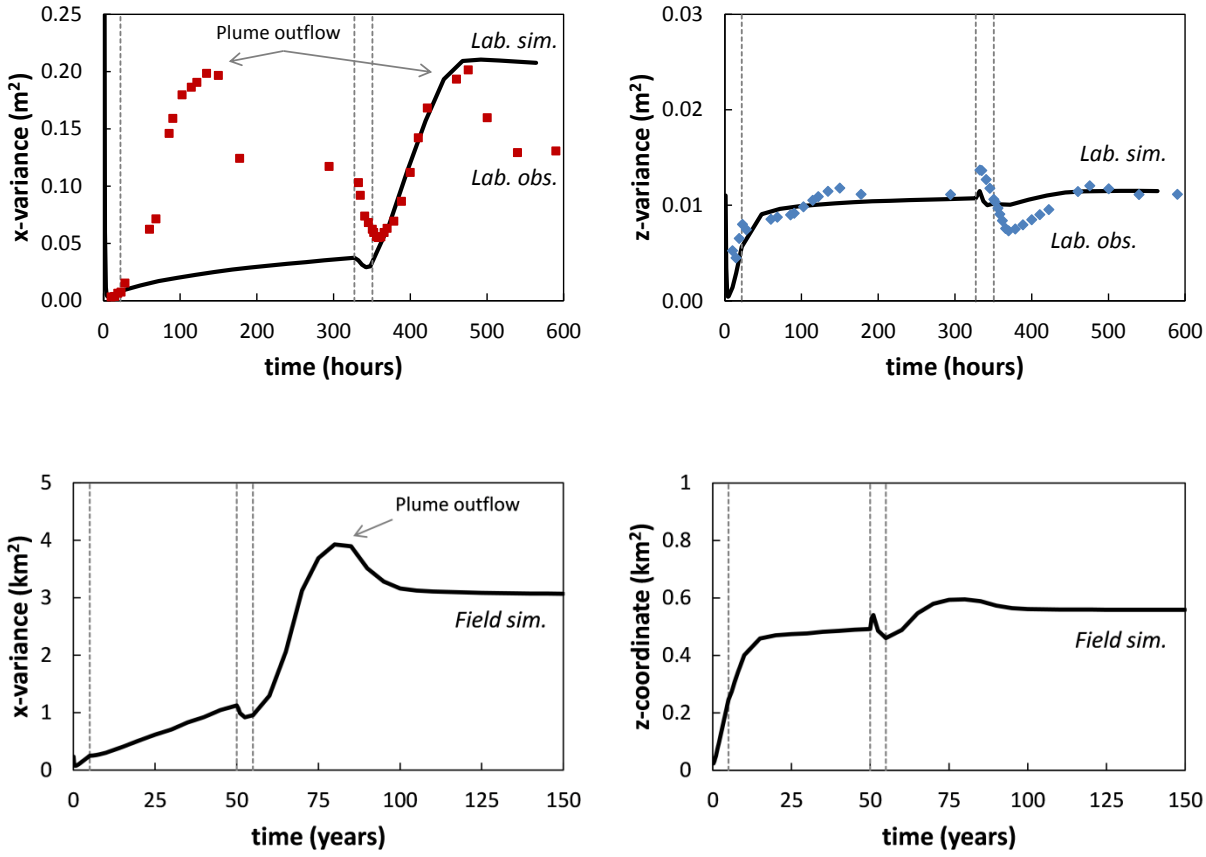

Figure 113 Horizontal (left) and vertical (right) variance of the plume estimated by the second spatial moment observed and simulated in the large tank homogeneous experiment (top) and in the field-scale homogeneous simulations.

The discrepancy between observed and simulated variance of the plume during the first redistribution period is due to the underestimated plume migration towards the outflow boundary; however, the simulated rate at which the variance increases after the second injection is in agreement with the laboratory observations (Figure 113, top). The second moment of the plume in the field-scale simulation (Figure 113, bottom) displays a similar trend to the laboratory-scale simulation; however, as shown in Figure 110, the faster migration during the first fluid redistribution and the plume outflow during the second fluid redistribution produce a variance evolution that better represents the laboratory observations.

End of 1st injection (27.4 hours)

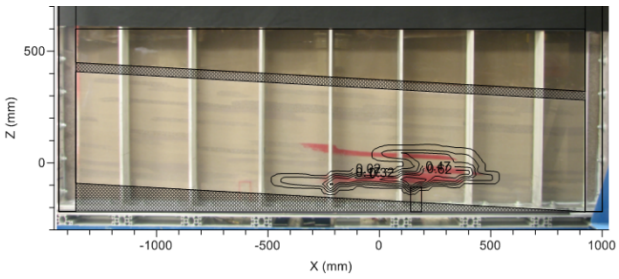

End of 1st fluid redistribution (283 hours)

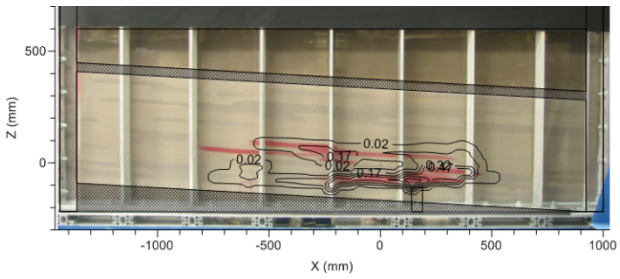

End of 2nd injection (410.7 hours)

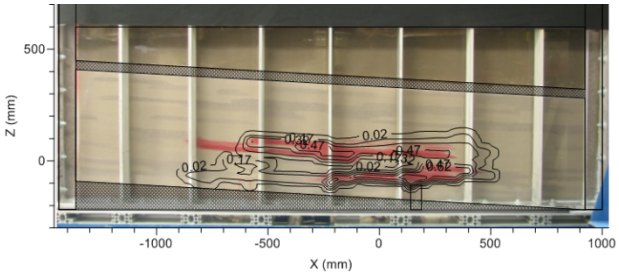

End of 2nd fluid redistribution (1349 hours)

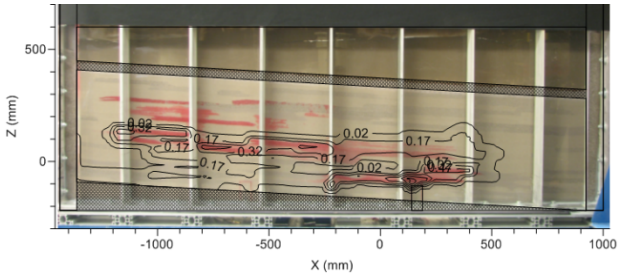

Figure 114 Saturation contours of Soltrol plume compared to the photographs at four representative times for the heterogeneous setup.

By overlapping simulated saturation contours and digital photographs it is possible to directly evaluate the goodness of model's predictions. As shown in Figure 114, there is some agreement between observations and simulations, at least during the plume distribution, until the

onset of the second injection event. However, at some point during the second fluid redistribution period, the simulated and observed plumes start to diverge significantly. One of the most interesting results from this heterogeneous experiment is represented by the rapid formation of secondary plumes after apparent equilibrium state of the plume during the second fluid redistribution period. These plumes eventually accumulate inside overlying layers with larger permeability, which eventually feed other secondary plumes. This type of flow patterns has been observed in field systems like the Utsira sand formation in the North Sea (Arts et al., 2008).

As expected, since the whole simulated NWP plume remained inside the flow domain, the 0^{th} moment corresponded to the total injected volume (Figure 115). As explained in section 5.1.3, the 0^{th} moment estimated from x-ray measurements quantified the plume volume above z=0, while the undetected NWP volume corresponded to the trapped portion of the plume below z=0, which in the case of the heterogeneous experiment, resulted to be approximately 400 ml.

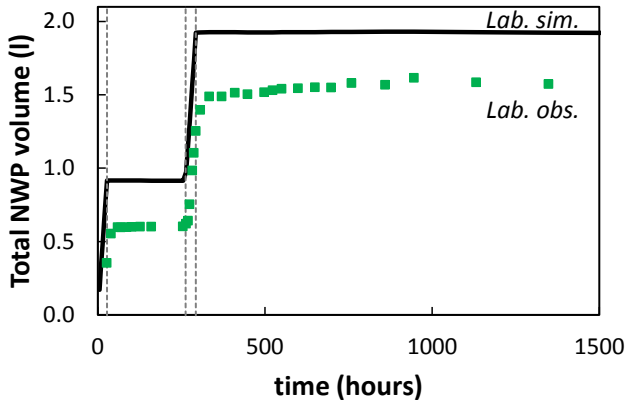

Figure 115 Zeroth moment evolution estimated from observed and simulated plume in the heterogeneous laboratory experiment.

Figure 116 presents observed versus predicted behavior of the first moment of the plume, showing failure of the model to capture the observed plume equilibrium after the first injection. The inability to match the observed behavior can be attributed to the incorrect representation of entry pressures for the laboratory sands involved in the experiment, leading to a faster propagation of the plume. Also, the predicted rate of plume migration after the second injection event seems to be overestimated at early times, while underestimated at late times.

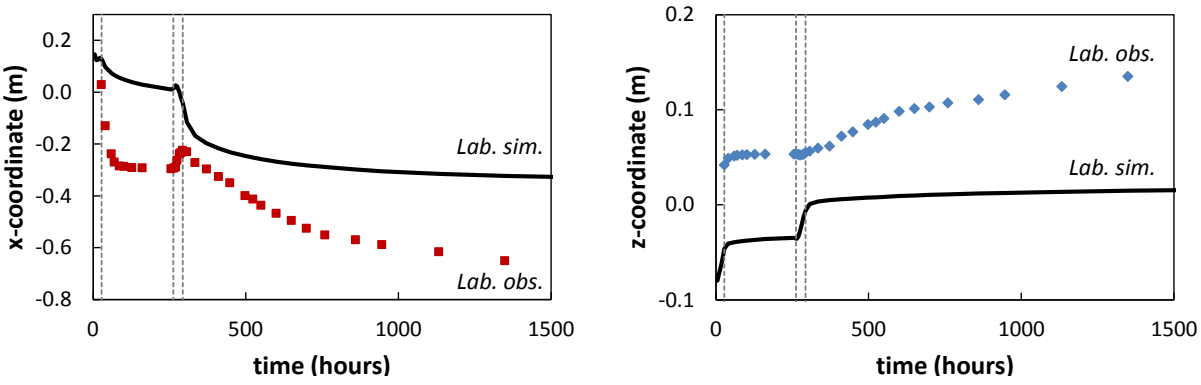

Figure 116 Horizontal (left) and vertical (right) coordinate of the plume's center of mass estimated by the first spatial moment observed and simulated in the large tank heterogeneous experiment. Vertical lines indicate the times of first injection cease (27.4 hours), and second injection onset and cease (283-410.7 hours).

The development of secondary plumes mentioned earlier can be verified by evaluating the second moment evolution along the horizontal direction. As shown in Figure 117, the observed horizontal variance reaches equilibrium early after cease of the second injection, although Figure 116 (left) shows that the horizontal center of mass continues to move leftwards. This behavior suggests that NWP saturations are redistributing within a zone of apparent stable variance. Around 500 hours, however, a secondary plume develops, filling overlying coarse layers and causing the horizontal spread of the plume to increase rapidly.

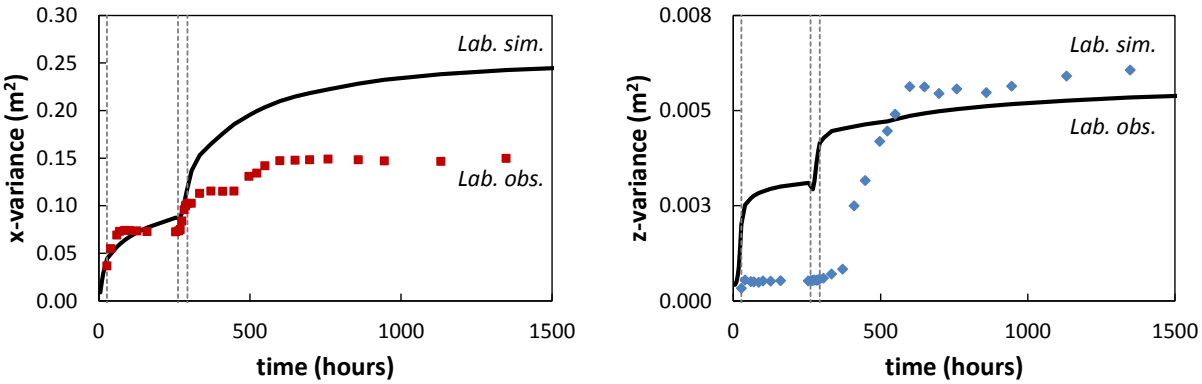

Figure 117 Horizontal (left) and vertical (right) variance of the plume estimated by the second spatial moment observed and simulated in the large tank heterogeneous experiment.

5.3 Numerical simulation of dissolution trapping phenomena

The goal of this numerical study was to evaluate the validity of the previous experimental findings for field-scale settings using a newly developed numerical model focusing on the influence of different permeabilities and thicknesses of low permeability layers on trapping of dissolved CO_2. A macroscopic (Darcian) numerical code simulating miscible flow of a binary fluid mixture was developed and tested. The developed code was verified with existing numerical solutions for unstable flow. The effects of porosity and permeability perturbations, and numerical grid resolution on density-dependent finger formations and model results were investigated. Then, the small tank experiments presented in Agartan et al. (2015a) (section 5) were simulated using the model for testing the ability of the model to represent convective and diffusive flow regimes observed in the experiments. Finally, using the numerical model, the sensitivity of permeability and thickness variations of relatively low permeability zones on trapping of dissolved CO_2 in multilayered formations was investigated in a field-scale setting. The Utsira formation in the Sleipner field having similar layered geological structure with the laboratory experiments (Agartan et al., 2015b) was simulated using the developed numerical model.

A single-phase, two-component, and density and viscosity-dependent flow and transport model was employed as a research tool to better understand contribution of diffusive and convective mixing processes on trapping of dissolved CO_2. This model uses a non-linear fully coupled solution method. The developed numerical model is based on a continuity equation (38), an Advection-Diffusion Equation (ADE) (39), and Darcy's Law (40) (Bear, 1972). Resulting non-linear coupled two partial differential equations (38) and (39) are discretized by the Finite Volume Method (FVM) and solved by Newton-Raphson (NR) method in a FORTRAN program. At each NR iteration, a preconditioned restarted Generalized Minimum Residual (GMRES) algorithm solves linearized system of equations.

$$\frac{\partial(\phi\rho)}{\partial t} + \nabla(\rho \boldsymbol{u}) = 0 \tag{38}$$

$$\frac{\partial(\phi\rho w)}{\partial t} + \nabla(\rho w \boldsymbol{u} - \phi D \rho \nabla w) = 0 \tag{39}$$

$$\boldsymbol{u} = -\frac{\boldsymbol{k}}{\mu}\left(\nabla P + \rho g \nabla z\right) \tag{40}$$

Continuity equation without the source term (Bear, 1972) is shown in equation (38), where ρ is the density of the solution (kg/m^3), u is the Darcy flux (m/s), and ϕ is the porosity (-). $\boldsymbol{u}$ is a vector in 2D and 3D. ADE (Bear, 1972) for the transport of dissolved CO_2 in brine is given in equation (39), where w is the mass fraction of the solute (kg/m^3), and D is the diffusion coefficient (m^2/s). In equation (40), Darcy's Law (Bear, 1972) is given, where k is the permeability of the medium (m^2), g is the gravitational acceleration (m/s^2), P is the pressure (Pa), and μ is the viscosity of the solution (Pa.s). In the small tank density-driven flow experiments, Agartan et al. (2015a) used propylene glycol (PG) for brine and red food dyed water for $scCO_2$, where density and viscosity of the solution only depend on the mass fraction of solute (water) as given in equations (41) and (42), respectively.

$$\rho = 85.935w^3 - 217.62w^2 + 88.425w + 1034.1 \tag{41}$$

$$\mu = 4.4968\times10^{-2}\exp\left(-3.8613w\right) \tag{42}$$

5.3.1 Verification with the Elder Problem

The numerical code was verified with the 1-D analytical solution of the ADE without density and viscosity-dependence to check the validity of the computational algorithms. In addition, the Elder problem (Elder, 1967) was solved and compared with existing numerical results to verify the ability of the model to simulate a fluid flow driven by density differences only (i.e. viscosity is fixed.).

Elder (1967) examined the convective flow experimentally and numerically. Due to limitations in the Hele-Shaw cell experiments, Elder (1967) studied thermally driven convection in a closed rectangular box shaped vertical model. The flow in the box was initiated by a vertical temperature gradient. In the numerical study, Elder (1967) employed a finite difference representation of the governing equations for vorticity, stream function, and thermal energy balance. Eighty lateral and forty vertical nodes were used, and time discretization was set to reach the first point of the comparison (1 year) in 20 time steps (Hassanzadeh et al., 2005; Simpson and Clement, 2003; Voss and Souza, 1987). Voss and Souza (1987) modified the Elder problem into a variable density groundwater flow. The fluid density was as a function of salt concentration.

In this study, we assumed that solute and temperature transport in porous media are governed by similar balance equations (using analogy between Fourier's law for conduction and Fick's law for diffusion). We solved the Elder problem in terms of salt mass concentration for a saltwater intrusion problem in a homogeneous porous medium initially saturated with fresh water. A 300 m long source of saltwater with a salt mass fraction of "1" was placed to the middle of the top as a fixed concentration boundary condition (Figure 118). Zero mass fraction of the salt was applied to the entire base. At each upper corner, a pressure was specified as "1 atm", and the initial pressure was hydrostatic. All other sides were set as no flow and no mass flux boundary conditions (Simpson and Clement, 2003). Simulation parameters for the Elder problem are given in Table 20. In the simulations, 160 lateral and 80 vertical grid cells were used, and maximum time step was 1 month.

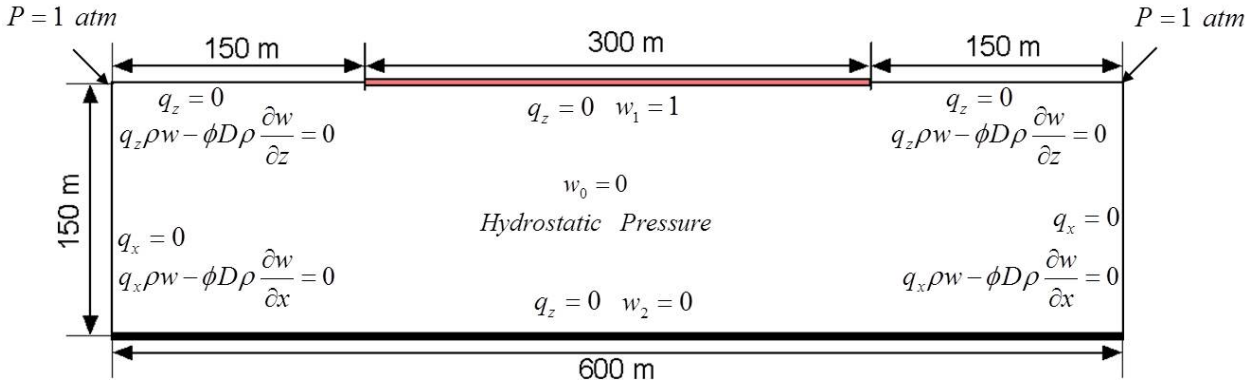

Figure 118 Initial and boundary conditions of the Elder problem.

Table 20 Simulation parameters for the Elder problem (Voss and Souza, 1987).

Parameter	Value
Permeability, k (m^2)	4.845×10^{-13}
Porosity, ø (-)	0.10
Diffusion Coefficient, D (m^2/s)	3.565×10^{-6}

The saltwater released into the fresh water, forced the solute to move into fresh water in the vicinity of the source zone through diffusion. This increased the density of water, and eventually, the denser fluid started to move towards the bottom of the porous medium by convective flow formed in the system. The 1-, 2-, 4-, 10-, 15-, and 20-year results of Elder (1967) and the present model are compared in terms of salt mass fraction distribution. The results for 0.2 and 0.6 ratios of salt mass fraction (w) inside the box to the maximum salt mass fraction

($w_1 = 1$) applied from the top boundary are given in Figure 119. The timing of the processes and the initiation, evolution, and final spreading of the convective fingers match reasonably well with the Elder's results. These results (Figure 119) verify the numerical solution methodology used in the model.

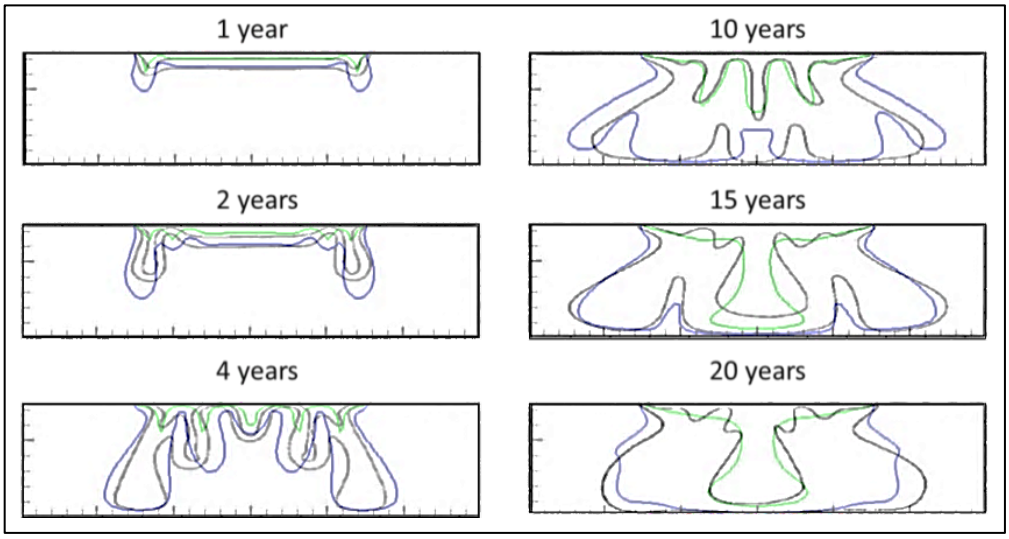

Figure 119 Comparison of the results of Elder (1967) (Black lines for 0.2 and 0.6 w / w_1) and the present code (Blue lines for 0.2 w / w_1 and green lines for 0.6 w / w_1).

5.3.2 Model Comparison with the Small Tank Experiments

a. Sensitivity of the Numerical Model Parameters

In the experiments conducted by Agartan et al. (2015a), the miscible fluid (red food dyed water as $scCO_2$) non-uniformly distributed in the source zone immediately after the injection-extraction period (lasting about ~15 seconds) (Figure 120). This non-uniform distribution might have occurred due to injection scheme, pore-scale heterogeneities, and other possible small-scale heterogeneities formed during the packing procedure of the sand materials. Perturbations in geometry, initial conditions, and material properties can trigger instabilities in transport paths of fluids. Density and viscosity gradients in the systems with perturbations lead to convective fingering phenomenon. Resolving the convective fingering accurately by a numerical model requires using very high spatial and temporal resolutions. Moreover, errors resulting from numerical solution procedure with finite tolerances have influence on onset of convection and finger evolution. The porosity and/or permeability perturbations should be added to the model to

overcome the numerical errors associated with the solution space (Pau et al., 2010). The sensitivity of the model parameters was examined by using the similar approach with Pau et al. (2009, 2010).

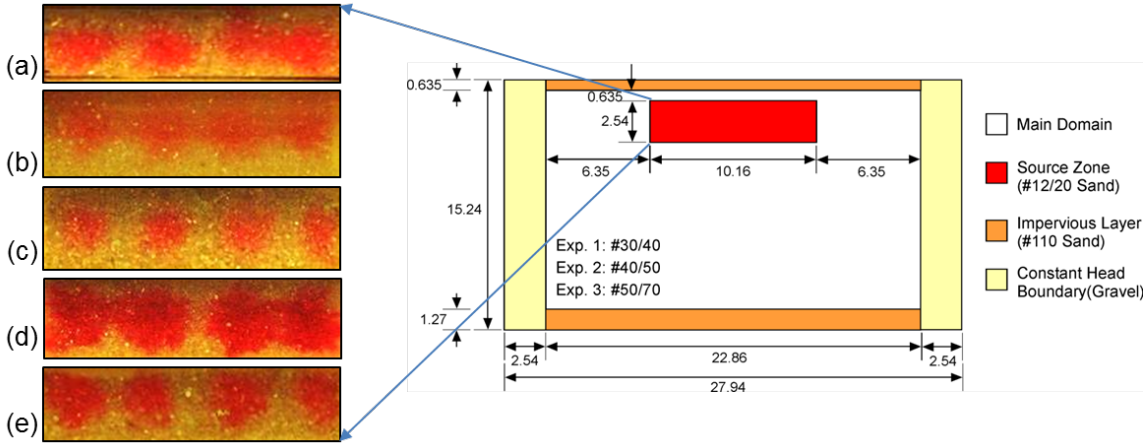

Figure 120 The distribution of the source in the source zone after injection-extraction period for (a) #30/40, (b) #40/50 and (c) #50/70 homogeneous, and (d) 2nd (multilayered system) and (e) 3rd (rectangular blocks) heterogeneous small tank experiments.

Pau et al. (2009; 2010) investigated the influences of simulation parameters, such as grid resolution, porosity and permeability perturbations, solver tolerances, and domain size, on the solution using the block-structured adaptive mesh refinement method. They assumed a 2-dimensional (2-D) isothermal and homogeneous domain with a layer of CO_2-saturated brine at the brine/CO_2 gas interface, which allows using a variable-density, single-phase, and incompressible model to treat the dissolution-diffusion-convection processes. The focus of their study is the dependence of the stabilized mass flux and the onset time of convection on the simulation parameters. The onset time of convection determines the time at which convection becomes an important transport mechanism. They found that the onset time decreases with increasing fluctuation strength, and the porosity fluctuations are more effective in triggering instability than permeability fluctuations.

In this study, the sensitivity of the grid resolution and porosity and permeability fluctuations on the model results were examined. The simulations were carried out for the surrogate fluid combination (PG and water) used by Agartan et al. (2015a) in the small tank experiments (Figure 121). The initial mass fraction of water in the 0.508 cm thick source zone was assumed to be 0.194. As the tank was a closed system, no flow boundary conditions for pressure and water concentration were assigned to the bottom and the vertical sides. The

boundary condition at the top was specified as constant pressure equal to atmospheric pressure, and no flux boundary condition was assumed for water. Fluid and formation properties are listed in Table 21.

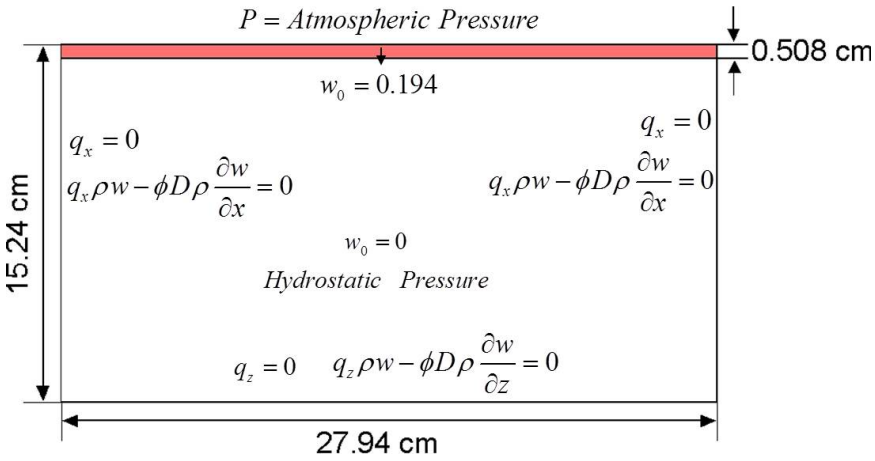

Figure 121 Initial and boundary conditions of the numerical model (not to scale).

Table 21 Fluid and formation properties.

Parameter	Value
Density of PG, ρPG (kg/m3)	1034.6
Viscosity of PG, μPG (Pa.s)	0.055
Density of water, ρw (kg/m3)	1000
Viscosity of water, μw (Pa.s)	0.001
Permeability, k (m2)	1.079×10-10
Effective diffusion coefficient, Deff (m2/s)	8.0×10-11
Porosity, ø (-)	0.325
Mass fraction of water, w (-)	0.194
Density increase due to water dissolution, Δρ (kg/m3)	9.1
Gravitational acceleration, g (m/s2)	9.81

The 1, 2, 5, 10, and 25% porosity and/or permeability perturbations were applied to trigger the fingers (Figure 122). The total water mass remained in the source zone were determined to analyze the influences of porosity and/or permeability fluctuations on the onset time of convection. The faster mass depletion indicates an early onset time of convection. The

results in Figure 122 showed that the onset time for convection decreases with increasing porosity fluctuations. This emphasized the effectiveness of variable porosity fluctuations in triggering convective instabilities compared to permeability fluctuations. In this system porosity fluctuation has more effect on the flow compared to the permeability variations.

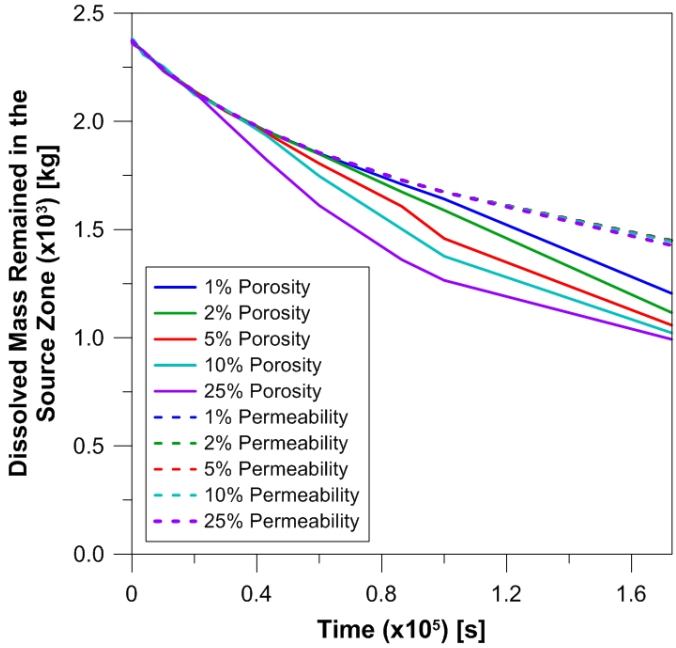

Figure 122 The effects of porosity (ø) and permeability (k) fluctuations to the onset of convection.

According to Riaz et al. (2006), for convective mixing studies, the grid resolution should be smaller than the critical wavelength (λ_c) of the convective finger to capture the initiation of convection accurately. The critical wavelength of this system was determined using equation (43), where $\Delta\rho$ (kg/m^3) is the density difference between the solution and the brine representative fluid (PG).

$$\lambda_c = \frac{2\pi\mu D}{0.07k\Delta\rho g} \tag{43}$$

λ_c was calculated to be 1.770 cm. The selected domain is almost 15 times longer than the critical wavelength. In the grid resolution study, the coarsest grid size was selected as 0.5080 cm, which was smaller than critical wavelength, and 0.25% porosity fluctuation was assigned. According to Pau et al. (2009; 2010), after reducing the grid size by half, the porosity fluctuation

should be doubled to get a better convergence. The same method was applied in this study. The grid sizes and corresponding porosity fluctuations are listed in Table 22.

The results are summarized in the graph in Figure 123. The total water mass remained in the source zone at different times converged to a single value for the porosity fluctuations which were greater than 2.0% (Figure 123). However, for the smaller porosity fluctuations, the significant variations in the total water mass were observed in the source zone because the applied perturbations were not enough to overcome numerical errors which generates fingers in the system.

Table 22 Grid sizes and porosity fluctuations.

Grid Size (cm)	Porosity Fluctuation (%)
0.5080	0.25
0.2450	0.50
0.1270	1.00
0.0847	1.50
0.0635	2.00
0.0508	2.50
0.0423	3.00

For this study, the coarser grid size should be equal or smaller than 0.0635 cm, and minimum porosity fluctuation should be equal or greater than 2.0% to overcome the effects of numerical errors and produce convective fingers as a result of porosity perturbations. Therefore, the results of the present study are consistent with the Pau et al.'s (2009; 2010) findings.

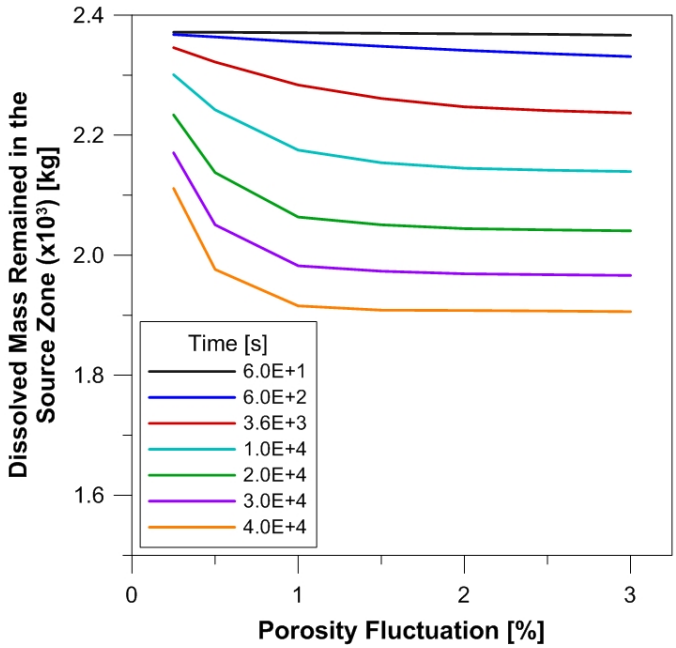

Figure 123 The effects of grid resolution to the onset of convection.

b. Numerical Simulations of the Small Tank Experiments

The small tank experiments presented under homogeneous and heterogeneous packing configurations by Agartan et al. (2015a) were simulated to test the ability of the model for representing the flow and transport processes observed and recorded in the experiments. The experiments were carried out using a small tank with 27.94 cm × 15.24 cm × 2.54 cm (length × height × width) dimensions. The simulations were performed for the surrogate fluid combinations of propylene glycol (PG) (brine) and water ($scCO_2$) which were used in the experiments.

In the experiments, the synthetic aquifer domain consisted of four zones that included the main mixing domain, the source zone, the impervious caprock and bedrock, and the gravel columns to control the flow across the tank (Figure 31). The permeability and porosity of the sands for tightly packed condition were determined in the prior experimental studies by Sakaki and Illangasekare (2007), Schroth et al. (1996), Smits et al. (2010), Wietsma et al. (2009), and Zhang et al. (2008). The permeability field in the tank could be different from the previously measured values due to imperfection of the packing. The sensitivity of the permeability suggested that when the permeability values close to the upper limit of the tightly packed conditions were assigned to the sands in the numerical models, the concentration distributions

matched reasonably well with the experimental results. The range of permeabilities and porosities are listed in Table 23.

Table 23 Properties of the sands.

Sand	Permeability ($\times 10^{-10}$) (m^2)	Porosity (-)
#12/20	3.830[a] - 5.230[b]	0.318[a]
#20/30	2.340[a] - 2.780[b]	0.320[a]
#30/40	1.080[a] - 1.520[c]	0.325[a]
#40/50	0.530[a] - 0.736[c]	0.334[a]
#50/70	0.311[a] - 0.346[e]	0.372
#50w	0.170[d] - 0.258[d]	0.301[d]

[a]Smits et al. (2010)
[b]Wietsma et al. (2009)
[c]Schroth et al. (1996)
[d]Sakaki and Illangasekare (2007)
[e] Zhang et al. (2008)

No flow and no flux boundary conditions for pressure and water concentration were assigned to left, right, and bottom boundaries. The top boundary was specified as atmospheric pressure and no flux for water concentration. The initial concentration of the water within the test domain was set to zero. The distribution of the source in the source zone after the injection, the small scale heterogeneities at the coarse/fine sand interfaces, and the imperfections of packing cause formation of non-uniform flow field which leads to the occurrence of convection. The final distributions of the source in the source zone shown in Figure 120 for all of the modeled experiments were discretized for each case. The equal amount of red food dyed water was assumed to be injected into each grid in 15 seconds, which was the total time of the injection-extraction cycle applied to the experiments by Agartan et al. (2015a). In addition, a 10% porosity fluctuation, which is greater than the critical value 2.0%, was added to the system to overcome the numerical errors. In order to characterize the onset time of convection accurately, the source zone was discretized with 0.0635 cm grid size, which is equal to the critical wavelength of the convective finger for this domain. The grid size increased to the sides of the tank.

An effective diffusion coefficient of 8×10^{-11} m^2/s was used to simulate all of the small tank experiments. An adaptive time stepping was used in the numerical model with a maximum

time step of 1 hour. The simulations were carried out for the same time periods with the experiments (7 days for homogeneous and 6.5 to 33 days for heterogeneous cases).

The simulation and experimental results were compared to verify the ability of the model to capture convective and diffusive flow regimes observed during the experiments. For homogeneous formations, the initiation and evolution of the density-driven convective fingers at variable permeabilities is important to simulate. In addition, the spreading characteristics of the dissolved mass at the transitions of the high/medium and low permeability sands should be captured. The timing of the observed processes and the total time of the experiment should also match with the simulation results.

The comparison of the general fingering and spreading characteristics of #30/40 sand homogeneous medium experiment (Agartan et al., 2015a) and numerical model is given in Figure 7. The accurate simulation of the homogeneous and layered media processes is very crucial because the goal is to investigate the mixing and storage in stratified systems. The formation of the fingers observed in the experiment at 12 hours is similar with the numerical model in Figure 124a and c, respectively. The results at 7 days (Figure 124b and d) match reasonably well for the final distribution of the dissolved mass in the domain in regarding to the finger depth and width and the total time of the processes.

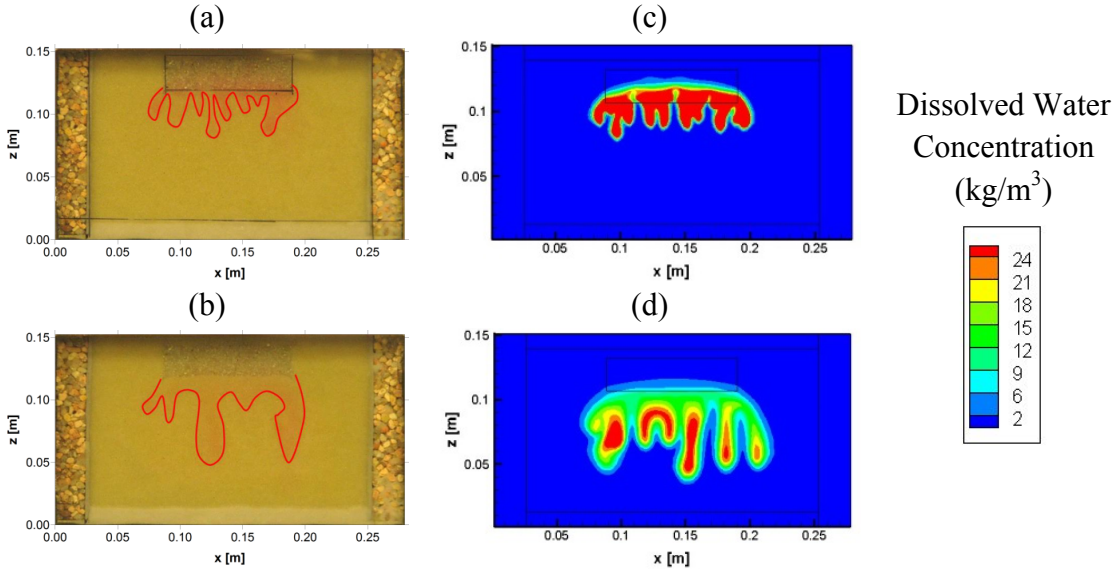

Figure 124 Experimental (a, b) and simulation (c, d) results of #30/40 sand homogeneous case: (a, c) 1.5 days, and (b, d) 1 week.

Figure 125 shows the comparison between the experimental and numerical model results in the layered heterogeneity case. In this experiment, Agartan et al. (2015a) used alternating

layers of #50w, #20/30, #40/50, and #30/40 sands. The total time of the experiment was 18 days. The results demonstrated that the spreading characteristics at the sand transitions including merging of fingers (Figure 125a and d), lateral spreading (Figure 125a and d), diffusion into the low permeability layer (Figure 125a, b, d, and e), and reformation of the fingers in the high or medium permeability sand layers (Figure 125b, c, e, and f) were simulated reasonably as well as the initiation of the fingers and the total timing of the processes.

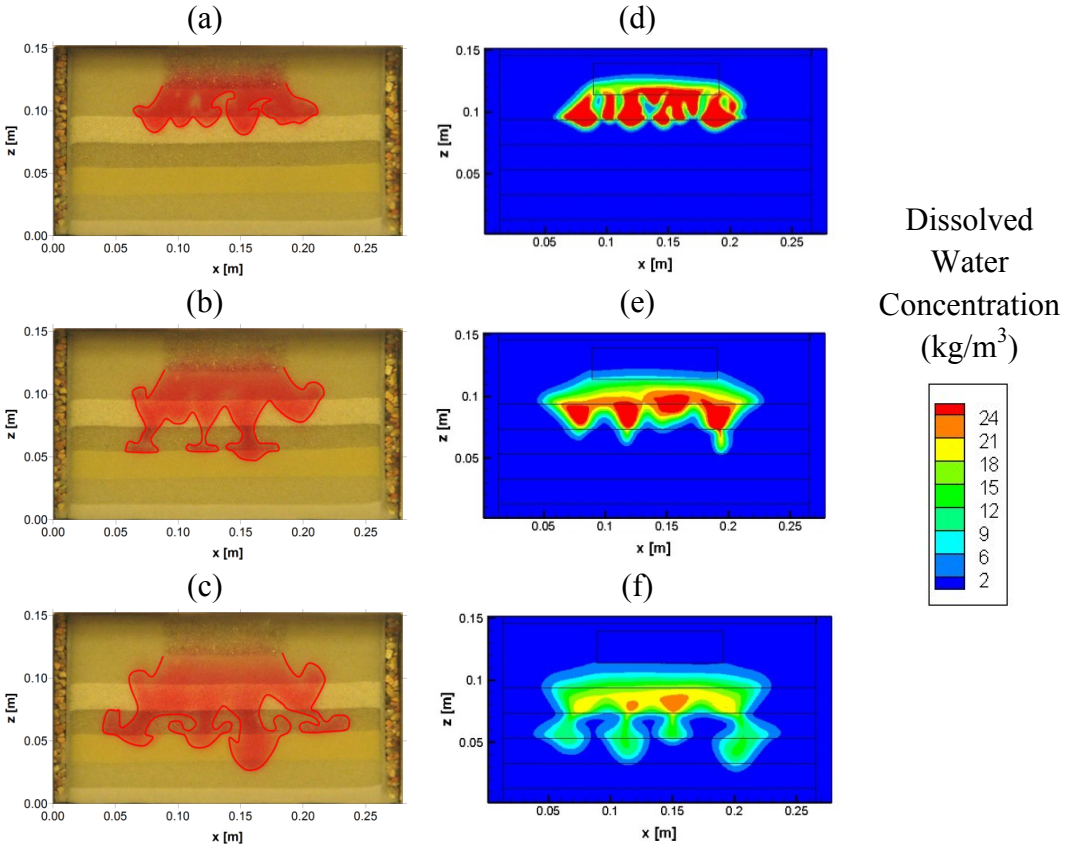

Figure 125 (a) Experimental (a. b, c) and simulation (d, e, f) results of layered media case: (a, d) 3 days, (b, d) 9 days, and (c, e) 18 days.

The experimental and simulation results for the propagation of the longest finger from the bottom of the source zone were compared for all cases. The results in Figure 125a showed that the evolution of the fingers at different permeabilities with time for homogeneous formations captured very well. The location of the longest finger estimated by the model at a certain time was comparable with the experimental results for the layered and block heterogeneities given in Figure 125d.

In addition to the visual comparison, the quantitative analysis was performed using the image processing method developed by Agartan et al. (2015a). For the image processing method,

the periodically taking pictures of the experiments were used to determine the dissolved water concentrations in the tank. The small tank was packed with different water concentrations using the sands listed in Table 23 to analyze the changes in the light intensities. Therefore, the relationships between light intensity and water concentrations were developed by Agartan et al. (2015a) for each sand. After the calculation of the concentrations, variations in the first and second spatial moments with time was determined for each experiment (Figure 125b, c, e, and f). First moment gives the location of the center of the mass, and second moment is related to the spreading of the plume from the center of the mass (Freyberg, 1986).

For the homogeneous formations, the first and second moments in z-direction were compared. From the generation of the fingers to the final distribution, the dependence of vertical spreading on the permeability of the medium was simulated accurately (Figure 125b and c). For example, for the experiment with higher permeability sand, the center of mass located in the deeper parts compared to others for the same time frame. The results of these tests stated that the code can capture the generation of density-driven convective fingers, the effects of permeability on spreading in homogeneous experiments.

The changes in the center of mass in z-direction and the spreading in x and z directions with time for layered and block heterogeneous cases provide a good match between experimental and numerical results for the processes observed at the transition of the different permeability sands in layered-heterogeneous media experiments (Figure 125e and f). The physics of density-driven flow in a layered medium were captured reasonably well by the developed model (Figure 125d, e, and f).

(a) (b)

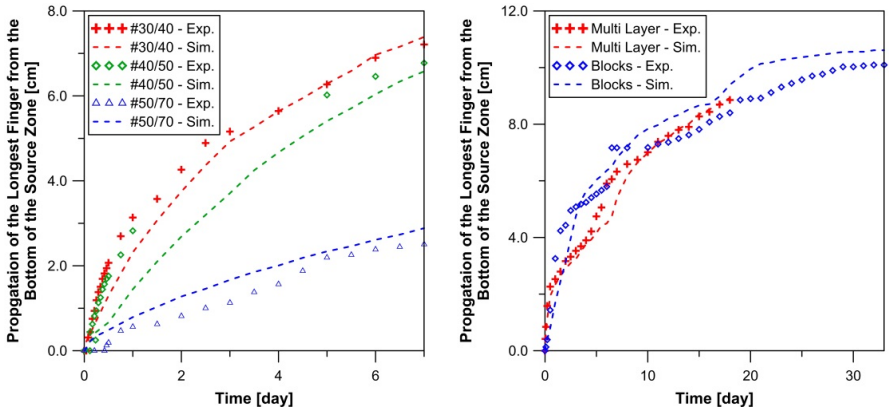

(c) (d)

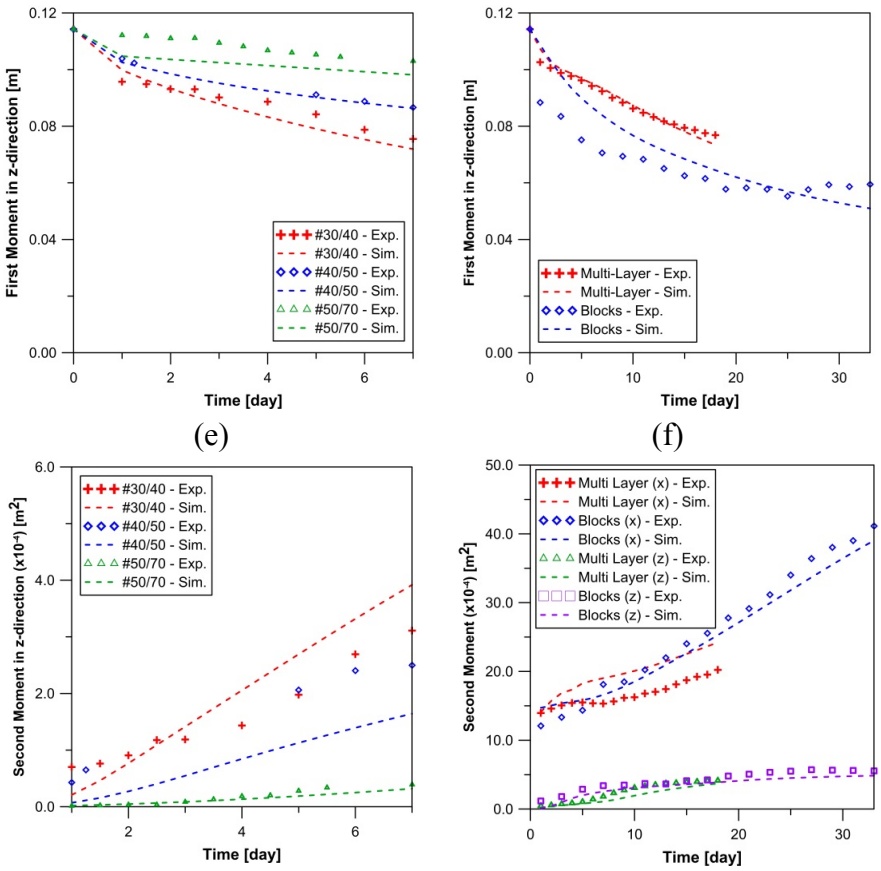

Figure 126 Comparison of the experimental and modeling results for homogeneous (a, c, e) and heterogeneous experiments (multilayered system and rectangular blocks heterogeneity) (b, d, f): Propagation of the tip of the longest finger for (a) homogeneous and (b) heterogeneous cases, first moments in z-direction for (c) homogeneous and (d) heterogeneous cases, and second moments in x- and z-directions for (e) homogeneous and (f) heterogeneous cases.

The capability of the model for representing the experimentally observed and recorded flow and transport processes was tested in order to simulate the selected scenarios accurately. The simulations were performed using the surrogate fluid combination (NaBr solution and water) at the large tank scale with 243.84 cm x 121.92 cm x 7.7 cm (L x H x W) internal dimensions under the same flow and transport conditions with the experiment. In the experiment, the synthetic porous medium composed of four main zones including the main mixing domain (#40/50), the source zone (#8), the low-permeability layer, and the vertical columns to control boundary conditions (#8). The low-permeability layer was packed with #110 sand and silt. An average permeability and porosity were assigned to silt material as 10-16 m2 and 35% (Freeze

and Cherry, 1979), respectively. The permeability field in the tank could be different from the previously measured values due to imperfections in the packing.

The constant head boundary conditions were assigned to the left and right vertical boundaries to simulate background hydraulic gradient (i=0.0008, analogues value to Gulf Coast from Hubbert, 1953). The time dependent flux boundary condition was assigned to the 50 cm long 1 cm thick zone in the middle of the source zone in order to capture the source creation accurately. The 560 ml of source fluid was injected with 10 ml/min flow rate, and then in the second period the 620 ml source was injected at 1ml/min rate. A 10% porosity fluctuation was added into the materials to trigger the fingers and represent imperfections in the packing. A diffusion coefficient of 1.6×10^{-10} m^2/s was used (Oostrom et al., 1992). An adaptive time stepping was used in the numerical model with a maximum time step of 1 hour. The simulations were carried out considering three periods as was simulated in the experiment: (1) the first background flow and source injection for 8 days, (2) the static conditions for 11 days, and (3) the second background flow (i=0.004) (16 days). Total time of the experiment and model was 35 days.

5.3.3 Simulation Results of the Heterogeneous Large Tank Experiment

The results of the heterogeneous medium experiment and the simulation were compared for each period in Figure 127. The model accurately captured the movement of the center of mass in x and z directions with time (Figure 128a and Figure 128b, respectively), the onset of fingering and the migration of density-driven fingers (Figure 128), the final distribution of the mass in the tank (Figure 127a), and the spreading of the mass under static conditions (Figure 128a and Figure 128b). However, only one of the fingers generated in the lower aquifer was simulated (Figure 127b). The reason of this can be the amount of dissolved mass accumulated on each side of the fresh water leakage (Figure 127a), and this depends on the location of the fingers generated from the source zone. The model simulated larger fingers at the edges of the source zone, whereas most of the fingers were generated in the middle of the source zone in the experiment. The higher concentration mass accumulated under the source zone generated the second finger in the lower aquifer in the experiment. When the second background flow started, the experiment needed some time to reach the steady state. However, in the model, the steady state flow was simulated simultaneously. This caused the differences in the mass depletion

curves of the experiment and the model at initial times. The oscillations in the flow rates of the upper aquifer observed in the experiments cannot fully characterized in the numerical model. After the second background flow, the majority of the mass was trapped in the silt zones located in left, middle, and right sides of the low-permeability layer in the experiment. The model captured the locations of the trapped mass (Figure 121). However, the model calculated the trapped mass as 10.43% whereas the results of the experiment reported as 12.50% (see Figure 129). The relative error between the experiment and simulation is calculated as 16%. The more mass was flushed away in the model as opposed to the experiment. The initial flow rates and the flow rates in the upper aquifer in the tank with respect the model can be reasons of this difference.

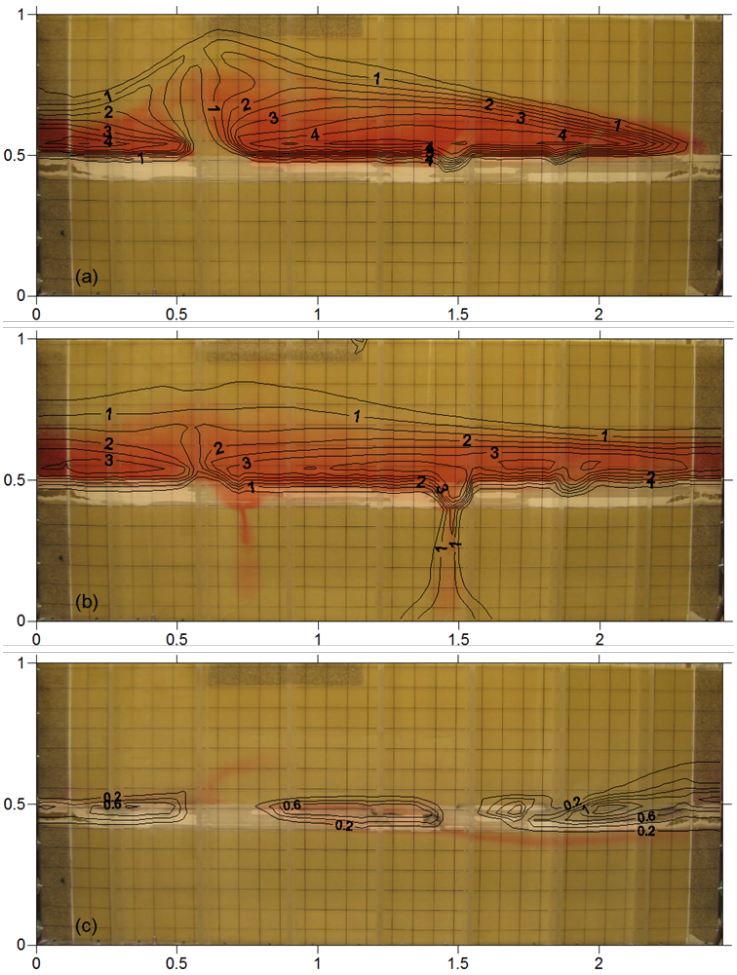

Figure 127 Comparison of the experimental and modeling results at the end of each period. (a) End of the first background flow, 8th day, (b) the static conditions, 19th day, and (c) the second background flow, 35th day (units are in m).

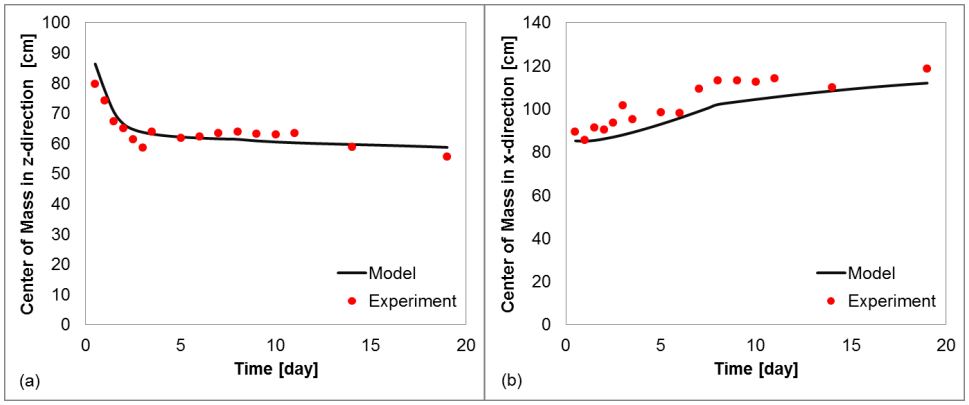

Figure 128 Comparison of results of experiment and modeling in the aspect of center of mass in (a) z and (b) x directions.

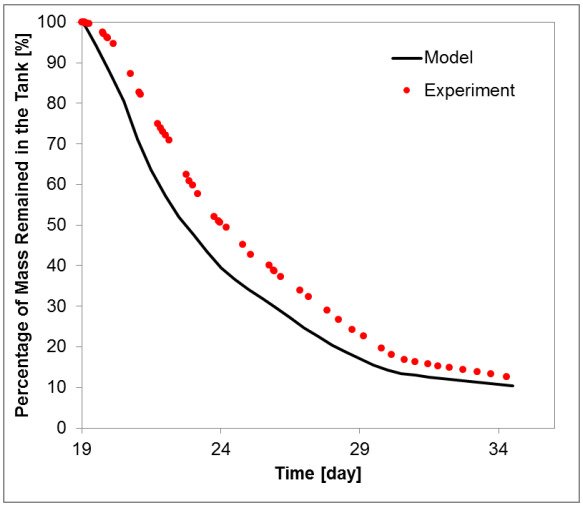

Figure 129 Comparison of the experimental and simulation results for the percentage of mass remained in the tank versus time.

5.3.4 Tested Scenarios

As mentioned before, the heterogeneity of the low-permeability layers varies depending on the fracture and/or the distribution of the particles. Based on this knowledge, the different randomly distributed fields of silt and #110 sand having the same one-to-one material ratio were simulated under the similar flow and transport conditions with the heterogeneous experiment. The realizations in Figure 130 were created using the same 2-D vertical rectangular array and the same SIS algorithm in SGeMS with the realization used to pack the low-permeability layer in the heterogeneous experiment. The correlation lengths and silt and #110 sand volume ratios of the selected cases are presented in Table 24 and Figure 130, respectively.

Table 24 Correlation lengths and distribution of the different realizations. Red color is for #110 sand, and blue color is for silt.

No.	Correlation Length (x) [m]	Correlation Length (z) [m]	Distribution
1	0.5	0.03810	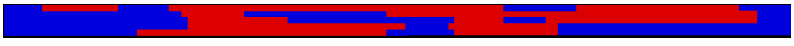

2	0.5	0.03810	
3	0.1	0.03810	
4	0.1	0.07620	
5	1.0	0.01905	

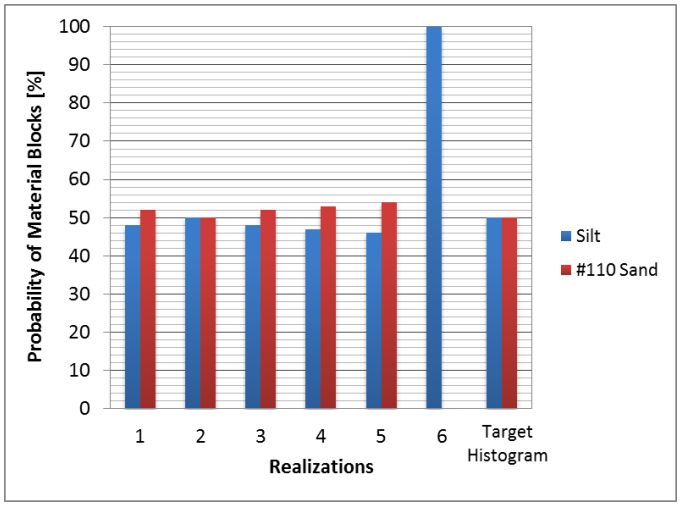

Figure 130 Probability of each material block for each case compared with the target histogram.

These realizations were selected to analyze the mixing and trapping of dissolved mass under variable vertical and horizontal #110 sand connectivity. The first realization in Table 24 is showing the packing of the low-permeability layer in the heterogeneous experiment. The second realization had the same correlation lengths with the first one (Table 24) but there were less #110 sand connectivity in vertical direction. In the third and fourth realizations, the more vertical connectivity was present in order to analyze the effects of enhanced vertical #110 sand connectivity and diffusion area of silt on mixing and storage. The last one had longer horizontal that doubles the source zone length and smaller vertical correlation lengths, and limited vertical connectivity between the two aquifers. These realizations were selected to investigate the behavior of the dissolved mass under different conditions, and the results of these simulations were compared with the pure silt case.

5.3.5 Modeling Results

The contributions of convective mixing, diffusion controlled trapping, and back diffusion to the mixing and long-term trapping of dissolved mass were investigated for different distributions of low-permeability materials with the same volume ratios, and the results were compared with the pure silt case. In all of the realizations including pure silt packing, the density-driven fingers were generated after the release of the source and the fingers got merged at the sand and low-permeability layer transition. The spreading of the dissolved mass after merging of the fingers showed variability depending on the distribution of silt and #110 sand. The results after each period (8^{th} day, 19^{th} day, and 35^{th} day) for each realization and silt are presented (Agartan, 2015).

The vertical connectivity in the low-permeability layer enhanced the leakage of the fresh water into the upper aquifer from the lower aquifer as observed in the heterogeneous experiment. The more connectivity of #110 sand in the realizations #3 and #4 caused more fresh water leakage (Figure 122d and Figure 123a). The limited vertical connectivity in the realizations #2 and #5 prevented the leakage of significant amounts of the fresh water and showed more diffusive spreading into the low-permeability layer (Figure 122a and Figure 123d, respectively). In the pure silt packing case, the similar spreading behavior was observed with the realizations #2 and #5 (Figure 133a).

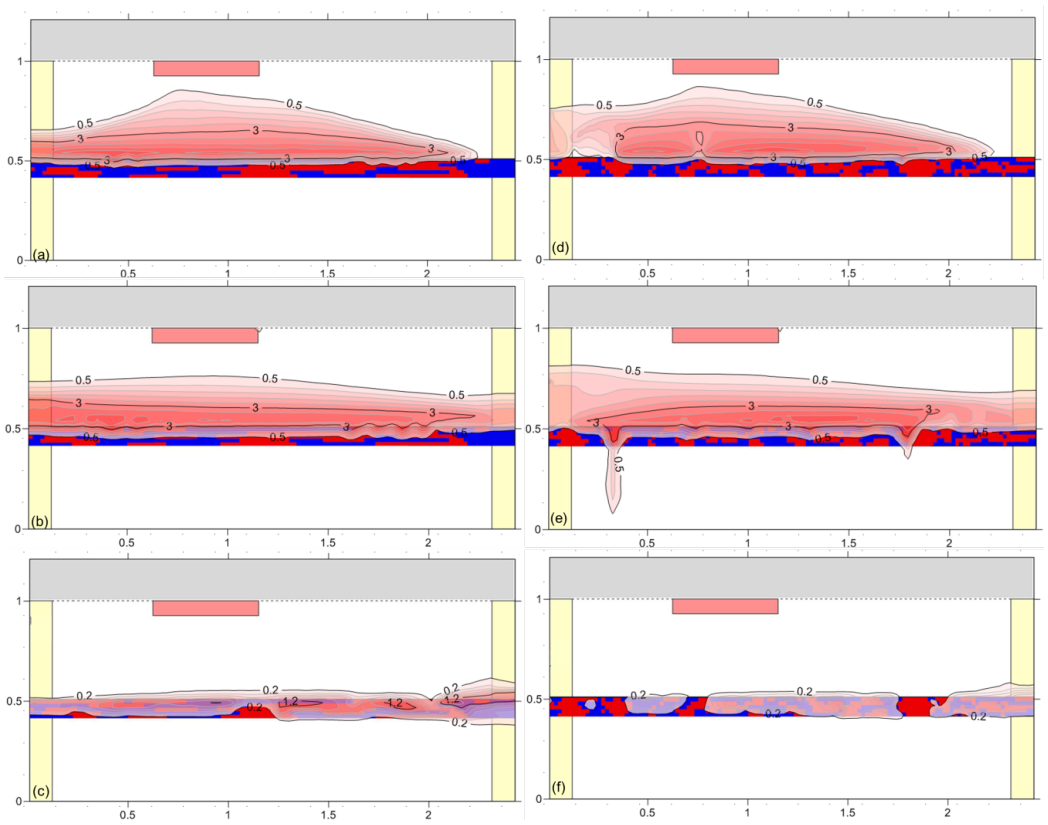

Figure 131 The results of realization #2 (a, b, c) and #3 (d, e, f) at the end of each period: (a, d) 8th day, (b, e) 19th day, and (c, f) 35th day, respectively.

Under the static conditions, the fresh water leakage from the lower aquifer stopped in realizations #3 and #4. The higher permeability connected pathways enhanced the generation of the fingers in the lower aquifers and the diffusion area between dissolved mass and the silt zones. During the movement of the dissolved mass into low-permeability layer and the lower aquifer, the fresh water replaced with it. For the realizations #3 and #4, the fresh water flow was mainly seen on the left and right ends of the tank in Figure 122e and Figure 123b, respectively. On the other hand, no fingers were generated in the lower aquifer in the realizations #2 (Figure 122b) and #5 (Figure 123e), and silt packing (Figure 133b) due to limited vertical connectivity between the aquifers. The mass continued to diffuse into the low-permeability layer. In realizations #2 and #5, the movement of the mass was faster with respect to silt packing due to the presence of relatively higher permeability #110 sand.

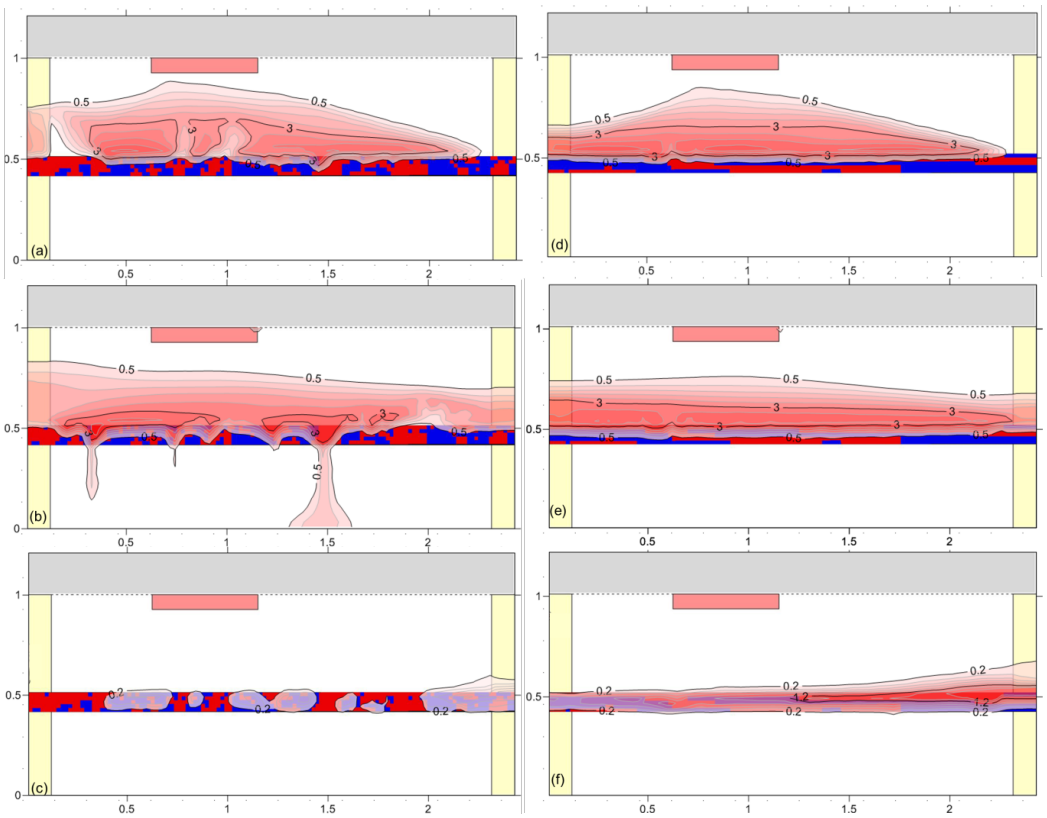

Figure 132 The results of realization #4 (a, b, c) and #5 (d, e, f) at the end of each period: (a, d) 8th day, (b, e) 19th day, and (c, f) 35th day, respectively.

The background water flow with higher rate as opposed to the 1st period was initiated on 19th day. The flow created pressure gradient between two aquifers as observed in the 1st period, and the leakage of fresh water into the upper aquifer started in the realizations #3 and #4. The dissolved mass in the domain was flushed away to estimate the storage in the silt zones. The leakage mechanisms in the realizations #3 and #4 declined the concentrations in the #110 sand zones, and this increased the concentration gradient from silt to sand. The irregularities in the flow rates of the upper aquifer due to experimental limitations contributed to the leakage of more fresh water. As a result, more mass was flushed away in these realizations. On the other hand, due to limited or no vertical connectivity of #110 sand in the realizations #2 and #5, and silt packing, more mass was stored in the low-permeability layer. The graph in Figure 134 showed the variations of the mass remained in the tank with time during the 3rd period. The results reported that the realization #5 having longer horizontal and smaller vertical correlation lengths was able to store more mass in the long-term as opposed to others (Agartan, 2015). The

increasing vertical #110 sand connectivity decreased the storage capacity of the low-permeability layer although it contributed to the storage of dissolved mass in the deeper aquifers.

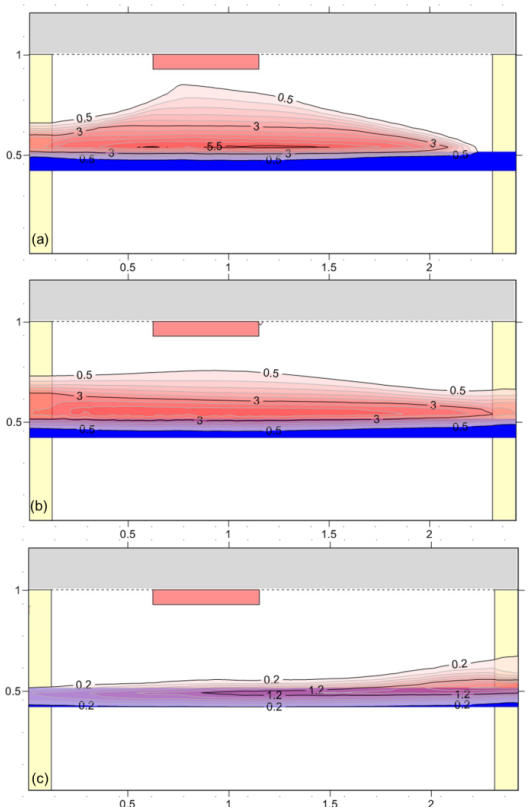

Figure 133 The results of pure silt packing at the end of each period: (a) 8th day, (b) 19th day, and (c) 35th day.

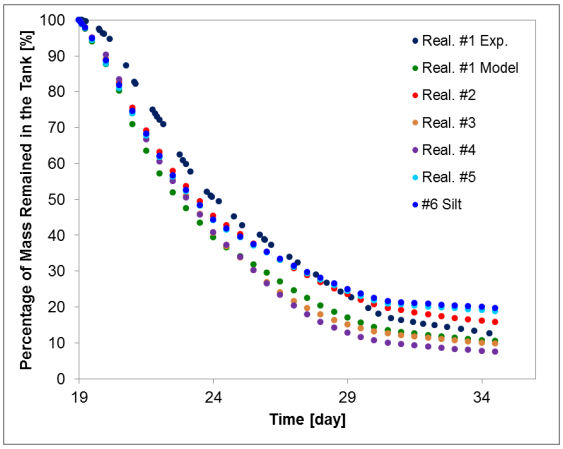

Figure 134 Percentage of mass remained in the source zone with time for different realizations and silt.

5.3.6 Numerical Models for the Utsira Formation in Norway

The Utsira formation located in the Sleipner field in the North Sea was studied in order to analyze the effects of variability permeability and thickness of low permeability layers on the trapping of dissolved CO_2 at field-scale systems. The Utsira formation is composed of Miocene-Pliocene aged sandstone having 200-300 m thickness (Chadwick et al., 2004; Zweigel et al., 2004; Arts et al., 2008). Porosity and permeability of the Utsira sandstone are 30-40% and 1×10^{-12} m^2 to 3×10^{-12} m^2, respectively (Arts et al., 2008; Herrera et al., 2010; Zweigel et al., 2004). The Utsira sandstone is evident as approximately 30 m thick composite layers (Zweigel et al., 2004). Seismic survey results by Hermanrud et al. (2009), Torp and Gale (2004), and Zweigel et al. (2004) showed that the composite sandstone layers are separated by nine 1-3 m thick discrete intra-reservoir shale layers. The thicker shale layer, which is 5-7 m, separates the uppermost leaf of the sandstone from the main reservoir beneath (Arts et al., 2008). There is an uncertainty on the geometries, distributions, and hydraulic properties of the shale layers. Herrera et al. (2010) modeled the shale layers with around 6×10^{-17} m^2 permeability. Johnson et al. (2004) used two different permeabilities for the shale layers as 3×10^{-15} m^2 and 3×10^{-18} m^2, and added 5% porosity.

a. Development of Numerical Model for the Utsira Formation

Several scenarios were developed for a simplified geology of the Utsira formation. Based on the information from the literature, the model domain was set up using the average thickness of the Utsira formation at 300 m (Figure 135). The length of the domain was assumed to be 400 m.

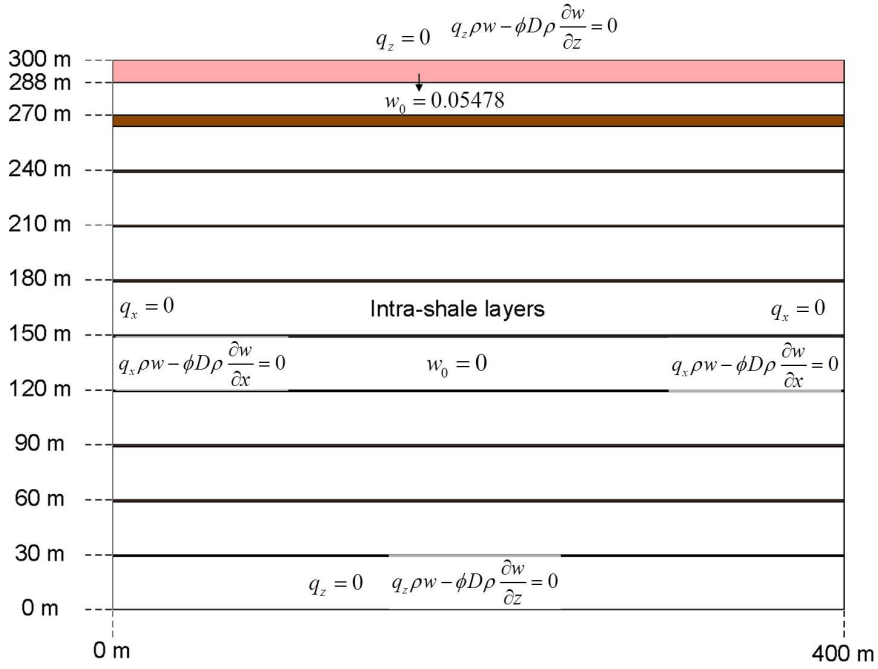

Figure 135 The Utsira formation scenarios for the determination of the effects of shale layer permeabilities and thicknesses on convective mixing and dissolution trapping (not to scale).

The domain was composed of 10 discrete composite sandstone-shale layers. Each composite layer was 30 m thick and included a sandstone layer and an underlying shale layer. The sandstone and shale layers were assumed to be horizontally continuous. The permeability and porosity of the sandstone layers were specified as 2×10^{-12} m^2 and 35%, respectively (Herrera et al., 2010; Torp and Gale, 2004). The porosity of the shale layers was 5% (Johnson et al., 2004). The diffusion coefficient was 2.06×10^{-9} m^2/s from Lindeberg and Bergmo (2003). Five distinct permeabilities and thicknesses were assigned to the shale layers (Table 25).

Table 25 Permeabilities and thicknesses of shale layers.

Parameters	Value
Permeability, k (m^2)	3×10^{-18}, 6×10^{-17}, 3×10^{-15}, 1×10^{-14}, and 3×10^{-14}
Thickness, H (m)	1, 2, 3, 6, and 10

For the sensitivity analysis of shale permeability, shale layer of 6 m thick was assumed to separate the uppermost sandstone layer from the lower composite sandstone-shale layers. The thickness of the lower shale layers were kept as 1 m. The permeability of these zones ranged from 3×10^{-18} m^2 to 3×10^{-14} m^2 (Table 25). For the sensitivity of shale thickness, the permeability of the shale layers was specified as $3\text{x}10^{-15}$ m^2. The thickness of the uppermost shale layer varied

from 1 m to 10 m (Table 25) but the rest of them were assumed to be 1 m thick. These simulations were carried out for dissolved CO_2 and brine. Density and viscosity of the fluids and solubility of CO_2 in brine were determined based on the pressure and temperature conditions in the Utsira formation. For all simulations, 12 m thick dissolved CO_2 at solubility was assumed to be trapped under the caprock (i.e., the top boundary) (Lindeberg et al., 1999). Mineralization was neglected in all of the simulations.

b. Density, Viscosity, and Solubility Calculations of Formation Brine and scCO2

The temperature at the top of the Utsira formation is 36.2 °C (Nooner et al., 2007). The pressure at the shale caprock and the Utsira formation is 87.5-90 bars and 80-110 bars, respectively (Johnson et al., 2004). Density, viscosity, and compressibility of the brine were calculated as 1018.53 kg/m^3, 0.73×10^{-3} Pa.s and 0.41×10^{-9} 1/Pa, respectively, using the salinity of the brine (3.05% by weight (Grimstad et al., 2009)) and pressure (90 bars) and temperature (36.2 °C) of the formation under the caprock. The solubility of $scCO_2$ in brine was determined to be 1.2575 mole/kg using the equation of state developed by Duan and Sun (2003) and Duan et al. (2006) under the specified pressure, temperature, and salinity conditions. The viscosity of the formation brine was assumed to be independent of the CO_2 concentration based on the study carried out by Phillips et al. (1981). The density of the dissolved CO_2 was calculated using equation (44) reported in Duan et al. (2006), where ρ_{CO_2} is the partial density of dissolved CO_2 (kg/m^3), MW_{CO_2} is the molecular weight of CO_2 (44.01 g/mole), V_ϕ is the molar volume of dissolved CO_2 (cm^3/g.mole) in equation (45), and T is the temperature (^{o}C). The density of aqueous phase with dissolved CO_2 is a linear function of CO_2 mass fraction as given in equation (46), where, ρ is the density of the solution (kg/m^3), ρ_b is the density of brine (1018.53 kg/m^3), and w is the mass fraction of CO_2 in the aqueous phase (-).

$$\rho_{CO_2} = \frac{MW_{CO_2}}{V_\phi} 10^3 \tag{44}$$

$$V_\phi = 37.51 - 9.585\times10^{-2}T + 8.740\times10^{-4}T^2 - 5.044\times10^{-7}T^3 \tag{45}$$

$$\frac{1}{\rho} = \frac{1-w}{\rho_b} + \frac{w}{\rho_{CO_2}} \tag{46}$$

c. Influence of Shale Layer Permeability in the Utsira Formation

Five scenarios of distinct shale layer permeabilities shown in Table 25 were simulated using the model configuration given in Figure 135. The simulations were continued for 1000 years. The 1000-year results in Figure 136, the mass remained in the source zone results in Figure 137a, and the first and second moment results in Figure 137c, and e, respectively, emphasized the significance of permeability variations on flow and storage of dissolved CO_2.

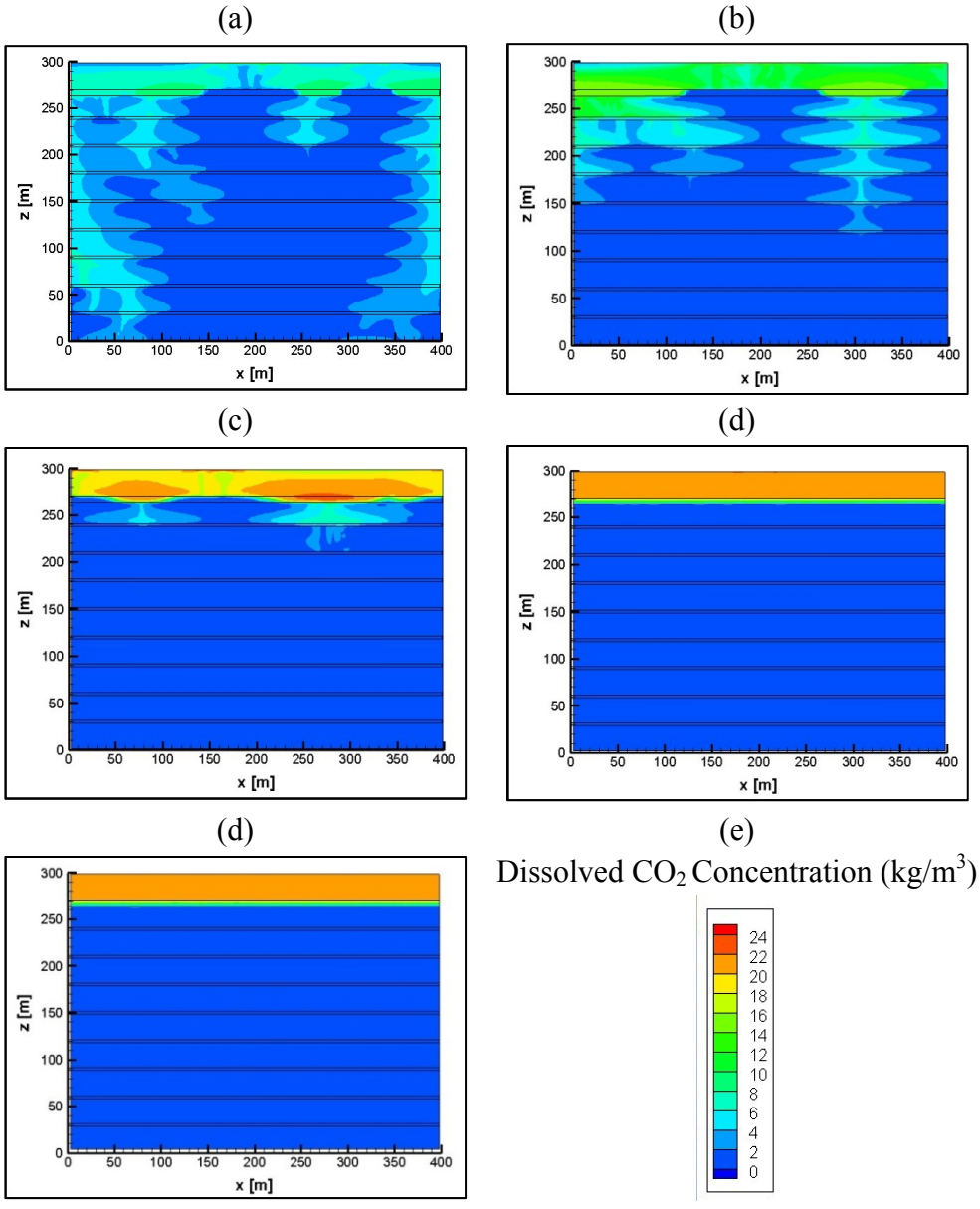

Figure 136 1000 year simulation results for determination of the effects of shale layer permeability on convective mixing and dissolution trapping of dissolved CO_2: (a) 3×10^{-14} m^2, (b) 1×10^{-14} m^2, (c) 3×10^{-15} m^2, (d) 6×10^{-17} m^2, and (e) 3×10^{-18} m^2.

Following the release of the source form the source zone as an initial condition, the onset of convection was observed at around 1st year (Figure 137a). Convection created a rapid decrease in CO_2 mass stored in the source zone (Figure 137a). Dissolved CO_2 reached to the uppermost shale layer at 10th year for all cases. The shale layer blocked the vertical flow of dense fluid as independent from its permeability due to significant reduction in advection/convection in the shale layer, leaving only slow diffusion (Figure 137a, c, and e). For relatively higher shale layer permeabilities, this blockage did not lead the accumulation of significant amount of dissolved CO_2 along the bedding between sandstone and shale as seen in Figure 136a, b, and c where convective mixing was still the dominant flow process. However, convective shutdown was observed at the transition from sandstone to relatively lower permeability shale layers where convective flux decreased and the domain began to fill with dissolved CO_2 due to slow diffusion rates in shale layers. Then, the concentration of dissolved CO_2 accumulated in the upper sandstone layer got equalized, and the system behaved like a continuous CO_2 source at the top for the cases in Figure 136d and e. The slow diffusion rates lead to the storage of dissolved CO_2 both in sandstone and shale layers for a long time, which also creates lateral spreading in the system. The lateral spreading enhances the diffusion area and the amount of diffused mass.

At 1000th year, while the accumulated dissolved CO_2 was still diffusing into the uppermost shale layer in the case of the lower permeabilities (6×10^{-17} m^2 and 3×10^{-18} m^2) (Figure 136d and e, respectively), a considerable amount of the dissolved mass reached the bottom of the formation for the highest permeability case (3×10^{-14} m^2) (Figure 136a). The convective mixing was also observed in deeper sandstone layers for higher shale layer permeabilities as seen in Figure 136a, b, and c. The onset time of convection in the deeper sandstone layers depends on the vertical permeability of the shale layers. For higher shale permeabilities, convection in the second sandstone layer started after tens of years. However, in the case of lower shale permeabilities, it might not be observed for more than 1000 years.

(a) (b)

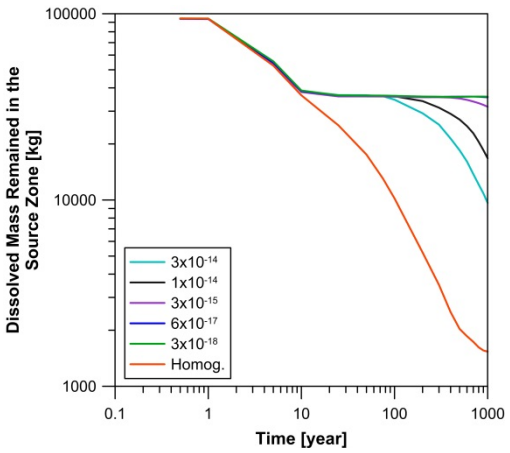
Dissolved Mass Remained in the Source Zone [kg]
100000
10000
1000
0.1
1
10
100
1000
Time [year]
3x10-14
1x10-14
3x10-15
6x10-17
3x10-18
Homog.

(c)

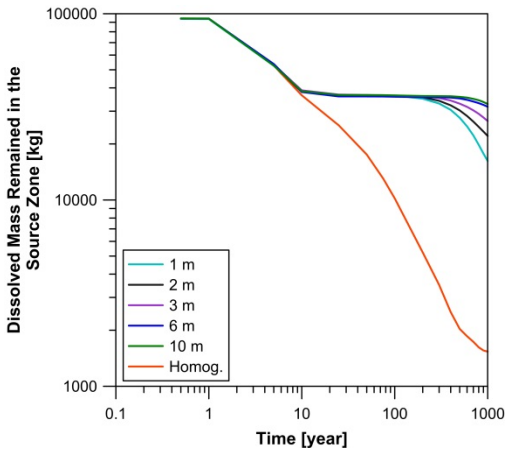
Dissolved Mass Remained in the Source Zone [kg]
100000
10000
1000
0.1
1
10
100
1000
Time [year]
1 m
2 m
3 m
6 m
10 m
Homog.

(d)

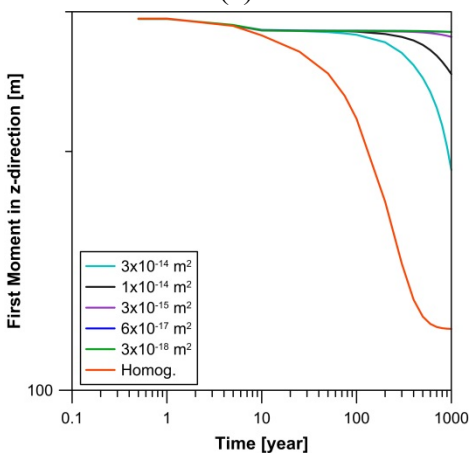
First Moment in z-direction [m]
100
0.1
1
10
100
1000
Time [year]
3x10-14 m2
1x10-14 m2
3x10-15 m2
6x10-17 m2
3x10-18 m2
Homog.

(e)

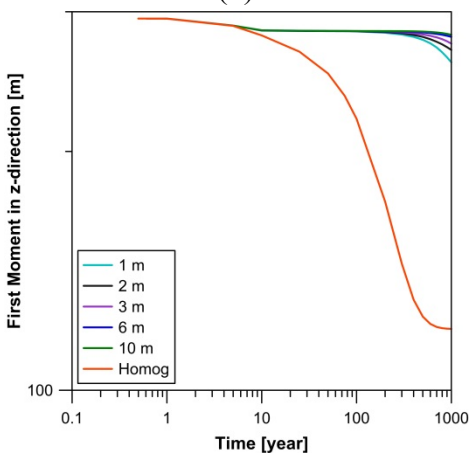
First Moment in z-direction [m]
100
0.1
1
10
100
1000
Time [year]
1 m
2 m
3 m
6 m
10 m
Homog

(f)

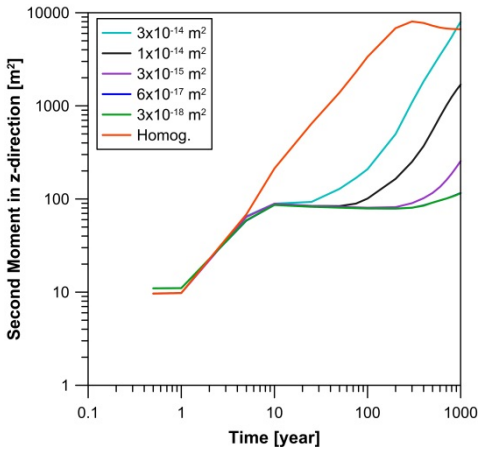
Second Moment in z-direction [m2]
10000
1000
100
10
1
0.1
1
10
100
1000
Time [year]
3x10-14 m2
1x10-14 m2
3x10-15 m2
6x10-17 m2
3x10-18 m2
Homog.

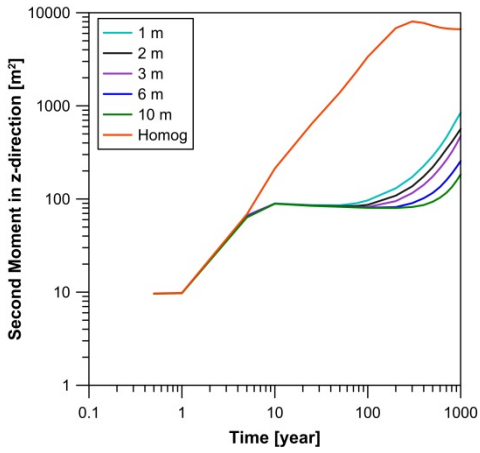
Second Moment in z-direction [m2]
10000
1000
100
10
1
0.1
1
10
100
1000
Time [year]
1 m
2 m
3 m
6 m
10 m
Homog

Figure 137 Variation of the total mass remained in the 12 m thick source zone for (a) permeability and (b) thickness analyses; first moments in z-direction for (c) permeability and (d) thickness analyses; second moments in z-direction for (e) permeability and (f) thickness analyses.

d. Influence of Shale Layer Thickness in the Utsira Formation

The thickness effects were evaluated for five different thicknesses of the uppermost shale layer (from 1 m to 10 m), while keeping the thickness of the other shale layers at 1 m. The concentration distributions of dissolved CO_2 after 1000 years for the scenarios are shown in Figure 138. The thickness of the uppermost shale layer has a considerable impact on the mixing, spreading, and trapping of dissolved CO_2 throughout the domain.

The onset of convection occurred at around 1st year as explained in previous chapter. The decrease in CO_2 mass in first 10-year was a result of convection observed in the upper sandstone layer (Figure 137b). The flow of dissolved CO_2 was slowed down by the uppermost shale layer at 10th year where convective shutdown was observed for a certain period of time depending on the thickness of the shale layer (Figure 137d and f). The time to initiate convection in the deeper sandstone layers depends on the thickness of the shale layer due to slow diffusion rates. The thicker shale layers (Figure 138d and e) leads to the storage of dissolved mass in the upper sandstone layer and the uppermost shale layer for a long time compared to the thinner cases (Figure 138a, b, and c) due to slow transport of dissolved CO_2 in shale layers. Nevertheless, the thinner shale layers do not retard the vertical movement of dissolved CO_2 for a long time which speeds up its spreading to the deeper parts of the domain (Figure 137 and Figure 138a, b, and c). Therefore, the system behaves similar to a convective mixing dominant homogeneous formation (Figure 138).

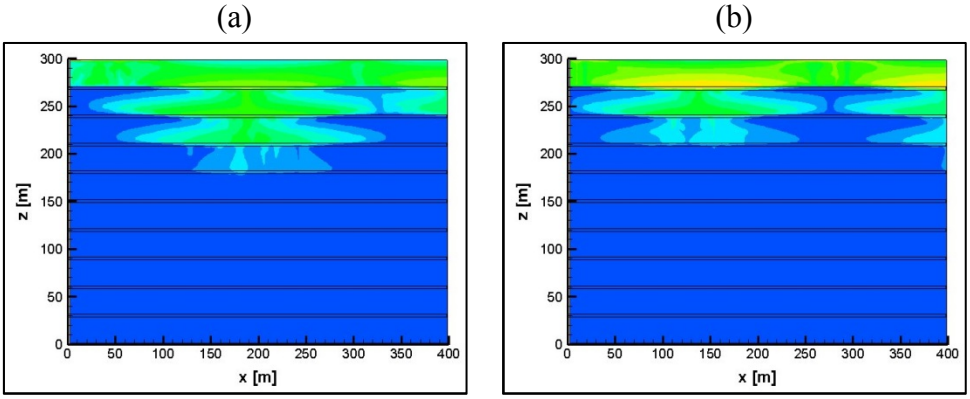

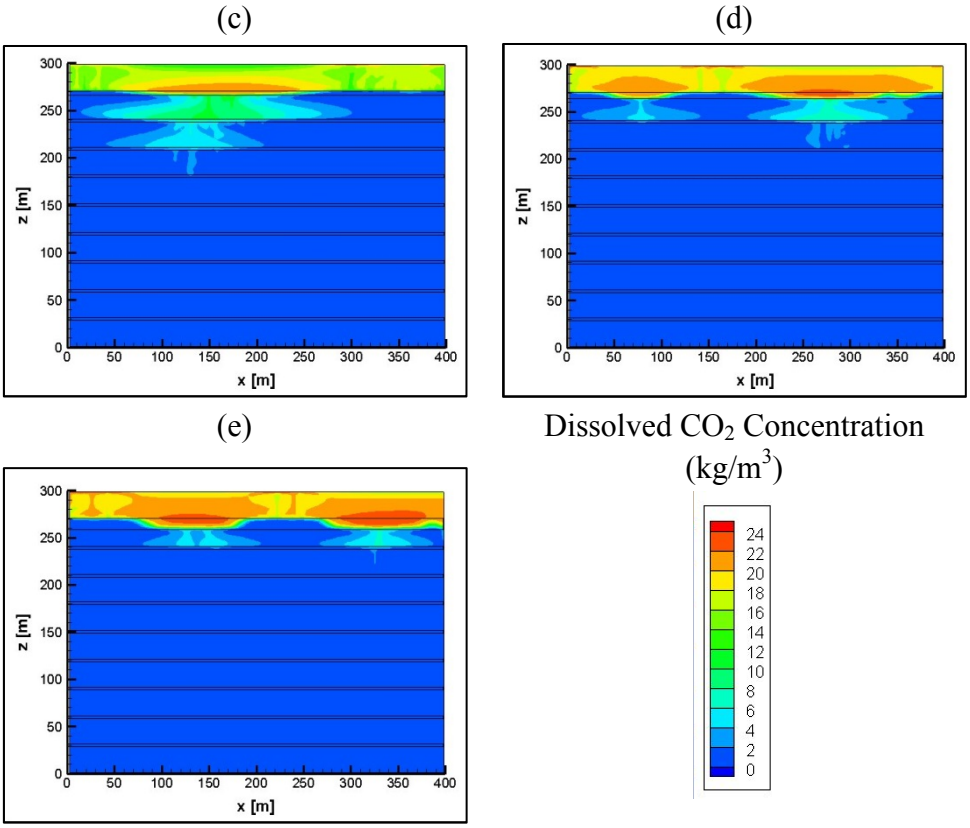

Figure 138 1000 year simulation for determination of the effects of shale layer thickness on convective mixing and dissolution trapping of dissolved CO_2: (a) 1m, (b) 2m, (c) 3m, (d) 6 m, and (e) 10 m.

The multilayered heterogeneity in the geologic formations affects the vertical movement and storage of dissolved CO_2. The presence of very low permeability layers with respect to the average permeability in the reservoir slows down the vertical spreading, and they are able to effectively lock dissolved mass (Agartan et al., 2015a). The thickness and permeability of these layers have an important impact on the mixing, spreading, and storage. The permeability of the shale layers affects the flow and storage of dissolved CO_2 more than their thickness as seen in Figure 137. Convection shutdown occurs depending on the physical and hydraulic properties of the low permeability layers. In this study, the total mass remained in the source zone and the spatial moment results in Figure 137 showed that the convective shutdown occurs at 10 years of simulation for all cases. For the lower permeability and thicker shale layers, convective shutdown decreases the convective flux and equalizes the dissolved CO_2 concentrations in the sandstone layers due to slow diffusion rates into and within the shale layers. This contributes to the storage of dissolved CO_2 in these layers for a long time. At the transition of the high/medium

and low permeability layers, a lateral spreading occurs which enhances the diffusion area and the diffused mass into the low permeability layers. In the field setting, the lateral spreading leads to the storage of more mass into low permeability layers.

In the case of relatively higher permeability and thinner shale layers, the system behaves like a homogeneous medium where convective mixing enhances the trapping of heavier fluid in deeper parts of the formation. The onset time of the convection in the deeper sandstone layers depends on the thickness and permeability of the shale layers. Convective mixing leads the dissolved mass to contact with host rock in a shorter time. Therefore, the contact area between the dissolved CO_2 and the host rock increases for potential mineralization, which is referred as the most secure way to store $scCO_2$ in deep geologic formations (Benson and Cook, 2005).

5.4 Stochastic analysis of large tank heterogeneous experiment

Starting from the heterogeneous configuration applied to the large tank experiment documented in section 5, a stochastic analysis was carried out to investigate the impact of sequential injection schemes on enhancing plume storage in synthetic reservoirs with variable statistical properties, such as variance and horizontal correlation length.

In this study, immiscible displacement experiments are carried out by using surrogate fluids to represent the injection of $scCO_2$ into the subsurface. The effect of capillary trapping is studied in a highly heterogeneous scenario using an injection strategy of two injections and two post-injections periods. During the post-injection the NWP is redistributed through the formation and a higher residual saturation is observed.

The heterogeneity of the tank was configured with six categories of silica sand grade. Table 26 includes the physical properties of these sands such as permeability (k), average porosity (φ_{avg}), average grain size (d_{50}), and uniformity coefficient (d_{60}/d_{10}). Data of the capillary pressure curves for these silica sands are extracted from Vargas-Johnson (2014).

Table 26 Physical properties of silica sands used in Trevisan (2015).

	Sieve size	k (m^2)	lnk	ϕ_{avg} (-)	d_{50} (mm)	d_{60}/d_{10} (-)
1	#16	5.64×10-10	-21.3	0.407	0.88	1.72
2	#20	2.13×10-10	-22.3	0.411		
3	#30	1.18×10-10	-22.9	0.433	0.49	1.50

4	#50	3.39×10-11	-24.1	0.426	0.30	1.94
5	#70	1.44×10-11	-25.0	0.418	0.19	1.86
6	#110	5.18×10-12	-26.0	0.334	0.10	~2.0

As a result of the experimental observations in the large tank experiments, where larger amounts of NWP could be immobilized after a secondary injection event, the need to investigate further this phenomenon using numerical modeling was recognized. In the following sections, we present a study to investigate the possibility enhancing capillary trapping by applying different injection strategies represented by multiple injection and post-injection phases using stochastic analysis.

5.4.1 Geostatistics

To generate four two-dimensional geostatistical spatial distributions of permeability we used a sequential indicator simulation (SIS) algorithm of the open source software geostatistical library GSLIB (Deutsch and Journel, 1998) coupled to the SGeMS (Remy et al., 2009). Each ensemble of permeability distributions is referred to as Simulation 1 through 4 and is composed by 500 equi-probable realizations.

Different logarithmic variances and correlation lengths are applied to each spatial distribution. The geostatistical parameters of each spatial distribution include mean, variances, and correlation lengths and are presented in Table 27. Figure 139 presents the probability distribution function of each sand category, while Figure 140 shows the experimental variograms of each simulation characterized by different variance and correlation length. Simulation 2 is based on the experimental scenario introduced in section 5.2.4 with a natural logarithmic mean and variance of -24.1 and 1.7, respectively, and a horizontal and vertical correlation length of 0.5 m and 0.04 m, respectively.

Table 27 Geostatistical parameters used for the spatial distributions of permeability (roman numerals indicate the number of injection events).

Simulation	Mean	Variance	Horizontal correlation length (m)	Vertical correlation length (m)	realizations	Injection strategy
1	-24.1	1.0	0.5	0.04	500	I, IV
2*	-24.1	1.7	0.5	0.04	500	I, II, III, IV

3	-24.1	2.9	0.5	0.04	500	I, IV
4	-24.1	1.7	0.2	0.04	500	I, IV

*Experimental case

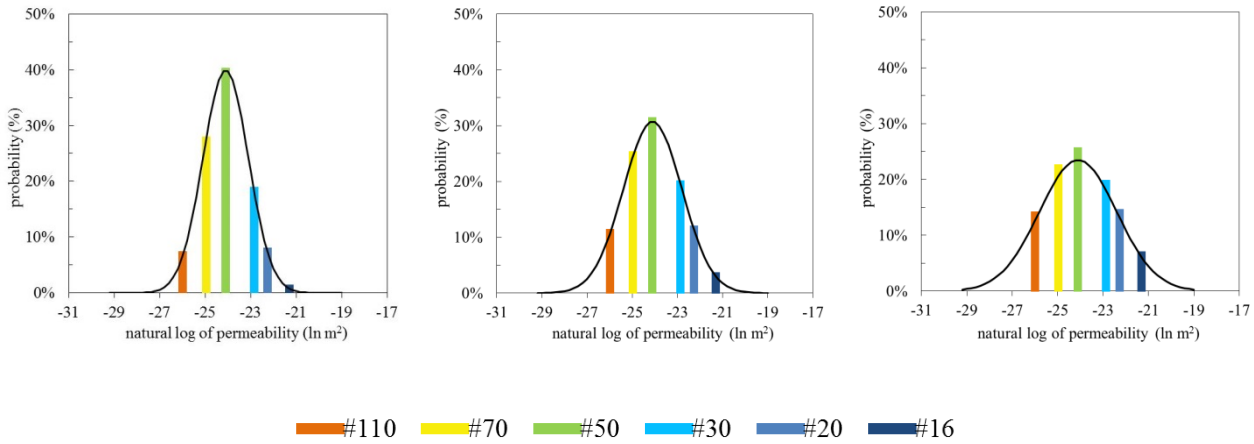

Figure 139. Histograms of the natural log of intrinsic permeability (in m^2) for the three heterogeneous spatial distributions with mean μ=-24.1 (#50 sand) and variance: (a) σ^2=1.0 (Simulation 1), (b) σ^2=1.7 (Simulation 2 and 4), and (c) σ^2=2.9 (Simulation 3).

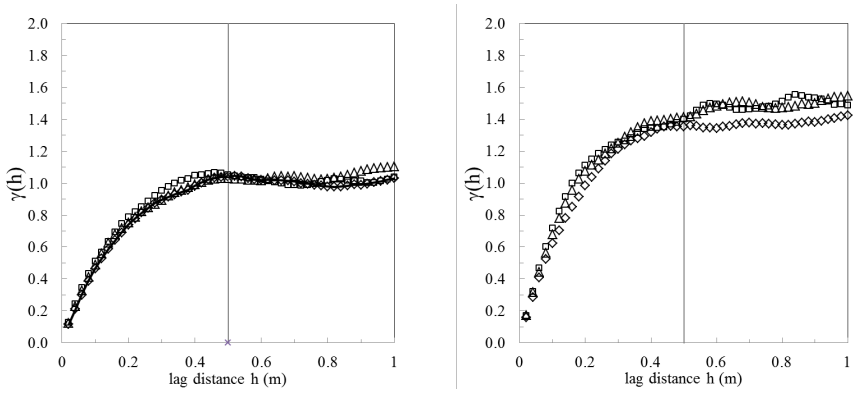

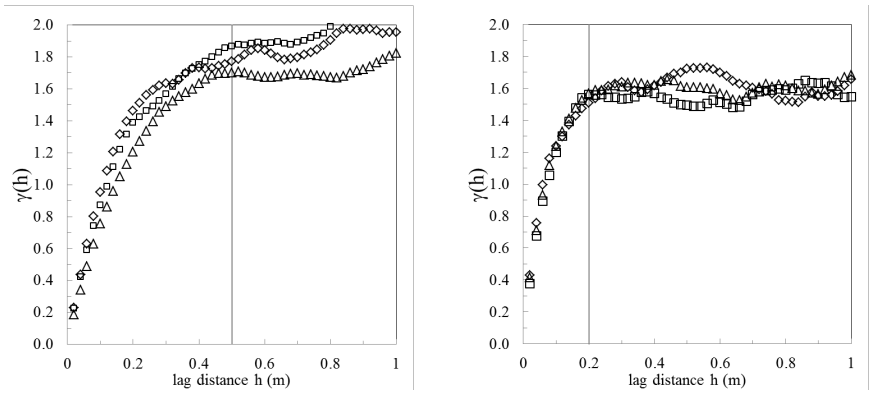

Figure 140 Experimental variograms showing the correlation length of some random realizations for: (a) Simulation 1, (b) Simulation 2, (c) Simulation 3, and (d) Simulation 4.

5.4.2 Numerical model setup

The stochastic analysis was performed using TPFLOW. TPFLOW is the in-house code developed by Abdullah Cihan at Lawrence Berkeley National Laboratory as a part of this research project. Monte Carlo simulations were performed using TPFLOW. In each simulation, the same total volume of 0.002 m^3 (2 l) of non-wetting phase (Soltrol 220) was injected into the formation based on several injection strategies. Each injection strategy has a specific time distribution within a total time of 24.16 days. Table 28 describes the four injection strategies I-IV. The number of cycles refers to the number of times that the injection phase and post-injection phase are repeated within the total time of 24.16 days. Thus, the injection strategy II, which includes two cycles, is constituted by (injection + post-injection) + (injection + post-injection) and applying the injection rates and lengths of Table 28 of the corresponding phase.

Table 28 Injection strategies applied to four different storage scenarios (roman numerals indicate the number of injection events).

Injection strategy	Injection phase		Post-injection phase	Simulation time (d)
	Injection rate (m^3/d)	Injection time (d)	Relaxation time (d)	
I	1.04×10^{-4}	1.90	22.26	24.16
II	1.04×10^{-4}	0.95	11.13	24.16
III	1.04×10^{-4}	0.62	7.43	24.16

IV	1.04×10^{-4}	0.47	5.57	24.16

A two-dimensional vertical cross-sectional model domain with the dimensions 2.44 m x 0.05 m x 0.50 m of the experimental setup in Trevisan (2015) was modeled. However, when evaluating the trapping performance of each injection strategy, the dimensions considered within the boundaries of the experimental tank are 2.28 m x 0.05 m x 0.50 m. A regular discretization of 0.02 m $\times$ 0.05 m $\times$ 0.02 m was used.

5.4.3 Results of the stochastic simulations

Four stochastic simulations referred to as Simulations 1 through 4 are carried out applying the permeability spatial distributions and injection strategies described in Table 27 and Table 28, respectively. A total volume of 2 l was introduced in each simulation and results are presented at the end of 24.2 days. A steady-state of the NWP plume is not observed during this interval of time. In the experimental study (Trevisan, 2015) for the heterogeneous case and two injections periods, the steady state was observed for a time greater than 80 days, while for the homogeneous case it was at 24 days. To meet the goal of this study to provide insight into the effect of the injection strategy on the capillary trapping efficiency in a heterogeneous media, the simulation time period was not constrained.

Results presented here are referred to the cases in which the NWP injected volume is trapped in a predetermined secure zone. This secure zone is defined as an area where there is no risk for potential leakage and for this study defined to be within the tank boundaries. Cases in which the plume moves to regions out of the secure zone (or tank boundaries) are discarded, since in theses cases, the plume is considered to have leaked through a fault or leaky well. Table 29 lists the number of realizations for each Simulation in which the total volume of NWP remained in the secure zone. Note that the number of cases in which the plume is trapped in the secure zone increases with the number of injection pulses, degree of homogeneity of the formation (lower variance), and lower correlation length.

Table 29 Number of cases in which the plume is trapped in the secure zone.

	Injection strategy			
Simulation	**I**	**II**	**III**	**IV**

1	182	-	-	237
2	134	151	165	168
3	60	-	-	94
4	367	-	-	416

Simulation 2-I, with only one injection and one relaxation cycles, has a total of 134 realizations (of 500) in which the NWP remains within the secure zone. The number of cases of realizations remaining in the secure zone for Simulation 2-II, 2-III and 2-IV are 151, 165, and 168, respectively. Increasing the number of injection and post-injection cycles from one to four (injection strategy I and IV, respectively) benefits the containment of the plume in the secure zone by 7%. The fact that the injection strategy IV produces better outcome in containing the plume in the desired area is also observable for Simulation 1, 3 and 4. The containment of plume is increased between 7% and 10% for these three simulations.

The impact of the variance on the containment of NWP is reflected in the results of Simulation 1, 2, and 3. Simulation 1 (1-I and 1-IV) produces more cases in which the NWP is trapped in the secure zone in comparison to Simulation 2 and 3. Low permeable facies hinder the vertical spread of the NWP, thus the plume is forced to travel horizontally through layers with higher permeability. Low permeability variance, such in Simulation 1, implies that there is less probability for the presence facies with lower and higher permeability than the mean permeability. Therefore NWP is distributed more vertically through the domain in Simulation 1 than in Simulation 2 and 3.

Simulations 4-I and 4-IV, with the lowest correlation length, present the greatest number of realizations in which the NWP is contained in the secure zone. In this simulation, the spatial distribution of the facies present shorter preferential path that enhances the escaping of the plume. On the other hand, Simulation 2, which is created with same variance as Simulation 4, produces fewer cases in which the NWP is contained in the tank boundaries. Greater correlation lengths of the facies enhance the escape of the NWP through preferential pathways of high permeability; therefore NWP is able to reach further areas of the formation by spreading horizontally.

Consistently, for all four spatial distributions of permeabilities, injection strategies involving more cycles of injection and post-injection produce a reduced and concentrated NWP

plume. Figure 141 shows the median saturation value for simulation 2 for the four injection strategies. Injection strategy I produced a larger of plume than injection strategy II, III and IV. Injection strategy IV has the less extended plume and higher saturations. Since the same volume of NWP was injected for all injection strategies, the observed saturation for injection strategy IV is higher in comparison to the saturation reached using other injection strategies.

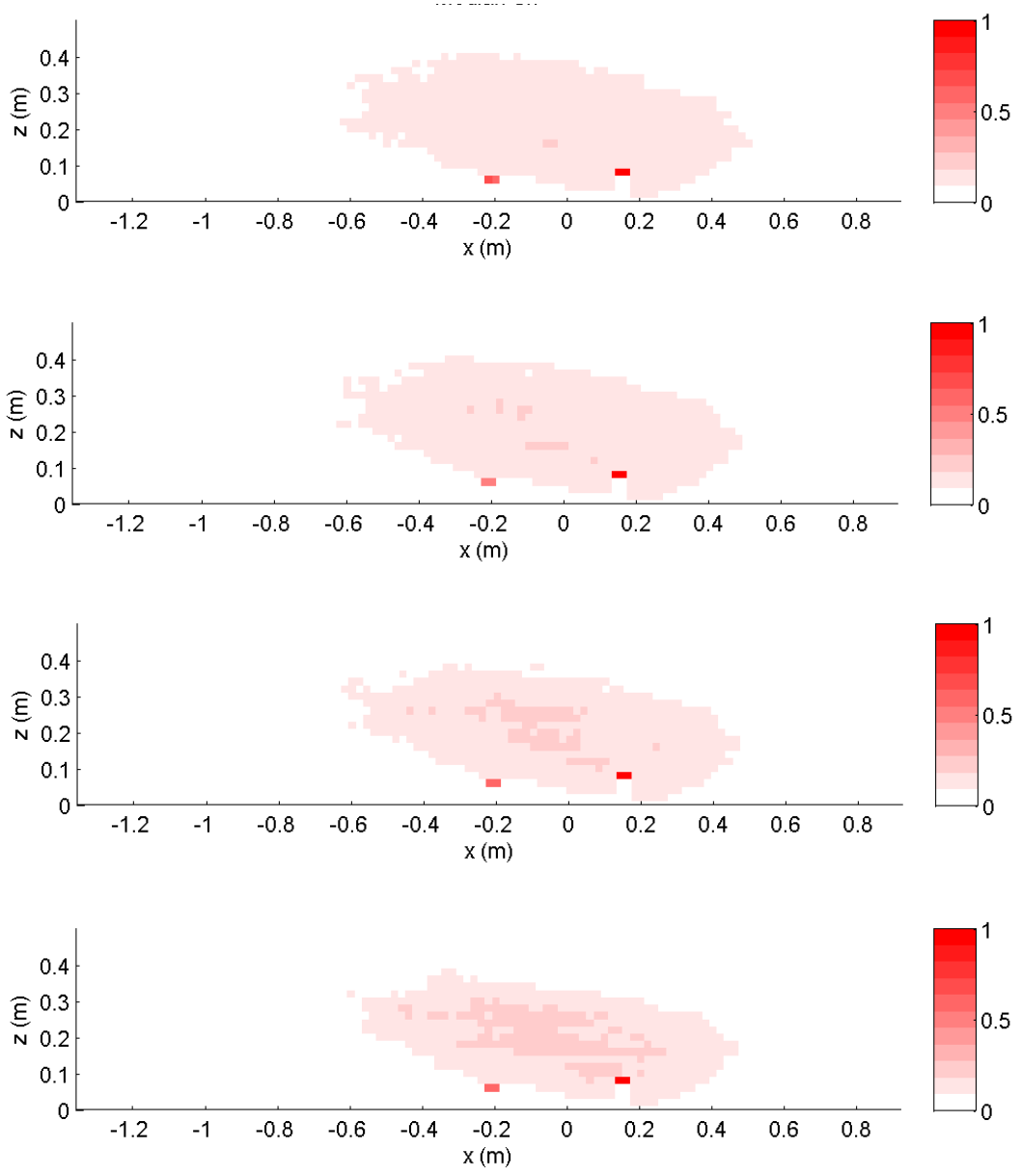

Figure 141 Median value of NWP saturation at time 24.2 days for simulations: (a) 2-I, (b) 2-II, (c) 2-III, and (d) 2-IV.(Calculated in Matlab plot of the plume for the Median Sn).

Comparison of the median saturation value for injection strategy I and IV of Simulations 1, 3 and 4 are included in Figure 142. Results displayed in this figure confirm that injection strategy IV generates compressed distributions of the NWP with higher saturation independently of the heterogeneity of the sand distributions or variance (Figure 142b, Figure 142d) and correlation length (Figure 142f). Note that Simulation 4 generated with a lower correlation length presents a higher distribution of the plume vertically reaching the top boundary in Figure 142e and Figure 142f. On the other hand, NWP plumes of Simulations 1, 2, and 3 (with greater correlation length) do not reach the top of the formation in Figure 141 and Figure 142a-Figure 142d.

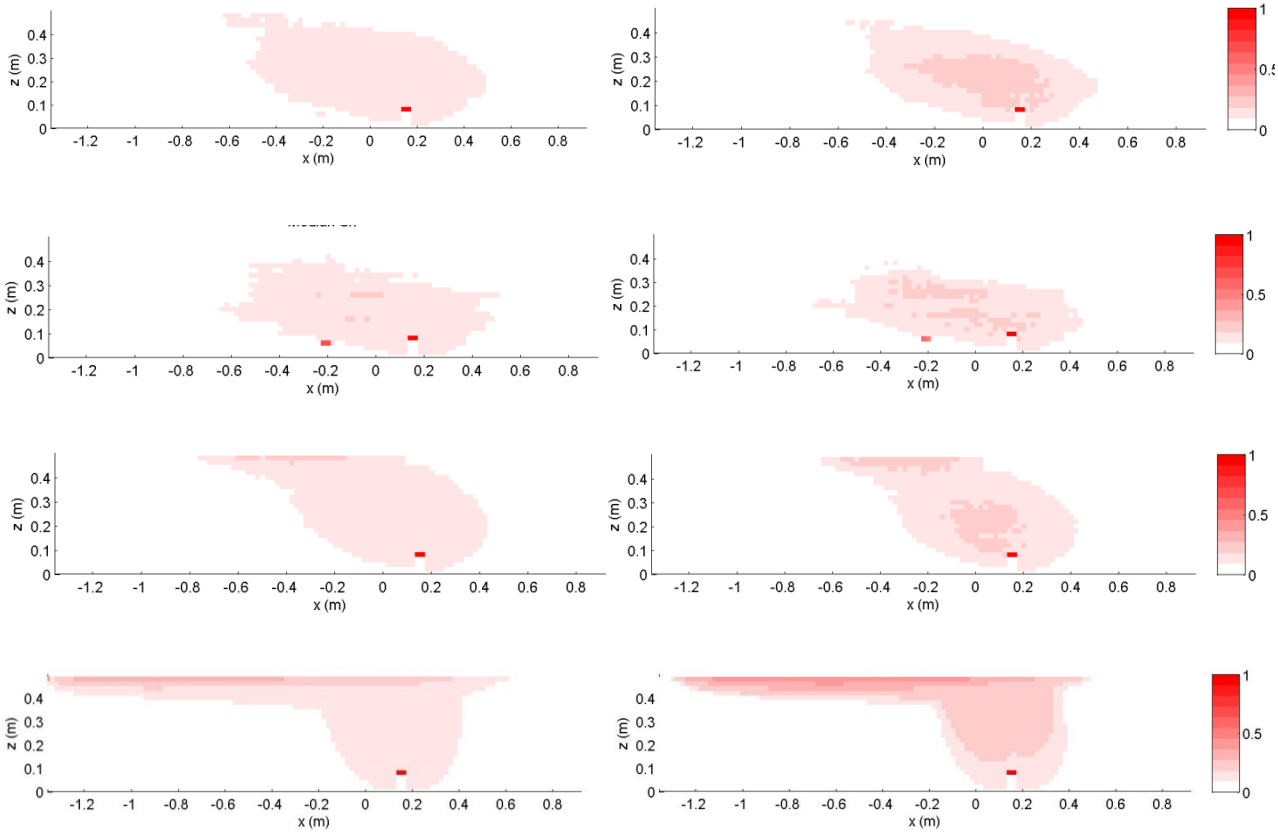

Figure 142 Median value of NWP saturation at time 24.2 days for simulations: (a), 1-I, (b) 1-IV, (c) 3-I, (d) 3-IV, (e) 4-I, (f) 4-IV, (g).

Also from Figure 141 and Figure 142 it can be appreciated that injection strategy IV presents lower spread of the plume in comparison to injection strategy I. The migration of the

NWP through the heterogeneous formation not only depends on the heterogeneity, but also on the injection strategy. The NWP migrates vertically until it finds a layer with lower permeability. Then NWP migrates horizontally through the higher permeable layer and is accumulated under the low permeable layer. If the capillary pressure exceeds the entry pressure of the low permeable formation, the NWP will penetrate it and advances through this layer. This phenomenon only occurs if enough NWP is concentrated under the low permeable layer. When applying more cycles, such that in injection strategy IV, the same volume of NWP is injected during more frequent and shorter injection periods. This allows repeated relaxations and redistributions of the NWP in the aquifer. On the other hand, when applying injection strategy I, the total volume of NWP is injected in only one injection period. Thus, more NWP is accumulated under the low permeable layer and entry pressure can be exceeded before plume redistribution starts.

This is also shown in Figure 143 where box-plots of the center of the NWP volume in the vertical direction are presented. The interpretation of the box-plots is as follows: middle lines are the median of the distributions, top and bottom edges are the first and third quartile, respectively, while the ending 'whiskers' above and below each box are the maximum and minimum values observed, respectively. Figure 143 displays lower z_c for injection strategy IV (red boxes) in comparison to its respective injection strategy I (grey boxes). For instance, Simulation 2-IV has a median and a minimum value of 0.23 m and 0.13 m respectively, whereas for Simulation 2-I are 0.24 m and 0.15 m, respectively.

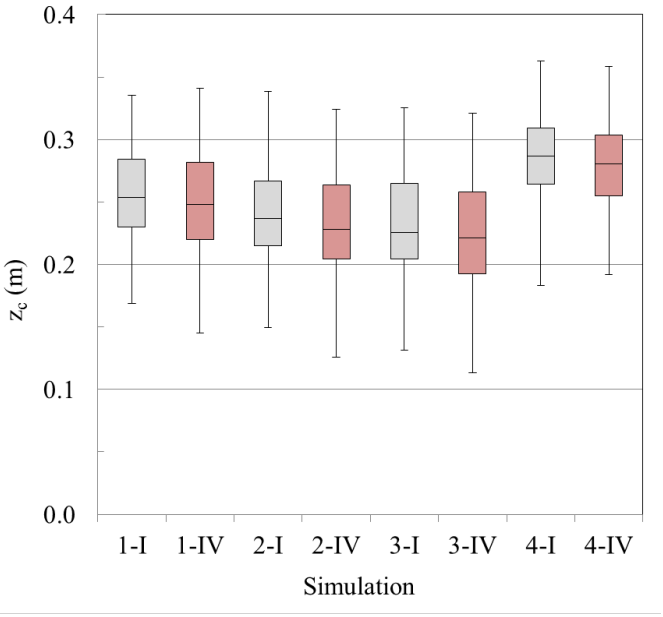

Figure 143 First spatial moment of the NWP in the vertical direction. Injection strategy I is in grey and IV in red.

To evaluate trapping effectiveness, we define an effective saturation of the NWP S_e as follows:

$$S_e = \frac{\sum_{i=1}^{NT} S_{NW_i}}{N_{NW}} \tag{47}$$

Where S_{NW_i} is the saturation of the NWP at cell i, NT is the number of cells within the secure zone, and N_{NW} is the number of cells that contain NWP, thus S_{NW_i}>0. Note that a smaller N_{NW} results into a greater S_e indicating efficient trapping

Figure 144 includes the box-plots for the effective saturation (Eq. (47)) and the number of cells that contain NWP at the final time for Simulations 1-4. Recurrently, injection strategy IV produces a greater S_e than injection strategy I as is shown in Figure 144a. Figure 144b shows that injection strategy IV invades less cells with NWP within the secure zone, thus the distribution of their plumes is accommodated in a smaller volume of the formation. Simulation 2-IV presents a greater variance for N_{NW} than Simulation 2-I. Simulation 2-IV has a maximum N_{NW} of 1337, whereas for Simulation 2-I is 1329. There are configurations of sands that include layers of high permeability interconnected, which can generate a larger spread of the NWP. Under these conditions, the NWP plume escapes from the secure zone when applying injection strategy I and the realization is not considered for the analysis. On the contrary, when applying

the injection strategy IV plume remains in the secure zone and is considered for the analysis, nonetheless with a high distribution of the plume. This greater spread of the NWP for injection strategy IV is also reflected in Figure 145.

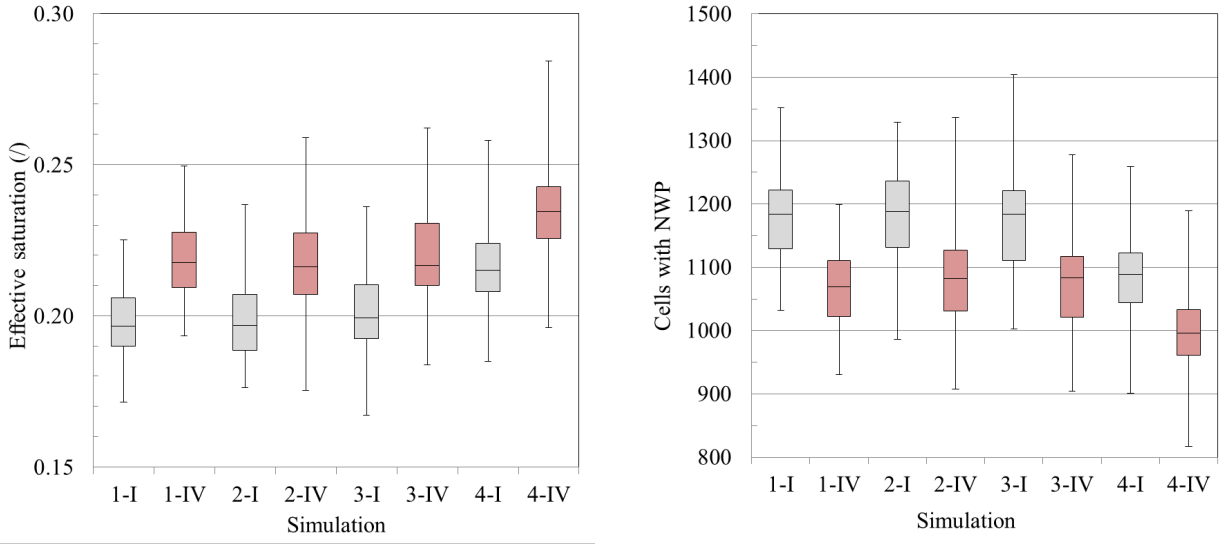

Figure 144 (a) Effective NWP saturation and (b) Number of cells containing NWP for Simulations 1-4. Injection strategy I is in grey and IV in red.

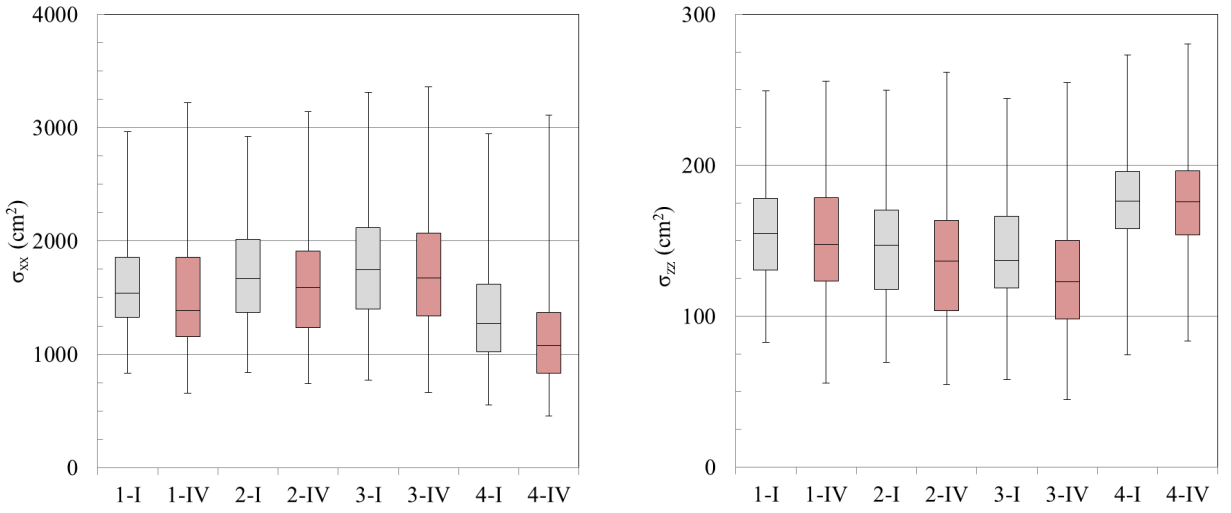

Figure 145 (a) Lateral and (b) Vertical spread of the plume for Simulations 1-4. Injection strategy I is in grey and IV in red. Variance units are in cm^2.

Figure 145 displays results of the lateral and vertical spread of the NWP in the secure zone. The fourth quartile of injection strategy IV is consistently greater than the fourth quartile of

injection strategy I for all simulations (1-4) and both spreads. Injection strategy IV generates more cases in which the total volume of the NWP is contained in the secure zone (see Table 29). However, the spread and distribution of these cases are larger and increases the variance for injection strategy IV. Note that the 75th of the cases for injection strategy IV produce a lower lateral and vertical spread than injection strategy I.

The injection strategy applied does not affect the distribution of the NWP into the sands. Figure 146 shows the median values of the NWP distribution in each sand normalized with their frequency. Sands of high permeability present more content of NWP, whereas the sand with the lowest permeability seems impermeable to the NWP.

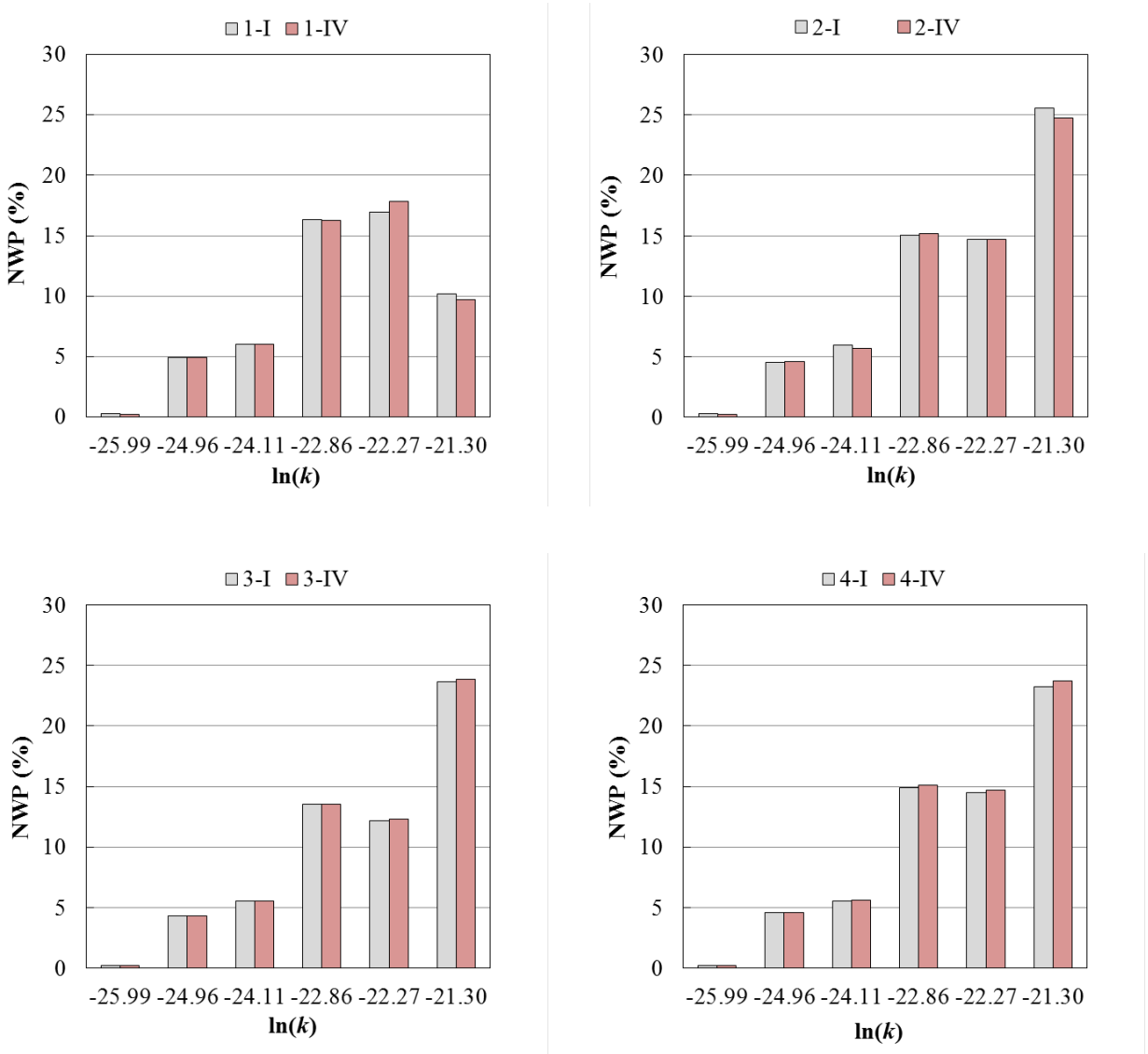

Figure 146 Median value of the non-wetting phase distribution in sands applying injection strategy I (in grey) and IV (in red) for: (a) Simulation 1, (b) Simulation 2, (c) Simulation 3, and (d) Simulation 4.

Figure 147 shows the median value of the NWP horizontal distribution. There are no big differences between injection strategy I and IV. Injection strategy I exhibits a higher median value closer to the edges of the secure zone (-1.36 m and 0.93 m). The variance and correlation length used to generate the spatial distribution of permeability in the aquifer has greater impact on the results than the injection strategy applied. Simulation 3, with the highest variance, presents an extended horizontal distribution of the NWP, while Simulation 4, with the lowest correlation length, presents a more compressed plume. Correlation length affects the vertical distribution of the non-wetting phase. Short correlation lengths show a vertical distribution concentrated around the injection well. Longer correlation lengths show that the plume tends to advance horizontally due to travel of the plume through long layers of permeable sand.

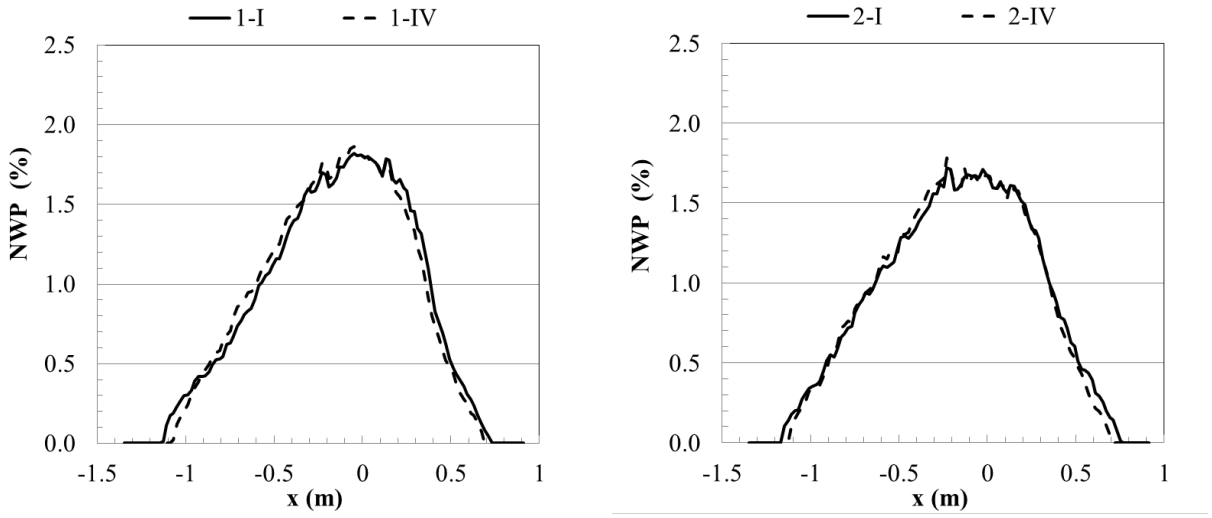

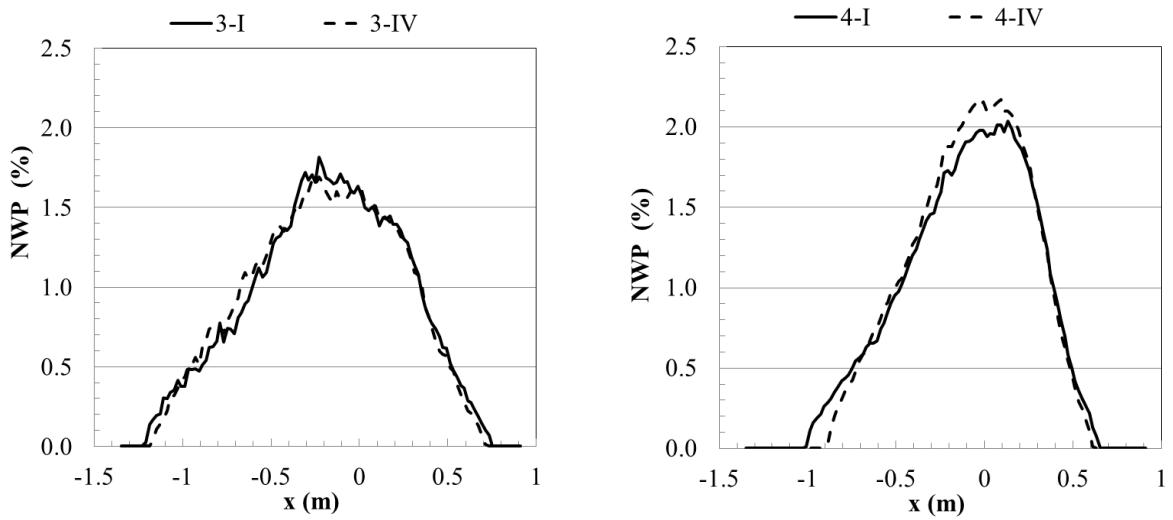

Figure 147 Median value of the NWP horizontal distribution applying injection strategy I (solid line) and IV (dashed line) for: (a) Simulation 1, (b) Simulation 2, (c) Simulation 3, and (d) Simulation 4.

6 SUMMARY OF FINDINGS

First, a summary of the key findings from each of the experimental and modeling tasks is presented under capillary trapping and dissolution trapping, separately. In Section 8, conclusions that are derived from these findings that are of scientific and practical value are presented with some recommendations for future work.

6.1 Summary findings of capillary and dissolution trapping investigation

Two experimental test scales were used. The medium tanks experiments were designed to improve the fundamental understanding of the processes, and the large tanks were used to up-scale the knowledge to the intermediate scale. Intermediate scale is a scale intermediary between the laboratory and the field scales. The data generated was also used in testing model algorithms developed in this research.

6.1.1 Capillary trapping experiments

The detailed results from the medium and large tank experiments were presented in section 5.1. The key findings from homogeneous and heterogeneous experiments are presented.

a. Homogeneous packing

Even though, homogeneity does not exist in natural formations, idealized conditions simulated in homogeneously packed test tanks allowed obtaining new insights that are useful in developing improved conceptual models. A summary of these observations and findings is presented.

- For displacements carried out at an equal capillary number Ca ~ O(10^{-5}), gravity segregation is predominant when the flow is characterized by higher Bond numbers, which for equal density difference are highly dependent on permeability of the formation porous material;
- A comparison of the rates at which the saturations reach final residual values at different depths below the caprock shows that the saturation at deeper locations reaches the residual faster. This observation supports the convenience of "inject low and let rise" injection schemes;
- To minimize the occurrence of mobile $scCO_2$ in the reservoir, a forced imbibition event such as a chase brine injection can eventually initiate a secondary drainage/imbibition cycle, leading to an enhanced immobilization of $scCO_2$ at locations far-off from the injection well.
- Clusters of immobile $scCO_2$ sub-zones with saturations higher than residual can be formed behind zones with lower residual saturation due to pore-scale heterogeneities. This trapping mechanism can be defined as a macroscale trapping;
- In idealized or relatively homogeneous formations, when a second injection is followed after the first $scCO_2$ placement, higher residual trapping saturations were achieved in zones that that have been previously gone through drainage/imbibition cycles.

b. Heterogeneous packing

The heterogeneous packing configurations that were created using sand in the small and large tank experiments may not necessarily represent all possible geologic conditions encountered in deep formations. However, these synthetic heterogeneities allowed to obtain new insights that are useful in developing improved conceptual models. A summary of these observations and findings is presented.

- Spatial variability of capillary entry pressure at coarse/fine lithological interfaces (texture transitions) exerts a major control on $scCO_2$ plume propagating in capillary-dominated regimes;
- How the permeability field is correlated in space influences the ability of capillary barriers at coarse/fine lithological interfaces to prevent migration of $scCO_2$ plume, thus enhancing trapping at saturations higher than residual;
- Buildup of $scCO_2$ above residual saturation at texture transitions can contribute towards the enhancement of trapping capacity; however, under forced imbibition, the trapped $scCO_2$ can be mobilized and the benefits of the enhanced trapping achieved through capillary barrier trapping will not be realized especially near injection wells;
- Currently available trapping models are only able to predict the final capillary-trapped of $scCO_2$ saturation at specific conditions that may not be relevant to all possible scenarios expected during $scCO_2$ injection (e.g. once a thorough wetting phase flow has flushed the reservoir);
- Forced imbibition events performed in heterogeneous systems can promote invasion of potential trapping zones that were not previously invaded, enhancing residual trapping at these locations. Although this mechanism might not contribute significantly to the overall trapping of $scCO_2$ through capillary trapping, it can help enhancing the contact area between the two fluids and eventually promote dissolution.
- Imposing constant $scCO_2$ injection pressures can lead to fluctuations in the flow rate, especially for heterogeneous systems with high permeability contrasts. This is a result of the plume fronts accumulating behind capillary barriers until entry pressures are reached and the $scCO_2$ preferentially moving into high permeability connected pathways. This can be relevant to field situations where formation injectivity can show significant variations spatially as a result of heterogeneity during the injection operation;
- Layer-type heterogeneity exerts a major control on the propagation and trapping of the plume, leading to longer displacement times, dampened vertical migration, and immobilization of larger volumes within high permeability zones.

6.1.2 Dissolution trapping experiments

It was found to be infeasible to use the same surrogate fluids used in the small tank in the large tank due to the need for large volumes that were toxic and costly. Hence, the large tanks experiments used different surrogate fluids to investigate mixing that contributes to dissolution trapping. The goal of the small tank experiments was to investigate the influences of magnitude of permeability in homogeneous formations and different permeability distribution in heterogeneous formations on flow and storage of dissolved CO_2. The large tank experiments were designed primarily to investigate the effects of layering and the interlayer coupling mechanisms on dissolution trapping. The key findings of the small and large tanks experiments are presented. The detailed results are in section 5.2.

- Convective mixing is the dominant process that contributes to dissolution trapping when the formation is homogeneous. When the formation permeability is medium to high, dissolution trapping depends on the permeability of the formation.
- In the presence of zones with low permeability, diffusion can play a role in mixing. When the formation geologic structure is defined by layering, convection may not be the dominant mixing mechanism in low-permeability zones.
- Although diffusion is a slow process compared to convection, it might increase the amount of dissolved mass immobilized in the low permeability zones, thus contributing to trapping.
- The solute with dissolved CO2 that is denser than the formation water accumulates at the high/low permeability lithological interfaces and spreads laterally. This spreading increases the area available for diffusion into the low permeability layers and hence increases trapping through diffusion.
- In geologic settings where high permeability zones are connected within a low-permeability primary host rock, the dissolved CO2 migrating through the connected pathways results in increased contact area for diffusion and hence significantly enhances trapping. The low-permeability host rock provides a zone for long-term trapping through potential mineralization.
- In the traditional conceptual models of convective mixing, the density-driven instabilities are triggered by the pore-scale heterogeneities and grain size variation at the layer transition. The large tank experiments allowed for the identification of another macro-scale mechanism that contributes to convective mixing. When two higher permeability layers are separated by a

semi-confining leaky formation, density driven flow of CO2 dissolved solute through vertical connected pathways, produce macroscopically generated convective mixing in the lower layer.

- In cases where two layers are interacting through a leaky confining layer, experimental results showed that lighter formation water can flow upward from lower layer to upper layer, contributing to mixing in upper layer while delaying downward migration. To our knowledge, this is the first study to reveal this type of mixing process in heterogeneous systems. These leakage processes have to be accounted for when estimating potential dissolution trapping capacities in heterogeneous geologic formations.

6.3 Characterization of porous media properties

6.3.1 Scaling of capillary pressure vs saturation

We evaluated the dielectric sensor method to obtain the $P_c - S_w$ relationships for the surrogate fluids and compared the results with those from two scaling methods as well as literature data measured for $scCO_2$/brine. As the surrogate fluids, we selected Soltrol and glycerol/water mixture, which had a similar viscosity, density ratio, and interfacial tension to those of $scCO_2$ and brine at typical sequestration conditions. In addition, the fluids were selected because they had a distinct difference in their dielectric constants, which allowed for the dielectric sensors to detect the phase saturation of the system. The following statements summarize characteristics of each method.

- Leverett scaling is perhaps the simplest and quickest method to obtain a rough estimates of scaling factor for the selected surrogate fluids. The method, however, requires a device to measure interfacial tension for both fluid pairs. Furthermore, our data suggest that the scaling factor may be different for the drainage and imbibition cycles.
- The entry pressure scaling method involves a relatively simple procedure that can be performed without any special devices. The disadvantage of this method was, like Leverett scaling, the scaling factor may need to be obtained separately for the drainage and imbibition cycles. An advantage of the entry pressure scaling method over Leverett scaling is that entry pressure scaling incorporates effects of both medium specific contact angle and interfacial tension.

- The dielectric sensor method is more time-consuming, but the direct measurement of $P_c - S_w$ data yielded S_r and S_i. For the surrogate fluid pair that we used, S_r values were not far from those of the air-water system. However, the method required some knowledge on calibrating the dielectric moisture sensor for this special pair of fluids. Furthermore, this method may not work as well for fluid pairs with a small contrast in the dielectric properties.
- The dielectric sensor method yielded reasonable measurements of the $P_c - S_w$ relationship for the surrogate fluids compared to the scaling methods, although neither scaling method agreed completely with the dielectric sensor data.
- At high saturation, the entry pressure scaling method agreed more closely with the dielectric sensor method, whereas at lower saturation Leverett scaling yielded a closer fit with the dielectric sensor data. The deviation between the dielectric sensor method and two scaling methods was lower during drainage than during imbibition. Although it involved some additional setting up, the dielectric sensor method provided the most direct, complete, and accurate measurement of the capillary pressure relationships.
- Although capillary pressure measurements were influenced by differences in the sand and fluid properties, our data with surrogate fluids seemed to be consistent with the $scCO_2$-brine data of Tokunaga et al. (2013). We therefore, find that our surrogate fluids approach under low pressure environments can be used to gain insight into $scCO_2$-brine behavior at reservoir conditions. The ability to study this behavior under low pressure conditions will make it much more feasible and practical to study larger-scale heterogeneous systems in a controlled environment.

6.3.2 Relative permeability functions

- Empirically derived constitutive models of $k_r - S_w$ based on measured capillary pressure - saturation data and the experimentally determined $k_r - S_w$ were used as inputs to the multiphase code TOUGH2/T2VOC to simulate the $scCO_2$ displacing brine in an intermediate scale experiment. The model simulation that used the directly measured relative permeability shows slightly better match with the experimentally observed plume propagation.
- The results suggest the need for continued research to determine the relative permeability functions in CO_2 sequestration modeling. The empirical methods such as Van Genuchten

(1980) or Mualam (1976) that have been developed for soil physics applications that involves liquid-gas systems may not be suitable for fluid-fluid systems in CO_2 sequestration.

6.4 Numerical modeling

6.4.1 Capillary trapping

Darcy-based multiphase flow simulations have been utilized to explore the dissimilarities between numerical predictions and experimental outcomes due to possible misinterpretation of some fundamental mechanisms. Specifically, several findings can be summarized as follow:

- Demonstrated the applicability of the selected analog fluid combination to mimic the $scCO_2$/brine system at reservoir conditions, by qualitative compassion of plume propagation observed in one small tank homogeneous experiment with simulations carried out with TOUGH2/T2VOC and ECO2N (DOD codes).
- The research code TPFLOW developed as a part of this project was used to homogeneous large tank experiment and a geometrically similar homogeneous field-scale scenario. The model was able to capture some of features such as sharp pinning of the interface, the effect of background hydraulic gradient, and the increase in plume size as a consequence of the second injection. The model did not reproduce the breakthroughs of the plume into the left boundary at the end of the first fluid redistribution, as well as the front instability during the first injection. The latter is a clear consequence of the inability of conventional two-phase flow approach based on macroscopic (Darcian) to model the unstable flow patterns observed in real cases.
- A discrepancy between observed and simulated variance of the plume during the first redistribution period was found. This is due to the underestimated plume migration towards the outflow boundary; however, the simulated rate at which the variance increases after the second injection was in agreement with the laboratory observations.
- For the homogeneous configuration of the large tank experiments, the horizontal component of the plume spreading near the well is overestimated by the numerical model during the injection phase. This short-term behavior can be attributed to overemphasis of viscous forces with respect to buoyancy forces.

- For the homogeneous configuration of the large tank experiments, the plume tip advancement is clearly underestimated by the numerical model. This long-term behavior indicates that the influence of capillary forces responsible for slow advancement of the front is not correctly reproduced.
- While the previous arguments are not in favor of Darcy-based simulations, other features, such as truthful reproduction of the background water flow influence over plume migration, as well as replication of the change in slope of the plume front, are properly displayed by numerical contours.
- With the purpose of testing the applicability of analog fluids to mimic the $scCO_2$/brine system at reservoir conditions, injection of large volumes of $scCO_2$ in a geometrically similar, field-scale homogeneous domain, is modeled using the same Darcy-based simulator. The application of spatial moment analysis allowed for the qualitative assessment of average plume properties to compare the overall movement along the horizontal and vertical component of the simulations conducted at both laboratory and field scales.
- The numerical simulation of the laboratory experiment for the heterogeneous configuration highlighted a shortcoming of the Darcy-based simulator, especially when the long-term behavior of the simulated plume consistently diverged from the one observed in the experiment. Once again, the slow advancement and accumulation of non-wetting phase behind capillary barriers, with subsequent formation of secondary plumes was not captured at all by the model.
- Further implementation of fundamental migration and trapping mechanisms associated with capillary forces needs to be carried out in order to correctly reproduce the migration patterns observed in the laboratory experiments. Such mechanisms are extremely important to assess storage performance at reservoir conditions, especially in far-field well areas.

Hysteresis effects and development of constitutive models

- Including hysteresis in the numerical models appears to significantly improve predictions of the plume migration and distribution during post-injection for both homogeneous and heterogeneous conditions.
- Redistribution of non-wetting fluid during post-injection estimated by the model without hysteresis is much more rapid than those obtained by the model with hysteresis and the laboratory experiment. The results indicate that the hysteresis can have significant impact on capillary trapping.

- The model results also indicate that discontinuous high permeability zones that are traversed by an injected CO_2 plume in a reservoir can contribute to long-term trapping of CO_2, but the numerical studies conducted here will need to be extended to field-scale for evaluating the effects of hysteresis at field-scale under realistic CO2 storage conditions.
- Further theoretical and computational research would be needed to find better models and more efficient algorithms for solving nonlinear hysteretic partial differential equations, as the existing methodology for solving two-phase flow equations with hysteresis is computationally much less efficient than the standard methods for models without hysteresis.

6.4.2 Dissolution trapping

a. Field-Scale Simulations on Multilayered Systems

In this numerical study, the geology similar to the Utsira formation which has thin shale layers interbedded in-between composite sandstones was simulated for a range of shale permeabilities and thicknesses. The important conclusions drawn from this modeling study are listed as:

- The presence of any low permeability layer in the system slows down the vertical spreading of dissolved plume.
- 1000-year simulation results for the studied cases highlighted the occurrence of convective shutdown around 10 years due to low permeabilities of the shale layers. Convective shutdown equalized the dissolved CO_2 concentration of the upper sandstone layer. The time to the occurrence of convective mixing in the deeper sandstone layers depends on the permeability and thickness of the shale layers.
- The permeability of the shale layers was found to have more influence on spreading than their thickness. In the presence of thin and relatively higher permeability shale layers, the formation behaved like a convective mixing dominant permeable homogeneous formation. On the other hand, the thick and lower permeability shale layers retarded the vertical movement and enhanced lateral spreading considerably due to slow diffusion rates. This increased the diffusion area between high/medium and low permeability zones and the amount of diffused dissolved CO_2 into shales.
- The stratification of the formation, such as thickness and hydraulic properties of the layers, influence the mixing and hence effective and secure trapping of dissolved CO_2. The effective

strategies can be developed to enhance trapping by taking the advantage of natural heterogeneity of the formation.

b. Intermediate-Scale Simulations for Different Intralayer Heterogeneities present in Low-Permeability Layers

The effects of intralayer heterogeneity present in the low-permeability layers were studied experimentally and numerically. The experimental findings were tested numerically for a number of different intralayer heterogeneity realizations. The main conclusions drawn from this study are as follows:

- The numerical modeling results indicated that the distribution of the low-permeability materials is important for the long-term storage of CO_2. The smaller horizontal and longer vertical correlation lengths contribute to the fingering in the lower aquifer. This leads to the storage of dissolved CO_2 in the deeper parts of the formation. In addition, the higher permeability connected pathways enhance the diffusion area and diffused mass into silt/shale. However, in the long-term, more of the stored mass will be flushed away because the leakage through these zones will carry fresh water. This will increase concentration gradients and diffusion of the mass stored in the silt zones to the aquifers.
- The longer horizontal and smaller vertical correlations lengths in low-permeability layers limit the flow of dissolved CO_2 into the lower aquifer. On the other hand, this kind of layers are able to store the diffused mass for a long time. This might contribute to the more stable trapping, mineralization, in the long-term.
- These findings are applicable to both CO_2 sequestration and the contaminant transport in the multilayered systems to investigate the effects of heterogeneity in the low-permeability zones on flow and storage of the dissolved CO_2/NAPL. The effective strategies should be considered to enhance the trapping by taking the advantage of formation heterogeneity in CO_2 sequestration.

6.4.3 Stochastic analysis

Conclusions of the stochastic analyses are the following:

- The stochastic analysis allowed for the investigation of ways to enhance capillary trapping by designing intermittent and phased injection strategies.

- Low permeable facies hinder the vertical spread of the $scCO_2$, thus the plume is forced to travel horizontally through layers with higher permeability. Low permeability variance, implies that there is less probability for the presence facies with lower and higher permeability than the mean permeability. Therefore $scCO_2$ is distributed more vertically through the domain.
- Greater correlation lengths of the facies enhance the escape of the $scCO_2$through preferential pathways of high permeability; therefore $scCO_2$ is able to reach further areas of the formation by spreading horizontally.
- Correlation length affects the vertical distribution of the non-wetting phase. Short correlation lengths show a vertical distribution concentrated around the injection well. Longer correlation lengths show that the plume tends to advance horizontally due to travel of the plume through long layers of permeable sand.
- High formation heterogeneity increases the storage efficiency of CO_2. Effective saturations is higher for scenarios with high heterogeneity (defined by high variances) due to capillary barrier effects at the texture interfaces.
- High formation heterogeneity also increases the probability of the CO_2 of finding a potential leaky pathway. High heterogeneity increases the probability of the CO_2 to migrate through high permeable connected pathways to regions of the reservoir that are further away from the injection point and in which leakage may exist.
- Injection schemes including more alternate phases of injection and non-injection were found to increase the trapping effectiveness and increase the number of cases in which the CO_2 plume was contained in the secure zone of the reservoir. The CO_2 volume, injected applying an injection strategy within more cycles, invades less volume of the reservoir, thus the distribution of the CO_2 plume is accommodated in a smaller volume within the secure zone.

7 CONCLUSIONS AND RECOMMENDATIONS

When ongoing research and development efforts bring CCS technology to the stage of commercialization, numerical models that can simulate the capillary and dissolution trapping of scCO2 will become critically needed tools for site selection, design of engineering operations, and permanence assessment. Numerical models will continually evolve benefiting from new

knowledge gained from their use under diversity of conditions expected at field sites. As in deep geologic carbon storage, applications are still limited to some pilot and demonstration sites, the model development, and field validation are still in their early evolutionary stages. Hence, in the application of these early models, the question remain how good they capture some of the basic processes that are central to the technology for accurate model predictions. A special challenge in deep geologic carbon storage is that the predictions have to be made for both short-term decision-makings during the injection phase and long-term post-injection management. As data for the assessment of long-term prediction capabilities of models are not available, strategies have to be developed to "test" these models. The research we completed was designed to improve the understanding of the fundamental processes of capillary trapping that is relevant to a relatively short injection phase and dissolution trapping that occurs during a long post-injection period. The summary of the results and finding presented in the last section was organized under the experimental and modeling tasks. *The findings will ultimately lead to improved models in site selection and assessment of carbon storage potential, design of injection strategies and assessment of permanence. The conclusions that were derived from the findings are presented.*

This research was able to overcome a major challenge in generating accurate experimental data for process understanding, characterization and model testing. It is known that the natural heterogeneity of typical sedimentary formations has a significant effect on the propagation of the $scCO_2$ plume and eventually accumulating mobile phase underneath the caprock. Fully characterizing the geologic heterogeneity at all relevant scales and making observations on the spatial and temporal distribution of the migration and trapping of $scCO_2$ are not practical. Laboratory experiments using $scCO_2$ under ambient conditions are also not feasible as it is technically challenging and cost prohibitive to develop large, two- or three-dimensional test systems with controlled high pressures to keep the $scCO_2$ in liquid form. Hence, an innovative approach that used surrogate fluids in place of $scCO_2$ and formation brine in multi-scale, multiple length scales in synthetic sand reservoirs was developed and implemented. We demonstrated the applicability of analog fluids to mimic the scCO2/brine system at reservoir conditions, by comparison of plume propagation observed in a homogeneous tank experiment with simulations carried out with TOUGH2/T2VOC and ECO2N. *The data generated in multi-scale systems will be valuable to other researchers to test models during various stages of development.*

Trapping experiments conducted under homogeneous and heterogeneous conditions are used to derive useful conclusions relevant to field implementation of CCS in deep geologic formations. Even though the conditions of idealized homogeneity do not exist in nature, some useful insights into capillary trapping in relatively homogeneous formations were obtained. The trapped vertical saturation distributions below the caprock observed after the injection showed that the saturation at deeper locations reaches the residual faster. This observation supports the value of "inject low and let rise" injection schemes. A chase brine injection in the homogeneous formation after the $scCO_2$ was fully immobilized, resulted in enhanced trapped saturations at locations further away from the injection well due to the imposition of a secondary drainage/ imbibition cycle. The existing theory suggests that the final saturation will reach a uniform residual value throughout the homogeneous formation. However, in our experiments, clusters of sub-zones of immobilized $scCO_2$ with saturations higher than residual were observed behind zones where the plume initially advanced and produced lower residual saturation. In these idealized or relatively homogeneous formations, when a second injection is followed after the first $scCO_2$ placement, higher residual trapping saturations were achieved in zones that that have previously gone through drainage/imbibition cycles. *These observations suggest that the use of residual saturation values as determined from the non-hysteretic constitutive models may underestimate the storage capacities of the formation.*

The limited number of heterogeneous packing configurations tested did not represent all possible geologic conditions encountered in deep formations. However, the results were useful to obtain new insights to develop improved conceptual models that will lead to better numerical simulators. We used soils with contrasting permeabilities to create lithological texture transitions. When $scCO_2$ reaches such an interface until sufficient capillary pressure builds up for the non-wetting phase to reach the entry pressure value of the finer formation, the $scCO_2$ accumulates at the interface. This phenomenon referred to as "capillary barrier effect" exerts a major control on $scCO_2$ plume propagation and trapping in capillary-dominated regimes. How the permeability field is correlated in space, determines the degree by which the capillary raping saturations get enhanced above residual saturations. After initial placement of $scCO_2$, conditions may develop either from natural or imposed conditions where imbibition of saltwater may occur. In these cases, the trapped $scCO_2$ can get mobilized, and the benefits of the enhanced trapping. achieved through capillary barrier effects will not be realized. Models currently used to

estimate trapping models were evaluated using the experimental data. These models were only able to predict the final capillary-trapped saturation at conditions that may not be relevant to all possible scenarios expected during $scCO_2$ injection. *This finding suggests the need for better methods to estimate trapping in heterogeneous formations where enhanced trapping saturation is possible.*

The experiments suggest that forced imbibition in heterogeneous formations could be used to enhance trapping to promote invasion into previously uninvaded potential trapping zones. This approach may not contribute significantly to the overall capillary trapping, but distributing the scCO2 mass over a larger reservoir zone will increase the contact area between the two fluids for increased mass transfer thus enhancing dissolution trapping. *Thus, possibility of increasing overall trapping through optimization of capillary and dissolution trapping should be considered when options exist for saltwater sweeping.*

In intermediate scale tanks, it was possible to create heterogeneities with adequate length scale to observe how the $scCO_2$ plume develops during injection. The results from these experiments are used to make conclusions on how the injection strategies could be used to enhance trapping. In formations with high permeability contrasts, under imposed constant injection pressures, fluctuation in the flow rate was observed. This flow rate change is a result of the plume getting directed into high permeability connected pathways as the pressures build up to overcome capillary barriers. In cases where layering defines the heterogeneity, the trapping and preferential migration controlled by capillary barriers contributes to longer displacement times, dampened vertical migration and immobilization of larger volumes in the high permeability zones. *These findings suggest that the injection pressures can be controlled to force the plume to migrate into high permeability zones of the reservoirs preferentially to enhance capillary trapping.*

The dissolution experiments focused on the issue of investigation under what conditions the conceptual models of trapping of dissolved scCO2 in brine is controlled by density-driven convective mixing. The basic hypothesis that guided this investigation was that when heterogeneities are present, other mixing processes and diffusion contribute to dissolution trapping. The experimental results established that convective mixing is the dominant process that contributes to dissolution trapping when the formation is relatively homogeneous. In formations where the permeability is medium to high, dissolution trapping depends on the

average permeability of the formation. As natural formations are not homogenous, the spatial variability will affect convective mixing. When the formation geologic structure is defined by layering, convection may not be the dominant mixing mechanism in low-permeability zones.

When vertically migrating density driven fingers with dissolved scCO2 encounters low permeability zones, diffusion becomes dominant thus contributing to trapping. This process that is significantly slow compared to convection, immobilizes the dissolved mass in the low permeability zones, thus contributing to trapping. The amount of mass that will diffuse into a low permeability formation depends on the diffusion coefficient, the concentration gradients across the high/low permeability texture interface and the surface area of the interface available for diffusion. The available interface surface area depends on how the denser solute accumulates and spreads. *These findings suggest that the additional trapping resulting from diffusion into and in low permeability zones have to be factored into in designing both conceptual and numerical models.* Under favorable geochemical conditions, these immobilized dissolve mass will be trapped through mineralization. However, depending on the long-term trends in concentrations in the higher permeability zones, the diffused mass can rebound through reverse diffusion.

In some geological settings, interconnected higher permeability zones embedded in a primarily low permeability matrix define the heterogeneity. Another process that is not factored in conventional dissolution trapping models has to be considered in these cases. Instead of convection where the fingers propagate vertically down, the heavier solute with dissolved scCO2 migrates through these connected pathways carrying the dissolved mass deeper into the formation. In addition to contributing to large scale mixing, the large interface areas between the higher permeability pathway and the low permeability matrix will contribute to a significant mass immobilization through diffusion. In cases when these connected pathways are within semi-confining layers that separate two formations with adequate carbon storage capacity, the head differences produce leakage. When the leakage is from lower to upper layers, the unaffected formation brine from lower formation results in a mixing process that is not described in conventional dissolution trapping models. *These conclusions suggest the need to incorporate this mixing and storage mechanisms into improved conceptual and numerical models. Site characterization methods should be designed to identify these pathways*.

The multi-scale experimental data generated were used to conduct model analysis with the following goals: (1) to develop new insights into fundamental processes to improve

conceptual models, (2) to test existing models and modeling methods to evaluate their ability to capture some of the processes that were observed in the experimental studies, (3) to validate new modeling algorithms developed as part of this research project. As a first step in this analysis, it was needed to develop and test the constitutive models of capillary pressure vs saturation and relative permeability vs. saturation for the surrogate fluids that were fluids that were used in the experiments. These tested models were then used to conduct simulations based on hypothetical field scenarios and to conduct stochastic analysis to study optimal scCO2 injection scenarios. The conclusions from the characterization and model analysis studied are presented next.

One of the major challenges in applying multi-phase models used in scCO2 storage studies is the need to obtain the constitutive models of capillary pressure and relative permeability. When cores are removed from the field, to obtain the constitutive model parameters for scCO2-brine systems, to keep the scCO2 in liquid form, it is necessary to maintain high pressures. In this research we tested different scaling methods to explore whether it is possible to use the constitutive models from data generate from one fluid pair (e.g. water-air) in a porous medium to obtain the constitutive model parameters for a second fluid pair (e.g. a surrogate fluid pair) in the same porous medium. If this is shown, it is feasible to obtain the scCO2-brine constitutive model parameters using a surrogate fluid pair under ambient laboratory conditions. Three scaling methods were tested. The simplest of these was Leverett scaling, the quickest method to obtain a rough estimates of scaling factor for the selected surrogate fluids. However, the scaling factor may be different for the drainage and imbibition cycles. Methods based on entry pressure and dielectric measurements were developed in this research. The entry pressure scaling method involves a relatively simple procedure that can be performed without any special devices. The disadvantage of this method was, like Leverett scaling; the scaling factor may need to be obtained separately for the drainage and imbibition cycles. An advantage of the entry pressure scaling method over Leverett scaling is that entry pressure scaling incorporates effects of both medium specific contact angle and interfacial tension. The dielectric sensor method was more time-consuming, but the direct measurement of Pc – Sw data yielded the residual and immobile saturations (Sr and Si) that was not possible in the other two methods. Although capillary pressure measurements were influenced by differences in the sand and fluid properties, our data with surrogate fluids seemed to be consistent with the scCO2-brine data of Tokunaga et al. (2013). *We, therefore, find that our surrogate fluids approach under low*

pressure environments can be used to gain insight into scCO2-brine behavior at reservoir conditions. The ability to study this behavior under low-pressure conditions will make it much more feasible and practical to study larger-scale heterogeneous systems in a controlled environment.

We also investigated the applicability of an approach used in soil physics applications to obtain the parameters of the constitutive models of relative permeability vs. saturation ($k_r - S_w$), empirically using the fitted parameters of the Pc – Sw constitutive model. If successful, this would have avoided the need for the direct measurement of relative permeability, that will be complex and expensive when using scCO2. The relative permeability functions obtained from the two methods were applied to simulate a tank experiment using DOE multiphase simulation codes TOUGH2/T2VOC. None of the two methods was able to match the experimental observation accurately, but the directly measured relative permeability showed slightly better match with the experimentally observed plume propagation. *We conclude that there is a need for continued research to determine the relative permeability functions in CO_2 sequestration modeling.*

For better prediction of capillary trapping, we developed new constitutive models for representing macroscopic hysteretic capillary-pressure saturation and relative permeability relationships. It is demonstrated through pore-scale simulations and measured core-scale data sets that this new approach is very promising to successfully represent hysteresis behavior and residual trapping observed during successively occurring drainage and imbibition processes. The numerical model with the hysteretic constitutive models appears to improve the predictive ability for the experimental results in the small tanks. The hysteretic numerical model appears to capture the plume migration reasonably well for both homogeneous and heterogeneous conditions. Redistribution of non-wetting fluid during post-injection estimated by the model without hysteresis is much more rapid than those obtained by the model with hysteresis and the laboratory experiment. *This finding indicates that numerical multiphase flow simulators with hysteresis effects included may lead to more accurate prediction of fluid distributions at field-scale geological systems*.

However, computational efficiency of the model with hysteresis is relatively low compared to the models without hysteresis. Further computational research would be needed to find more efficient algorithms for solving nonlinear hysteretic partial differential equations. The

model results also indicate that discontinuous high permeability zones that are traversed by an injected CO_2 plume in a reservoir can contribute to long-term trapping of CO_2, but the numerical studies conducted here will need to be extended to large-tank and field for evaluating the effects of hysteresis at field-scale under realistic CO_2 storage conditions. *Fundamental migration and trapping mechanisms associated with capillary forces need to be correctly implemented in model algorithms. These mechanisms are extremely important to assess storage performance at reservoir conditions, especially in far-field well areas.*

The experimental simulations on dissolution were limited few packing configurations. The diffusive and convective mixing processes on trapping of dissolved CO2 was further studied using a single-phase, two-component, and density and viscosity-dependent flow and transport model developed in this research. Two settings were used in the numerical studies. The first was a sensitivity study on a model domain with geology similar to the Utsira formation containing thin shale layers interbedded in-between composite sandstones. The second, was a designed based on the test domain of the intermediate-scale test tank with different intralayer heterogeneities present in low-permeability formation. The results of these studies are used to further establish the conclusions derived in the experiments on mixing and dissolution trapping in naturally heterogeneous formations.

As dissolution is a process that contributed to trapping during longer durations, the Utsira formation based simulations were conducted for 1000-years. When convective fingers encountered a low permeability shale layer, a convective shutdown occurred, bringing the concentrations in the upper layer to a uniform value, thus enhancing trapping in the upper layer of the formation. The time at which this shutdown occurred depended on the permeability and thickness of the shale layers. In the presence of thin, but relatively higher permeability shale, the formation effectively behaved like a convective mixing dominant permeable homogeneous formation. In cases of where thick and lower permeability shale layers are present, the vertical movement and enhanced lateral spreading at the layer interfaces slowed considerably due to slow diffusion rates. This increased the diffusion area at the interface, this enhancing trapping in the in the shale by storing diffused dissolve mass.

The numerical model that was partially validated using the experimental data in the intermediate-scale tank was used to conduct simulations where geostatistical parameters were used to quantify the formation heterogeneity of the semi-confined layer separating higher

permeable layers. The smaller horizontal and longer vertical correlation lengths in this semi-confining layer contribute to the fingering that produced convective mixing in the lower aquifer. Larger horizontal and smaller vertical correlations lengths in low-permeability layers limited the transport of dissolved CO2 into the lower aquifer. However, layers with these features are able to store the diffused mass for a long time periods through immobilization of dissolved mass. These mechanisms might contribute to the more stable trapping, mineralization, in the long-term. *These findings as well as the findings from the field based sensitivity studies allows us to conclude that as was in the case of capillary trapping, effective strategies can be developed to enhance dissolution trapping by taking advantage of the natural heterogeneity of the formation.*

The final model analysis is presented to make conclusions on how the natural heterogeneity could be factored in when designing CO2 injection strategies. Stochastic analysis was performed using the developed multiphase model to investigate ways to enhance capillary trapping by designing intermittent and phased injection strategies. As was established in the experimental studies, high formation heterogeneity (defined by high variance of logarithm of hydraulic conductivity) increases the storage efficiency of CO2. Effective saturations were found to be higher for scenarios with high heterogeneity due to capillary barrier effects. High heterogeneity increased the probability of the CO2 to migrate through high permeable connected pathways to regions of the reservoir that are further away from the injection point where potential leakage pathways in the caprock (e.g. faults or abandoned wells) may exist. *This very preliminary study finding suggests that by using information on the heterogeneity, time-phased CO2 injection schemes can be developed to enhance capillary trapping and secure permanence by confining the trapping zones to safe zones of the formation by minimizing potential for possible leakage.*

Based on the key conclusions, the following recommendations are made:

- The fundamental formulations of multiphase flows have to be revisited to evaluate their ability to capture heterogeneity-controlled trapping processes at all relevant scales.
- Further research is needed to develop and test physically-based constitutive models of capillary pressure-saturation and relative permeability applicable to natural rocks.
- Further research would be needed to find better models and more efficient algorithms for solving nonlinear hysteretic partial differential equations, as the existing methodology for

solving two-phase flow equations with hysteresis is computationally much less efficient than the standard methods for models without hysteresis.

- Further research is needed to develop upscaling methodologies and/or efficient multi-scale modeling approaches for improving predictive ability of the models at field-scale. This is needed for taking into account heterogeneities at multiple scales and appropriately employing multiphase model parameters that are measured typically at laboratory-scale.
- In site characterization, attention should be given to identify low permeability zones where dissolved CO2 can be immobilized for long-term trapping.
- The contribution of leakage occurring between higher permeability formations through semi-confining layers should be factored into conceptual and numerical models of mixing used in dissolution trapping analysis.
- In site characterization, attention should be given to identify low permeability zones where dissolved CO2 can be immobilized for long-term trapping.
- The contribution of leakage occurring between higher permeability formations through semi-confining layers should be factored into conceptual and numerical models of mixing used in dissolution trapping analysis.

8 LIST OF ACRONYMS AND ABBREVIATIONS

$scCO_2$	Supercritical CO_2
NWP	Non-wetting phase
$\rho_{nw/w}$	Density (non-wetting/wetting phase)
$\mu_{nw/w}$	Dynamic viscosity (non-wetting/wetting phase)
IFT	Interfacial tension
Φ_{avg}	Average porosity
d_{50}	Mean particle size
d_{60}/d_{10}	Uniformity coefficient
$S_{nw}^{r,max}$	Maximum residual non-wetting phase saturation
IC	Ion chromatography
GC	Gas chromatography
PG	Propylene glycol
MEG	Methanol/Ethylene glycol mixture
RGB	Red-Green-Blue
FID	Flame ionized detector
SIS	Sequential indicator simulator
SGeMS	Stanford Geostatistical Modeling Software
1-D	One-dimensional
2-D	Two-dimensional
3-D	There-dimensional
ADE	Advection diffusion equation
Ra	Rayleigh Number [-]
S_w	Wetting phase saturation
S_{nw}	Non-wetting phase saturation
w	Mass fraction of the 2nd component [-]
ρ	Density [kg/m^3]
μ	Viscosity [kg/m.s]
k	Permeability [m^2]

k_{rw}	Relative permebility of wetting phase
k_{rnw}	Relative permebility of non-wetting phase
H	Thickness of the domain [m]
g	Gravitational acceleration [m/s^2]
D	Diffusion coefficient [m^2/s]
u	Darcy flux [m/s]
P	Pressure [Pa]
λ_c	Critical wavelength [cm]
MW	Molecular weight [g/mole]
V_φ	Molar volume of dissolved CO_2 (cm^3/g.mole)
T	Temperature [˚C]

9 TECHNOLOGY TRANSFER ACTIVITIES

Based on the research conducted by two Masters students (Hiroko Mori and Javier Vargas-Johnson), two PhD students (Luca Trevisan and Elif Agartan), one postdoctoral researcher (Ana González-Nicolás), and the collaboration with Lawrence Berkeley National Laboratory, several peer-reviewed journal publications and conference proceeding were produced. The researcgh findings were presented at a number of national and international conferences. The PI was a key note speaker at a number of conferences where the research findings were presented. These talks included the European Geological Union Darcy Medal talk of 2012, key note talk at THA 2015 International Conference on "Climate Change and Water & Environment Management in Monsoon Asia" 28-30 January 2015, Bangkok, Thailand and key note talk at "The Water Energy Nexus: Sustainability and Global Challenges", April 17, 2014, Beijing, China

10 PUBLICATIONS

Peer-reviewed journal publications

Cihan, A., Birkholzer, J., Illangasekare, T.H., Zhou, Q., 2014. A modeling approach to represent hysteresis in capillary pressure-saturation relationship based on fluid connectivity in void space. *Water Resour Res* **50**, 119-131.

Trevisan, L., Cihan, A., Agartan, E., Mori, H., Fagerlund, F., Birkholzer, J.T., Zhou, Q., Illangasekare, T.H., 2014. Investigation of mechanisms of supercritical CO_2 trapping in deep saline reservoirs using surrogate fluids at ambient laboratory conditions. *International Journal of Greenhouse Gas Control* **29**, 35-49.

Agartan, E., Trevisan, L., Cihan, A., Birkholzer, J., Zhou, Q., Illangasekare, T.H., 2015. Experimental study on effects of geologic heterogeneity in enhancing dissolution trapping of supercritical CO_2. *Water Resour Res*, (in press).

Mori, H., Sakaki, T., Illangasekare. T. H. (2015). Laboratory study of geological carbon sequestration using surrogate fluids: Dielectric measurement and scaling of capillary

pressure - saturation relationships. *International Journal of Greenhouse Gas Control* (accepted).

Mori, H., Trevisan, L., Illangasekare, T.H. Evaluation of relative permeability functions as inputs to multiphase flow models simulating supercritical CO_2 behavior in deep geologic formations. *International Journal of Greenhouse Gas Control* (submitted).

Trevisan, L., Pini, R., Cihan, A., Birkholzer, J.T., Zhou, Q., Illangasekare, T.H. Experimental analysis of spatial correlation effects on capillary trapping of supercritical CO_2 at the intermediate laboratory scale in heterogeneous porous media. *Water Resour Res* (submitted).

Agartan, E., Cihan, A., Birkholzer, J.T., Zhou, Q., Illangasekare, T.H. Effects of Stratigraphy of Deep Layered Geologic Formations on Trapping of Dissolved CO_2, *Water Resour Res* (under review).

Trevisan, L., Pini, R., Cihan, A., Birkholzer, J.T., Zhou, Q., Illangasekare, T.H. Process understanding for capillary trapping enhancement of supercritical CO_2 in complex heterogeneous media through intermediate scale testing (in preparation).

González-Nicolás, A., Trevisan, L., Illangasekare, T.H. Enhancing Trapping Effectiveness through the Optimization of Injection of Supercritical CO_2 in Heterogeneous Formations (in preparation).

Agartan, E., Cihan, A., Birkholzer, J.T., Zhou, Q., Illangasekare, T.H. (2015), Study of the Effects of Formation Heterogeneity in the Semi-Confining Shale Layers in Enhancing Mixing, Contributing to Dissolution Trapping of CO_2, Water Resour. Res., (in preparation).

Conference proceedings

Illangasekare, T.H., Trevisan, L., Agartan, E., Vargas-Johnson, J., Plampin, M., Pini, R., Pawar, R., Cihan, A., Birkholzer, J.T., Zhou, Q. Experimental Investigation of CO_2 Trapping and Leakage Mechanisms in Deep Geologic Formations for Model Improvement. Fall Meeting of the American Geophysical Union, San Francisco, CA, Dec 2014 (oral presentation).

Agartan, E., Cihan, A., Birkholzer, J.T., Zhou, Q., Illangasekare, T.H. Effects of Stratigraphy of Deep Layered Geologic Formations on Trapping of Dissolved CO_2. Fall Meeting of the American Geophysical Union, San Francisco, CA, Dec 2014 (poster presentation).

Trevisan, L., Pini, R., Cihan, A., Birkholzer, J.T., Zhou, Q., Illangasekare, T.H., 2014. Experimental Investigation of Supercritical CO_2 Trapping Mechanisms at the Intermediate

Laboratory Scale in Well-defined Heterogeneous Porous Media. Energy Procedia 63, 5646-5653 (oral presentation).

Cihan, A., Birkholzer, J.T., Trevisan, L., Bianchi, M., Zhou, Q., Illangasekare, T., 2014. A Connectivity-Based Modeling Approach for Representing Hysteresis in Macroscopic Two-Phase Flow Properties. Energy Procedia 63, 3456-3463 (oral presentation).

Trevisan, L., Pini, R., Cihan, A., Birkholzer, J.T., Zhou, Q., Illangasekare, T.H. Experimental analysis of trapping phenomena at the intermediate laboratory scale in well-defined heterogeneous porous media. Gordon Research Conference, Lewiston, ME, Jul 2014 (poster presentation).

Agartan, E., Cihan, A., Birkholzer, J.T., Zhou, Q., Illangasekare, T.H. Effects of Lithology of Deep Layered Geologic Formations on Trapping of Dissolved Supercritical CO_2. Gordon Research Conference, Lewiston, ME, Jul 2014 (poster presentation).

Illangasekare, T.H.. Plampin, M., Trevisan, L., Agartan, E., Vargas-Johnson, J., Mori, Sakaki, T., Pawar, R., Cihan, A., Birkholzer, J.T., Zhou, Q. Intermediate scale experimental investigation of CO_2 trapping and leakage mechanisms in deep geologic formations for model improvement. 6th International Conference on Porous Media, Milwaukee, WI, May 2014 (oral presentation).

Trevisan, L., Cihan, A., Fagerlund, F., Agartan, E., Mori, H., Birkholzer, J.T., Zhou, Q., Illangasekare, T.H. Investigation of multiphase modeling approaches for behavior of super critical CO_2 in deep formations using analog fluids in the laboratory. Fall Meeting of the American Geophysical Union, San Francisco, CA, Dec 2013 (poster presentation).

Trevisan, L., Illangasekare, T.H., Cihan, A., Vargas-Johnson, J., Agartan, E., Mori, H., Birkholzer, J.T., Zhou, Q. Investigation of multiphase modeling approaches for behavior of super critical CO_2 in deep formations using analog fluids in the laboratory. Carbon storage R&D project review meeting, Pittsburgh, PA, Aug 2013 (poster presentation).

Illangasekare, T.H., Agartan, E., Trevisan, L., Cihan, A., Birkholzer, J.T., Zhou, Q. A fundamental study of convective mixing contributing to dissolution trapping of CO_2 in heterogeneous geologic media using surrogate fluids and numerical modeling. General Assembly of the European Geophysical Union, Vienna, Austria, Apr 2013 (oral presentation).

Agartan, E., Illangasekare, T.H., Cihan, A., Birkholzer, J.T., Zhou, Q., Trevisan, L. Intermediate scale testing and modeling for improving fundamental understanding of heterogeneity effect on density-driven convective fingers and dissolution trapping in deep geologic formations. Gordon Research Conference, Les Diablerets, Switzerland, Jun 2012 (poster presentation).

Illangasekare, T.H., Plampin, M., Trevisan, L., Agartan, E., Mori, H., Sakaki, T., Cihan, A., Birkholzer, J.T., Zhou, Q., Pawar, R., Zyvoloski, G. Multiple scale physical and numerical modeling for improved understanding of mechanisms of trapping and leakage of CO_2 in deep geologic formations. General Assembly of the European Geophysical Union, Vienna, Austria, Apr 2012 (oral presentation).

Trevisan, L., Illangasekare, T.H., Rodriguez, D., Sakaki, T., Cihan, A., Birkholzer, J.T., Zhou, Q. Experimental methods for the simulation of supercritical CO_2 injection at laboratory scale aimed to investigate capillary trapping. Fall Meeting of the American Geophysical Union, San Francisco, CA, Dec 2011 (poster presentation).

Cihan, A., Birkholzer, J.T., Zhou, Q., Trevisan, L., Illangasekare, T.H., Rodriguez, D., Sakaki, T. A Numerical modeling study of effect of heterogeneity on capillary trapping of geologically sequestrated CO_2. Fall Meeting of the American Geophysical Union, San Francisco, CA, Dec 2011 (poster presentation).

Illangasekare, T.H., Trevisan, L., Rodriguez, D., Cihan, A., Birkholzer, J.T., Zhou, Q. A fundamental study of migration an entrapment of supercritical CO_2 in heterogeneous deep geologic formations: intermediate scale testing and modeling. General Assembly of the European Geophysical Union, Vienna, Austria, Apr 2011 (oral presentation).

Masters and doctoral theses

Mori, H., 2013. The study of constitutive relationships of multi-phase flow for geological carbon sequestration. Hydrologic Science and Engineering (Master). Colorado School of Mines, Golden, CO.

Vargas-Johnson, J., 2014. Development of experimental methods for intermediate scale testing of deep geologic CO_2 sequestration trapping processes at ambient laboratory conditions. Hydrologic Science and Engineering (Master). Colorado School of Mines, Golden, CO.

Trevisan, L., 2015. Study of trapping mechanisms of supercritical carbon dioxide in deep heterogeneous geological formations through intermediate-scale testing and modeling. Civil and Environmental Engineering (PhD). Colorado School of Mines, Golden, CO.

Agartan, E., 2015. Fundamental study on the effects of heterogeneity on trapping of dissolved CO_2 in deep geological formations through intermediate scale testing and numerical modeling. Civil and Environmental Engineering (PhD). Colorado School of Mines, Golden, CO.

11 REFERENCES

Agartan, E. (2015), A fundamental study on the effects of heterogeneity on trapping of dissolved CO_2 in deep geologic formations through intermediate-scale testing and numerical modeling, PhD Dissertation, Civil and Environmental Engineering. Colorado School of Mines, Golden, CO.

Agartan, E., L. Trevisan, A. Cihan, J. Birkholzer, Q. Zhou, and T. H. Illangasekare (2015a), Experimental study on effects of geologic heterogeneity in enhancing dissolution trapping of supercritical CO_2, Water Resour. Res., (in press).

Agartan, E., A. Cihan, J. Birkholzer, Q. Zhou, and T.H. Illangasekare (2015b), Effects of stratigraphy of deep layered geologic formations on trapping of dissolved CO_2, Water Resour. Res., (under review).

Aggelopoulos, C. A., and C. D. Tsakiroglou, 2012. Effects of micro-heterogeneity and hydrodynamic dispersion on the dissolution rate of carbon dioxide in water-saturated porous media, International Journal of Greenhouse Gas Control, 10, 341-350.

Akbarabadi, M., Piri, M., 2013. Relative permeability hysteresis and capillary trapping characteristics of supercritical CO_2/brine systems: An experimental study at reservoir conditions. Adv Water Resour 52, 190-206.

Al Mansoori, S., Iglauer, S., Pentland, C.H., Bijeljic, B., Blunt, M.J., 2009. Measurements of Non-Wetting Phase Trapping Applied to Carbon Dioxide Storage. Enrgy Proced 1, 3173-3180.

Amaechi, B., Iglauer, S., Pentland, C.H., Bijeljic, B., Blunt, M.J., 2014. An Experimental Study of Three-Phase Trapping in Sand Packs. Transp. Porous Media 103, 421-436.

Arts, R., Chadwick, A., Eiken, O., Thibeau, S., Nooner, S., Netherlands Institute of Applied Geoscience TNO - National Geological Survey, British Geological Survey, Statoil Research Centre, E, T., P Plc , Lamont-Dohery Geological Observatory of Columbia University, 2008. Ten years' experience of monitoring CO_2 injection in the Utsira Sand at Sleipner, offshore Norway. First Break 26, 65-72.

Bachu, S., 2000. Sequestration of CO_2 in geological media: criteria and approach for site selection in response to climate change. Energ Convers Manage 41, 953-970.

Bachu, S., Adams, J.J., 2003. Sequestration of CO_2 in geological media in response to climate change: capacity of deep saline aquifers to sequester CO_2 in solution. Energ Convers Manage 44, 3151-3175.

Bachu, S., Bonijoly, D., Bradshaw, J., Burruss, R., Holloway, S., Christensen, N.P., Mathiassen, O.M., 2007. CO_2 storage capacity estimation: Methodology and gaps. International Journal of Greenhouse Gas Control 1, 430-443.

Bachu, S., Gunter, W.D., Perkins, E.H., 1994. Aquifer Disposal of CO_2 - Hydrodynamic and Mineral Trapping. Energ Convers Manage 35, 269-279.

Backhaus, S., Turitsyn, K., Ecke, R.E., 2011. Convective Instability and Mass Transport of Diffusion Layers in a Hele-Shaw Geometry. Phys Rev Lett 106.

Bandara, U.C., Tartakovsky, A.M., Palmer, B.J., 2011. Pore-scale study of capillary trapping mechanism during CO_2 injection in geological formations. International Journal of Greenhouse Gas Control 5, 1566-1577.

Barth, G.R., Hill, M.C., Illangasekare, T.H., Rajaram, H., 2001. Predictive modeling of flow and transport in a two-dimensional intermediate-scale, heterogeneous porous medium. Water Resour Res 37, 2503-2512.

Bear, J., 1972. Dynamics of fluids in porous media. American Elsevier Pub. Co., New York.

Beck, J. L., 1972. Convection in a box of porous material saturated with fluid, Physics of Fluids, 15(8), 1377-1383.

Bennion, D.B., Bachu, S., 2006. Dependence on Temperature, Pressure, and Salinity of the IFT and Relative Permeability Displacement Characteristics of CO_2 Injected in Deep Saline Aquifers, 2006 SPE Annual Technical Conference and Exhibition. Society of Petroleum Engineers, San Antonio, Texas, U.S.A.

Benson, S.M., Cole, D.R., 2008. CO_2 Sequestration in Deep Sedimentary Formations. Elements 4, 325-331.

Benson, S. M., and P. Cook, 2005. Underground geological storage, in Intergovernmental Panel on Climate Change Special Report on Carbon Dioxide Capture and Storage, coordinating author P. Freund, pp. 195–276, Cambridge Univ. Press, Cambridge, U. K.

Berg, S., Ott, H., 2012. Stability of CO_2-brine immiscible displacement. International Journal of Greenhouse Gas Control 11, 188-203.

Birkholzer, J.T., Zhou, Q.L., Tsang, C.F., 2009. Large-scale impact of CO_2 storage in deep saline aquifers: A sensitivity study on pressure response in stratified systems. International Journal of Greenhouse Gas Control 3, 181-194.

Brooks, R. H., and Corey, A. T., 1964. Hydraulic properties of porous media. Hydrology Papers, Colorado State University, (March).

Burdine, N. T., 1953. Relative permeability calculations from pore size distribution data. Journal of Petroleum Technology, 5(3), 71-78.

Bryant, S.L., Lakshminarasimhan, S., Pope, G.A., 2008. Buoyancy-Dominated Multiphase Flow and Its Effect on Geological Sequestration of CO_2. Spe J. 13, 447-454.

Buscheck, T.A., Sun, Y.W., Chen, M.J., Hao, Y., Wolery, T.J., Bourcier, W.L., Court, B., Celia, M.A., Friedmann, S.J., Aines, R.D., 2012. Active CO_2 reservoir management for carbon storage: Analysis of operational strategies to relieve pressure buildup and improve injectivity. International Journal of Greenhouse Gas Control 7, 268-268.

Capuano, R. M. (1993), Evidence of fluid flow in microfractures in geopressured shales, AAPG Bulletin, 77(8), 1303-1314.

Chadwick, R. A., R. Arts, O. Eiken, G. A. Kirby, E. Lindeberg, and P. Zweigel, 2004. 4D seismic imaging of an injected CO2 plume at the Sleipner Field, central North Sea, Geological Society of London In: Davies, Richard J., (ed.) 3D seismic technology: application to the exploration of sedimentary basins. London, UK, Geological Society of London, 311-320. (Geological Society of London Memoir, 29).

Chen, J., Hopmans, J. W., and Grismer, M. E., 1999. Parameter estimation of two-fluid capillary pressure–saturation and permeability functions. Advances in Water Resources, 22(5), 479–493.

Cheng, N.S., 2008. Formula for the viscosity of a glycerol-water mixture. Ind Eng Chem Res 47, 3285-3288.

Cihan, A., Tyner, J. S., and Perfect, E., 2009. Predicting relative permeability from water retention: A direct approach based on fractal geometry. Water Resources Research, 45(4), W04404.

Cinar, Y., Jessen, K., Berenblyum, R., Juanes, R., Orr, F.M., 2006. An experimental and numerical investigation of crossflow effects in two-phase displacements. Spe J. 11, 216-226.

Cinar, Y., Riaz, A., Tchelepi, H.A., 2009. Experimental Study of CO_2 Injection Into Saline Formations. Spe J. 14, 588-594.

Combarnous, M. A., and S. A. Bories, 1975. Hydrothermal convection in saturated porous media, Adv. Hydroscience, 10, 231–307.

Cooper, C. A., R. J. Glass, and S. W. Tyler, 1997. Experimental investigation of the stability boundary for double-diffusive finger convection in a Hele-Shaw cell, Water Resour. Res., 33(4), 517-526.

Corbett, P.W.M., Ringrose, P.S., Jensen, J.L., Sorbie, K.S., 1992. Laminated Clastic Reservoirs: The Interplay of Capillary Pressure and Sedimentary Architecture, SPE Annual Technical Conference and Exhibition. Society of Petroleum Engineers, Washington, D.C.

Craig, F.F., 1993. The reservoir engineering aspects of waterflooding. Henry L. Doherty Memorial Fund of AIME, Richardson, Tex.

Craig, F.F.J., Sanderlin, J.L., Moore, D.W., Geffen, T.M., 1957. A Laboratory Study of Gravity Segregation in Frontal Drives. Petroleum Transactions, AIME 210, 275-282.

Dane, J. H., Oostrom, M., & Missildine, B. C. (1992). An improved method for the determination of capillary pressure-saturation curves involving TCE, water and air. Journal of contaminant hydrology, 11(1), 69-81

Dane, J. H., C. Hofstee, and A. T. Corey, 1998. Simultaneous measurement of capillary pressure, saturation, and effective permeability of immiscible liquids in porous media, Water Resour. Res., 34(12), 3687–3692.

Demond, A. H., and Roberts, P. V., 1993. Estimation of two-phase relative permeability relationships for organic liquid contaminants. Water resources research, 29(4), 1081–1090.

Deutsch, C.V., Journel, A.G., 1998. GSLIB geostatistical software library and user's guide, 2.0, 2nd ed. ed. Oxford University Press, New York.

DiCarlo, D.A., Jessen, K., Orr, F.M., 2007. Compositional gravity drainage 2: experimental measurements using an analog system. Transp. Porous Media 69, 159-174.

Doughty, C., Pruess, K., 2004. Modeling supercritical carbon dioxide injection in heterogeneous porous media. Vadose Zone J 3, 837-847.

Doughty, C., Pruess, K., Benson, S.M., Hovorka, S.D., Knox, P.R., Green, C.T., 2001. Capacity investigation of brine-bearing sands of the Frio formation for geologic sequestration of CO_2.

Duan, Z., and R. Sun, 2003. An improved model calculating CO_2 solubility in pure water and aqueous NaCl solutions from 273 to 533 K and from 0 to 2000 bar, Chemical Geology, 193(3), 257-271.

Duan, Z.H., Sun, R., Zhu, C., Chou, I.M., 2006. An improved model for the calculation of CO2 solubility in aqueous solutions containing Na+, K+, Ca2+, Mg2+, Cl-, and SO42-. Mar Chem 98, 131-139.

Eichel, H., Helmig, R., Neuweiler, I., Cirpka, O.A., 2005. Upscaling of Two-Phase Flow Processes in Porous Media, in: Das, D.B., Hassanizadeh, S.M. (Eds.), Upscaling Multiphase Flow in Porous Media: From Pore to Core and Beyond. Springer, pp. 237-257.

Elder, J. W., 1967. Steady free convection in a porous medium heated from below, J. Fluid Mech., 27(1), 29-48.

Ennis-King, J., Paterson, L., 2003. Engineering Aspects of Geological Sequestration of Carbon Dioxide, SPE Asia Pacific Oil and Gas Conference and Exhibition. Society of Petroleum Engineers Melbourne, Australia.

Ennis-King, J., Preston, I., Paterson, L., 2005. Onset of convection in anisotropic porous media subject to a rapid change in boundary conditions. Phys Fluids 17.

Ennis-King, J., and L. Paterson (2007), Coupling of geochemical reactions and convective mixing in the long-term geological storage of carbon dioxide, International Journal of Greenhouse Gas Control, 1(1), 86-93.

Epherre, J. F., 1977. Criterion for the appearance of natural convection in an anisotropic porous layer, Intl Chem. Engng, 17, 615–616.

Fagerlund, F., Illangasekare, T.H., Niemi, A., 2007. Nonaqueous-phase liquid infiltration and immobilization in heterogeneous media: 1. Experimental methods and two-layered reference case. Vadose Zone J 6, 471-482.

Falta, R.W., Pruess, K., Finsterle, S., Battistelli, A., 1995. T2VOC User's Guide. Lawrence Berkeley Laboratory, Berkeley, CA.

Farajzadeh, R., H. Salimi, P. L. J. Zitha, and H. Bruining, 2007. Numerical simulation of density-driven natural convection in porous media with application for CO_2 injection projects, International Journal of Heat and Mass Transfer, 50(25), 5054-5064.

Farajzadeh, R., F. F. Zinati, P. L. J. Zitha, and J. Bruining, 2008. Density-driven natural convection in dual layered and anisotropic porous media with application for CO2 injection projects, paper presented at 11th European Conference on the Mathematics of Oil Recovery, Bergen, Norway.

Farajzadeh, R., Ranganathan, P., Zitha, P.L.J., Bruining, J., 2011. The effect of heterogeneity on the character of density-driven natural convection of CO_2 overlying a brine layer. Adv Water Resour 34, 327-339.

Fernandez-Garcia, D., Illangasekare, T.H., Rajaram, H., 2004. Conservative and sorptive forced-gradient and uniform flow tracer tests in a three-dimensional laboratory test aquifer. Water Resour Res 40.

Fischer, U., Celia, M. A., 1999. Prediction of relative and absolute permeabilities for gas and water from soil water retention curves using a pore-scale network model. Water Resources Research, 35(4), 1089-1100.

Firoozabadi, A., Cheng, P., 2010. Prospects for Subsurface CO_2 Sequestration. Aiche J 56, 1398-1405.

Flett, M., Gurton, R., Taggart, I., 2004. The Function of Gas-Water Relative Permeability Hysteresis in the Sequestration of Carbon Dioxide in Saline Formations, SPE Asia Pacific Oil and Gas Conference and Exhibition. Society of Petroleum Engineers Perth, Australia.

Flett, M., Gurton, R., Weir, G., 2007. Heterogeneous saline formations for carbon dioxide disposal: Impact of varying heterogeneity on containment and trapping. J Petrol Sci Eng 57, 106-118.

Freyberg, D.L., 1986. A Natural Gradient Experiment on Solute Transport in a Sand Aquifer .2. Spatial Moments and the Advection and Dispersion of Nonreactive Tracers. Water Resour Res 22, 2031-2046.

Freeze, R. A., and J. A. Cherry (1979), Groundwater, Englewood Cliffs, NJ: Printice-Hall Inc, 604p.

Garcia, J. E., 2001. Density of aqueous solutions of CO_2, Lawrence Berkeley National Laboratory, Oak Ridge, Tenn.

Gasda, S.E., Celia, M.A., Nordbotten, J.M., 2006. Significance of Dipping Angle on CO_2 Plume Migration in Deep Saline Aquifers, in: Philip J. Binning Peter Engesgaard, H.D., George F. Pinder and William G. Gray (Ed.), XVI International Conference on Computational Methods in Water Resources, Denmark.

Gasda, S.E., Nilsen, H.M., Dahle, H.K., 2013. Impact of structural heterogeneity on upscaled models for large-scale CO_2 migration and trapping in saline aquifers. Adv Water Resour 62, 520-532.

Glass, R. J., 1993. Modeling gravity-driven fingering in rough-walled fractures using modified percolation theory, paper presented at 4th Annual High-Level Radioactive Waste Management Conference, Am. Soc. of Civ. Eng., Las Vegas, Nev.

Golding, M.J., Huppert, H.E., Neufeld, J.A., 2013. The effects of capillary forces on the axisymmetric propagation of two-phase, constant-flux gravity currents in porous media. Phys Fluids 25.

Green, C.P., Ennis-King, J., 2010. Effect of Vertical Heterogeneity on Long-Term Migration of CO_2 in Saline Formations. Transp. Porous Media 82, 31-47.

Grimstad, A. A., S. Georgescu, E. Lindeberg, and J. F. Vuillaume, 2009. Modelling and Simulation of Mechanisms for Leakage of CO_2 from Geological Storage, Energy Procedia, 1(1), 2511-2518.

Han, W.S., Lee, S.Y., Lu, C.A., McPherson, B.J., 2010. Effects of permeability on CO_2 trapping mechanisms and buoyancy-driven CO_2 migration in saline formations. Water Resour Res 46.

Hassanzadeh, H., M. Pooladi-Darvish, and D. Keith, 2005. Modeling of Convective Mixing in CO_2 Storage, Journal of Canadian Petroleum Technology, 44(10).

Hassanzadeh, H., M. Pooladi-Darvish, and D. W. Keith, 2007. Scaling behavior of convective mixing, with application to geological storage of CO_2, AIChE Journal, 53(5), 1121-1131.

Hassanzadeh, H., Pooladi-Darvish, M., Keith, D.W., 2009. Accelerating CO_2 Dissolution in Saline Aquifers for Geological Storage - Mechanistic and Sensitivity Studies. Energ Fuel 23, 3328-3336.

Held, R.J., Illangasekare, T.H., 1995. Fingering of Dense Nonaqueous Phase Liquids in Porous-Media .1. Experimental Investigation. Water Resour Res 31, 1213-1222.

Hermanrud, C., T. Andresen, O. Eiken, H. Hansen, A. Janbu, J. Lippard, J., H. N. Bolas, T. H. Simmenes, G. M. G. Teige, and S. Østmo, 2009. Storage of CO_2 in saline aquifers–Lessons learned from 10 years of injection into the Utsira Formation in the Sleipner area, Energy Procedia, 1(1)

Herrera, P. A., J.M. Nordbotten, B.F. El-Faour, E. Keilegavlen, and H.K. Dahle, 2010. The impact of natural heterogeneity on CO_2 migration deep saline aquifers.

Hesse, M.A., Woods, A.W., 2010. Buoyant dispersal of CO_2 during geological storage. Geophys Res Lett 37.

Hidalgo, J. J., and J. Carrera, 2009. Effect of dispersion on the onset of convection during CO_2 sequestration, J. Fluid Mech., 640, 441.

Hitchon, B., 1996. Aquifer disposal of carbon dioxide : hydrodynamic and mineral trapping : proof of concept. Geoscience Pub., Sherwood Park, Alta.

Hofstee, C., Oostrom, M., Dane, J.H., Walker, R.C., 1998. Infiltration and redistribution of perchloroethylene in partially saturated, stratified porous media. J Contam Hydrol 34, 293-313.

Holzbecher, E. O., 1998. Modeling Density-Driven Flow in Porous Media: Principles, Numerics, Software, Springer, Berlin, Germany.

Horton, C. W., and F. T. Rogers, 1945. Convection currents in a porous medium, Journal of Applied Physics, 16(6), 367-370.

Hubbert, M.K., 1953. Entrapment of petroleum under hydrodynamic conditions. Aapg Bull 37, 1954-2026.

Ide, S.T., Jessen, K., Orr, F.M., 2007. Storage of CO_2 in saline aquifers: Effects of gravity, viscous, and capillary forces on amount and timing of trapping. International Journal of Greenhouse Gas Control 1, 481-491.

Illangasekare, T.H., Ramsey, J.L., Jensen, K.H., Butts, M.B., 1995. Experimental-Study of Movement and Distribution of Dense Organic Contaminants in Heterogeneous Aquifers. J Contam Hydrol 20, 1-25.

IPCC, 2005. IPCC special report on carbon dioxide capture and storage. Cambridge University Press, for the Intergovernmental Panel on Climate Change, Cambridge.

Jerauld, G.R., 1997. Prudhoe Bay Gas/Oil Relative Permeability. SPE Reservoir Engineering 12, 66-73.

Johnson, J. W., J. J. Nitao, and K. G. Knauss, 2004. Reactive transport modeling of CO_2 storage in saline aquifers to elucidate fundamental processes, trapping mechanisms and sequestration partitioning, Geological Storage of Carbon Dioxide, 233, 107-128.

Juanes, R., Spiteri, E.J., Orr, F.M., Blunt, M.J., 2006. Impact of relative permeability hysteresis on geological CO_2 storage. Water Resour Res 42.

Klute, A., and Dirksen, C., 1986. Conductivities and diffusivities of unsaturated soils. Methods of soil analysis. Part, 1, 687-734.

Kneafsey, T. J., and K. Pruess, 2010. Laboratory flow experiments for visualizing carbon dioxide-induced, density-driven brine convection, Transport in Porous Media, 82(1), 123-139.

Koltermann, C.E., Gorelick, S.M., 1996. Heterogeneity in sedimentary deposits: A review of structure-imitating, process-imitating, and descriptive approaches. Water Resour Res 32, 2617-2658.

Kopp, A., Class, H., Helmig, R., 2009. Investigations on CO_2 storage capacity in saline aquifers Part 1. Dimensional analysis of flow processes and reservoir characteristics. International Journal of Greenhouse Gas Control 3, 263-276.

Krevor, S.C.M., Pini, R., Li, B.X., Benson, S.M., 2011. Capillary heterogeneity trapping of CO_2 in a sandstone rock at reservoir conditions. Geophys Res Lett 38.

Krevor, S.C.M., Pini, R., Zuo, L., Benson, S.M., 2012. Relative permeability and trapping of CO_2 and water in sandstone rocks at reservoir conditions. Water Resour Res 48.

Kueper, B.H., Abbott, W., Farquhar, G., 1989. Experimental observations of multiphase flow in heterogeneous porous media. J Contam Hydrol 5, 83-95.

Kueper, B.H., Frind, E.O., 1991. Two-phase flow in heterogeneous porous media: 2. Model application. Water Resour Res 27, 1059-1070.

Kumar, A., Noh, M., Pope, G.A., Sepehrnoori, K., Bryant, S., Lake, L.W., 2005. Reservoir Simulation of CO_2 Storage in Deep Saline Aquifers. Spe J. 10, 336-348.

Kuo, C.W., Perrin, J.C., Benson, S.M., 2011. Simulation studies of effect of flow rate and small scale heterogeneity on multiphase flow of CO_2 and brine. 10th International Conference on Greenhouse Gas Control Technologies 4, 4516-4523.

Lake, L.W., 1989. Enhanced oil recovery. Prentice Hall, Englewood Cliffs, N.J.

Land, C., 1968. Calculation of Imbibition Relative Permeability for Two- and Three-Phase Flow From Rock Properties. Spe J. 8, 149-156.

Lapwood, E. R., 1948. Convection of a fluid in a porous medium, Proc. Camb. Phil. Soc., 44, 508-521.

Larkin, R., 2010. Hydrodynamic Trapping of CO_2 Geosequestered in Saline Aquifers, SPE Improved Oil Recovery Symposium, Tulsa, Oklahoma, USA.

Lengler, U., De Lucia, M., Kuhn, M., 2010. The impact of heterogeneity on the distribution of CO2: Numerical simulation of CO2 storage at Ketzin. International Journal of Greenhouse Gas Control 4, 1016-1025.

Lenhard, R.J., Oostrom, M., Simmons, C.S., White, M.D., 1995. Investigation of Density-Dependent Gas Advection of Trichloroethylene - Experiment and a Model Validation Exercise. J Contam Hydrol 19, 47-67.

Leverett, M. C., 1941. Capillary behavior in porous solids, Trans. Am. Inst. Min. Metall. Pet. Eng., 142, 152–169.

Lindeberg, E., E. Causse, and A. Ghaderi (1999), Evaluation of to what extent CO2 accumulations in the Utsira formations are possible to quantify by seismic by August 1999, SINTEF Petroleum Research report, 54.5148. 00/01/99, 13p. Restricted.

Lindeberg, E., and P. Bergmo, 2003. The long-term fate of CO_2 injected into an aquifer, Greenhouse Gas Control Technologies, 1, 489-494.

Løvoll, G., Meheust, Y., Maloy, K.J., Aker, E., Schmittbuhl, J., 2005. Competition of gravity, capillary and viscous forces during drainage in a two-dimensional porous medium, a pore scale study. Energy 30, 861-872.

Lyle, S., Huppert, H.E., Hallworth, M., Bickle, M., Chadwick, A., 2005. Axisymmetric gravity currents in a porous medium. J Fluid Mech 543, 293-302.

MacMinn, C.W., Juanes, R., 2013. Buoyant currents arrested by convective dissolution. Geophys Res Lett 40, 2017-2022.

McKibbin, R., and M J. O'Sullivan, 1980. Onset of convection in a layered porous medium heated from below, J. Fluid Mech., 96 (Part 2), 375-393.

McKibbin, R., and P. A. Tyvand, 1982. Anisotropic modelling of thermal convection in multilayered porous media, J. Fluid Mech., 118(1), 315-339.

Mori, H., 2013. The study of constitutive relationships of multi-phase flow for geological carbon sequestration. Hydrologic Science and Engineering (Master). Colorado School of Mines, Golden, CO.

Mori, H., Sakaki, T., Illangasekare, H., 2015. Laboratory study of geological carbon sequestration using surrogate fluids: Measurement and scaling of capillary pressure and saturation relationships. International Journal of Greenhouse Gas Control.

Mualem, Y., 1976. A new model for predicting the hydraulic conductivity of unsaturated porous media. Water Resour. Res., 12, 513–522.

Neufeld, J.A., Hesse, M.A., Riaz, A., Hallworth, M.A., Tchelepi, H.A., Huppert, H.E., 2010. Convective dissolution of carbon dioxide in saline aquifers. Geophys Res Lett 37.

Neuzil, C. E. (1986), Groundwater flow in low-permeability environments, Water Resources Research, 22(8), 1163-1195.

Neuzil, C. E. (1994), How permeable are clays and shales?, Water Resources Research, 30(2), 145-150.

Nield, D. A., and A. Bejan, 2006. Convection in Porous Media. Springer, USA.

Nield, D. A., and A. V. Kuznetsov, 2007. The effect of combined vertical and horizontal heterogeneity on the onset of convection in a bidisperse porous medium, International Journal of Heat and Mass Transfer, 50(17), 3329-3339.

Nield, D. A., and C. T. Simmons, 2007. A discussion on the effect of heterogeneity on the onset of convection in a porous medium, Transport in Porous Media, 68(3), 413-421.

Nooner, S. L., O. Eiken, C. Hermanrud, G. S. Sasagawa, T. Stenvold, and M. A. Zumberge (2007), Constraints on the in situ density of CO2 within the Utsira formation from time-lapse seafloor gravity measurements, International Journal of Greenhouse Gas Control, 1(2), 198-214, doi: 10.1016/S1750-5836(07)00018-7.

Nordbotten, J.M., Celia, M.A., 2011. Geological storage of CO_2 modeling approaches for large-scale simulation. John Wiley & Sons, Hoboken.

Nordbotten, J.M., Celia, M.A., Bachu, S., 2005. Injection and storage of CO_2 in deep saline aquifers: Analytical solution for CO_2 plume evolution during injection. Transp. Porous Media 58, 339-360.

Oak, M.J., Ehrlich, R., 1988. A New X-Ray Absorption Method for Measurement of Three-Phase Relative Permeability. SPE Reservoir Engineering 3.

Obi, E.O.I., Blunt, M.J., 2006. Streamline-based simulation of carbon dioxide storage in a North Sea aquifer. Water Resour Res 42.

Ohsumi, T., N. Nakashiki, K. Shitashima, and K., Hirama, 1992. Density change of water due to dissolution of carbon dioxide and near-field behavior of CO_2 from a source on deep-sea floor, Energy Convers. Mgmt., Vol. 33, No. 5-8, pp. 685-690

Oostrom, M., J. S. Hayworth, J. H. Dane, and O. Güven, 1992. Behavior of dense aqueous phase leachate plumes in homogeneous porous media, Water Resour. Res., 28(8), 2123-2134.

Oostrom, M., Dane, J.H., Wietsma, T.W., 2007. A review of multidimensional, multifluid, intermediate-scale experiments: Flow behavior, saturation imaging, and tracer detection and quantification. Vadose Zone J 6, 610-637.

Pau, G. S., Bell, J. B., Pruess, K., Almgren, A. S., Lijewski, M. J. and Zhang, K., 2009. Numerical studies of density-driven flow in CO2 storage in saline aquifers. In Procedings Tough Workshop, Lawrence Berkeley National Laboratory, Berkeley, California.

Pau, G. S., J. B. Bell, K. Pruess, A. S. Almgren, M. J. Lijewski, and K. Zhang, 2010. High-resolution simulation and characterization of density-driven flow in CO2 storage in saline aquifers, Advances in Water Resources, 33(4), 443-455.

Pentland, C.H., El-Maghraby, R., Georgiadis, A., Iglauer, S., Blunt, M.J., 2011. Immiscible Displacements and Capillary Trapping in CO_2 Storage. 10th International Conference on Greenhouse Gas Control Technologies 4, 4969-4976.

Pentland, C.H., Itsekiri, E., Al Mansoori, S.K., Iglauer, S., Bijeljic, B., Blunt, M.J., 2010. Measurement of Nonwetting-Phase Trapping in Sandpacks. Spe J. 15, 274-281.

Perrin, J.C., Benson, S., 2010. An Experimental Study on the Influence of Sub-Core Scale Heterogeneities on CO_2 Distribution in Reservoir Rocks. Transp. Porous Media 82, 93-109.

Phillips, S. L., A. Igbene, J. A. Fair, H. Ozbek, and M. Tavana, 1981. A technical databook for geothermal energy utilization, Lawrence Berkeley National Laboratory, Report LBL-12810, Berkeley, CA.

Pini, R., Benson, S.M., 2013a. Characterization and scaling of mesoscale heterogeneities in sandstones. Geophys Res Lett 40, 3903-3908.

Pini, R., Benson, S.M., 2013b. Simultaneous determination of capillary pressure and relative permeability curves from core-flooding experiments with various fluid pairs. Water Resour Res 49, 3516-3530.

Pini, R., Krevor, S.C.M., Benson, S.M., 2012. Capillary pressure and heterogeneity for the CO_2/water system in sandstone rocks at reservoir conditions. Adv Water Resour 38, 48-59.

Plug, W.J., Bruining, J., 2007. Capillary pressure for the sand-CO_2-water system under various pressure conditions. Application to CO_2 sequestration. Adv Water Resour 30, 2339-2353.

Prasad, A., and C. T. Simmons, 2003. Unstable density-driven flow in heterogeneous porous media: A stochastic study of the Elder [1967b] "short heater" problem, Water Resour. Res., 39(1), 1007.

Pruess, K., Garcia, J., 2002. Multiphase flow dynamics during CO_2 disposal into saline aquifers. Environ Geol 42, 282-295.

Pruess, K., Oldenburg, C., Moridis, G., 1999. TOUGH2 User's Guide, Version 2.0.

Pruess, K., Spycher, N., 2007. ECO2N - A fluid property module for the TOUGH2 code for studies of CO_2 storage in saline aquifers. Energ Convers Manage 48, 1761-1767.

Pruess, K., Xu, T.F., Apps, J., Garcia, J., 2003. Numerical Modeling of aquifer disposal of CO_2. Spe J. 8, 49-60.

Pruess, K., and K. Zhang, 2008. Numerical modeling studies of the dissolution-diffusion-convection process during CO_2 storage in saline aquifers, Lawrence Berkeley National Laboratory, Paper LBNL-1243E, Berkeley, CA.

Qi, R., LaForce, T.C., Blunt, M.J., 2009. Design of carbon dioxide storage in aquifers. International Journal of Greenhouse Gas Control 3, 195-205.

Rahunanthan, A., Furtado, F., Marchesin, D., Piri, M., 2014. Hysteretic enhancement of carbon dioxide trapping in deep aquifers. Computat Geosci.

Ranganathan, P., R. Farajzadeh, H. Bruining, and P. L. Zitha, 2012. Numerical simulation of natural convection in heterogeneous porous media for CO_2 geological storage, Transport in Porous Media, 95(1), 25-54.

Rayleigh, L., 1916. On convection currents in a horizontal layer of fluid, when the higher temperature is on the underside, The London, Edinburgh, and Dublin Philosophical Magazine and Journal of Science, 32(192), 529-546.

Rees, D. A. S., and A. P. Bassom, 2000. The onset of Darcy-Benard convection in an inclined layer heated from below, Acta Mechanica, 144(1), 103-118.

Remy, N., Boucher, A., Wu, J., 2009. Applied geostatistics with SGeMS : a user's guide. Cambridge University Press, Cambridge, UK ; New York.

Riaz, A., Hesse, M., Tchelepi, H.A., Orr, F.M., 2006. Onset of convection in a gravitationally unstable diffusive boundary layer in porous media. J Fluid Mech 548, 87-111.

Richardson, J. G., 1961. Flow through porous media. Handbook of Fluid Dynamics, 16, edited by V.I Streeter, McGraw-Hill Nook Co., Inc., New York, 16-3 through 16-112.

Ringrose, P.S., Sorbie, K.S., Corbett, P.W.M., Jensen, J.L., 1993. Immiscible flow behaviour in laminated and cross-bedded sandstones. J Petrol Sci Eng 9, 103-124.

Saadatpoor, E., Bryant, S.L., Sepehrnoori, K., 2010. New Trapping Mechanism in Carbon Sequestration. Transp. Porous Media 82, 3-17.

Saeedi, A., Rezaee, R., Evans, B., Clennell, B., 2011. Multiphase flow behaviour during CO2 geo-sequestration: Emphasis on the effect of cyclic CO2-brine flooding. J Petrol Sci Eng 79, 65-85.

Sakaki, T., Illangasekare, T.H., 2007. Comparison of height-averaged and point-measured capillary pressure-saturation relations for sands using a modified Tempe cell. Water Resour Res 43.

Sakaki, T., Limsuwat, A., Smits, K. M., Illangasekare, T. H., 2008. Empirical two-point α-mixing model for calibrating the ECH2O EC-5 soil moisture sensor in sands. Water Resour Res, 44(4).

Sakaki, T., A. Limsuwat, T. H. Illangasekare, 2011. A simple method for calibrating dielectric soil moisture sensors: Laboratory validation in sands, Vadose Zone Journal, 10:526-531.

Sakaki, T., Schulte, P. E., Cihan, A., Christ, J. A., Illangasekare, T. H., 2013. Airflow Pathway Development as Affected by Soil Moisture Variability in Heterogeneous Soils. Vadose Zone Journal, 12(1).

Schincariol, R. A., and F. W. Schwartz, 1990. An experimental investigation of variable density flow and mixing in homogeneous and heterogeneous media, Water Resour. Res., 26(10), 2317-2329.

Schincariol, R. A., F. W. Schwartz, and C. A. Mendoza, 1994. On the generation of instabilities in variable density flow, Water Resour. Res., 30(4), 913-927.

Schincariol, R. A., F. W. Schwartz, and C. A. Mendoza, 1997. Instabilities in variable density flows: Stability and sensitivity analyses for homogeneous and heterogeneous media, Water Resour. Res., 33(1), 31-41.

Schroth, M.H., Ahearn, S.J., Selker, J.S., Istok, J.D., 1996. Characterization of miller-similar silica sands for laboratory hydrologic studies. Soil Sci Soc Am J 60, 1331-1339.

Schroth, M.H., Istok, J.D., Selker, J.S., Oostrom, M., White, M.D., 1998. Multifluid flow in bedded porous media: laboratory experiments and numerical simulations. Adv Water Resour 22, 169-183.

Simmons, C. T., T. R. Fenstemaker, and J. M. Sharp, 2001. Variable-density groundwater flow and solute transport in heterogeneous porous media: approaches, resolutions and future challenges, Journal of Contaminant Hydrology, 52(1), 245-275.

Simmons, C.T., P. Bauer-Gottwein, T. Graf, W. Kinzelbach, H. Kooi, L. Li, V. Post, H. Prommer, R. Therrien, C. Voss, J. Ward, and A. Werner, 2010. Variable density groundwater flow: From modelling to applications, In Groundwater Modelling in Arid and Semi-Arid Areas, International Hydrology Series, ed. H. Wheater, S. Mathias, and X. Li, 87–118, Cambridge, UK: Cambridge University Press.

Simpson, M. J., and T. P. Clement, 2003. Theoretical analysis of the worthiness of Henry and Elder problems as benchmarks of density-dependent groundwater flow models, Advances in Water Resources, 26(1), 17-31.

Singh, V., Cavanagh, A., Hansen, H., Nazarian, B., Iding, M., Ringrose, P., 2010. Reservoir Modeling of CO_2 Plume Behavior Calibrated Against Monitoring Data From Sleipner, Norway, SPE Annual Technical Conference and Exhibition, Florence, Italy.

Smits, K. M., T. Sakaki, A. Limsuwat, and T. H. Illangasekare, 2010. Thermal conductivity of sands under varying moisture and porosity in drainage–wetting cycles, Vadose Zone Journal, 9(1), 172-180

Spiteri, E.J., Juanes, R., Blunt, M.J., Orr, F.M., 2005. Relative-Permeability Hysteresis: Trapping Models and Application to Geological CO_2 Sequestration, SPE Annual Technical Conference and Exhibition, Dallas, Texas.

Spiteri, E.J., Juanes, R., Blunt, M.J., Orr, F.M., 2008. A new model of trapping and relative permeability hysteresis for all wettability characteristics. Spe J. 13, 277-288.

Stegemeier, G.L., 1977. Mechanisms of Entrapment and Mobilization of Oil in Porous Media, in: Shah, D.O.a.S., R. S. (Ed.), Improved oil Recovery by Surfactant and Polymer Flooding. Elsevier, New York, p. 588.

Suekane, T., Nobuso, T., Hirai, S., Kiyota, M., 2008. Geological storage of carbon dioxide by residual gas and solubility trapping. International Journal of Greenhouse Gas Control 2, 58-64.

Suekane, T., Soukawa, S., Iwatani, S., Tsushima, S., Hirai, S., 2005. Behavior of supercritical CO2 injected into porous media containing water. Energy 30, 2370-2382.

Tchelepi, H.A., Orr, F.M., 1994. Interaction of Viscous Fingering, Permeability Heterogeneity, and Gravity Segregation in Three Dimensions. SPE Reservoir Engineering 9, 266-271.

Tokunaga, T. K., Wan, J., Jung, J. W., Kim, T. W., Kim, Y., Dong, W., 2013. Capillary pressure and saturation relations for supercritical CO2 and brine in sand: High-pressure Pc (Sw) controller/meter measurements and capillary scaling predictions. Water Resources Research, 49(8), 4566-4579.

Torp, T.A., Gale, J., 2004. Demonstrating storage of CO_2 in geological reservoirs: The Sleipner and SACS projects. Energy 29, 1361-1369.

Trevisan, L., Cihan, A., Agartan, E., Mori, H., Fagerlund, F., Birkholzer, J.T., Zhou, Q., Illangasekare, T.H., 2014. Investigation of mechanisms of supercritical CO_2 trapping in deep saline reservoirs using surrogate fluids at ambient laboratory conditions. International Journal of Greenhouse Gas Control 29, 35-49.

Trevisan, L., 2015. Study of trapping mechanisms of supercritical carbon dioxide in deep heterogeneous geological formations through intermediate-scale testing and modeling, Civil and Environmental Engineering. Colorado School of Mines, Golden, CO.

Tsai, P. A., K. Riesing, and H. A. Stone, 2013. Density-driven convection enhanced by an inclined boundary: Implications for geological CO_2 storage, Physical Review E, 87(1), 011003.

Tsang, C.F., Benson, S.M., Kobelski, B., Smith, R.E., 2002. Scientific considerations related to regulation development for CO_2 sequestration in brine formations. Environ Geol 42, 275-281.

Tuller, M., and Or, D., 2002. Unsaturated Hydraulic Conductivity of Structured Porous Media A Review of Liquid Configuration–Based Models. Vadose Zone Journal, 1(1), 14-37.

van Genuchten, M.T., 1980. A Closed-Form Equation for Predicting the Hydraulic Conductivity of Unsaturated Soils. Soil Sci Soc Am J 44, 892-898.

Vargas-Johnson, J., 2014. Development of experimental methods for intermediate scale testing of deep geologic CO_2 sequestration trapping processes at ambient laboratory conditions, Hydrologic Science and Engineering. Colorado School of Mines, Golden, CO.

Voss, C. I., and W. R. Souza, 1987. Variable density flow and solute transport simulation of regional aquifers containing a narrow freshwater-saltwater transition zone, Water Resour. Res., 23(10), 1851-1866.

Whittaker, S., Rostron, B., Hawkes, C., Gardner, C., White, D., Johnson, J., Chalaturnyk, R., Seeburger, D., 2011. A decade of CO_2 injection into depleting oil fields: monitoring and research activities of the IEA GHG Weyburn-Midale CO_2 Monitoring and Storage Project. 10th International Conference on Greenhouse Gas Control Technologies 4, 6069-6076.

Wietsma, T. W., M. Oostrom, M. A. Covert, T. E. Queen, and M. J. Fayer, 2009. An automated tool for three types of saturated hydraulic conductivity laboratory measurements, Soil Science Society of America Journal, 73(2):466-470.

Wildenschild, D., Armstrong, R.T., Herring, A.L., Young, I.M., Carey, J.W., 2011. Exploring capillary trapping efficiency as a function of interfacial tension, viscosity, and flow rate. Energy Procedia 4, 4945-4952.

Zhang, C.Y., Werth, C.J., Webb, A.G., 2008. Investigation of surfactant-enhanced mass removal and flux reduction in 3D correlated permeability fields using magnetic resonance imaging. J Contam Hydrol 100, 116-126.

Zhao, B., MacMinn, C.W., Huppert, H.E., Juanes, R., 2014. Capillary pinning and blunting of immiscible gravity currents in porous media. Water Resour Res 50, 7067-7081.

Zhao, B.Z., MacMinn, C.W., Szulczewski, M.L., Neufeld, J.A., Huppert, H.E., Juanes, R., 2013. Interface pinning of immiscible gravity-exchange flows in porous media. Phys Rev E 87.

Zweigel, P., R. Arts, A. E. Lothe, and E. B. Lindeberg, 2004. Reservoir geology of the Utsira Formation at the first industrial-scale underground CO_2 storage site (Sleipner area, North Sea), Geological Society, London, Special Publications, 233(1), 16